The Dissertation Committee for Marta Sans Escofet Certifies that this is the approved version of the following Dissertation:

Advancements in Ambient Ionization Mass Spectrometry Towards Improved Ovarian Cancer Research and Diagnosis

Committee:

Livia Schiavinato Eberlin, Supervisor

Jennifer S. Brodbelt

Richard M. Crooks

Robert Tibshirani

Advancements in Ambient Ionization Mass Spectrometry Towards Improved Ovarian Cancer Research and Diagnosis

by

Marta Sans Escofet

Dissertation

Presented to the Faculty of the Graduate School of

The University of Texas at Austin

in Partial Fulfillment

of the Requirements

for the Degree of

Doctor of Philosophy

The University of Texas at Austin

May 2020

Dedication

To my parents, Ramon and Joana

Acknowledgements

I am extremely grateful for all the opportunities and support I have received during graduate school. It has been a truly exciting and enlightening experience, and I owe that to everyone who has been with me throughout this journey. First of all, I would like to thank my parents, Ramon and Joana, and my sister Mireia for always being my number one fans. Mom and dad, staying close to you despite being 5,000 miles apart has been a source of strength for me every day. Thank you for always being there during my good and bad moments and for your advice and words of encouragement. Your relationship inspires me, I admire everything you have accomplished together for our family with all your hard work. Thank you for teaching me the importance of enjoying everything you do and to live life at the fullest. Love you and miss you very much. To my sister Mireia, thank you for always believing in me and for being my first teacher when I was still your little baby sister. Thank you for making me an auntie to the cutest little boy, Biel. Receiving your pictures and videos with him always puts a smile on my face and lightens up my days. I have always admired how passionate you are about everything that you do, you have the biggest heart in the world, and I love you so very much. To the rest of my family, my grandparents, cousins, aunts, and uncles, thank you for all your support and for following my American adventures, I love you all. To my 95-year-old grandparent, Paco, thank you for teaching me the importance of diligent work from a young age. “Voluntat i constància” (“will and persistence”) are your two favorite words. You are the definition of resilience. Your desire to continue to learn new things every day is an inspiration to me and many others. Thank you for always keeping an interest in everything I do. I admire and love you so much. To my childhood friends from home, after all these years growing up together you have

become an extension of my family, I miss and love you all. To Rebe and Claudia, thank you sharing my passion for science, for coming to visit, and for bringing with you a piece of home. I am so thankful we got to spend last year on the same side of the ocean again and share more adventures together. Claudia, I love sharing the PhD life with you, and I hope we get to continue our Thanksgiving tradition for many more years. I love you both dearly.

To my graduate advisor and mentor, Professor Livia S. Eberlin, I will never be able to thank you enough for everything you have done for me. These past four and a half years have gone by so quickly and I have enjoyed them very much. You have had such a positive impact on my PhD experience and my development as a scientist; thank you for believing in me and always offering your support and guidance. It has been a pleasure to accompany you during the beginning of your career as a professor and to witness all the great things you have already accomplished with your hard work and dedication. I have learned so much from you both professionally and personally and I am so grateful to have you in my life. Your commitment and love to your family is inspiring and I feel empowered having someone like you to look up to during my future life and career endeavors. I hope that I can continue to represent everything you have taught me while I become an independent scientist, and that one day I can give it all back to future generations. Thank you, Livia!

To everyone in the Eberlin lab, I feel incredibly lucky to have gotten the chance to share this journey with you all, past and current members, new and older ones. I don't think I will ever find such a welcoming and nice environment to come and work in every day. I will miss our daily lunch sessions so much! To Jialing, thank you for everything you have taught me and for all your help during my graduate school career. Thank you for always taking care of me and treating me like your little sister, I appreciate our relationship very much. Clara, I am so thankful that I got to share my graduate experience with you. We

have been together since the first semester, and I will really miss seeing you every day. Thank you for always making me laugh, for sharing all your stories with me and for listening to mine. I am very proud of everything you have accomplished and cannot wait to see what comes next for you; it is going to be awesome. To Alena, Kyana, and Rachel, thank you. We have shared so much together; I have seen you go from first year graduate students to the amazing scientists you have now become, which makes me feel so proud! Thank you for always being there for me. To Anna and Mike, thank you for being the best office buddies, you both are hilarious, and I appreciate you so much. Anna, thank you for all your help with experiments and data analyses (and for the emotional support), could not have done all those droplet images without you! Mike, I will miss our sandwich and taco runs for lunch! Mary, my little editor, thank you so much for all your help and for always being so kind. To Abby, thank you for your support and honesty, and for all the hugs. Sydney, thank you for your positive energy even in the stressful moments, like the once we have been experiencing lately! Monica, thank you for being the sweetest person and for all your hard work on the MADI project. Keep it up! You will do so great. To Sunil, thank you for being such a great and fast learner and for all your great work this past year. To the newer members, Praj, Ashish, Meredith, it has been great to spend some time with you and I wish you all the best. I would also like to acknowledge John, the other OG! Thank you for all your help and productive work all these years, you are such a genius but most importantly a great person as well. And of course, thank you to the irreplaceable Angie! Thank you for making even the most complicated problems seem easy to solve, and for your super positive and vibrant energy. Thank you to the best lab ever, I will miss you all very much.

I have also been very fortunate to have met some great people in the chemistry department, my fellow fifth year graduate students, my “bunch of nerds”. I am so glad we

got to share graduate school together and thank you for making it more fun. To Olja, my roomie, thank you for being such a loyal friend and for always being there for me. Thank you for understanding and sharing my struggles being away and so far from home. I miss you already! To Michelle, thank you for being so sweet and for always being ready to have fun and unwind. To Josh, Mason, Ryan, Dylan, Jason, you guys are the best and I will miss you all! I hope we can all stay in touch and wish you all the best.

I would also like to thank my committee members for their time and support. Prof. Brodbelt, thank you for your guidance and assistance. I really appreciate the relationship we have developed throughout these years, and I will miss our tennis sessions! To Prof. Tishirani, it has been such an honor to get to collaborate with you and I really appreciate you agreeing to participate as a member of my committee. Thank you for being so kind and for all your help with our work. To Prof. Crooks, thank you for your time and for being so supportive of our group and research, I really appreciate it. I am also very grateful for all the great administration and resources at the College of Natural Sciences and the department of Chemistry at UT. Betsy Hamblen, thank you for being the best department mom and for always helping us get through anything! You are so kind. To Po-Tsan Ku, thank you for helping me navigate through the job finding process and for always greeting me with encouragement and smiles. To my great collaborators, Bryan Wygant and Prof. Mullins, thank you very much for your help! Bryan, thank you for introducing me to Stella and for all the hard work that you have put in that project. To Tim Hooper, thank you so much for making a lot of our experiments possible with all your hard work developing anything and everything that we ask! And thank you for always being so nice and cheerful.

One of the highlights of my doctoral work has been getting to collaborate with great scientists and clinicians at Baylor College of Medicine and at the MD Anderson Cancer Research Center and to witness firsthand the excellent work they do every day. To Dr.

Sood, Dr. Liu, Dr. Suliburk, Dr. Carter, among others, thank you so much for all your help and guidance with our projects. I have learned so much working with all of you and I am extremely grateful for that.

I would also like to express my gratitude to the funding agencies that have supported the work described in this dissertation, the National Institute of Health, the National Cancer Institute, the Cancer Prevention and Research Institute of Texas and the Welch Foundation. I am also grateful and honored to have received the Excellence in Research award from the department of Chemistry and the University Graduate Continuing Fellowship from the Office of Graduate Studies at UT.

And finally, I would like to thank my fiancé, Oscar, for always supporting my career aspirations and believing I can do it all. Thank you for following me to Austin, for listening to my sciency spiels and being curious about my research, and for always having the best advice. You are my rock, your words of encouragements throughout this journey have been truly invaluable and I love you very much.

Abstract

Advancements in Ambient Ionization Mass Spectrometry Towards Improved Ovarian Cancer Research and Diagnosis

Marta Sans Escofet, PhD

The University of Texas at Austin, 2020

Supervisor: Livia Schiavinato Eberlin

Ovarian cancer is a highly aggressive disease accounting for the majority of deaths from gynecological malignancies. Investigating the molecular mechanisms driving disease development and progression can improve early detection and drive the introduction of novel treatment strategies to ameliorate patient outcomes. Enhancing the accuracy and efficiency of ovarian cancer surgeries by introducing molecular information to rapidly assess tissue samples and guide cancer excision could also offer significant benefits to the management of ovarian cancer. Ambient ionization mass spectrometry (MS) methods are capable of obtaining biomolecule information directly from tissue samples with minimal sample preparation requirements and experimental simplicity, providing a suitable platform to conduct these investigations. Desorption electrospray ionization (DESI) was introduced in 2004 as the first ambient ionization MS technique and has been widely applied to investigate healthy and cancerous human tissue sections towards identifying potential cancer molecular markers and developing predictive statistical models towards improved cancer diagnosis. Alternative ambient ionization methods utilizing direct liquid extraction-based mechanisms have also been developed to improve the analytical

capabilities of ambient ionization MS and expand applications in tissue analysis and cancer diagnosis. Overall, this dissertation presents the application and development of ambient ionization MS methods for ovarian cancer research and improved diagnostics. First, the use of DESI-MS to distinguish between malignant and borderline ovarian tumors, as well as determine metabolic markers associated with disease aggressiveness is described. Going beyond cancer diagnosis, we next apply DESI-MS to identify trends in metabolic composition resulting from the expression of the fatty acid binding protein (FABP4) gene, a molecular determinant of ovarian cancer metastasis and residual disease post-surgery. An alternative liquid extraction-based ambient ionization MS approach is also described in this dissertation to improve spatial control in MS imaging and profiling applications from biological tissue sections. The capabilities of this method are tested with various biological samples, including ovarian cancer tissue. Finally, we discuss the development of an ambient MS technology, the MasSpec Pen, envisioned for nondestructive, rapid, *ex vivo* and *in vivo* assessment of surgical specimens. We demonstrate the capabilities of this system to provide accurate diagnoses from ovarian fresh-frozen specimens *ex vivo* across different sample sets, utilizing various healthy and ovarian cancer tissue types and mass spectrometry platforms.

Table of Contents

List of Tables

List of Figures

Chapter 1: Introduction

AMBIENT IONIZATION MASS SPECTROMETRY FOR DIRECT TISSUE ANALYSIS AND IMPROVED CANCER DIAGNOSIS: FROM BIOMEDICAL RESEARCH TO INTRAOPERATIVE USE

The powerful capabilities of mass spectrometry (MS) for biomolecule analysis have transformed bioanalytical and biomedical research, unwrapping new opportunities in biomarker discovery and cancer diagnostics. The development of electrospray ionization (ESI) and matrix assisted laser desorption ionization (MALDI) in the early 90's revolutionized the use of MS by facilitating the characterization of intact biomolecules with improved analytical performance (1-3). MALDI-MS analyses also provided the capability to desorb and ionize analytes from a solid-state sample surface, allowing the investigation of heterogenous environments at both cellular and molecular levels directly from tissue sections, and driving the field towards molecular imaging applications with MS (4,5). Combining the rich molecular and spatial information obtained from tissue MS imaging with advanced data modeling and statistics tools has since become an incredibly powerful approach to investigate cancer pathogenesis, identify potential molecular markers, and develop molecular classifiers for improved cancer diagnosis (6,7). With the introduction of ambient ionization techniques in 2004, rich molecular information could now be obtained *in situ*, under ambient conditions, with experimental simplicity and minimal sample preparation, thus more suitable for the analysis of biological tissue samples and introduction into a clinical workflow (8,9). In the last two decades, ambient ionization MS methods have been increasingly used for biomedical and cancer research, with particular focus on tissue imaging and spatial profiling (10). New developments and methods aimed at improving the analytical and clinical capabilities of ambient MS to facilitate implementation in various research and clinical environments have also been pursued

(11,12). Nowadays, ambient ionization MS methods are applied or envisioned for use in various facets of cancer research and diagnostics, from tissue imaging and molecular profiling in basic and translational research studies, to rapid assessment of clinical samples for preoperative or intraoperative use, including *in vivo* use during cancer surgeries (Figure 1.1).

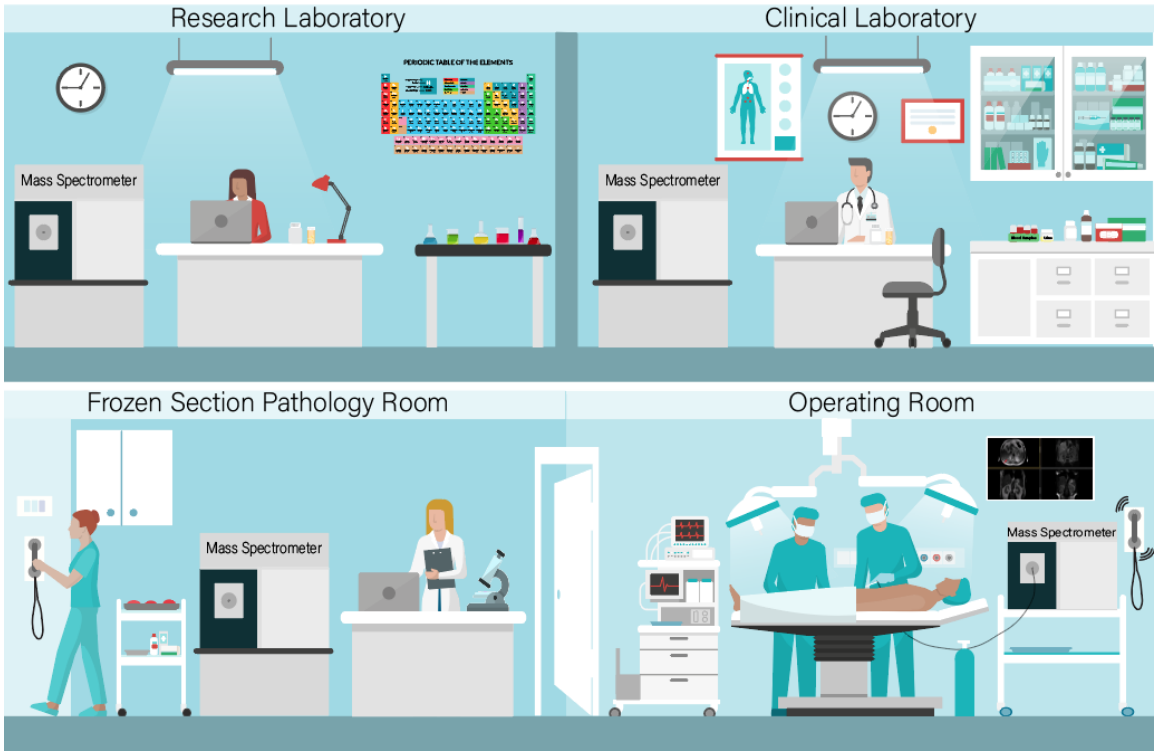

Figure 1.1: Applications and envisioned uses of ambient ionization MS technologies in biomedical research and the clinical space.

Ambient ionization MS technologies have been extensively used to evaluate biological samples by biomedical and bioanalytical researchers. The capabilities for direct and *in situ* analysis of biological samples with ambient ionization MS methods provide high suitability for introduction into various diagnostic workflows in clinical laboratories. Ambient ionization MS technologies for rapid intraoperative evaluation of surgical specimens could be incorporated in the frozen section pathology laboratory and the operating room for direct *ex vivo* and *in vivo* analysis.

Desorption electrospray ionization (DESI), developed by the Cooks group at Purdue University in 2004, was the first and to date most widely used ambient ionization MS technique for tissue imaging towards improved cancer diagnosis (8). DESI utilizes a spray of charged droplets to desorb and ionize molecules from the surface analyzed (Figure 1.2A) (13). In the imaging mode, the spray is rastered across the surface of the tissue sample, providing molecular information associated to a particular location, or pixel, as shown in Figure 1.2B. The spatial resolution or pixel size of the images obtained with DESI-MS is commonly between 100-200 μm, allowing to resolve histological features within or above those dimensions. Biological sample analysis by this method requires minimal sample preparation, only involving the deposition of a frozen section of the tissue sample of interest on a glass slide. Using a histologically compatible solvent system for DESI-MS analysis, tissue integrity can be preserved to allow subsequent evaluation by pathology of the same tissue section analyzed (14). Most suited towards the detection of smaller biomolecules (<1500 Da) such as metabolites, fatty acids, and various types of lipids, DESI-MS has been widely used to image human tissue samples and investigate metabolic aberrations associated with multiple cancer types (10,15-19). Various studies, for example, have focused on the diagnosis and stratification of brain cancer with DESI-MS , allowing identification of cancer subtype, grade, tumor cell concentrations (20,21), and prognostic genetic mutations (22), based on the detection of a metabolic pattern or specific oncometabolites.

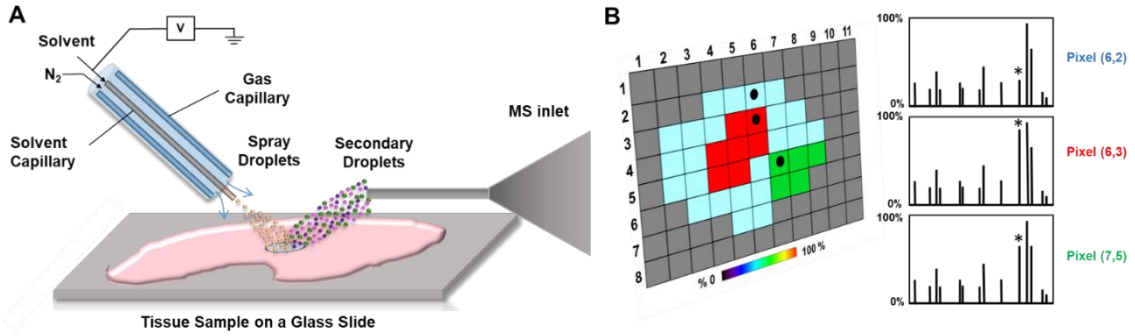

Figure 1.2: DESI-MS imaging.

A spray of charged solvent droplets are directed to the sample surface for desorption and ionization of surface analytes (A). In a DESI-MS imaging experiment, spatial coordinates are recorded for the data obtained, with each pixel corresponding to a single mass spectrum, allowing correlation of spatial and molecular information (B).

The success of DESI-MS in cancer research has also inspired the development of alternative liquid extraction approaches for tissue section analysis and imaging under ambient conditions (23). Utilizing a direct liquid extraction- instead of a spray-based approach, methods such as liquid microjunction surface sampling (LMJ-SS) (24), liquid extraction surface analysis (LESA) (25), and nanospray desorption electrospray ionization (nano-DESI) (26), have also been applied for spatial profiling and imaging of tissue samples. For example, an LMJ-SS system was recently used to determine hormone levels from pituitary tumor tissue sections, demonstrating potential to provide protein biomarker information by ambient ionization MS at the time of surgical resection (27). Overall, the longer solvent-sample interaction times provided by direct liquid extraction coupled to a direct nanospray or an ESI source have led to enhanced ionization efficiency and overall sensitivity compared to DESI-MS. In terms of spatial resolution, nano-DESI has allowed to resolve spatial features close to cellular dimensions (>10 μm)) (28,29), while the LMJ-SSP and LESA have been applied to sample larger areas (600-1000 μm) in biological tissues (30). Importantly, the area sampled by liquid extraction techniques is commonly

restricted to the diameter of the capillaries or probes used, which is intrinsic to each approach and thus results in limited and impractical tunability of the spatial resolution. Therefore, methods that would enable to practically and precisely tune spatial resolution in liquid extraction ambient ionization MS could improve performance for direct MS profiling and imaging by adapting the true pixel size to the desired application. A summary of the characteristics and performance metrics for these methods is provided in Table 1.1.

Table 1.1: Liquid extraction ambient ionization MS methods for tissue section analysis. * A spatial resolution as low as 20 µm has been reported for DESI-MS (31) , but larger pixel sizes are more commonly obtained for these experiments. ** Detection of proteins by DESI-MS was enhanced by ion mobility (32,33).[1]

Method	Mechanism	Spatial Resolution (SR – µm)	How is SR controlled?	Molecular Coverage
DESI 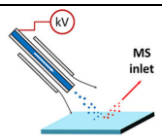	Charged droplet spray (<5 µL/min)	100-200*	Solvent flowrate	Metabolites, lipids, proteins (<16,000 Da).**
LMJ-SSP 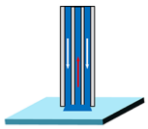	Liquid extraction by continuous solvent flow (<100 µL/min)	600-1000	Probe diameter	Metabolites, lipids, proteins (< 16,000 Da).
LESA 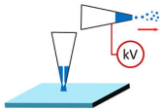	Liquid extraction by discrete droplet deposition and re-aspiration (1-2 µL)	600-1000	Pipette tip diameter	Metabolites, lipids, proteins (< 64,000 Da).
Nano-DESI 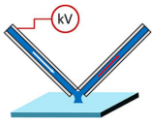	Liquid extraction by continuous solvent flow (<1 µL/min)	10-100	Solvent flowrate and capillary diameter	Metabolites, lipids, proteins (<16,000 Da).

[1] The figures in this table are adapted with permission from Laskin J, Lanekoff I. Ambient Mass Spectrometry Imaging Using Direct Liquid Extraction Techniques. Anal Chem 2016; 88, 1, 52-73. Copyright © 2016, American Chemical Society.

Although powerful, the ambient ionization MS methods described above are limited to the analysis of thin tissue sections or flat biological surfaces, and currently best suited for trained and skilled users in a research laboratory. In the clinical space, the capability to provide an easy-to-use MS-based tool capable of acquiring powerful molecular information from *in vivo* or freshly excised tissue specimens during a surgical procedure, removing the need for tissue excision and processing, would be highly transformative. Towards that end, a new realm of ambient ionization MS methods offering the exciting opportunity to provide real-time surgical guidance and tissue diagnosis based on molecular information provided by MS analyses has emerged. Envisioned for use by surgeons and surgical staff in the operating room, additional considerations such as technical simplicity, automation, biocompatibility, and patient safety are of critical importance for these methods. The first MS-based technique developed for *in vivo*, intraoperative use is rapid evaporative ionization MS, or the "iKnife", which combines a hand-held electro-cauterization device, a common tool used during surgical operations, with MS (34,35). The iKnife technology provides means to transfer and detect ions generated through thermal evaporation during tissue electrocauterization, thus relying on tissue damage for ion production. In the last ten years, various other approaches for *in vivo* MS analysis have also been developed, utilizing laser, liquid, or solid extraction probes, among others, aiming to minimize tissue damage during analysis (36) (Figure 1.3). Although still under development, some of these methods have shown promising results for direct, rapid, *ex vivo* cancer diagnosis, and feasibility for *in vivo* use during human surgery has been demonstrated during pilot clinical tests (35,37,38).

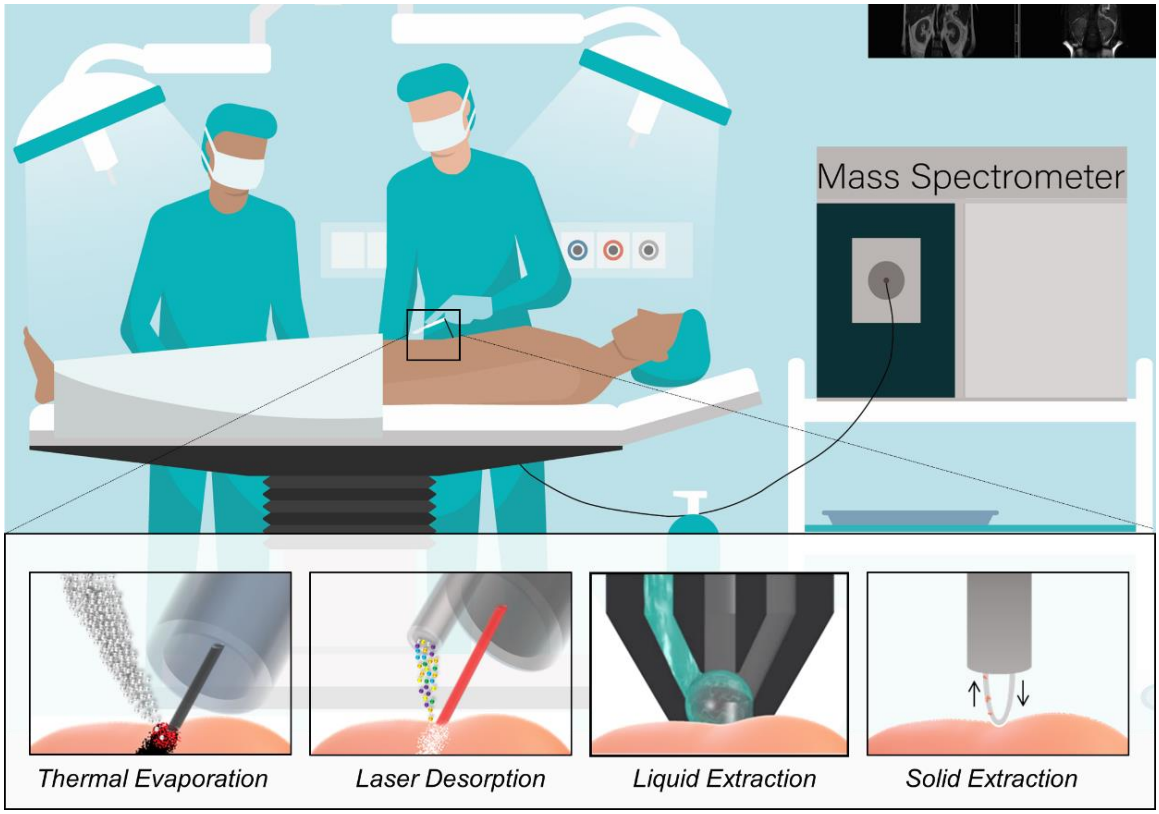

Figure 1.3: Ambient ionization MS hand-held probes developed for *in vivo* and *ex vivo* use during human surgeries for near-real time tissue assessment and cancer diagnosis.

CRITICAL NEED FOR IMPROVED MOLECULAR CHARACTERIZATION AND CLINICAL MANAGEMENT OF OVARIAN CANCER

Ambient ionization MS technologies provide a powerful set of tools to improve the detection and management of ovarian cancer. Ovarian cancer is the fifth leading cause of all cancer-related deaths in women, responsible for the majority of deaths associated with gynecological malignancies (39,40). The highly aggressive behavior and commonly late detection of this disease result in low 5-year survival rates, averaging at 47%, and reaching as low as 30% for metastatic ovarian cancer. Recurrence rates up to 80% have been reported, attributed to residual disease after surgery, as well as resistance to platinum-based

chemotherapy, among other factors (41). It is estimated that in 2020, about 22,000 new cases will be diagnosed in the U.S. (42). Ovarian cancer is highly heterogeneous in histology and includes great molecular diversity, with serous carcinoma being the most common form. High-grade serous carcinomas (HGSC) are rapidly growing serous carcinomas characterized by tumor cells with large and atypical irregular nuclei, as well as various genetic aberrations, such as those affecting the BRCA1, BRCA2 and TP53 pathways (43). HGSC are the most aggressive type, and account for 90% of all serous ovarian cancers. Borderline serous tumors (BOT), on the other hand, are benign neoplasms with slow proliferation rates and no stromal invasion (44). BOT can develop into malignant low-grade serous carcinomas (LGSC), which are significantly rarer than HGSC and present with improved clinical prognosis despite responding less frequently to platinum-based chemotherapy (45). LGSC are histologically defined by micro-papillary patterns and tumor cells with small uniform nuclei (41). While it is well established that ovarian serous carcinomas develop through different molecular pathways, further studies are needed to understand the mechanisms driving aggressiveness and invasiveness (46). Moreover, a large proportion of ovarian serous carcinomas are now believed to originate from precursor lesions in the fallopian tubes instead of the ovarian epithelium (47). This new hypothesis has resulted in a shift in ovarian cancer research and prevention strategies, raising additional questions about the tumorigenesis of this deadly disease (48).

The primary course of treatment for serous ovarian cancer patients is a combination of surgical resection and chemotherapy. Cytoreductive surgery with the objective of removing as much tumor volume as possible is critical to maximize patient survival, as residual disease post-surgery has been associated with poor patient prognosis and recurrent disease (49). Surgical resection is also commonly the first chance to diagnose and stage the disease, which is critical to establish a targeted treatment and management plan (50). Thus,

providing an accurate diagnostic assessment at the time of surgical intervention as well as evaluating the extent of the disease during cytoreduction to minimize residual disease is critical to guide patient care. Prior to surgical intervention, the administration of chemotherapy can facilitate cytoreductive efforts for advanced and aggressive ovarian cancers by decreasing tumor volume and proliferation (51). Yet, the resulting scarring or fibrotic tissue can be challenging to distinguish from other tumor and metastatic sites, complicating resection and leading to poor surgical outcomes. Current intraoperative diagnostic procedures to evaluate ovarian tissue biopsies and guide surgical resection involve traditional histopathological evaluation, or frozen section analysis, which is time (~30 minutes) and labor-intensive and requires skilled technicians and pathologists to produce and interpret results. Thus, this method can prolong operative time, which is costly and can subject the patient to increased risks of infection and extended hypoperfusion from anesthesia. If a diagnosis cannot be derived intraoperatively, specimens are processed post-operatively over several days, which entails increased health care costs, and places the patient at additional health risks, discomfort and anxiety (52).

Evaluating the molecular composition of ovarian cancer tissues by ambient ionization MS methods for improved molecular characterization and tissue diagnosis can be a powerful approach to address current challenges in the clinical management of ovarian cancer. Investigating metabolic changes associated with cellular histology and genetic expression can provide important insights into the pathogenesis of serous ovarian cancer and help determine molecular features associated with disease aggressiveness and metastasis. Ambient MS imaging approaches offer suitable capabilities to conduct these investigations, allowing correlation of molecular and spatial information, while preserving sample integrity for subsequent pathological evaluation. Identification of potential ovarian cancer markers by ambient MS methods could also lead to new targets for innovative

treatment approaches, thus improving patient survival and decreasing disease recurrence. The generation of classification algorithms capable of rapidly (~ 5 min) providing a diagnosis based on metabolic data obtained by ambient MS analysis, such as DESI-MS, could help introduce detailed molecular information to current workflows for ovarian cancer frozen section evaluation, providing complementary guidance for more accurate diagnosis and personalized patient care. Translating these diagnostic capabilities to the operating room through direct *in vivo* tissue assessment by MS could be highly transformative by providing near-real time diagnostic feedback to expedite surgical decision-making. Discrimination of tumor masses and metastatic sites from healthy or fibrotic tissue directly through *in vivo* MS sampling prior to excision could greatly facilitate and expedite ovarian cancer cytoreduction, diminishing likelihood of residual disease and damage to healthy tissue. Altogether, the use of ambient MS technologies towards improved molecular characterization of ovarian cancer tissue samples as well as their implementation in the clinical space for *ex vivo* and *in vivo* assessment of ovarian tissue samples could offer powerful insights into ovarian cancer tumorigenesis and substantial improvements over current diagnostic methods to positively impact the management and care of ovarian cancer patients. The research projects discussed in this dissertation are aimed at addressing current challenges in ovarian cancer research and diagnosis with ambient ionization MS technology.

RESEARCH OBJECTIVES

My dissertation research has focused on developing ambient ionization MS methods for improved characterization of cancer tissue samples and applying them to investigate and improve detection of ovarian cancer. The objectives of this research were two-fold: (1) utilize DESI-MS imaging to determine metabolic features associated with

ovarian cancer aggressiveness and generate statistical models capable of producing accurate ovarian cancer diagnoses based on DESI-MS data; and (2) develop alternative liquid extraction-based sampling approaches to address current challenges in ambient ionization MS methods for both *ex vivo* and *in vivo* characterization of cancer tissue samples. The studies described in the following five chapters demonstrate the potential of ambient ionization MS technology for ovarian cancer research and improved diagnosis.

Chapter 2 of this dissertation describes the in-depth investigation of ovarian cancer tissue samples with DESI-MS imaging. Normal ovarian as well as HGSC and serous BOT frozen tissue sections were analyzed to detect metabolic trends correlated to tumor development and malignancy. DESI-MS imaging allowed visualization of spatial features in the tissue sections corresponding to various cellular environments, such as stroma and necrosis. The least absolute shrinkage and selector operator (Lasso) method (53), developed by our collaborator at Stanford University, Prof. Tibshirani, was used to generate classification models to distinguish between normal, HGSC, and BOT ovarian tissue samples and to identify predictive markers of ovarian cancer aggressiveness. Various metabolite, fatty acid, and complex glycerophospholipid and sphingolipid species were selected as important to characterize normal and cancerous ovarian tissue samples, supporting the role of metabolic aberrations in ovarian cancer development and aggressiveness and providing additional insights into ovarian carcinogenesis. The statistical classifiers generated from DESI-MS imaging data allowed identification of ovarian tissue samples with high predictive accuracies (>90%). The results obtained in this study suggested DESI-MS as a powerful approach to spatially and molecularly characterize ovarian cancer tissue samples, as well as to rapidly provide a cancer diagnosis from frozen tissue sections based on altered metabolic features.

Going beyond cancer diagnosis and capitalizing on the capabilities of DESI-MS to characterize ovarian cancer tissue, Chapter 3 describes the investigation of the effects of the fatty acid binding protein gene (FABP4) expression in ovarian cancer metabolism. Dr. Anil K. Sood and his research group at the MD Anderson Cancer Research Center previously identified the FABP4 gene as a molecular determinant of residual disease in ovarian cancer, resulting in overall poorer patient prognosis (49,54). In this study, we aimed to improve the understanding of the molecular mechanisms behind the role of the FABP4 gene in driving ovarian cancer aggressiveness and metastasis. Frozen human and mice tissue samples were provided by the Sood research lab and analyzed by DESI-MS imaging in our laboratory. Metabolic features detected from multivariate statistical analyses of DESI-MS data, including Lasso and Significance Analysis of Microarrays (SAM) (55), were correlated with FABP4 expression levels. Focusing only on data obtained from regions of high tumor concentrations revealed a unique set of metabolic trends associated with high and low expression of the FABP4 gene, from fatty acid unsaturation and oxidation levels to lysophospholipid and cardiolipin abundance. This study elucidated certain metabolic determinants of ovarian cancer aggressiveness and metastasis beyond histopathological characterization, laying a strong precedent for future studies investigating as well as developing novel therapeutic strategies to target these metabolic aberrations.

Chapters 2 and 3 of this dissertation provide powerful examples of the capabilities of ambient ionization MS methods, particularly DESI-MS, to analyze and examine the metabolic composition of ovarian tissue sections. Chapter 4 describes the development of an alternative liquid extraction ambient ionization MS approach for metabolite and lipid analysis, providing improved spatial control during direct liquid sampling and extraction from biological samples. This method involves the deposition of solvent droplet arrays (~2-

50 nL) onto sample surfaces by a piezoelectric liquid dispenser, followed by droplet aspiration and ionization through a fused capillary emitter for MS analysis. Tuning the volume and thus diameter of the droplet deposited with the piezoelectric dispenser allows practical and precise control over the area being sampled and the imaging spatial resolution (250-650 µm). Direct sampling and aspiration of the droplet in contact with the tissue sample through the fused silica capillary enables efficient analyte extraction and ionization for MS analysis. The solvent system and experimental parameters were optimized for improved metabolite and lipid detection with this approach. This method was tested using various biological tissues and samples, including normal and cancerous ovarian samples, demonstrating potential for controlled spatial and metabolic profiling of biological samples with imaging pixel sizes ranging from 380 to 500 µm. Future work on this technology includes design and engineering refinements to allow automation, increased spatial resolution and improved sample throughput. Efforts to optimize this method for protein analysis from tissue are currently underway, as well as exploring potential additives for tuning solvent composition for enhanced chemical coverage. The capability to decouple the extraction and ionization processes with this method will also be exploited to investigate the mechanisms driving molecular detection with liquid extraction ambient ionization MS methods.

The ambient ionization MS approaches described in the previous chapters can be used to investigate tissue samples in the research space and could potentially be introduced into a clinical workflow by analyzing excised surgical specimens processed as tissue sections. Chapter 5 in this dissertation describes the development and application of an innovative ambient ionization MS technology tailored to the analysis of tissue samples *in vivo* and *ex vivo* directly after excision, removing requirements for frozen tissue section preparation. The device, called the MasSpec Pen and developed in our laboratory in

collaboration with Prof. Thomas Milner's laboratory at the University of Texas, is a handheld and biocompatible sampling probe that uses a droplet of water to extract molecular information from the surface of a tissue. Following extraction, the droplet is then transported to a mass spectrometer for analysis. The sampling and data acquisition process can be performed in under 10 seconds, providing metabolic characterization of tissue samples in near-real time. Unlike the iKnife technology, molecular sampling and ionization rely on direct liquid extraction with a discrete water droplet, which is completely nondestructive to the tissue sample analyzed. The MasSpec Pen was utilized to analyze banked *ex vivo* tissue specimens of various cancer types, including ovarian cancer, and tested *in vivo* using murine models of breast cancer. Using the Lasso method, the molecular information obtained from the analyses was found to be predictive of tissue and cancer type.

With a high reoccurrence rate of ~80%, associated partly to remaining residual disease after surgery, as well as the need for rapid tissue diagnosis during surgery to determine an effective treatment plan, the management of ovarian cancer could greatly benefit from a technology like the MasSpec Pen to help guide patient care. Initial efforts to validate the MasSpec Pen technology for ovarian cancer diagnosis prior to *in vivo* testing in human surgeries are discussed in Chapter 6. In this study, the performance of the MasSpec Pen for *ex vivo* ovarian cancer diagnosis was rigorously evaluated across different sample sets, various healthy and cancerous ovarian tissue types, including fallopian tube, HGSC, and LGSC samples, and mass spectrometry systems. Overall, high performance was obtained, demonstrating the potential and robustness of the metabolic profiles obtained by MasSpec Pen analysis to serve as molecular fingerprints for rapid diagnosis of ovarian cancer specimens. A pilot clinical study is currently planned to evaluate feasibility for *in vivo* use of this technology in ovarian cancer surgeries.

Finally, Chapter 7 provides a concluding summary of this dissertation, as well as a discussion on future directions of the research described. A personal perspective on the field of ambient ionization MS for cancer research and diagnosis, including current challenges and hopes, is also included in Chapter 7.

REFERENCES

1. Fenn JB, Mann M, Meng CK, Wong SF, Whitehouse CM. Electrospray Ionization for Mass-Spectrometry of Large Biomolecules. Science 1989;246:64-71
2. Siuzdak G. The emergence of mass spectrometry in biochemical research. Proc Natl Acad Sci U S A 1994;91:11290-7
3. Karas M, Bachmann D, Bahr U, Hillenkamp F. Matrix-Assisted Ultraviolet-Laser Desorption of Nonvolatile Compounds. International Journal of Mass Spectrometry and Ion Processes 1987;78:53-68
4. Norris JL, Caprioli RM. Analysis of Tissue Specimens by Matrix-Assisted Laser Desorption/Ionization Imaging Mass Spectrometry in Biological and Clinical Research. Chem Rev 2013;113:2309-42
5. Schwamborn K, Caprioli RM. INNOVATION Molecular imaging by mass spectrometry - looking beyond classical histology. Nat Rev Cancer 2010;10:639-46
6. Seeley EH, Caprioli RM. MALDI imaging mass spectrometry of human tissue: method challenges and clinical perspectives. Trends Biotechnol 2011;29:136-43
7. Alexandrov T. MALDI imaging mass spectrometry: statistical data analysis and current computational challenges. Bmc Bioinformatics 2012;13
8. Takats Z, Wiseman JM, Gologan B, Cooks RG. Mass spectrometry sampling under ambient conditions with desorption electrospray ionization. Science 2004;306:471-3
9. Cooks RG, Ouyang Z, Takats Z, Wiseman JM. Ambient mass spectrometry. Science 2006;311:1566-70
10. Ifa DR, Eberlin LS. Ambient Ionization Mass Spectrometry for Cancer Diagnosis and Surgical Margin Evaluation. Clin Chem 2016;62:111-23
11. Wu CP, Dill AL, Eberlin LS, Cooks RG, Ifa DR. Mass spectrometry imaging under ambient conditions. Mass Spectrom Rev 2013;32:218-43
12. Hanel L, Kwiatkowski M, Heikaus L, Schluter H. Mass spectrometry-based intraoperative tumor diagnostics. Futur Sci Oa 2019;5
13. Costa AB, Cooks RG. Simulated splashes: Elucidating the mechanism of desorption electrospray ionization mass spectrometry. Chem Phys Lett 2008;464:1-8
14. Eberlin LS, Ferreira CR, Dill AL, Ifa DR, Cheng L, Cooks RG. Nondestructive, histologically compatible tissue imaging by desorption electrospray ionization mass spectrometry. Chembiochem 2011;12:2129-32

15. Porcari AM, Zhang JL, Garza KY, Rodrigues-Peres RM, Lin JQ, Young JH, et al. Multicenter Study Using Desorption-Electrospray-Ionization-Mass-Spectrometry Imaging for Breast-Cancer Diagnosis. Anal Chem 2018;90:11324-32

16. Eberlin LS, Tibshirani RJ, Zhang J, Longacre TA, Berry GJ, Bingham DB, et al. Molecular assessment of surgical-resection margins of gastric cancer by mass-spectrometric imaging. Proc Natl Acad Sci U S A 2014;111:2436-41

17. Guenther S, Muirhead LJ, Speller AV, Golf O, Strittmatter N, Ramakrishnan R, et al. Spatially resolved metabolic phenotyping of breast cancer by desorption electrospray ionization mass spectrometry. Cancer Res 2015;75:1828-37

18. Calligaris D, Feldman DR, Norton I, Brastianos PK, Dunn IF, Santagata S, et al. Molecular typing of meningiomas by desorption electrospray ionization mass spectrometry imaging for surgical decision-making. Int J Mass Spectrom 2015;377:690-8

19. Eberlin LS, Dill AL, Costa AB, Ifa DR, Cheng L, Masterson T, et al. Cholesterol Sulfate Imaging in Human Prostate Cancer Tissue by Desorption Electrospray Ionization Mass Spectrometry. Anal Chem 2010;82:3430-4

20. Eberlin LS, Norton I, Orringer D, Dunn IF, Liu XH, Ide JL, et al. Ambient mass spectrometry for the intraoperative molecular diagnosis of human brain tumors. P Natl Acad Sci USA 2013;110:1611-6

21. Jarmusch AK, Pirro V, Baird Z, Hattab EM, Cohen-Gadol AA, Cooks RG. Lipid and metabolite profiles of human brain tumors by desorption electrospray ionization-MS. P Natl Acad Sci USA 2016;113:1486-91

22. Santagata S, Eberlin LS, Norton I, Calligaris D, Feldman DR, Ide JL, et al. Intraoperative mass spectrometry mapping of an onco-metabolite to guide brain tumor surgery. P Natl Acad Sci USA 2014;111:11121-6

23. Laskin J, Lanekoff I. Ambient Mass Spectrometry Imaging Using Direct Liquid Extraction Techniques. Anal Chem 2016;88:52-73

24. Van Berkel GJ, Kertesz V. Application of a Liquid Extraction Based Sealing Surface Sampling Probe for Mass Spectrometric Analysis of Dried Blood Spots and Mouse Whole-Body Thin Tissue Sections. Anal Chem 2009;81:9146-52

25. Kertesz V, Van Berkel GJ. Fully automated liquid extraction-based surface sampling and ionization using a chip-based robotic nanoelectrospray platform. J Mass Spectrom 2010;45:252-60

26. Roach PJ, Laskin J, Laskin A. Nanospray desorption electrospray ionization: an ambient method for liquid-extraction surface sampling in mass spectrometry. Analyst 2010;135:2233-6

27. Kertesz V, Calligaris D, Feldman DR, Changelian A, Laws ER, Santagata S, et al. Profiling of adrenocorticotropic hormone and arginine vasopressin in human

pituitary gland and tumor thin tissue sections using droplet-based liquid-microjunction surface-sampling-HPLC-ESI-MS-MS. Anal Bioanal Chem 2015;407:5989-98

28. Laskin J, Heath BS, Roach PJ, Cazares L, Semmes OJ. Tissue imaging using nanospray desorption electrospray ionization mass spectrometry. Anal Chem 2012;84:141-8

29. Nguyen S, Sontag R, Carson J, Corley R, Ansong C, Laskin J. Towards High-Resolution Tissue Imaging Using Nanospray Desorption Electrospray Ionization Mass Spectrometry Coupled to Shear Force Microscopy. J Am Soc Mass Spectr 2018;29:316-22

30. Blatherwick EQ, Van Berkel GJ, Pickup K, Johansson MK, Beaudoin ME, Cole RO, et al. Utility of spatially-resolved atmospheric pressure surface sampling and ionization techniques as alternatives to mass spectrometric imaging (MSI) in drug metabolism. Xenobiotica 2011;41:720-34

31. Tillner J, Wu V, Jones EA, Pringle SD, Karancsi T, Dannhorn A, et al. Faster, More Reproducible DESI-MS for Biological Tissue Imaging. J Am Soc Mass Spectr 2017;28:2090-8

32. Garza KY, Feider CL, Klein DR, Rosenberg JA, Brodbelt JS, Eberlin LS. Desorption Electrospray Ionization Mass Spectrometry Imaging of Proteins Directly from Biological Tissue Sections. Anal Chem 2018;90:7785-9

33. Towers MW, Karancsi T, Jones EA, Pringle SD, Claude E. Optimised Desorption Electrospray Ionisation Mass Spectrometry Imaging (DESI-MSI) for the Analysis of Proteins/Peptides Directly from Tissue Sections on a Travelling Wave Ion Mobility Q-ToF. J Am Soc Mass Spectrom 2018

34. Schaefer K-C, Denes J, Albrecht K, Szaniszlo T, Balog J, Skoumal R, et al. In Vivo, In Situ Tissue Analysis Using Rapid Evaporative Ionization Mass Spectrometry. Angew Chem Int Edit 2009;48:8240-2

35. Balog J, Sasi-Szabo L, Kinross J, Lewis MR, Muirhead LJ, Veselkov K, et al. Intraoperative Tissue Identification Using Rapid Evaporative Ionization Mass Spectrometry. Science Translational Medicine 2013;5

36. St John ER, Rossi M, Pruski P, Darzi A, Takats Z. Intraoperative tissue identification by mass spectrometric technologies. Trac-Trend Anal Chem 2016;85:2-9

37. St John ER, Balog J, McKenzie JS, Rossi M, Covington A, Muirhead L, et al. Rapid evaporative ionisation mass spectrometry of electrosurgical vapours for the identification of breast pathology: towards an intelligent knife for breast cancer surgery. Breast Cancer Res 2017;19

38. Phelps DL, Balog J, Gildea LF, Bodai Z, Savage A, El-Bahrawy MA, et al. The surgical intelligent knife distinguishes normal, borderline and malignant gynaecological tissues using rapid evaporative ionisation mass spectrometry (REIMS). Br J Cancer 2018;118:1349-58

39. Jemal A, Siegel R, Ward E, Hao YP, Xu JQ, Thun MJ. Cancer Statistics, 2009. Ca-Cancer J Clin 2009;59:225-49

40. Torre LA, Trabert B, DeSantis CE, Miller KD, Samimi G, Runowicz CD, et al. Ovarian Cancer Statistics, 2018. Ca-Cancer J Clin 2018;68:284-96

41. Lheureux S, Gourley C, Vergote I, Oza AM. Epithelial ovarian cancer. Lancet 2019;393:1240-53

42. Society AC. Cancer Facts & Figures 2020. Atlanta: American Cancer Society 2020

43. Bowtell DDL. The genesis and evolution of high-grade serous ovarian cancer. Nat Rev Cancer 2010;10:803-8

44. Hart WR. Borderline epithelial tumors of the ovary. Modern Pathol 2005;18:S33-S50

45. Matulonis UA, Sood AK, Fallowfield L, Howitt BE, Sehouli J, Karlan BY. Ovarian cancer. Nat Rev Dis Primers 2016;2

46. Bowtell DD, Bohm S, Ahmed AA, Aspuria PJ, Bast RC, Beral V, et al. Rethinking ovarian cancer II: reducing mortality from high-grade serous ovarian cancer. Nat Rev Cancer 2015;15:668-79

47. Kurman RJ, Shih Ie M. Molecular pathogenesis and extraovarian origin of epithelial ovarian cancer--shifting the paradigm. Hum Pathol 2011;42:918-31

48. Karnezis AN, Cho KR, Gilks CB, Pearce CL, Huntsman DG. The disparate origins of ovarian cancers: pathogenesis and prevention strategies. Nat Rev Cancer 2017;17:65-74

49. Tucker SL, Gharpure K, Herbrich SM, Unruh AK, Nick AM, Crane EK, et al. Molecular biomarkers of residual disease after surgical debulking of high-grade serous ovarian cancer. Clin Cancer Res 2014;20:3280-8

50. Md Arshad NZ, Ng BK, Md Paiman NA, Abdullah Mahdy Z, Mohd Noor R. Intra-Operative Frozen Sections for Ovarian Tumors - A Tertiary Center Experience. Asian Pac J Cancer Prev 2018;19:213-8

51. Nick AM, Coleman RL, Ramirez PT, Sood AK. A framework for a personalized surgical approach to ovarian cancer. Nat Rev Clin Oncol 2015;12:239-U78

52. Macario A. What does one minute of operating room time cost? J Clin Anesth 2010;22:233-6

53. Tibshirani R. Regression shrinkage and selection via the Lasso. J Roy Stat Soc B Met 1996;58:267-88

54. Gharpure K, Pradeep S, Sans M, Rupaimoole R, Ivan C, Wu SY, et al. FABP4 as a molecular determinant of residual disease in ovarian cancer. Nat Commun 2017;In Revision

55. Tusher VG, Tibshirani R, Chu G. Significance analysis of microarrays applied to the ionizing radiation response. P Natl Acad Sci USA 2001;98:5116-21

Chapter 2: Metabolic Markers and Statistical Prediction of Serous Ovarian Cancer Aggressiveness by Ambient Ionization Mass Spectrometry Imaging[2]

INTRODUCTION

Epithelial ovarian cancer is a complex disease that includes great molecular and histologic diversity, with serous carcinoma being the most common form (1). Ovarian cancer accounts for the majority of deaths for gynecological malignancies due to the detection of advanced and aggressive disease at a late stage (2). High-grade serous cancer (HGSC) is the most aggressive ovarian epithelial cancer and accounts for 70% of all ovarian epithelial cancers diagnosed (3). HGSC is characterized by extensive genetic instability, and TP53 mutations are universally found in these tumors (4). Conversely, borderline serous ovarian tumors (BOT) or serous tumors of low-malignant potential are noninvasive neoplasms with favorable patient prognosis and represent approximately 15% of serous ovarian tumors (5). BOTs can progress to malignant low-grade serous carcinoma (LGSC), but the clinical outcome is still advantageous in comparison with HGSCs (4, 6). HGSC and BOTs present distinct tumor invasion behaviors, with HGSC growing rapidly and spreading among healthy tissue, whereas BOTs slowly proliferate without stromal invasion. Although histopathologic analysis is routinely employed for diagnosis of serous ovarian tumors, sensitive methods that provide molecular information to diagnose and stratify patients could serve as complimentary tools for more accurate and personalized diagnosis, as well as for the detection of early molecular markers to improve disease

[2] Adapted with permission from Sans M, Gharpure K, Tibshirani R, Zhang J, Liang L, Liu J, et al. Metabolic Markers and Statistical Prediction of Serous Ovarian Cancer Aggressiveness by Ambient Ionization Mass Spectrometry Imaging. Cancer Res 2017;77:2903-13. Copyright © 2017, American Association for Cancer Research. Sans M performed the experiments, data analyses, and prepared the manuscript. Gharpure K assisted in sample collection. Tibshirani R. generated the statistical methods and prediction results. All authors contributed editing the manuscript.

management (7–9). Moreover, characterization of the molecular differences between malignant and borderline serous ovarian tumors could provide new insights to unravel the biological mechanisms driving tumor invasion and aggressiveness (10, 11).

Mass spectrometry imaging techniques have been increasingly used for spatial and molecular characterization of cancerous tissues (12–14). In particular, desorption electrospray ionization mass spectrometry (DESI-MS) imaging allows simultaneous detection of hundreds of lipids and metabolites directly from tissue samples with minimal sample preparation (15). DESI-MS employs an electrospray stream to desorb and ionize molecular species present on the sample surface (16). When performed in the imaging mode, chemical maps displaying the spatial distribution of molecular ions are obtained (17). Multivariate statistical analysis of the large spatial and molecular data information obtained is essential to derive molecular signatures that are predictive of disease state. DESI-MS imaging is powerful for biomarker discovery as it allows visualization of tissue heterogeneity and thus unambiguous correlation of histologic features and molecular information to build tissue-based molecular classifiers. This methodology has been used to investigate diagnostic lipid and metabolic signatures of human cancerous tissues including brain (18), breast (19), gastric (20), and others (21–23). Mouse models of human ovarian HGSC have been recently investigated using DESI-MS imaging, and differences in metabolic species were observed between healthy and tumorous tissues (24). Here, we report the use of DESI-MS imaging to investigate the molecular profiles of serous ovarian tumors and characterize lipids and metabolites that could potentially serve as markers of aggressive disease. Two-dimensional (2D) molecular images allowed correlation between molecular signatures and regions with specific histologic features. Classification models built using the least absolute shrinkage and selector operator (Lasso) technique (25, 26) were tested to predict disease state and tumor aggressiveness. Predictive species selected

by the statistical models were tentatively identified by high mass accuracy/high mass resolution and tandem mass spectrometry analysis as lipids and metabolites of biological relevance. Our results demonstrate the capabilities of DESI-MS for characterizing serous ovarian tumors and for the identification of potential predictive markers of disease aggressiveness.

MATERIALS AND METHODS

Banked human ovarian tissues

A total of 78 frozen human tissue specimens including 15 normal ovarian tissues, 15 BOT, and 48 HGSC samples were obtained from the Cooperative Human Tissue Network and MD Anderson Tissue Bank under approved IRB protocol. Tissue samples were sectioned at 16 µm thick sections using a CryoStar NX50 cryostat (Thermo Scientific). After sectioning, the glass slides were stored in a -80 ºC freezer. Prior to MS imaging, the glass slides were dried for approximately 15 minutes.

DESI-MS imaging

A 2D Omni Spray (Prosolia Inc.) coupled to an LTQ-Orbitrap Elite was utilized for tissue imaging. DESI-MS imaging was performed in the negative and positive ion modes from *m/z* 100 to 1,500, using a hybrid mass spectrometer that allows for tandem MS experiments, high mass accuracy (<5 ppm mass error), and high mass resolution (60,000 resolving power) measurements. A spatial resolution of 200 µm was used. Ion images were assembled using Biomap and MSiReader software. The histologically compatible solvent system dimethylformamide: acetonitrile (DMF:ACN) 1:1 (v/v) was used for negative ion mode analysis, at a flow rate of 1.2 µL/min (17). For positive ion mode analysis, pure ACN was used, at a flow rate of 3 µL/min. The N_2 pressure was set to 185 psi. For ion

identification, high mass resolution/accuracy measurements using the same tissue sections analyzed were conducted using CID and HCD methods, using the Orbitrap for analysis.

Histopathology and light microscopy

The same tissue sections analyzed by DESI-MS imaging were subjected afterward to a standard hematoxylin and eosin (H&E) staining protocol. Pathologic evaluation was performed by Drs. Jinsong Liu and Li Liang using light microscopy. Regions of clear diagnosis were assigned and delineated in the glass slides. Light microscopy images of the H&E-stained slides were taken using the EVOS FL Auto Cell Imaging System (Invitrogen, Thermo Fisher Scientific). Statistical analysis MS data corresponding to the areas of interest were extracted from the ion images using MSiReader software. The *m/z* range was discretized by performing hierarchical clustering and cutting the resulting dendrogram at distance 0.05. Peaks appearing in more than 10% of the pixels were kept for analysis. For two-class classification (normal vs. HGSC, and HGSC vs. BOT), logistic regression was performed with Lasso regularization using the "glmnet" package (26) in the R language. Regularization parameters were determined by 3-fold cross-validation (CV) analysis. The data were randomly divided in a training and validation set of samples, 50–50 per patient basis. For three-class classification (normal vs. BOT vs. HGSC), a customized training approach was employed as previously described (27).

RESULTS

Molecular imaging of serous ovarian cancers

DESI-MS imaging was performed in the negative and positive ion modes for a total of 78 tissue samples, including 15 normal ovarian, 15 BOT, and 48 HGSC tissues obtained from two independent tissue banks. A patient demographic table is included in Table A1.1.

Characteristic metabolic profiles for HGSC, serous BOT, and normal ovary samples were observed in both polarities and presented a remarkable diversity of metabolic species. In the negative ion mode, small metabolites, saturated and unsaturated fatty acids, sphingolipids (SP), and several classes of glycerophospholipids (GP) such as ceramides (Cer), cardiolipins (CL), glycerophosphoethanolamines (PE), glycerophosphoglycerols (PG), glycerophosphoserines (PS), and glycerophosphoinositols (PI) were observed (Figure 2.1A), whereas additional biologically relevant lipid species, such as glycerophosphocholines (PC), triacylgycerols (TG), and sphingomyelins (SM) were seen in the positive ion mode (Figure 2.2A).

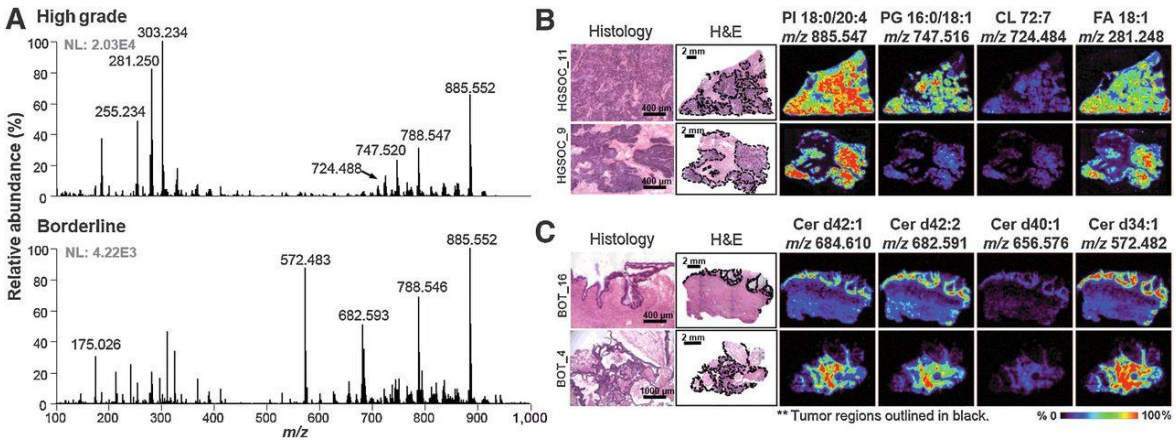

Figure 2.1: Analysis by DESI-MSI in the negative ion mode.

(A) Representative metabolic profiles for high-grade SOC and serous borderline. Top, high-grade; bottom, borderline. (B) Representative ion images for high-grade SOC tissue samples. (C) Representative ion images for borderline tumor samples. Tumor areas are outlined in black on H&E slides. Areas of red intensity within the ion images represent highest (100%) and black lowest (0%) relative abundances. Lipid species are described by number of fatty-acid chain carbons and double bonds.

After DESI-MS imaging, the same tissue sections were stained with H&E and subjected to detailed pathologic evaluation (17). Specific histologic features characteristic of HGSC and serous BOT tissues were observed and annotated for all samples analyzed,

as shown in Figures 2.1 and 2.2 for four representative samples for negative and positive ion mode, respectively. HGSCs exhibit solid growth or large and complex papillae, with heterogeneous nuclei shape and sizes, and extensive stromal invasion (1,4). DESI-MS imaging in the negative ion mode allowed visualization of regions with tumor clusters in HGSC, as outlined in black for samples HGSC_9 and HGSC_11 in Figure 2.1B. For example, high relative abundances of *m/z* 885.547, *m/z* 747.516, *m/z* 724.484, and *m/z* 281.248 were observed in regions with high density of tumor cells. In the positive ion mode, PC species including PC 36:3, PC 34:1, and PC 32:1 were found at high relative abundances in high-grade carcinoma regions, allowing clear visualization of these regions in comparison with surrounding stroma. Interestingly, *m/z* 901.648, tentatively identified as ubiquinone or Coenzyme Q10 with a mass error of -1.1 ppm, was noticeably selective to the presence of tumor in HGSC samples (Figure 2.2B).

Conversely, serous BOTs are commonly associated with noninvasive components, characterized by increased epithelial proliferation and nuclear atypia, exhibiting multiple papillae with ordered branching (5, 6). Serous BOT samples present a distinct histologic architecture characterized by tumor growth within the lining of the stroma. Ion images of serous BOT samples BOT_4 and BOT_16 are shown in Figures 2.1C and 2.2C. As observed for HGSC samples, high relative abundance of PI 18:0/20:4 was seen in the tumor region in comparison with stromal areas. Yet, high relative abundances of Cer species such as Cer d42:1, Cer d42:2, Cer d40:1, and Cer d34:1 was highly specific to the discrete tumor regions in BOT samples. In the positive ion mode, ubiquinone (*m/z* 901.648) also presented higher relative abundances in serous BOT regions. Other species such as PC 36:3 or 36:4 were also abundant within the tissue slides but not as specific to the BOT tumor areas. On the other hand, cholesteryl ester (CE) 18:2 was observed to be more abundant in the surrounding stromal regions.

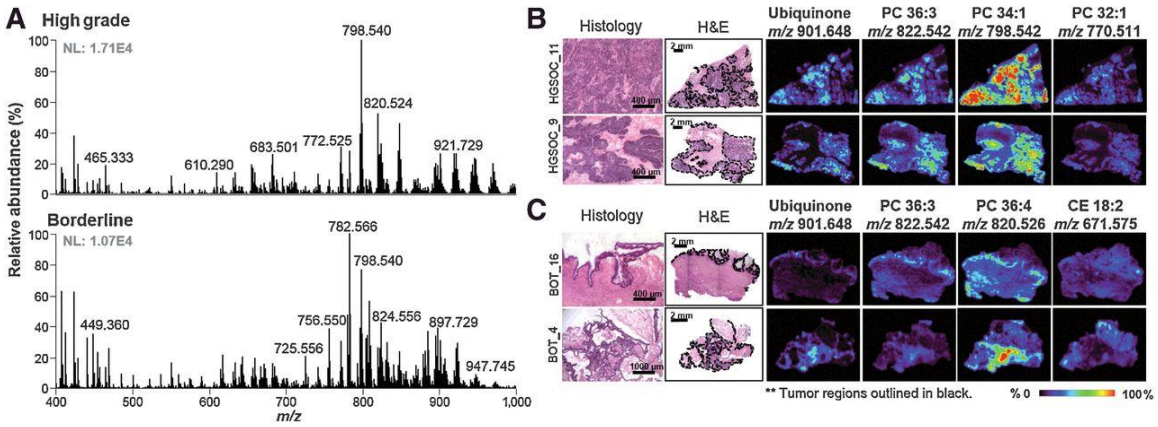

Figure 2.2: Analysis by DESI-MSI in the positive ion mode.

(A) Representative metabolic profiles for high-grade SOC and serous borderline. Top, high-grade; bottom, borderline. (B) Representative ion images for high-grade SOC tissue samples. (C) Representative ion images for borderline tumor samples. Tumor areas are outlined in black on H&E slides. Areas of red intensity within the ion images represent highest (100%) and black lowest (0%) relative abundances. Adjacent tissue sections were used for negative and positive ion mode analysis. Lipid species are described by number of fatty-acid chain carbons and double bonds.

Normal ovarian tissue samples presented stromal regions with heterogeneous features such as corpus luteum, follicles, or benign cysts (Figure A1.1). Healthy stromal ovarian tissue consistently displayed a lower overall signal intensity for lipid species when compared with HGSC tissue samples in the negative ion mode. Moreover, a higher relative abundance of PI 20:4/18:1, *m/z* 885.547, in comparison with PS 18:0/18:1, *m/z* 788.547, was consistently observed in both BOT and HGSC tumors, when compared with normal ovarian tissues. However, certain species, such as ascorbic acid, *m/z* 175.025, were more prominent in normal tissue. In the positive ion mode, characteristic mass spectra were observed from normal stromal regions, with high relative abundance of PCs such as PC 34:1, and other less abundant lipid species such as PC 36:1 or diacylglycerol (DG) 28:4.

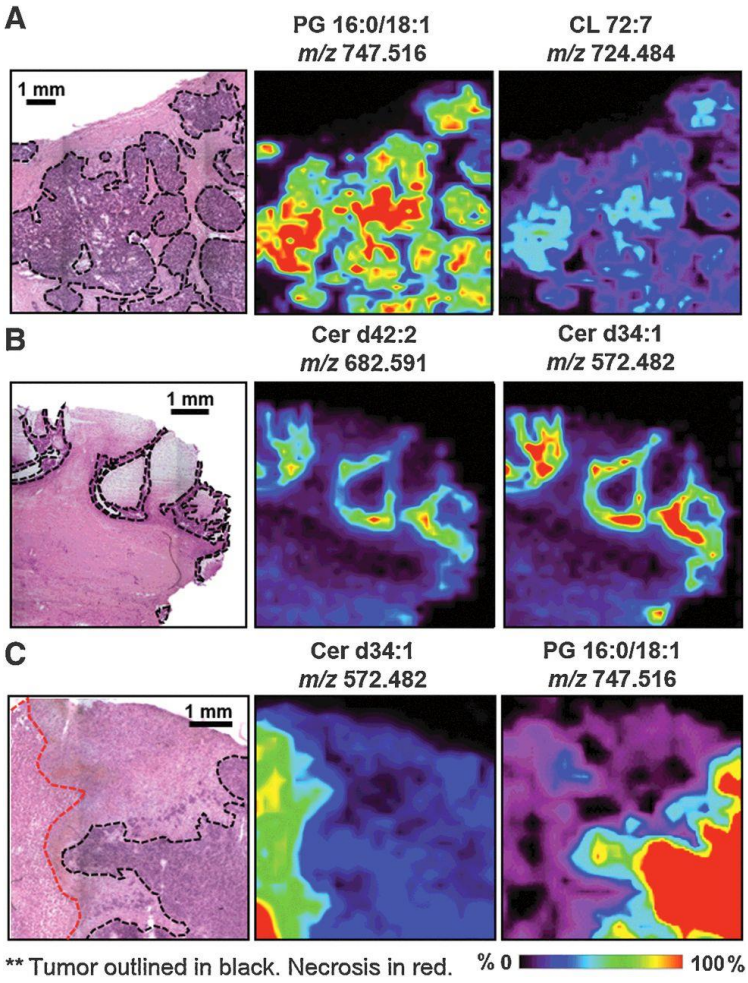

Figure 2.3: Magnified regions for samples HGSC_11 (A), BOT_16 (B), and HGSC_1 (C), with selected ion images that correlate to and outline the presented histologic heterogeneities.

Lipid species are described by number of fatty-acid chain carbons and double bonds. The tumor areas are outlined in black, necrotic areas in red. Areas of red intensity within the ion images represent highest (100%) and black lowest (0%) relative abundances.

Notably, the spatial resolution used for DESI-MS imaging (200 µm) enabled visualization of key features of tumor heterogeneity in serous ovarian tumor tissues. Figure 2.3 shows magnified regions for three tumor samples, with selected ion images that directly correlate and clearly outline histologic details of these tissues. For example, necrotic regions within the HGSC_1 tissue sample (outlined in red Figure 2.3C) showed a very

distinct lipid profile, characterized by high relative abundance of Cer species such as *m/z* 682.591 and *m/z* 600.513 (Figure A1.2). Necrosis is a typical cell injury present in high-grade carcinomas and was absent in BOT tumors (1,4). In HGSC and BOT samples, the molecular composition of tumor regions allowed clear visualization and discrimination of cancer and adjacent stromal regions. The distinct molecular compositions associated with normal ovarian tissues, and borderline and high-grade tumors strongly suggest lipid and metabolite species as potential biomarkers for cancer diagnosis and aggressiveness.

Statistical prediction and molecular diagnosis of HGSC

DESI-MS imaging of tissue samples results in a large amount of molecular and spatial information (hundreds of molecular ions/hundreds of data points/sample) and thus calls for refined statistical evaluation to define what changes in molecular expression are significantly different between phenotypes and to build robust statistical classifiers. The Lasso method was performed on a random training set of samples to yield a model with parsimonious sets of *m/z* values for discriminating between the classes. A mathematical weight for each mass spectral feature was calculated by the Lasso depending on the importance that the feature had in characterizing a certain class. The predictive accuracy of the model with the selected features was evaluated using an independent validation set and presented as agreement (%) with pathologic results.

To classify HGSC pixels in comparison with normal tissue, MS data were extracted from tumor-concentrated regions or stromal areas within the selected tissues slides. First, we built a classifier for HGSC using a training subset of samples (8 normal, 23 HGSC). Three-fold CV was performed on a pixel by- pixel basis using a total of 20,082 pixels evaluated in the negative ion mode, resulting in an overall agreement of 97.1%. The statistical model was then applied to the validation set of samples (7 normal, 25 HGSC),

which resulted in an overall agreement of 96.5% for 18,671 pixels (Figure 2.4A). The area under the receiver operating characteristic curve values (AUC = 0.98 for CV; AUC = 0.97 for validation set) demonstrate the high performance for normal versus HGSC discrimination. Analysis per patient allowed correct classification of 100% of the patients in CV, whereas 1 HG sample was misclassified as normal out of the total 25 validation set samples (Table A1.2). A subset of 25 *m/z* values selected by the Lasso as most significant contributors to the model were tentatively identified as small metabolites, saturated and polyunsaturated fatty acids, and GPs (Table A1.3). The positive ion mode data were also analyzed by the Lasso to predict HGSC. Following the same strategy, overall agreements of 96.7% (AUC = 0.96) and 95.5% (AUC = 0.95) for CV and validation sets were achieved, respectively (Figure 2.4B). The Lasso selected 21 *m/z* values characteristic for the model, the majority of which were identified as PCs, CEs, and TGs (Table A1.3). These results demonstrate DESI-MS and Lasso's capabilities of diagnosing the most aggressive form of serous ovarian cancers, which is relevant due to the high occurrence and poor prognosis of HGSC compared with other subtypes (4).

Statistical prediction of cancer aggressiveness for HGSC and BOT tissues

HGSC and BOT tumors present very distinct behaviors including tumor invasion and aggressiveness. Investigating the molecular differences between HGSC and BOT subtypes can assist in the identification of potential biomarkers of disease aggressiveness. Molecular classifiers to predict BOT and HGSC were built using the Lasso for DESI-MS data. In the negative ion mode, the classifier was developed using a training set of samples (32 samples, 18,190 pixels), resulting in an overall agreement of 93.2% with pathologic analysis by CV. The remaining data (31 samples, 13,422 pixels) used to test the molecular model yielded 91.8% agreement with evaluation by pathology. Using positive ion mode

data, agreements of 90.4% (29 samples, 20,852 pixels) and 97.5% (32 samples, 15,134) were obtained for the training and test sets, respectively (Table A1.4). From the species selected as predictive markers by the molecular classifier, 41 *m/z* values were identified as metabolites, fatty acids, complex SP, or GP in the negative and positive ion modes (Table A1.5).

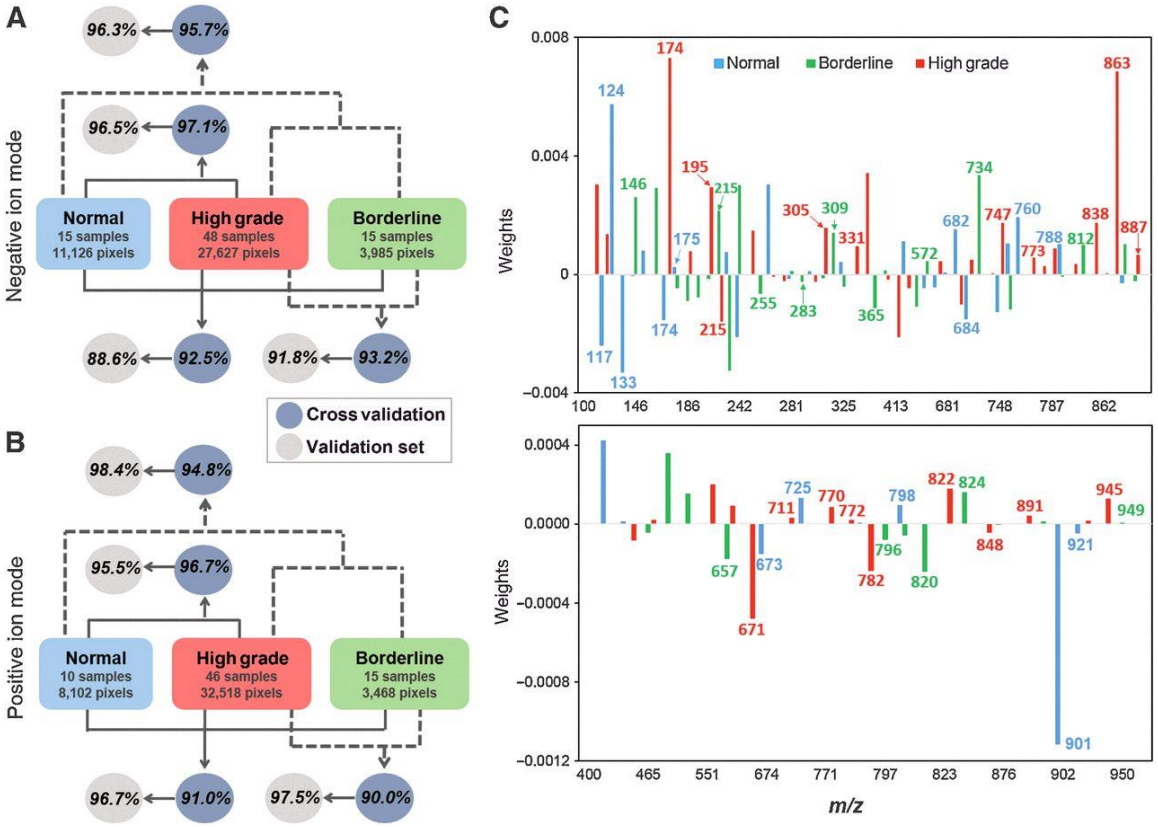

Figure 2.4: Lasso per pixel prediction results for normal, HGSC, and BOT classification. Negative ion mode (A) and positive ion mode (B). Agreements are calculated based on percentage of correctly classified pixels over total pixels classified. See Tables A1.2, A1.4, and A1.6 for complete pixel and patient classification results. (C) Weights attributed to selected *m/z* values by the Lasso, represented by nominal mass, for negative ion mode (top) and positive ion mode (bottom). Positive weights represent higher relative abundances; negative weights represent lower relative abundances. Chemical attribution for selected species is provided in Table 2.1.

Per patient analysis revealed 3 BOT samples misclassified overall: BOT_2, BOT_6, and BOT_13, which were then re-evaluated by pathology (Table A1.4). Remarkably, invasive carcinoma features were identified within the tissue sample for BOT_2, which are commonly associated with the development of LGSC. The surgical report for BOT_6 revealed that the patient's contralateral ovary consisted of well-differentiated (low-grade) adenocarcinoma, indicative of malignant behavior. Samples BOT_6 and BOT_13 were defined by pathology as serous BOT with unusual extensive micropapillary growth patterns and architectural complexities, thus supporting the distinct molecular features detected by DESI-MS that are not characteristic of the BOT molecular model.

Statistical prediction of serous ovarian cancers and normal ovarian tissues

Next, we evaluated the ability of our method to discriminate three classes of ovarian tissues: normal, BOT, and HGSC. Lasso was performed on negative ion mode DESI-MS data from 15 normal, 15 BOT, and 48 HGSC tissue samples. A customized training approach was utilized to provide localized molecular models for predicting each data subset, which has been previously applied to MS imaging data (27). A total of 20,225 pixels (39 samples) were used for CV, leading to an overall agreement of 92.5%. The remaining 22,513 pixels (39 samples) were evaluated as an independent validation set with an overall 88.6% agreement (Figure 2.4A). Positive ion mode analysis from a total of 10 normal, 15 BOT, and 46 HGSC tissue samples provided an overall agreement of 91.0% in CV (25,839 pixels) and 96.7% overall accuracy for the validation set of samples (18,249 pixels; Figure 2.4B). In all the analyses, the highest Lasso error rates were due to misclassification of pixels diagnosed as BOT by histopathology as either normal or HGSC, whereas higher accuracy was observed for normal and HGSC classes (Table A1.6). Interestingly, the same BOT samples misclassified by the two-class comparison between HGSC and BOT were

also predicted as carcinomas by the three-class molecular model for normal, BOT and HGSC. These results emphasize that metabolic features detected by our method can serve as a robust predictive signature of cancer and disease aggressiveness.

To evaluate the overall discrimination between healthy and tumor samples, per-pixel results for HGSC and BOT were combined and compared with the results for normal tissues. Overall agreements of 95.7% and 96.3% were achieved in the negative ion mode for the CV and validation sets, respectively (Figure 2.4A). Positive ion mode data also enabled successful discrimination between healthy and tumorous tissues with overall agreements of 94.8% for CV and 98.4% for the validation set (Figure 2.4B). The few normal pixels classified as HGSC were from samples NL_13 and 14, which presented higher stromal cell density compared with the remaining normal samples (Table A1.2). Collectively, these results support lipid and metabolites profiles as predictive molecular features to distinguish healthy, borderline, and aggressive serous ovarian cancers.

Molecular markers of ovarian cancer aggressiveness

The Lasso analysis of normal, HGSCs, and serous BOTs selected subsets of molecular features that were highly predictive and characteristic of disease state. An ion whose peak abundance is important for characterizing a certain class is given a positive weight, whereas ions whose low abundances or absence are important receive a negative weight. Note that trends of increased or decreased mass spectral relative abundance and 2D distributions in tissues were in agreement with the mathematical weight given by the Lasso for all of the selected molecular features. Figure 4C shows the statistical weights for the selected *m/z* values for the three-class normal, versus BOT, versus HGSC classification model, showing a high diversity of molecular species. Tentative chemical identification of the selected ions was performed using high mass accuracy/high mass resolution and

tandem MS analyses in comparison with literature reports, lipids and metabolites databases, and chemical standards. Table 2.1 provides a list of the *m/z* values contributing to the model and the attributed weights, which were identified as 38 and 21 molecular species in the negative mode and positive ion mode, respectively. Attributed molecular formulas are included in Table A1.7, with corresponding mass errors for each assigned *m/z* value. Similar *m/z* values were selected for the two-class molecular model for high-grade versus borderline tumors (Table A1.5), supporting the potential role of those metabolic species as markers of tumor aggressiveness.

The selected molecular ions identified include metabolites, fatty acids, and complex lipids, which play important biological roles. Within the small metabolites, gluconic acid (*m/z* 195.051) was given a positive weight for HGSC class and a negative weight for BOT class. Fragmentation patterns for *m/z* 195.051 and gluconic acid standard obtained with tandem MS analyses for structural confirmation as well as DESI-MS ion images are provided in Figure A1.3. Interestingly, the nonoxidized form of gluconic acid, hexose or glucose (*m/z* 215.033), was observed in higher relative abundance in BOT tissues. An ion at *m/z* 174.041, identified as N-acetylaspartic acid (NAA), was selected as an important predictive feature for HGSC. Interestingly, NAA has been previously reported as a marker of normal brain parenchyma when compared with gliomas (28). Amino acid taurine and ascorbic acid were also selected as predictive markers of healthy ovarian tissues when compared with tumor tissue, both receiving positive weights for the normal tissue class. On the other hand, succinate and malate received negative weights for normal tissue class in comparison with serous ovarian tumors. Note that identification of metabolite species was performed using DESI-MS tandem MS analyses in comparison with standards and literature reports, and high accuracy measurements (<1.7 ppm), although isomeric

interferences at the same monoisotopic mass could still occur. Representative tandem MS spectra for the metabolites described are provided in Figure A1.4.

Differences in fatty acid abundances and degrees of saturation were also observed between the three tissue subtypes. Polyunsaturated fatty acids, such as FA 20:3 and FA 22:4, were given positive weights for characterizing the HGSC class. Interestingly, monounsaturated fatty acids FA 18:1 and FA 20:1 were given positive weights for characterizing serous BOTs, whereas saturated fatty acids (FA 16:0 and FA 18:0) and monoacylglycerol (MG 16:0) were given negative weights for serous BOTs. These results suggest fatty acid metabolism, including their abundances and degrees of saturation, could play a role in serous ovarian tumor proliferation and aggressiveness, as previously shown for other cancers types (29, 30).

Several GP species were also selected as important molecules in characterizing the three classes. In the negative ion mode, PG and PI species such as PG 16:0/18:1 or PI 18:0/18:1 received positive weights by the Lasso almost exclusively for HGSC classification. Positive weights for characterizing healthy ovarian tissue were obtained for PS species such as *m/z* 760.515 (PS 16:0/18:1). Furthermore, the molecular model built by the Lasso to discriminate between HGSC and healthy tissue (Table A1.3) pinpointed additional GP markers such as CL. Positive weights were assigned to CL 72:8 and CL 72:7 to characterize HGSC, suggesting a role for these lipids in tumor growth and proliferation (31). In the positive ion mode, several PC species were selected as predictive markers. For example, several C32 PC species were given positive weights for characterization of HGSC class, whereas PC34:1 received positive weight for healthy ovarian tissue. For BOT, several PC species received negative weights, whereas PC 36:2 provided positive correlations for characterizing the serous tumor subtype. The overall positive weights and increase in the relative abundances of PC species observed for HGSC class were in

agreement with the positive weight attributed to *m/z* 104.107, identified as the choline head group. Notably, previous studies have also reported elevated levels for PC species in human epithelial ovarian cancer cells, which was related to tumor proliferation and differentiation (32, 33). Representative tandem MS spectra for lipid species detected in the negative ion mode and positive ion mode are provided in Figures A1.4 and A1.5, respectively.

Glycosphingolipids such as Cer were also selected as predictive by our classification models. In the negative ion mode for example, Cer d42:3 and Cer d42:2 were given positive weights to characterize the healthy ovary class, whereas Cer d42:1 and Cer d34:1 received negative weights. On the other hand, Cer d34:1and GlcCer d34:1 received positive weights for serous BOT tissue class, whereas Cer d34:2 received a negative weight. In the positive ion mode, SM 34:1 received a positive weight for the normal ovarian tissue class. Changes in glycosphingolipids expression have been previously reported in epithelial ovarian cancer by MALDI-MSI (34). These variations in Cer in normal tissue and BOT present interesting insights to the disease, as different fatty acid chain lengths of Cer species have been associated to different functions in cancer pathogenesis (35).

Glycolipids such as TG presented high relative abundances in the mass spectra of both tumor subtypes, with distinctive chain lengths and saturation levels characteristic of HGSC and BOT. Sterol lipids such as CEs, which are important for cell membrane functionality, were selected as predictive markers of HGSC. For example, CE 20:4 was attributed a positive weight for HGSC class, whereas CE 18:2 received a negative weight. For the normal ovarian tissue class, CE 18:1 received a negative weight by the statistical model. The largest weight for the model was attributed to ubiquinone, the fully oxidized form of coenzyme Q, one of the electron carriers of the electron transfer chain that is used for ATP synthesis and cell signaling for proliferation (36). Ubiquinone presented notably increased relative abundances in tumorous areas in comparison with surrounding normal

stroma (Figure 2.2), which suggests a potential role for this molecule as a marker for serous ovarian cancer.

Table 2.1: Identified species selected by the Lasso as significant contributors to the molecular model for normal, borderline, and high-grade SOC classification with attributed statistical weights.

Chemical species were tentatively identified by high mass accuracy/high mass resolution and tandem MS analyses. Positive weights represent higher relative abundances; negative weights represent lower relative abundances. Double negative and double positives correspond to greater contributions to the model. Negative ion mode: Lasso weights: "++" "- -" ≥ |0.001|; "+" "-" <|0.001|. Positive ion mode: Lasso weights: "++" "- -" ≥|0.0001|; "+" "-" <|0.0001|. Molecular formulas and mass errors are provided in Table A1.7. Representative tandem mass spectra for selected *m/z* species are provided in Figures A1.3-A1.5.

NEGATIVE ION MODE				
Attribution	**Weights by Lasso**			**Detected *m/z***
	Normal	**Borderline**	**High-Grade**	
Succinate	- -		++	117.020
Taurine	++			124.008
Malate	- -			133.014
Glutamic acid	-	++		146.046
N-acetylaspartic acid	- -		++	174.041
Ascorbic acid	+	-		175.025
Gluconic acid		-	++	195.051
Hexose		++	- -	215.033
Phosphatidic acid	+	- -		226.996
FA 16:0		-		255.233
FA 18:2			-	279.233
FA 18:1	-	+		281.248
FA 18:0		-		283.264
FA 20:4	+		-	303.233
FA 20:3		-	++	305.248
FA 20:1		++		309.280
FA 22:4			+	331.264
MG 16:0		- -		365.246
Cer d34:2		- -		570.466
Cer d34:1	-	+		572.481
Cer d42:3	+			680.575
Cer d42:2	++		-	682.590
Cer d42:1	- -		+	684.607
GlcCer d34:1		++		734.535
PE 36:2			+	742.538
PG 16:0/18:1	- -		++	747.520
PS 16:0/18:1	++			760.515
PG 18:1/18:1			+	773.533
PG 18:0/18:1			+	775.548
PS 18:1/18:1 or 18:0/18:2			+	786.528

Table 2.1 continuation.

PS 18:0/18:1	++	-		788.547
PG 20:4/18:1			+	795.515
PS 18:0/20:3		+		812.544
PS 18:0/22:4			++	838.56
PI 18:0/18:2			+	861.552
PI 18:0/18:1			++	863.567
PI 18:0/20:4	-	++		885.552
PI 18:0/20:3		-	+	887.563
POSITIVE ION MODE				
Choline group		-	++	104.107
DG 36:3		- -	+	657.487
CE 18:2			- -	671.575
CE 18:1	- -			673.591
CE 20:4			+	711.548
SM 34:1	++			725.558
PC 32:1			+	770.511
PC 32:0			+	772.527
PC 34:1	+		- -	782.569
PC 34:2		-		796.526
PC 34:1	+	-		798.542
PC 36:4		- -		820.526
PC 36:3			++	822.542
PC 36:2		++		824.558
PC 38:4			-	848.558
22:1-Glc-Cholesterol			+	891.704
TG 52:3		+		895.716
Ubiquinone	- -			901.648
TG 54:4	-		+	921.729
TG 56:6			++	945.729
TG 56:4		+		949.759

Statistical prediction of intratumor heterogeneity

All the previous analyses described were performed by comparing normal, BOT, and HGSC pixels across tissue samples obtained from a total of 78 different patients. To evaluate our method performance in detecting tissue heterogeneity within the same patient tissue sample, we selected 5 HGSC samples that contained clear regions of stroma tissue adjacent to tumor within the same tissue section. Individual statistical classifiers were built for each patient using negative ion mode data. Lasso prediction results are presented in Table A1.8. Excellent agreements with pathologic classification were observed for all 5 patients (5,440 pixels), with an overall accuracy of 99.5% obtained for all patients combined. To visualize our method's performance in predicting heterogeneous tissue

regions within the same tissue section, we plotted the statistical results for 4 patients analyzed, showing pixels classified as HGSC in red and pixels classified as stroma in green (Figure 2.5). As observed, high spatial agreement between the predictive images and the pathologic diagnosis delineated in the optical images of the H&E stained sections was achieved.

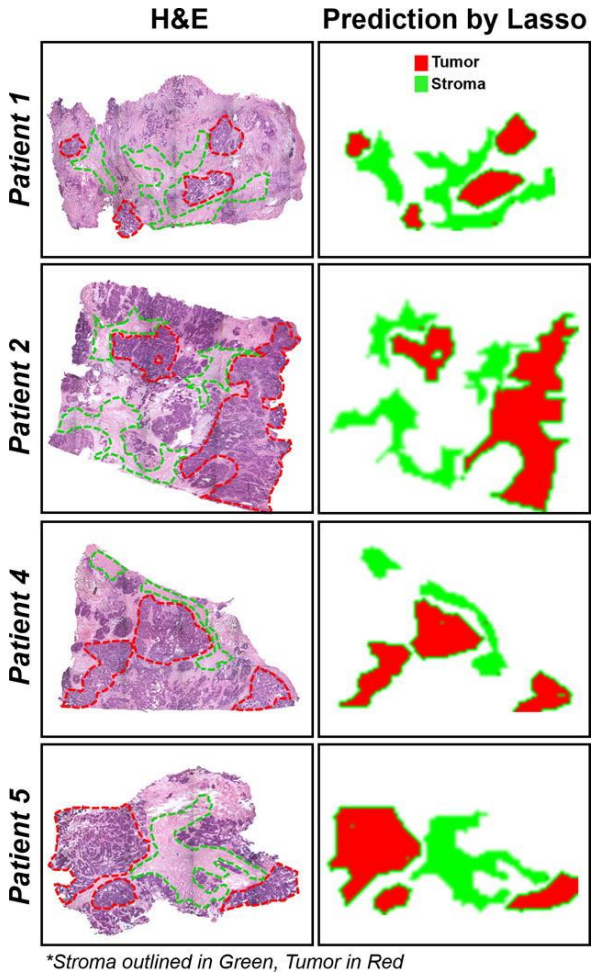

Figure 2.5: Prediction images of tumor and stroma tissue regions by the Lasso for four HGSC patients.

Regions of tumor (red) and stroma (green) are outlined on the optical images of H&E-stained tissues in the left column. The right column shows the corresponding predictions by the Lasso for the areas selected.

DISCUSSION

DESI-MS analysis of serous ovarian tumors allowed a detailed investigation of metabolic profiles characteristic of disease state and aggressiveness in the negative and positive ion modes. Different metabolic composition and relative abundances allowed clear identification of healthy ovarian tissues, HGSC, and serous BOT, within adjacent normal stroma and necrotic regions. DESI-MS imaging and pathologic evaluation of the same tissue section were essential for study, allowing high specificity for selecting areas of interest and extracting molecular information for statistical evaluation. MS imaging enabled visualization of features within heterogeneous tumor regions, even for fine papillary branches present in serous BOT. This approach is powerful for investigating diagnostic molecular signatures as it accounts for cellular heterogeneity and thus increases the performance of the tissue-trained statistical classifiers. Here, we report an extensive investigation into the molecular profiles for HGSC and serous BOT, identifying metabolites, fatty acids, and complex lipids as potential markers to discriminate aggressive and noninvasive tumors.

Alterations in the abundances of lipids and metabolites between healthy ovarian and tumorous serous tissues were detected by DESI-MS imaging, which reflect abnormalities in cancer cell metabolism. High relative abundance of ascorbic acid (vitamin C), a natural oxidant from dietary origin, was observed in normal ovarian tissue. The role of vitamin C in maintaining proper functioning of the ovary has been previously described in the literature, such as for the development and survival of ovarian follicles (37). Several molecules were identified as important predictive markers of disease state and cancer aggressiveness, which may become important diagnostic markers and serve as novel targets for therapeutic approaches. Gluconic acid, a metabolite that connects the glucose and pentose phosphate pathways, was identified as a predictive marker for discrimination

between HGSC and serous BOT and is thus a possible marker of ovarian cancer aggressiveness. Remarkably, gluconic acid has been previously found to discriminate between stages pT2 and pT3 of prostate cancer (38). Succinate and malate, intermediates in the citric acid cycle, were also identified as predictive markers of serous ovarian cancers. The oncogenic activity of succinate has been previously reported, and accumulation of malate has been shown to enhance fatty acid and cholesterol biosynthesis, enabling tumor growth (39).

Alterations in fatty acid and complex lipid metabolism were also detected by our approach. Previous studies have outlined the importance of fatty-acid synthesis in tumor biology due to their ability to modulate the fluidity of lipid membranes and affect cellular machinery (40). Moreover, unsaturated fatty acids have been associated with clinically aggressive tumors and were reported to stimulate the proliferation of human breast cancer cells, whereas saturated fatty acids induced cell death (29, 30). Our results suggest that alterations in fatty-acid unsaturation levels may play a role in serous ovarian cancer proliferation and aggressiveness. For example, polyunsaturated fatty acids, such as FA 20:3 and FA 22:4, were observed at high relative abundances in HGSC tissues and were given positive weights by the Lasso for this tissue class. To satisfy the high proliferating necessities of tumor cells, GPs are synthesized for continuous membrane production (41). During the review of this article, a related study was published aiming to diagnose different types of epithelial ovarian cancer based on lipid profiles by DESI-MS (42). Our results show good agreement with some of the changes in GPs identified for normal and carcinoma differentiation, such as PS 36:1 and PS 34:1, which showcases the potential of DESI-MS as a robust tool for tissue characterization. In our study, several PG and PI species were identified as predictive markers for tumor aggressiveness, with increased relative abundance in HGSC samples. CLs, which are complex GP species present almost

exclusively in the inner mitochondrial membrane, were also observed in increased relative abundances in HGSC tissue when compared with normal tissue (31). Moreover, increased relative abundances of ubiquinone, a component of the mitochondrial respiratory chain, was also found to be characteristic of serous ovarian tumors (36). Interestingly, mutations in mitochondrial DNA have been reported for human ovarian carcinomas, suggesting that alterations in mitochondria play a role in ovarian cancer tumorigenesis (43).

Another interesting group of lipid molecules identified as potential biomarkers by DESI-MS analysis was Cer. Ceramides are SP, which have been studied for their role in apoptosis and have been found to be overexpressed in necrotic tissue (35, 44). Here, we identified many Cer species with different fatty-acid chain lengths and saturation levels, which can help understand many of the underexplored biological functionalities of these molecules (35). LGSC, which evolve from BOTs, commonly present more chemo resistant responses than high-grade carcinomas (45). Notably, Cer have been investigated for their role as potential biomarkers of chemotherapy response, and in this study, high relative abundances of Cer species such as Cer d34:1 or GalCer d34:1 were characteristic of BOT (35). This finding could be of clinical importance, as it could help understand the mechanisms involved in chemotherapy response of serous carcinomas (4). Future studies will be pursued to investigate the biological pathways related to the expression of the molecules identified, which may help elucidate the pathogenesis of serous ovarian cancers and identify novel markers for early detection.

The classification models generated by the Lasso were successful in interpreting the large data sets, identifying molecular predictors of each tissue type as well as providing robust statistical classifiers. HGSC was classified with high accuracy in comparison with healthy stromal ovarian tissues, for both negative and positive ion mode data (96.4% overall agreement). Due to the recent findings proposing the distal end of the fallopian tube

as the site of origin of HGSC (4), we plan to analyze fallopian tube molecular profiles to investigate the biological processes by which high-grade carcinoma initiates. A three-class classification model to differentiate between normal, BOT, and HGSC was also built resulting in an overall agreement of 91.9% with pathologic evaluation. Overall, our method allowed discrimination between normal tissue and tumorous tissues including BOT and HGSC with 96.2% overall agreement.

Importantly, we also investigated predictive markers of tumor aggressiveness by directly comparing borderline and aggressive serous tumors using a two-class molecular model. Due to the contrasting biological pathways involved in BOT (which can develop to LGSC) and HGSC, both serous ovarian cancers were anticipated to entail distinct molecular features (4). The two-class classification models DESI-MS imaging data presented an overall accuracy of 93.0% in predicting HGSC and BOT, which demonstrates the clinical value of this technique in differentiating tumors with distinct invasive and aggressive behaviors. Remarkably, the three BOT samples misclassified as HGSC were re-evaluated by pathologic analysis and presented unusual histologic features associated with the development of low-grade carcinomas. The results suggest that changes in molecular composition detected by DESI-MS could be indicative of malignant behavior in borderline samples. We plan a follow-up study to investigate more clinically relevant cases as well as to further explore the molecular mechanism of development from borderline to malignant tumors.

Proposed priorities to reduce ovarian cancer incidence and improve patient outcome include the identification of biomarkers for prevention and early disease detection and the development of an integrated molecular view of the disease (7, 46, 47). Our results suggest that DESI-MS addresses these concerns by providing molecular information of a diverse group of lipids and metabolites that can serve as potential new markers of serous

ovarian cancer. Moreover, predictive markers of HGSC and BOT tumors were identified that may be used for the development of new therapeutic targets and preventive screening. Importantly, the ease and speed by which diagnostic molecular information can be obtained by DESI-MS and other relative ambient ionization techniques make this technology attractive for clinical use (48). Thus, we suggest DESI-MS as a potential clinical technology to integrate metabolic markers with clinical and pathologic approaches to provide more accurate tissue diagnosis and improve management of serous ovarian cancer patients.

REFERENCES

1. Mino-Kenudson M, Chirieac LR, Law K, Hornick JL, Lindeman N, Mark EJ, et al. A novel, highly sensitive antibody allows for the routine detection of alk-rearranged lung adenocarcinomas by standard immunohistochemistry. Clin Cancer Res 2010;16:1561–71.
2. Jones S, Anagnostou V, Lytle K, Parpart-Li S, Nesselbush M, Riley DR, et al. Personalized genomic analyses for cancer mutation discovery and interpretation. Sci Transl Med 2015;7.
3. McDonnell LA, Heeren RMA. Imaging mass spectrometry. Mass Spectrom Rev 2007;26:606 – 43.
4. Walch A, Rauser S, Deininger S-O, Hoefler H. Maldi imaging mass spectrometry for direct tissue analysis: A new frontier for molecular histology. Histochem Cell Biol 2008;130:421–34.
5. Seeley EH, Caprioli RM. Molecular imaging of proteins in tissues by mass spectrometry. Proc Natl Acad Sci USA 2008;105:18126 –31.
6. Braun RM, Blenkinsopp P, Mullock SJ, Corlett C, Willey KF, Vickerman JC, Winograd N. Performance characteristics of a chemical imaging time-of-flight mass spectrometer. Rapid Comm Mass Spectrom 1998;12: 1246 –52.
7. Sarsby J, Griffiths RL, Race AM, Bunch J, Randall EC, Creese AJ, Cooper HJ. Liquid extraction surface analysis mass spectrometry coupled with field asymmetric waveform ion mobility spectrometry for analysis of intact proteins from biological substrates. Anal Chem 2015;87: 6794 – 800.
8. Yang J, Caprioli RM. Matrix precoated targets for direct lipid analysis and imaging of tissue. Anal Chem 2013; 85:2907–12.
9. Carado A, Kozole J, Passarelli M, Winograd N, Loboda A, Bunch J, et al. Biological tissue imaging with a hybrid cluster sims quadrupole time-of-flight mass spectrometer. Appl Surf Sci 2008;255:1572–5.
10. Kiss A, Smith DF, Jungmann JH, Heeren RMA. Cluster secondary ion mass spectrometry microscope mode mass spectrometry imaging. Rap Commun Mass Spectrom 2013;27:2745–50.
11. Klitzing HA, Weber PK, Kraft ML. Secondary ion mass spectrometry imaging of biological membranes at high spatial resolution. Meth Mol Biol 2013;950:483–501.
12. Nemes P, Vertes A. Laser ablation electrospray ionization for atmospheric pressure, in vivo, and imaging mass spectrometry. Anal Chem 2007;79:8098 –106.
13. Santos VG, Regiani T, Dias FFG, Romao W, Jara JLP, Klitzke CF, et al. Venturi easy ambient sonic-spray ionization. Anal Chem 2011;83:1375– 80.

14. Alberici RM, Simas RC, Sanvido GB, Romao W, Lalli PM, Benassi M, et al. Ambient mass spectrometry: Bringing ms into the ”real world“. Anal Bioanal Chem 2010;398: 265–94.

15. Wu C, Dill AL, Eberlin LS, Cooks RG, Ifa DR. Mass spectrometry imaging under ambient conditions. Mass Spectrom Rev 2013;32:218 – 43.

16. Hsu C-C, Dorrestein PC. Visualizing life with ambient mass spectrometry. Curr Opin Biotechnol 2015;31: 24 –34.

17. Harris GA, Galhena AS, Fernandez FM. Ambient sampling/ ionization mass spectrometry: Applications and current trends. Anal Chem 2011;83:4508 –38.

18. Ellis SR, Bruinen AL, Heeren RMA. A critical evaluation of the current state-of-the-art in quantitative imaging mass spectrometry. Anal Bioanal Chem 2014;406: 1275– 89.

19. Takats Z, Wiseman JM, Gologan B, Cooks RG. Mass spectrometry sampling under ambient conditions with desorption electrospray ionization. Science 2004;306: 471–3.

20. Badu-Tawiah AK, Eberlin LS, Ouyang Z, Cooks RG.Chem aspects of the extractive methods of ambient ionization mass spectrometry. Ann Rev Phys Chem 2013;64:481–505.

21. Ifa DR, Wiseman JM, Song Q, Cooks RG. Development of capabilities for imaging mass spectrometry under ambient conditions with desorption electrospray ionization (desi). Int J Mass Spectrom 2007;259:8 –15.

22. Eberlin LS, Norton I, Orringer D, Dunn IF, Liu X, Ide JL, et al. Ambient mass spectrometry for the intraoperative molecular diagnosis of human brain tumors. Proc Natl Acad Sci USA 2013;110:1611– 6.

23. Campbell DI, Ferreira CR, Eberlin LS, Cooks RG. Improved spatial resolution in the imaging of biological tissue using desorption electrospray ionization. Anal Bioanal Chem 2012;404:389 –98.

24. Kertesz V, Van Berkel GJ. Improved imaging resolution in desorption electrospray ionization mass spectrometry. Rapid Commun Mass Spectrom 2008;22:2639 – 44.

25. Hiraoka K, Nishidate K, Mori K, Asakawa D, Suzuki S. Development of probe electrospray using a solid needle. Rapid Commun Mass Spectrom 2007;21:3139 – 44.

26. Mandal MK, Yoshimura K, Saha S, Ninomiya S, Rahman MO, Yu Z, et al. Solid probe assisted nanoelectrospray ionization mass spectrometry for biological tissue diagnostics. Analyst 2012;137:4658 – 61.

27. Kerian KS, Jarmusch AK, Cooks RG. Touch spray mass spectrometry for in situ analysis of complex samples. Analyst 2014;139:2714 –20.

28. Schaefer K-C, Denes J, Albrecht K, Szaniszlo T, Balog J, Skoumal R, et al. In vivo, in situ tissue analysis using rapid evaporative ionization mass spectrometry. Angew Chem Int Ed 2009;48:8240 –2.

29. Balog J, Szaniszlo T, Schaefer K-C, Denes J, Lopata A, Godorhazy L, et al. Identification of biological tissues by rapid evaporative ionization mass spectrometry. Anal Chem 2010;82:7343–50.

30. Wiseman JM, Puolitaival SM, Takats Z, Cooks RG, Caprioli RM. Mass spectrometric profiling of intact biological tissue by using desorption electrospray ionization. Angew Chem Int Ed 2005;44:7094 –7.

31. Wiseman JM, Ifa DR, Song QY, Cooks RG. Tissue imaging at atmospheric pressure using desorption electrospray ionization (desi) mass spectrometry. Angew Chem Int Ed 2006;45:7188 –92.

32. Dill AL, Ifa DR, Manicke NE, Zheng O, Cooks RG. Mass spectrometric imaging of lipids using desorption electrospray ionization. J Chromatogr B Analyt Technol Biomed Life Sci 2009;877:2883–9.

33. Eberlin LS, Ferreira CR, Dill AL, Ifa DR, Cheng L, Cooks RG. Non-destructive, histologically compatible tissue imaging by desorption electrospray ionization mass spectrometry.Chembiochem 2011;12:2129 –32.

34. Tata A, Zheng J, Ginsberg HJ, Jaffray DA, Ifa DR, Zarrine- Afsar A. Contrast agent mass spectrometry imaging reveals tumour heterogeneity. Anal Chem 2015;87: 7683–9.

35. Eberlin LS, Ferreira CR, Dill AL, Ifa DR, Cooks RG. Desorption electrospray ionization mass spectrometry for lipid characterization and biological tissue imaging. Biochim Biophys Acta Mol Cell Biol Lipids 2011;1811: 946 – 60.

36. Bishop JM. Molecular themes in oncogenesis. Cell 1991;64:235– 48.

37. Corda D, Zizza P, Varone A, Filippi BM, Mariggio S. The glycerophosphoinositols: Cellular metabolism and biological functions. Cell Mol Life Sci 2009;66:3449 – 67.

38. Soga T. Cancer metabolism: Key players in metabolic reprogramming. Cancer Sci 2013;104:275– 81.

39. Utsugi T, Schroit AJ, Connor J, Bucana CD, Fidler IJ. Elevated expression of phosphatidylserine in the outermembrane leaflet of human tumor-cells and recognition by activated human blood monocytes. Cancer Res 1991;51:3062– 6.

40. Dobrzynska I, Szachowicz-Petelska B, Sulkowski S, Figaszewski Z. Changes in electric charge and phospholipids composition in human colorectal cancer cells. Mol Cell Biochem 2005;276:113–9.

41. Masterson TA, Dill AL, Eberlin LS, Mattarozzi M, Cheng L, Beck SDW, et al. Distinctive glycerophospholipid profiles of human seminoma and adjacent normal tissues by desorption electrospray ionization imaging mass spectrometry. J Am Soc Mass Spectrom 2011;22: 1326 –33.

42. Dill AL, Eberlin LS, Costa AB, Zheng C, Ifa DR, Cheng L, et al. Multivariate statistical identification of human bladder carcinomas using ambient ionization imaging mass spectrometry. Chem-Eur J 2011;17:2897–902.

43. Dill AL, Eberlin LS, Zheng C, Costa AB, Ifa DR, Cheng LA, et al. Multivariate statistical differentiation of renal cell carcinomas based on lipidomic analysis by ambient ionization imaging mass spectrometry. Anal Bioanal Chem 2010;398:2969 –78.

44. Eberlin LS, Tibshirani RJ, Zhang J, Longacre TA, Berry GJ, Bingham DB, et al. Molecular assessment of surgical-resection margins of gastric cancer by massspectrometric imaging. Proc Natl Acad Sci USA 2014; 111:2436 – 41.

45. Eberlin LS, Dill AL, Golby AJ, Ligon KL, Wiseman JM, Cooks RG, Agar NYR. Discrimination of human astrocytoma subtypes by lipid analysis using desorption electrospray ionization imaging mass spectrometry. Angew Chem Int Edit 2010;49:5953– 6.

46. Eberlin LS, Norton I, Dill AL, Golby AJ, Ligon KL, Santagata S, et al. Classifying human brain tumors by lipid imaging with mass spectrometry. Cancer Res 2012;72: 645–54.

47. Santagata S, Eberlin LS, Norton I, Calligaris D, Feldman DR, Ide JL, et al. Intraoperative mass spectrometry mapping of an onco-metabolite to guide brain tumor surgery. Proc Natl Acad Sci USA 2014;111:11121– 6.

48. Eberlin LS, Gabay M, Fan AC, Gouw AM, Tibshirani RJ, Felsher DW, Zare RN. Alteration of the lipid profile in lymphomas induced by myc overexpression. Proc Natl Acad Sci USA 2014;111:10450 –5.

49. Morrish F, Isern N, Sadilek M, Jeffrey M, Hockenbery DM. C-myc activates multiple metabolic networks to generate substrates for cell-cycle entry. Oncogene 2009;28:2485–91.

50. Wolfer A, Wittner BS, Irimia D, Flavin RJ, Lupien M, Gunawardane RN, et al. Myc regulation of a ”poorprognosis“ metastatic cancer cell state. Proc Natl Acad Sci USA 2010;107:3698 –703.

51. Gerbig S, Golf O, Balog J, Denes J, Baranyai Z, Zarand A, et al. Analysis of colorectal adenocarcinoma tissue by desorption electrospray ionization mass spectrometric imaging. Anal Bioanal Chem 2012;403:2315–25.

52. Sjolander A, Yamamoto K, Huber BE, Lapetina EG. Association of p21ras with phosphatidylinositol 3-kinase. Proc Natl Acad Sci USA 1991;88:7908 –12.

53. Mandal MK, Saha S, Yoshimura K, Shida Y, Takeda S, Nonami H, Hiraoka K. Biomolecular analysis and cancer diagnostics by negative mode probe electrospray ionization. Analyst 2013;138:1682– 8.

54. Calligaris D, Feldman DR, Norton I, Brastianos PK, Dunn IF, Santagata S, Agar NYR. Molecular typing of meningiomas by desorption electrospray ionization mass spectrometry imaging for surgical decisionmaking. Int J Mass Spectrom 2015;377:690 – 8.

55. Calligaris D, Caragacianu D, Liu X, Norton I, Thompson CJ, Richardson AL, et al. Application of desorption electrospray ionization mass spectrometry imaging in breast cancer margin analysis. Proc Natl Acad Sci USA 2014;111:15184 –9.

56. Guenther S, Muirhead LJ, Speller AVM, Golf O, Strittmatter N, Ramakrishnan R, et al. Spatially resolved metabolic phenotyping of breast cancer by desorption electrospray ionization mass spectrometry. Cancer Res 2015;75:1828 –37.

57. Pavlides S, Whitaker-Menezes D, Castello-Cros R, Flomenberg N, Witkiewicz AK, Frank PG, et al. The reverse warburg effect aerobic glycolysis in cancer associated fibroblasts and the tumor stroma. Cell Cycle 2009; 8:3984 – 4001.

58. Balog J, Sasi-Szabo L, Kinross J, Lewis MR, Muirhead LJ, Veselkov K, et al. Intraoperative tissue identification using rapid evaporative ionization mass spectrometry. Sci Transl Med 2013;5.

59. Golf O, Strittmatter N, Karancsi T, Pringle SD, Speller AVM, Mroz A, et al. Rapid evaporative ionization mass spectrometry imaging platform for direct mapping from bulk tissue and bacterial growth media. Anal Chem 2015;87:2527–34.

60. Schaefer K-C, Szaniszlo T, Guenther S, Balog J, Denes J, Keseru M, et al. In situ, real-time identification of biological tissues by ultraviolet and infrared laser desorption ionization mass spectrometry. Anal Chem 2011; 83:1632– 40.

61. Agar NYR, Golby AJ, Ligon KL, Norton I, Mohan V, Wiseman JM, et al. Development of stereotactic mass spectrometry for brain tumor surgery. Neurosurg 2011;68: 280 –90.

62. Schaefer K-C, Balog J, Szaniszlo T, Szalay D, Mezey G, Denes J, et al. Real time analysis of brain tissue by direct combination of ultrasonic surgical aspiration and sonic spray mass spectrometry. Anal Chem 2011;83: 7729 –35

63. Kerian KS, Jarmusch AK, Pirro V, Koch MO, Masterson TA, Cheng L, Cooks RG. Differentiation of prostate cancer from normal tissue in radical prostatectomy specimens by desorption electrospray ionization and touch spray ionization mass spectrometry. Analyst 2015;140: 1090 – 8.

64. Chen C-H, Lin Z, Garimella S, Zheng L, Shi R, Cooks RG, Ouyang Z. Development of a mass spectrometry sampling probe for chemical analysis in surgical and endoscopic procedures. Anal Chem 2013;85:11843–50.

65. Bojko B, Pawliszyn J. In vivo and ex vivo spme: A low invasive sampling and sample preparation tool in clinical bioanalysis. Bioanalysis 2014;6:1227–39.

66. Fatou B, Wisztorski M, Focsa C, Ziskind M, Salzet M, Fournier I. Development of a novel instrument for exvivo and in-vivo real-time analysis. Oral session presented at: 63rd ASMS Conference on Mass Spectrometry and Allied Topics; 2015 May 31–Jun 4; St. Louis, MO.

67. Abdelmoula WM, Skraskova K, Balluff B, Carreira RJ, Tolner EA, Lelieveldt BPF, et al. Automatic generic registration of mass spectrometry imaging data to histology using nonlinear stochastic embedding. Anal Chem 2014;86:9204 –11.

68. Bemis KD, Harry A, Eberlin LS, Ferreira C, van de Ven SM, Mallick P, et al. Cardinal: An r package for statistical analysis of mass spectrometry-based imaging experiments. Bioinformatics 2015;31:2418 –20.

69. Krasny L, Hoffmann F, Ernst G, Trede D, Alexandrov T, Havlicek V, et al. Spatial segmentation of maldi ft-icr msi data: A powerful tool to explore the head and neck tumor in situ lipidome. J AmSoc Mass Spectrom 2015; 26:36 – 43.

70. Chen H, Gamez G, Zenobi R. What can we learn from ambient ionization techniques? J Am Soc Mass Spectrom 2009;20:1947– 63.

71. Eberlin LS, Dill AL, Costa AB, Ifa DR, Cheng L, Masterson T, et al. Cholesterol sulfate imaging in human prostate cancer tissue by desorption electrospray ionization mass spectrometry. Anal Chem 2010;82:3430 – 4.

72. Mandal MK, Yoshimura K, Chen LC, Yu Z, Nakazawa T, Katoh R, et al. Application of probe electrospray ionization mass spectrometry (pesi-ms) to clinical diagnosis: Solvent effect on lipid analysis. J Am Soc Mass Spectrom 2012;23:2043–7.

73. Calligaris D, Norton I, Feldman DR, Ide JL, Dunn IF, Eberlin LS, et al. Mass spectrometry imaging as a tool for surgical decision-making. J Mass Spectrom 2013; 48:1178 – 87.

74. Abbassi-Ghadi N, Veselkov K, Kumar S, Huang J, Jones E, Strittmatter N, et al. Discrimination of lymph node metastases using desorption electrospray ionisationmass spectrometry imaging. ChemCommun2014;50: 3661– 4.

Chapter 3. Investigating the Effects of FABP4 Expression in Ovarian Cancer Metabolism[3]

INTRODUCTION

Primary cytoreductive surgery followed by adjuvant chemotherapy is the standard treatment for ovarian cancer. Several reports have established a link between residual disease after surgery and shorter overall and progression-free survival, as well as poor response to adjuvant chemotherapy (1-3). Incomplete resection can result from the presence of numerous, dense nodules that simply cannot be removed, distant tumor metastasis, location of tumor near critical organs (e.g., porta hepatis), and extensive mesenteric involvement. Thus, while a surgeon's skill is important, residual disease could occur because the intrinsic biology of the tumor creates a highly metastatic and infiltrative disease pattern, making complete resection infeasible (3,4). A large retrospective study showed that initial disease distribution could also affect patient survival despite aggressive cytoreductive efforts (5). Considering the impact of residual disease on patient survival, many studies are now focusing on the development of predictive models for residual disease. However, currently there is little understanding of the biological mechanisms that could lead to residual disease in ovarian cancer.

Previous studies have shown that high expression of fatty acid binding protein 4 (FABP4) can be a reliable molecular predictor of residual disease in high-grade serous ovarian cancer (4). FABP4 is implicated in atherosclerosis, diabetes, inflammatory response, and angiogenesis (6-12). In prostate and ovarian cancers, FABP4 acts as a key

[3] Adapted with permission from Gharpure KM, Pradeep S, Sans M, Rupaimoole R, Ivan C, Wu SY, et al. FABP4 as a key determinant of metastatic potential of ovarian cancer. Nat Commun 2018;9(1):2923. Copyright © 2018, Springer Nature. The data presented in this chapter was collected, analyzed and interpreted by Sans M. Samples were provided by Dr. Sood's laboratory at the MD Anderson Cancer Research Center along with clinical and molecular data. Gharpure KM, Pradeep S, and Sans M prepared the manuscript. All other others contributed in revising the manuscript.

mediator between adipocytes and cancer progression (13,14). However, FABP4 regulation and the functional implications of FABP4 overexpression in increasing the metastatic potential of ovarian cancer cells remain to be investigated. In this study, we contributed to the investigation of the underlying tumor biology responsible for the aggressive pattern of tumor metastasis using desorption electrospray ionization mass spectrometry (DESI-MS) imaging to investigate the downstream effects of FABP4 expression in ovarian cancer metabolism. As discussed in Chapter 1, we have previously applied DESI-MS in combination with multivariate statistical methods to evaluate and detect metabolic markers associated with ovarian cancer aggressiveness (15). Here, we aim to go beyond cancer diagnosis and subtyping, and apply this technology to explore changes in the metabolic levels detected by DESI-MS associated with the expression of the FABP4 gene.

MATERIALS AND METHODS

Tumor samples

High-grade ovarian tumor samples were obtained from the Cooperative Human Tissue Network (CHTN) and the MD Anderson Tissue Bank under an approved IRB protocol and written consent was obtained for the use of patient samples for research. The details regarding the quality control for the samples obtained from CHTN can be found at https://www.chtn.org/quality.html

In vivo mouse models

Female athymic nude mice were purchased from Taconic Farms (Hudson, NY) and housed in pathogen-free conditions by our collaborators in Dr. Anil K. Sood's laboratory at the University of Texas MD Anderson Cancer Research Center. The mice were cared for according to the guidelines of the American Association for Accreditation for

Laboratory Animal Care International and the US Public Health Service Policy on Humane Care and Use of Laboratory Animals. All *in vivo* experiments and protocols were approved by MD Anderson's Institutional Animal Care and Use Committee. To establish the tumors, 1 × 106 cells/mouse A2780 cells, 8 × 105 cells/mouse HeyA8 MDR-Luc cells, or 1 × 106 cells/mouse Ovcar 5-Luc cells were injected into the ovary. No therapeutic intervention was conducted in the experiment in which FABP4-overexpressing cells were injected. For all therapeutic experiments, a siRNA dose of 200 μg kg−1 was used, and the treatments were started 1 week after cell injections. The mice were divided into two groups: control and treatment, 10 mice/group. Mice in the control group received control siRNA incorporated into neutral DOPC liposomes. Mice in the treatment group received FABP4 siRNA incorporated into DOPC liposomes. The doses were given twice weekly intraperitoneally. The mice were monitored daily for any toxic effects. Tumor tissues were then frozen in optimal cutting temperature media or snap frozen.

DESI-MS imaging

DESI-MS imaging was conducted as described previously (15,16). A 2D Omni Spray (Prosolia Inc., Indianapolis, IN) coupled to an LTQ-Orbitrap Elite mass spectrometer (Thermo Scientific, San Jose, CA) was used for tissue imaging. DESI-MS imaging was performed in the negative and positive ion mode from *m/z* 100–1500, using a hybrid LTQ-Orbitrap mass spectrometer which allows for tandem MS experiments, high mass accuracy (<5 ppm mass error), and high mass resolution (240,000 resolving power) measurements. The spatial resolution of the imaging experiments was 200 μm. Spatially accurate ion images were assembled using BioMap and MSiReader software. The histologically compatible solvent system dimethylformamide:acetonitrile (DMF:ACN) 1:1 (v/v) was used for negative ion mode analysis, at a flow rate of 1.2 μl min^{-1}. For positive ion mode

analysis, pure ACN was used, at a flow rate of 3 µl/min. The N2 pressure was set to 185 psi. For ion identification, high mass resolution/accuracy measurements using the same tissue sections analyzed were conducted. Tandem MS analyses were performed using both the Orbitrap and the linear ion trap for mass analysis.

Histopathology and light microscopy

The same tissue sections analyzed by DESI-MS imaging were subjected afterwards to standard H&E staining protocol. Light microscopy images of the H&E stained slides were taken using the EVOS FL Auto Cell Imaging System (Invitrogen, Thermo Fisher Scientific, Waltham, MA, USA).

Statistical analysis

MS data corresponding to the areas of interest were extracted using MSiReader software. The m per z range was discretized by performing hierarchical clustering and cutting the resulting dendrogram at distance 0.05. Peaks appearing in more than 10% of the pixels were kept for analysis. Logistic regression was performed with Lasso regularization using the "glmnet" package (17) in the R language. Regularization parameters were determined by 3-fold cross-validation analysis. The data were randomly equally divided into training and validation sets of samples, 50-50 per patient basis. The training set was used to build a model by cross-validation (CV) based on assigned statistical weights to specific lipid and metabolites important for classification of samples as having either high- or low-FABP4 expression. To determine trends in molecular composition, Significance Analysis of Microarrays (SAM) was used, providing a list of statistically significant *m/z* features between the high- and low-FABP4 expression groups.

RESULTS

Effect of FABP4 expression on human ovarian cancer tissue metabolites

To explore the effects of FABP4 on metabolic changes in human ovarian cancer tissues, we evaluated metabolic and lipid trends related to FABP4 gene expression by DESI-MS imaging. Gene expression levels for each tissue sample were provided by our collaborators in Dr. Anil K. Sood's laboratory at the MD Anderson Cancer Research Center using quantitative real-time PCR. In this study, a total of 31 high-grade ovarian cancer tissue samples were analyzed by DESI-MSI in both negative and positive ion modes to investigate a broad range of lipid and metabolites related to FABP4 expression. Using this approach, only the data specific to the tumor region were selected and evaluated, thus eliminating the inclusion of stromal lipids and metabolites.

SAM analysis was conducted to identify statistically significant *m/z* values (mass to charge ratios) detected by DESI-MSI characteristic of low- or high-FABP4 expression. Positive SAM scores represent higher relative abundance in samples with low-FABP4-expression, and negative SAM scores represent higher relative abundance in samples with high-FABP4-expression. Negative ion mode data revealed 361 and 289 monoisotopic *m/z* values associated with low or high FABP4 expression, respectively, with false discovery rate (FDR) of <3.8%. From these, 238 *m/z* values were tentatively identified by high mass accuracy measurements and tandem MS analysis (Table A2.1) as small metabolites, fatty acids (FA), ceramides (Cer), glycerolipids (GL), monoacylglycerophosphates (PA), glycerophosphoethanolamines (PE), glycerophosphoglycerols (PG), glycerophosphoinositols (PI), glycerophosphoserines (PS), and cardiolipins (CL). Molecular formulas detected *m/z* and mass errors in ppm are provided in Table A2.2 for the species identified. Fatty acid and metabolite composition were observed to significantly

differ between the two expression groups. For example, higher unsaturation and oxidation of fatty acid species was selected as characteristic of high FABP4 expression. A significant number of m/z values related to high FABP4 expression corresponded to GL, PE, PG, and lysophospholipid species, such as LysoPE, LysoPG, and LysoPI. On the other hand, CL species were almost exclusively selected with the low-FABP4-expression type. These variations in lipid composition suggest alterations in metabolism and biosynthesis due to the changes in the expression of the FABP4 gene.

We then applied the Lasso (Least absolute shrinkage and selector operator) (17) method to evaluate if predictive statistical models could be built to classify samples as having low- or high-FABP4 expression based on metabolite composition (Table 3.1). The samples were randomly divided into a training and validation set of samples (50:50). Results based on negative ion mode data yielded an overall agreement of 81.6% and 0.79 area under the curve (AUC) value for the training set performance. The remaining independent set of samples were classified with an overall agreement of 56.1% and AUC value of 0.60. In positive ion mode data, an overall agreement of 74.2% for CV (AUC = 0.73) and 61.7% agreement for the validation set (AUC = 0.58) were achieved. To improve prediction of FABP4 expression, positive and negative ion mode data were combined to build a comprehensive model. Using this approach, 66.7% of high-FABP4 patients and 100% of low-FABP4 patients were successfully classified in patient-by-patient analysis.

Table 3.1: Confusion matrix showing lasso classification of high-grade serous cancer samples into high and low FABP4 expression based on DESI-MS lipid and metabolite data in negative, positive and combined polarities.

Results are shown for pixels and patient classification both for the training set (cross-validation) and validation set. Agreement is calculated comparing lasso prediction to FABP4 expression provided by qRT-PCR. AUC – Area Under the Curve.

			Lasso Prediction				
		qRT-PCR	**High FABP4**	**Low FABP4**	**Agreement (%)**	**Overall Agreement (%)**	**AUC**
Negative Ion Mode							
Per Pixel	**Cross-Validation**	High FABP4	1925	671	74.2	81.6	0.79
		Low FABP4	1218	6450	84.1		
	Validation Set	High FABP4	1003	1189	45.8	56.1	0.6
		Low FABP4	1084	1906	63.8		
Positive Ion Mode							
Per Patient	**Cross-Validation**	High FABP4	5	1	83.3	80	0.79
		Low FABP4	3	11	78.6		
	Validation Set	High FABP4	4	2	66.7	63.6	0.6
		Low FABP4	2	3	60		
Per Pixel	**Cross-Validation**	High FABP4	1248	531	70.2	74.2	0.73
		Low FABP4	2271	6823	75		
	Validation Set	High FABP4	661	705	48.4	61.7	0.58
		Low FABP4	1049	2169	67.4		
Per Patient	**Cross-Validation**	High FABP4	5	1	83.3	73.7	0.73
		Low FABP4	4	9	69.2		
	Validation Set	High FABP4	2	2	50	50	0.58
		Low FABP4	3	3	50		
Combined Polarities							
Per Patient	**Cross-Validation**	High FABP4	4	2	66.7	85.7	-
		Low FABP4	0	8	100		

Evaluating lipid and metabolite changes due to FABP4 expression from *in vivo* mouse models

To further investigate direct changes in lipid and metabolite levels due to the changes in FABP4 expression, we analyzed *in vivo* tissues from high-grade ovarian cancer mouse models. Using DESI-MS imaging, we compared tumor tissues of FABP4 siRNA group (low FABP4 expression, n = 3) to control siRNA samples (high FABP4 expression, n = 3). SAM analysis revealed 627 monoisotopic *m/z* values characteristic of FABP4 silencing, with FDR < 5.5%. From the selected *m/z* values, a total of 184 species (59 increased in low FABP4, 125 increased in high FABP4) were identified as metabolites, FA and complex lipids, with attributed SAM scores associated to FABP4 expression (Table A2.3). Overall, the majority of the lipid classes received negative SAM scores, thus being associated to high FABP4 expression. For example, FA and monoacylglycerophosphates (PA) were selected exclusively for characterization of the control siRNA samples. On the other hand, Cer species were associated with low expression of the FABP4 gene. These trends were also reflected by the relative abundances observed in the ion images as shown in Figure 3.1, where all the lipid species shown except for the Cer d42:1 displayed higher relative abundances within the high FABP4 samples. Remarkably, comparison between the metabolic species selected by SAM analysis for both human and mouse samples resulted in a total of 76 common *m/z* values related to high or low FABP4 expression (Table 3.2). Among these, various FA species were associated with high expression of the FABP4 gene in both the mice and human samples. Interestingly, common GL and PI species for both animal samples were specific to the high FABP4 class, while Cer species were characteristic of tissues with low FABP4 expression. Differences in FA chain length and saturation level were also observed within the same GP class. For example, longer FA chain in PE and lysoPE species were associated with high FABP4 expression, while longer

FA chain in PS lipids were characteristic to tissue samples with lower FABP4 expression. These similar metabolic trends observed in both human and mice samples strongly suggest and corroborate the effects of the FABP4 gene in metabolism and biosynthesis.

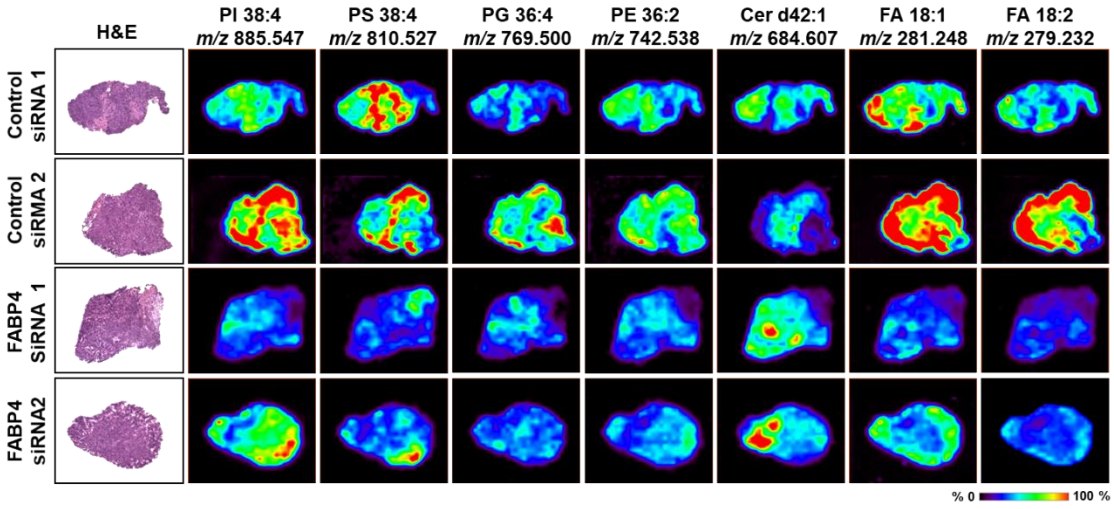

Figure 3.1: DESI-MS ion images of *in vivo* tumor samples from control siRNA and FABP4 siRNA treatment groups.

Areas of red intensity within the ion images represent highest (100%) and black lowest (0%) relative abundances. Lipid species are described by head group, number of fatty-acid chain carbons, and double bonds.

Table 3.2: Lipid and metabolite species related to low and high expression of the FABP4 gene in both human and mice samples based on SAM analysis from DESI-MS imaging data.

siFABP4 - LOW FABP4 EXPRESSION		***CONTROL - HIGH FABP4 EXPRESSION***			
Attribution	**Molecular Formula**	**Attribution**	**Molecular Formula**	**Attribution**	**Molecular Formula**
Metabolites		*Metabolites*		*Fatty Acids*	
Succinate	$C_4H_5O_4$	Taurine	$C_2H_6NO_3S$	FA 18:3	$C_{18}H_{29}O_2$
Glutathione	$C_{10}H_{16}N_3O_6S$	Xanthine	$C_5H_3O_2N_4$	FA 18:2	$C_{18}H_{31}O_2$
Glycerophosphoethanolamines		*Glycerophosphoethanolamines*		FA 18:1	$C_{18}H_{33}O_2$
LysoPE 18:1	$C_{24}H_{45}NO_8P$	LysoPE 16:0	$C_{21}H_{43}NO_6P$	FA 18:0	$C_{18}H_{35}O_2$
PE 18:1/18:1	$C_{41}H_{77}NO_8P$	LysoPE 18:0	$C_{23}H_{47}NO_7P$	FA 19:0	$C_{19}H_{37}O_2$
PE 22:6/16:0	$C_{43}H_{73}NO_8P$	PE P-18:0/18:4	$C_{41}H_{73}NO_7P$	FA 20:5	$C_{20}H_{29}O_2$
Glycerophosphoglycerols		PE P-38:4	$C_{43}H_{77}NO_7P$	FA 20:4	$C_{20}H_{31}O_2$
PG 18:0/18:1	$C_{42}H_{80}O_{10}P$	PE 20:4/18:1	$C_{43}H_{75}NO_8P$	FA 18:2	$C_{18}H_{32}O_2Cl$
PG 18:0/18:0	$C_{42}H_{82}O_{10}P$	PE 40:5	$C_{45}H_{79}NO_8P$	FA 18:1	$C_{18}H_{34}O_2Cl$
PG 42:7	$C_{48}H_{80}O_{10}P$	PE 22:4/18:0	$C_{45}H_{81}NO_8P$	FA hydroxy 20:4	$C_{20}H_{31}O_3$
Ceramides		*Glycerophosphoglycerols*		FA 22:6	$C_{22}H_{31}O_2$
Cer d18/16:0	$C_{34}H_{69}NO_3Cl$	LysoPG 18:2	$C_{24}H_{44}O_9P$	FA 22:5	$C_{22}H_{33}O_2$
Cer m18:1/22:0	$C_{40}H_{79}NO_2Cl$	LysoPG 18:1	$C_{24}H_{46}O_9P$	FA 22:4	$C_{22}H_{35}O_2$
Cer m42:1	$C_{42}H_{83}NO_2Cl$	LysoPG 22:6	$C_{28}H_{44}O_9P$	FA 22:3	$C_{22}H_{37}O_2$
Cer d42:1	$C_{42}H_{83}NO_3Cl$	PG 16:0/18:1	$C_{40}H_{76}O_{10}P$	FA 20:4	$C_{20}H_{32}O_2Cl$
Cer d42:0	$C_{42}H_{85}NO_3Cl$	PG 18:2/18:2	$C_{42}H_{74}O_{10}P$	FA 24:5	$C_{24}H_{37}O_2$
Cer d18:1/26:1	$C_{44}H_{85}NO_3Cl$	PG 18:2/18:1	$C_{42}H_{76}O_{10}P$	FA 24:4	$C_{24}H_{39}O_2$
Cer d18:1/26:0	$C_{44}H_{87}NO_3Cl$	PG 18:1/18:1	$C_{42}H_{78}O_{10}P$	FA 22:4	$C_{22}H_{36}O_2Cl$
Cardiolipins		PG 20:4/20:4	$C_{46}H_{74}O_{10}P$	*Glycerophosphoinositols*	
CL 70:7	$C_{79}H_{138}O_{17}P_2$	*Cardiolipins*		LysoPI 18:0	$C_{27}H_{52}O_{12}P$
CL 70:6	$C_{79}H_{140}O_{17}P_2$	CL 72:4	$C_{81}H_{148}O_{17}P_2$	LysoPI 20:4	$C_{29}H_{48}O_{12}P$
CL 74:10	$C_{83}H_{140}O_{17}P_2$	*Glycerolipids*		PI 20:3/17:1	$C_{46}H_{80}O_{13}P$
CL 74:9	$C_{83}H_{142}O_{17}P_2$	MG 18:0/0:0	$C_{21}H_{40}O_4Cl$	PI 18:1/20:4	$C_{47}H_{80}O_{13}P$
Glycerophosphoserines		DG 36:3/0:0	$C_{39}H_{70}O_5Cl$	PI 18:0/20:4	$C_{47}H_{82}O_{13}P$
PS P-36:2	$C_{42}H_{77}NO_9P$	DG 36:2/0:0	$C_{39}H_{72}O_5Cl$	PI 18:0/20:3	$C_{47}H_{84}O_{13}P$
PS P-36:1	$C_{42}H_{79}NO_9P$	*Glycerophosphoserines*		PI 18:0/22:6	$C_{49}H_{82}O_{13}P$
PS 18:0/18:1	$C_{42}H_{79}NO_{10}P$	PS 18:1/18:2	$C_{42}H_{75}NO_{10}P$	PI 18:0/22:4	$C_{49}H_{86}O_{13}P$
PS 40:2	$C_{46}H_{85}O_{10}NP$	PS 18:0/20:4	$C_{44}H_{77}O_{10}NP$		
PS 40:1	$C_{46}H_{87}O_{10}NP$	PS 39:4	$C_{45}H_{79}NO_{10}P$		
PS 18:1/24:1	$C_{48}H_{89}O_{10}NP$				
PS 18:1/24:0	$C_{48}H_{91}O_{10}NP$				

DISCUSSION

The integration of DESI-MS imaging with multivariate statistical analyses offers the powerful capability to carefully evaluate changes in lipid and metabolite levels associated with other molecular and histological features in a tissue sample. Metabolic changes in ovarian cancer have been studied before (18,19). However, without spatial information, it is difficult to determine whether the metabolic alterations are occurring in the tumor or stromal compartment. To focus on the tumor compartment, we employed DESI-MS imaging, which allowed us to identify the chemical species present in the tissue as well as their spatial distribution. Analysis of the data, specific to tumor compartment of patient samples revealed that a unique metabolic profile is associated with the expression of FABP4. Higher unsaturation and oxidation of fatty acids and lysophospholipids were observed in higher relative abundance in samples with higher FABP4 expression. Several studies have suggested that unsaturated fatty acids play a key role in pathways leading to tumor progression by activating the beta catenin pathway, downregulating PTEN or increasing cancer cell adhesion (19-22). Fatty acid oxidation has also been shown to increase metastasis in breast and ovarian cancer models (14,23). Lysophospholipids have also been known to stimulate cancer cell migration and they are also considered as potential biomarkers for ovarian cancer (24,25). High expression of FABP4 can thus regulate various metabolites and protein pathways that can lead to aggressive metastasis of ovarian cancer. This data elucidating the key metabolic determinants of ovarian cancer metastasis thus lay a strong foundation for future studies which can focus on the development of therapeutic strategies targeting these species.

REFERENCES

1. du Bois A, Reuss A, Pujade-Lauraine E, Harter P, Ray-Coquard I, Pfisterer J. Role of surgical outcome as prognostic factor in advanced epithelial ovarian cancer: a combined exploratory analysis of 3 prospectively randomized phase 3 multicenter trials: by the Arbeitsgemeinschaft Gynaekologische Onkologie Studiengruppe Ovarialkarzinom (AGO-OVAR) and the Groupe d'Investigateurs Nationaux Pour les Etudes des Cancers de l'Ovaire (GINECO). Cancer-Am Cancer Soc 2009;115:1234-44

2. Hoskins WJ, Bundy BN, Thigpen JT, Omura GA. The influence of cytoreductive surgery on recurrence-free interval and survival in small-volume stage III epithelial ovarian cancer: a Gynecologic Oncology Group study. Gynecol Oncol 1992;47:159-66

3. Nick AM, Coleman RL, Ramirez PT, Sood AK. A framework for a personalized surgical approach to ovarian cancer. Nat Rev Clin Oncol 2015;12:239-U78

4. Tucker SL, Gharpure K, Herbrich SM, Unruh AK, Nick AM, Crane EK, et al. Molecular biomarkers of residual disease after surgical debulking of high-grade serous ovarian cancer. Clin Cancer Res 2014;20:3280-8

5. Hamilton CA, Miller A, Miller C, Krivak TC, Farley JH, Chernofsky MR, et al. The impact of disease distribution on survival in patients with stage III epithelial ovarian cancer cytoreduced to microscopic residual: a Gynecologic Oncology Group study. Gynecol Oncol 2011;122:521-6

6. Aragones G, Saavedra P, Heras M, Cabre A, Girona J, Masana L. Fatty acid-binding protein 4 impairs the insulin-dependent nitric oxide pathway in vascular endothelial cells. Cardiovasc Diabetol 2012;11:72

7. Djousse L, Gaziano JM. Plasma levels of FABP4, but not FABP3, are associated with increased risk of diabetes. Lipids 2012;47:757-62

8. Holm S, Ueland T, Dahl TB, Michelsen AE, Skjelland M, Russell D, et al. Fatty Acid binding protein 4 is associated with carotid atherosclerosis and outcome in patients with acute ischemic stroke. Plos One 2011;6:e28785

9. Makowski L, Brittingham KC, Reynolds JM, Suttles J, Hotamisligil GS. The fatty acid-binding protein, aP2, coordinates macrophage cholesterol trafficking and inflammatory activity. Macrophage expression of aP2 impacts peroxisome proliferator-activated receptor gamma and IkappaB kinase activities. J Biol Chem 2005;280:12888-95

10. Elmasri H, Ghelfi E, Yu CW, Traphagen S, Cernadas M, Cao H, et al. Endothelial cell-fatty acid binding protein 4 promotes angiogenesis: role of stem cell factor/c-kit pathway. Angiogenesis 2012;15:457-68

11. Harjes U, Bridges E, McIntyre A, Fielding BA, Harris AL. Fatty acid-binding protein 4, a point of convergence for angiogenic and metabolic signaling pathways in endothelial cells. J Biol Chem 2014;289:23168-76

12. Harjes U, Bridges E, Gharpure KM, Roxanis I, Sheldon H, Miranda F, et al. Antiangiogenic and tumour inhibitory effects of downregulating tumour endothelial FABP4. Oncogene 2017;36:912-21

13. Herroon MK, Rajagurubandara E, Hardaway AL, Powell K, Turchick A, Feldmann D, et al. Bone marrow adipocytes promote tumor growth in bone via FABP4-dependent mechanisms. Oncotarget 2013;4:2108-23

14. Nieman KM, Kenny HA, Penicka CV, Ladanyi A, Buell-Gutbrod R, Zillhardt MR, et al. Adipocytes promote ovarian cancer metastasis and provide energy for rapid tumor growth. Nat Med 2011;17:1498-503

15. Sans M, Gharpure K, Tibshirani R, Zhang J, Liang L, Liu J, et al. Metabolic Markers and Statistical Prediction of Serous Ovarian Cancer Aggressiveness by Ambient Ionization Mass Spectrometry Imaging. Cancer Res 2017;77:2903-13

16. Eberlin LS, Tibshirani RJ, Zhang J, Longacre TA, Berry GJ, Bingham DB, et al. Molecular assessment of surgical-resection margins of gastric cancer by mass-spectrometric imaging. Proc Natl Acad Sci U S A 2014;111:2436-41

17. Tibshirani R. Regression shrinkage and selection via the Lasso. J Roy Stat Soc B Met 1996;58:267-88

18. Ke C, Li A, Hou Y, Sun M, Yang K, Cheng J, et al. Metabolic phenotyping for monitoring ovarian cancer patients. Sci Rep 2016;6:23334

19. Tania M, Khan MA, Song Y. Association of lipid metabolism with ovarian cancer. Curr Oncol 2010;17:6-11

20. Johanning GL, Lin TY. Unsaturated fatty acid effects on human breast cancer cell adhesion. Nutr Cancer 1995;24:57-66

21. Kim H, Rodriguez-Navas C, Kollipara RK, Kapur P, Pedrosa I, Brugarolas J, et al. Unsaturated Fatty Acids Stimulate Tumor Growth through Stabilization of beta-Catenin. Cell Rep 2015;13:495-503

22. Vinciguerra M, Carrozzino F, Peyrou M, Carlone S, Montesano R, Benelli R, et al. Unsaturated fatty acids promote hepatoma proliferation and progression through downregulation of the tumor suppressor PTEN. J Hepatol 2009;50:1132-41

23. Park JH, Vithayathil S, Kumar S, Sung PL, Dobrolecki LE, Putluri V, et al. Fatty Acid Oxidation-Driven Src Links Mitochondrial Energy Reprogramming and Oncogenic Properties in Triple-Negative Breast Cancer. Cell Rep 2016;14:2154-65

24. Monet M, Gkika D, Lehen'kyi V, Pourtier A, Vanden Abeele F, Bidaux G, et al. Lysophospholipids stimulate prostate cancer cell migration via TRPV2 channel activation. Biochim Biophys Acta 2009;1793:528-39

25. Sutphen R, Xu Y, Wilbanks GD, Fiorica J, Grendys EC, LaPolla JP, et al. Lysophospholipids are potential biomarkers of ovarian cancer. Cancer Epidem Biomar 2004;13:1185-+

Chapter 4. Spatially Controlled Molecular Analysis of Biological Samples Using Nanodroplet Arrays and Direct Droplet Aspiration[4]

INTRODUCTION

Mass spectrometry (MS) imaging and spatial profiling allows untargeted and label-free chemical and spatial characterization of hundreds of molecular species from biological samples (1,2). Secondary ion mass spectrometry (SIMS) and matrix assisted laser desorption ionization (MALDI) are the most well-established techniques for MS imaging and profiling of biological samples under vacuum (3-7). Ambient ionization MS techniques offer an alternative approach for direct and in situ analysis of biological samples with minimal sample preparation requirements and at atmospheric pressure conditions (8). Within the ambient ionization MS techniques, liquid extraction MS approaches rely on the use of solvent to extract molecular information from a sample surface, allowing low sample abrasiveness and tunable analyte extraction for tissue imaging and analysis (9). A variety of methods using liquid extraction have been employed to directly analyze biological tissue samples (9,10), including spray-based methods such as desorption electrospray ionization (DESI) (11,12), as shown in Chapter 2 and 3 of this dissertation, and direct liquid extraction methods such as liquid microjunction surface sampling probe (LMJ-SSP) (13), liquid extraction surface analysis (LESA) (14,15), nanospray desorption electrospray ionization (nano-DESI) (16,17), and the Single-Probe (18). The range of molecular species detectable by each method is commonly dictated by their extraction and ionization mechanisms, generally most effective at analyzing small molecules, such as lipids and metabolites. Direct liquid extraction methods allow longer solvent-sample interaction times and are

[4] Adapted with permission from Sans M, Krieger A, Wygant, B. R., Garza, K.Y M, et al. Spatially controlled Molecular Analysis of Biological Samples using Nanodroplet Arrays and Direct Aspiration. J. Am. Soc. Mass Spectrom. 2020;31,2,418-428. Copyright © 2020, American Chemical Society. Sans M performed all experiments and data analyses and prepared the manuscript. Krieger A, Wygant, B.R, and Garza, K.Y.M assisted with experiments and data analysis. All authors reviewed the manuscript.

often coupled to a direct nanospray or an ESI source for enhanced ionization efficiency and overall sensitivity.

Mass spectrometry imaging by liquid extraction techniques can be performed at various spatial resolutions. High spatial resolution imaging has been demonstrated by nano-DESI (>10μm) (19,20), and the Single Probe (~8.5 μm) (18), while other methods, such as LESA and the LMJ-SSP, allow direct sampling of larger tissue regions with a spatial resolution of ~600-1000 μm (21). Spatial resolution in liquid extraction techniques is generally related to the size of the sampling area and/or probe, which is intrinsic to each individual approach. For example, in LMJ-SSP, nano-DESI, and the Single-Probe, the spatial resolution is often restricted to the diameter of the capillaries used to generate the micro junction or liquid bridge, while in LESA, the spatial resolution is determined by the diameter of the sampling tip (9). Although feasible, the ability to precisely control and tune the spatial resolution of these methods for different applications can be impractical and requires change in hardware such as the sampling probe used. Moreover, precisely determining the dimension of the sampling area, and the spatial resolution, can be challenging. Several experimental approaches have been proposed to measure spatial resolution, either by using standardized grids, measuring the probe trace across a surface, resolving a feature of known dimensions, or evaluating relative changes in the abundance of a specific m/z feature as the a probe is rastered across the surface (2,18,19,22). Therefore, methods that would enable practical and precise tuning, control, and accurate measurements of the spatial resolution in liquid extraction techniques could improve their applicability and performance for direct MS profiling and imaging.

Here, we report the development of an alternative approach for spatially controlled imaging and spatially controlled analysis of metabolites and lipids from biological tissue samples. This method allows precise tuning and deposition of arrays of solvent droplets

(~2-50 nL) onto sample surfaces using a piezoelectric liquid handling dispenser, followed by droplet aspiration and ionization through a fused capillary emitter for MS analysis. The spatial resolution is directly controlled by the diameter of the droplet in contact with the tissue sample, which can be precisely tuned with the piezoelectric dispenser. Efficient analyte extraction and transport is achieved by directly and entirely sampling the droplet through the fused silica capillary. In the imaging mode, arrays of droplets can be formed to cover areas of interest for molecular analysis. Here, we apply this method to image tissue samples with high spatial control using different droplet sizes (390, 420, and 500 µm), as well as profiling of human cells. Overall, our results demonstrate this approach is valuable for spatial profiling of biological tissue and imaging at tunable and well-controlled spatial resolution.

MATERIALS AND METHODS

System design

A multi-channel piezoelectric dispenser consisting of a print head assembly, which can hold four 2 mL fluid reservoirs and four piezoelectric microdispensing devices (MJ-AT-01-80, MicroFab, TX) was used. For these experiments, only one microdispensing device was used at a time. A pneumatic line was used to transfer solvent from the reservoir to the dispensing tip. The print head assembly was mounted on a 3-dimensional positioner (CH Instruments, TX) that had a 50 mm range in the x, y, and z directions, with a resolution of 0.1 micrometers.(23)

A blunt, platinum-coated fused silica capillary (OD 360 µm – ID 100µm, New Objective Inc., MA) cut at a length between 12 to 15mm comprised the nanospray emitter. The angle and position of the conductive emitter were controlled using an arm coupled to a rotation and XYZ mount (Newport Corporation, CA). Voltage was supplied to the emitter

via a voltage pin in the arm holder connected to the emitter clasp. A bent extended DESI transfer tube was used for analyte transfer from the emitter to the MS. The arm was mounted on a 2D moving stage (Prosolia Inc., IN). Two Dino Lite Microscope cameras (AnMo Electronics Corporation, Taiwan) were used to assist careful alignment of the emitter.

Microscope glass slide treatment

Glass slides were treated with dichlorodimethylsilane to produce hydrophobic substrates for tissue mounting. To produce the hydrophobic substrates, glass slides were soaked in a 50:3 solution of n-hexane (95%+, Fisher) and dichlorodimethylsilane (99%+, Acros Organics) for 5 minutes, before being soaked in only n-hexane for an additional 5 minutes. They were then dried at 60°C for 1 hour in a vacuum oven to dry and cure.

Tissue and biological sample analysis

Mouse brain tissue samples were purchased from Bioreclamation IVT. Normal and tumor ovarian and brain human tissues were acquired from the Cooperative Human Tissue Network under approved IRB protocol. Samples were kept frozen at -80 °C prior to analysis and sectioned onto the treated glass slides at 16 µm using a CryoStar NX50 cryostat (Thermo Fisher Scientific). For diagnosis and slide annotation, tissue samples were stained with a standard hematoxylin & eosin (H&E) staining procedure and evaluated by expert pathologists. Ovarian cell pellets were obtained from the MD Anderson Tissue Bank and kept frozen at -80 °C. Sample aliquots (10-20 µL) were deposited onto microscope slides and allowed to dry before analysis.

Mouse brain homogenate

Mouse brain homogenates were prepared by thawing and thoroughly mixing a whole mouse brain organ with a cordless microtube homogenizer (Cole-Parmer, IL). The resulting tissue mixture was added into a peel-away mold (Thermo Scientific, MA) and frozen overnight at -80 °C. The frozen mouse brain homogenate was then sectioned at 16 µm using a CryoStar NX50 cryostat (Thermo Fisher Scientific) and mounted onto microscope glass slides.

Imaging workflow and data analysis

For tissue section analysis, a line of consecutive dimethylformamide (DMF) droplets was dispensed across the entire length of the tissue section, stepping the dispenser head in the y-direction after each droplet. After the vertical array was deposited on the tissue sample, the sample slide was placed in the slide holder of the 2D moving stage. After droplet deposition, the droplet array was aligned to the capillary emitter, allowing sequential transfer of individual droplets to the MS. Note that with this configuration, slight changes in the total contact time between the droplet and the sample surface (extraction time), occurred between the first and subsequent droplets (<30 sec between first and last) (Figure A3.1). A washing step using pure methanol to flush the capillary emitter was incorporated between each line of droplets. Mass analysis was performed using a Q Exactive Orbitrap (Thermo Fisher Scientific, CA) in the negative ion mode from m/z 100 to 1,500, at 70,0000 mass resolving power. The resulting raw data for each droplet was averaged (2-3 scans) using Thermo Xcalibur software and extracted as a xlsx file format. Note that the number of averaged scans was kept consistent for each droplet analyzed within a sample. Existing software for image plotting was not compatible to the data format obtained from these experiments, and instead ion images were built in R Studio by plotting

the absolute abundance of an ion of interest in two dimensions, with every pixel corresponding to an individual droplet. The gtools, readxl, rowr, grDevices and viridis packages in R were used. The source code and associated documentation can be found in the GitHub repository (https://bitbucket.org/eberlinlab/madi-image/src/master/). Tandem mass spectrometry analysis was performed for identification during analysis using high-energy collisional dissociation (HCD). Cosine similarity analysis was performed in the CRAN R language.

DESI-MS analysis

DESI-MS analyses of mouse brain tissue samples were performed for comparison purposes. A 2D Omni Spray (Prosolia Inc., IN) coupled to a Q Exactive mass spectrometer (Thermo Scientific, CA) was used. DESI-MS was performed in the negative ion mode from m/z 100 to 1500, at 70,000 resolving power. Pure DMF and DMF: acetonitrile (ACN) were used as the solvent systems, at a flow rate of 1.5 µL/min to achieve a matching spatial resolution of 500 µm.

RESULTS

Design and development

To provide controllable and precise spatial resolution for ambient ionization MS profiling and imaging, we used a piezoelectric picoliter dispenser for accurate deposition of individual solvent droplets onto tissue samples, coupled to effective analyte transfer from tissue samples to the MS for sensitive analysis. The piezoelectric picoliter dispenser system utilizes pneumatic lines to transport solvent to the dispensing tips (Figure 4.1A). For these experiments, a single dispensing tip was used. Single droplets of sub-nanoliter volume (500 pL for DMF, Figure A3.2) were dispensed by controlling the voltage

differential applied to a set of electrodes attached to a piezoelectric material bonded to a glass micropipette. Dispensing multiple droplets on the sample in the same location results in a droplet of increased volume and diameter. The diameter of the resulting droplets in contact with the tissue sample was thus effectively controlled by adjusting the number of droplets dispensed per spot. The position of the piezoelectric tip was carefully controlled by a 3-dimensional positioner, allowing precise deposition of droplet arrays.

Utilizing a single piezoelectric tip, we deposited a line of consecutive solvent droplets onto the tissue surface in the y-direction (Figure 4.1B). Deposited droplets were then aspirated to the MS using a fused silica capillary (OD 360 μm, ID 100 μm) aligned to the MS inlet. Positioning and angle of the capillary was controlled using an arm coupled to an XYZ and a rotation mount, as shown in Figure 4.1C and Figure A3.3. An extended transfer tube was used to enable a wider range of motion in the y-direction. Taking advantage of the differential between the ambient pressure (~1.0 bar) and the fore vacuum pressure provided by the front end of the mass spectrometer (1.6-1.9 mbar), droplets were sequentially aspirated after being placed in contact with the distal end of the emitter, while the proximal end of the emitter was inserted into the transfer tube. In this way, the droplet was directly introduced into the MS system, thus minimizing sample loss. The fused silica emitter was platinum coated at the distal end to allow the application of a voltage bias between the MS inlet and the end of the capillary, while the proximal end of the emitter was not coated to prevent electrical arcing or discharge. The voltage cord was connected to the arm through a metal pin, as shown and described in Figure A3.3.

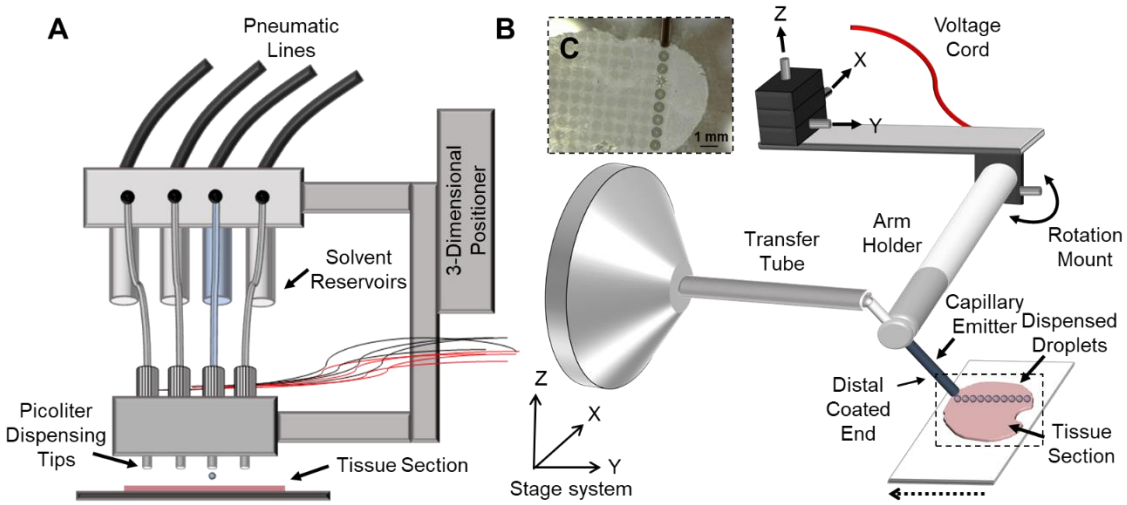

Figure 4.1: System design and development.

A picoliter dispenser was used to deposit individual solvent droplets in the y-direction onto tissue samples for MS imaging (A). The printhead assembly was coupled to a 3-dimensional positioner to allow accurate positioning of the solvent droplets onto the tissue section, which was held static on a slide holder. Line of DMF droplets after being deposited onto a mouse brain sample by the picoliter dispenser deposited (B). After dispensing a line of droplets, the tissue sample is mounted on a 2D moving stage, where a capillary emitter aligned with the MS inlet is used to individually transport and ionize droplets containing solvated analytes extracted from the tissue surface (C).

Metabolite and lipid analysis in the negative ion mode

Several solvent systems commonly used for metabolite and lipid extraction and analysis by solvent based ambient ionization MS techniques were tested in the negative ion mode, including DMF, water, ethanol, methanol, and ACN (24). Properties of the solvent systems investigated can be found in Table A3.1. Similar molecular species were detected with all the solvent systems tested, although qualitative changes in the metabolite and lipid

profiles were observed (Figure A3.4). DMF was selected as the solvent system for further analysis in the negative ion mode for its high lipid solubility, high surface tension, low vapor pressure, and limited adhesion to tissue sections. The high surface tension of DMF (37 mN/m) allowed the formation of droplets at high contact angles, even on the mildly hydrophilic surfaces of tissue sections, facilitating aspiration by the capillary emitter. To correlate droplet dispensing volume with droplet size, and thus spatial resolution, DMF droplets containing between 5 (2.5 nL) and 100 individual drops (50 nL) were dispensed at a rate of approximately 1 droplet per second on mouse brain homogenate tissue sections. Optical images were used to measure the diameter of the droplets deposited onto tissues, which ranged from 250 to 650 µm at the volumes tested. Importantly, highly reproducible diameters were measured between droplet replicates (RSD=1.5%, n=161), with a clear correlation between the number of dispensed droplets and overall supported droplet diameter (Figure 4.2, Table A3.2). The droplet diameters were also observed to stay consistent and monodispersed following droplet dispensing for tens of seconds until significant evaporation is observed, as shown in Figure A3.5 for droplets of 20, 15 and 10 nL volumes. These results demonstrate that reliable and tunable droplet deposition can be achieved using the piezoelectric system, providing precise control over the area sampled, and thus spatial resolution.

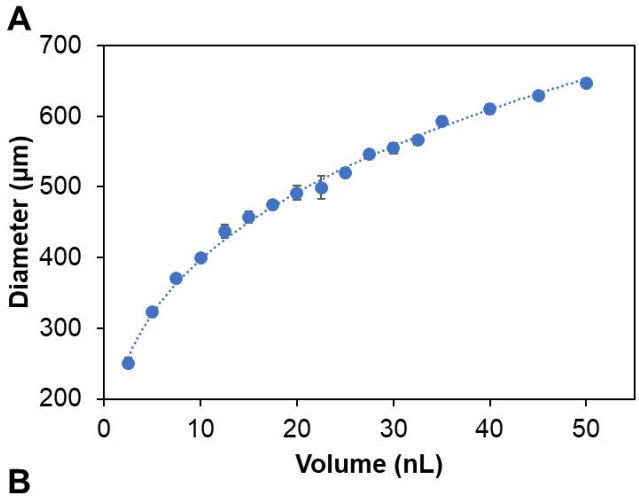

B

Volume (nL)	Diameter (µm)	Volume (nL)	Diameter (µm)
50.0	647.0	20.0	491.4
45.0	629.0	17.5	474.3
40.0	610.3	15.0	457.3
35.0	593.2	12.5	437.1
32.5	566.1	10.0	399.6
30.0	554.5	7.5	370.6
27.5	546.5	5.0	322.6
25.0	519.6	2.5	250.7
22.5	499.1	--	--

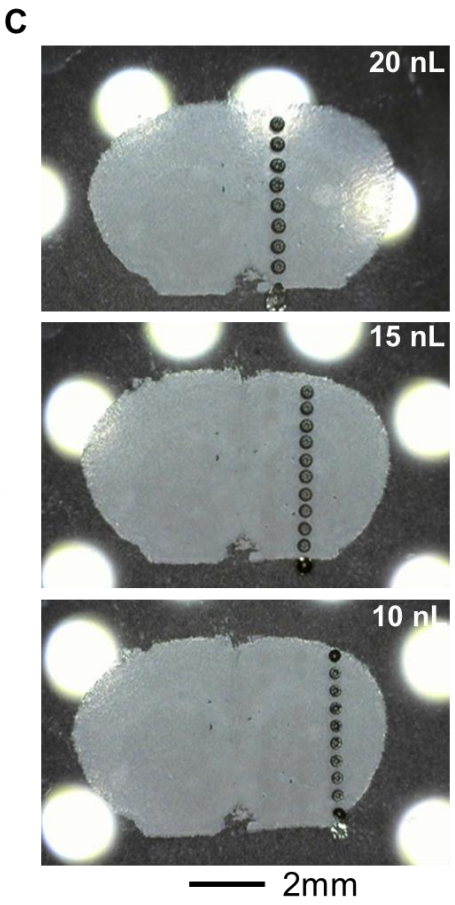

Figure 4.2: Correlation between dispensed DMF droplet volume and spatial resolution (droplet diameter µm) for MS imaging (A,B).

See Table A3.2 for additional metrics. Optical images of mouse brain tissue sections with lines of 20, 15, and 10 nL droplets deposited onto (C).

Next, various parameters of the system, such as fused silica capillary positioning, inlet temperature, and source voltage, were optimized with the goal of maximizing transfer of the deposited droplet from the tissue to the mass spectrometer and mass spectral intensity of analytes. Optimization was performed by dispensing replicate arrays of 20 nL droplets onto mouse brain homogenate sections, and subsequently analyzing them at different parameters (n=7-10 replicates for each parameter). First, silica capillary positioning was evaluated. Optimal transfer of the deposited droplets to the mass spectrometer was achieved by placing the silica capillary approximately 1-2 millimeters inside the extended transfer tube, aligned to the center of the tube orifice, and angled approximately 60-70° degrees relative to the sample surface. At this geometry, maximal droplet aspiration and transfer was observed, with minimal solvent remaining at the tissue surface. Optimal inlet temperature was then determined by varying the inlet temperature from 200-400°C. As observed in Figure 4.3A, the total ion count (TIC) values increased at higher temperatures, reaching maximum values at 350 °C, followed by a decrease in abundance at 400 °C. These results suggest that increasing inlet temperature enhances ionization efficiency likely by facilitating solvent evaporation. A similar trend in ion abundance as a function of inlet temperature was also observed by selecting several species commonly detected in the mass spectra, and separately plotting the sum of absolute abundances according to molecular type: metabolites (small carbohydrates and amino acids), fatty acids, and lipids (including sphingolipids and glycerophospholipids) (Figure 4.3B). Next, we evaluated the effect of source voltage (0.25 – 1.75 kV) on the ion intensity detected. Higher TIC values were observed at an applied voltage between 1.25 – 1.5 kV (Figure 4.3C), while a drop in TIC values was detected at 1.75 kV. Interestingly, optimal voltage values appeared to differ between distinct molecular classes (Figure 4.3D). For example, while lipid species present qualitatively higher ion abundances at high potentials (> 1.25 kV), fatty acids and

metabolite species were detected at lower ion counts, suggesting that smaller molecules may become unstable at higher electric fields. Note that the application of an external electric field was not necessary to produce detectable ion signals for larger (>100 nL) droplets. For the remaining experiments described, a voltage of 1.5 kV and inlet temperature of 350 °C were selected as optimal parameters for the analysis of metabolites, fatty acids, and other lipids by this method.

Monitoring the effects of inlet temperature and source voltage on performance and signal detected provide insights into the ionization process of this approach. We hypothesize that droplet formation, desolvation, and charge separation occur following a similar mechanism as in electrospray ionization (ESI) or nanospray (25), assisted by the pressure drop and temperature increase between the atmospheric environment and the inlet tube, as well as the application of a voltage differential. As shown in Figure A3.6, similar mass spectra profiles in terms of species detected and their relative abundances were observed by this method and ESI analysis of a mouse lipid extract solution, supporting the hypothesis of a similar ionization mechanism to ESI.

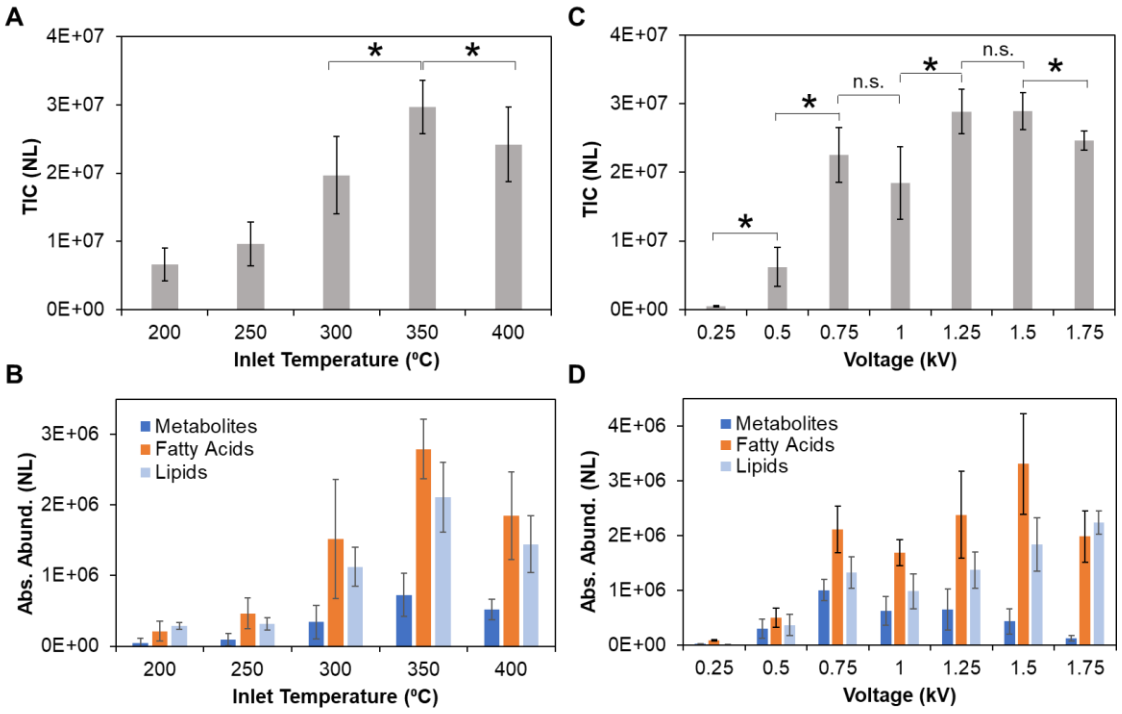

Figure 4.3: Optimization of the inlet temperature applied to the capillary emitter (A,B) and applied source voltage (C,D).

Effect on method performance was evaluated based on total ion current (A,B) and absolute abundance of metabolites (*m/z* 124.006 and 174.041), fatty acids (*m/z* 281.248 and 303.233), and lipids (*m/z* 600.515, 654.568, 747.521, 766.545, 790.540, 834.530, 888.625) (C,D). (A) *, p-value < 0.025; n.s., not significant. (B) *, p-value < 0.008 ; n.s., not significant.

MS imaging of mouse brain tissue samples

To demonstrate the imaging capabilities and spatial control of this approach, serial sections of mouse brain tissue samples were analyzed using various droplet sizes, including 387 ± 12 µm (~10 nL), 424 ± 11 µm (~15 nL) and 496 ± 12 µm (~20 nL) (Table A3.3). Row and column spacing was added between the droplets to avoid overlap in sampling, resulting in pixel sizes of 500x460 µm, 550x510 µm, and 600x560 µm, respectively. DMF droplets were dispensed as individual lines in the y-direction (top to bottom) at a rate of approximately 1 s per droplet, and analyzed sequentially at an average of 4 s of data acquisition per droplet, resulting in a total dispensing and analysis time per line of approximately 90 s, as shown in Figure A3.1. The effect of extraction time (3-90 s) in the magnitude of the TIC detected was also evaluated. As shown in Figure A3.7, no statistically significant differences were observed in TIC between the various extraction times in the time scale described (ANOVA p-value = 0.079,). Importantly, the time of analysis per line was notably below droplet evaporation time (>160 sec for 10nL, >190 sec for 15 nL, and >250 sec for 20nL). Each of the images were acquired in under 1 h, including the time added for the washing cycles and for transferring the glass slide between the dispensing and 2D moving stages in between lines. During analysis, spikes in the ion current corresponding to the individually analyzed droplets were observed in the resulting ion chromatograms (Figure A3.8). The mass spectra obtained from different regions of the tissue presented high relative abundance of several metabolites, fatty acids, and lipid species characteristic of white and grey matter of mouse brain tissue (Figure 4.4B)(26,27). A list of the most abundant *m/z* ratios detected, and their corresponding molecular attributions assigned based on high mass accuracy and MS/MS measurements during discrete droplet sampling (Figure A3.9) is provided in Table A3.4. The spatial distribution of the ions detected were also characteristic of brain tissue, with high relative abundances

of sulfatide species such as ST 18:0 (*m/z* 806.548) and ST 24:1 (*m/z* 888.625) in white matter, and other lipid species including PG 34:1 (*m/z* 747.520) and PE 40:6 (*m/z* 790.540) in grey matter (Figure 4.4B). Reproducible spatial distributions of lipid species detected were observed at the three different spatial resolutions explored, with improved definition of white matter features at higher spatial resolutions. Note that detection of similar lipid species has been reported in spatially resolved LESA-MS experiments of mouse brain tissue sections in the negative ion mode, although using different solvent systems (27,28). When comparing the these results to the mass spectra obtained by DESI from mouse brain tissue sections using the same DMF solvent, similar species were also detected, although at different relative abundances (for more discussion, please see additional results in Appendix A3, Figure A3.10 and Figure A3.11).

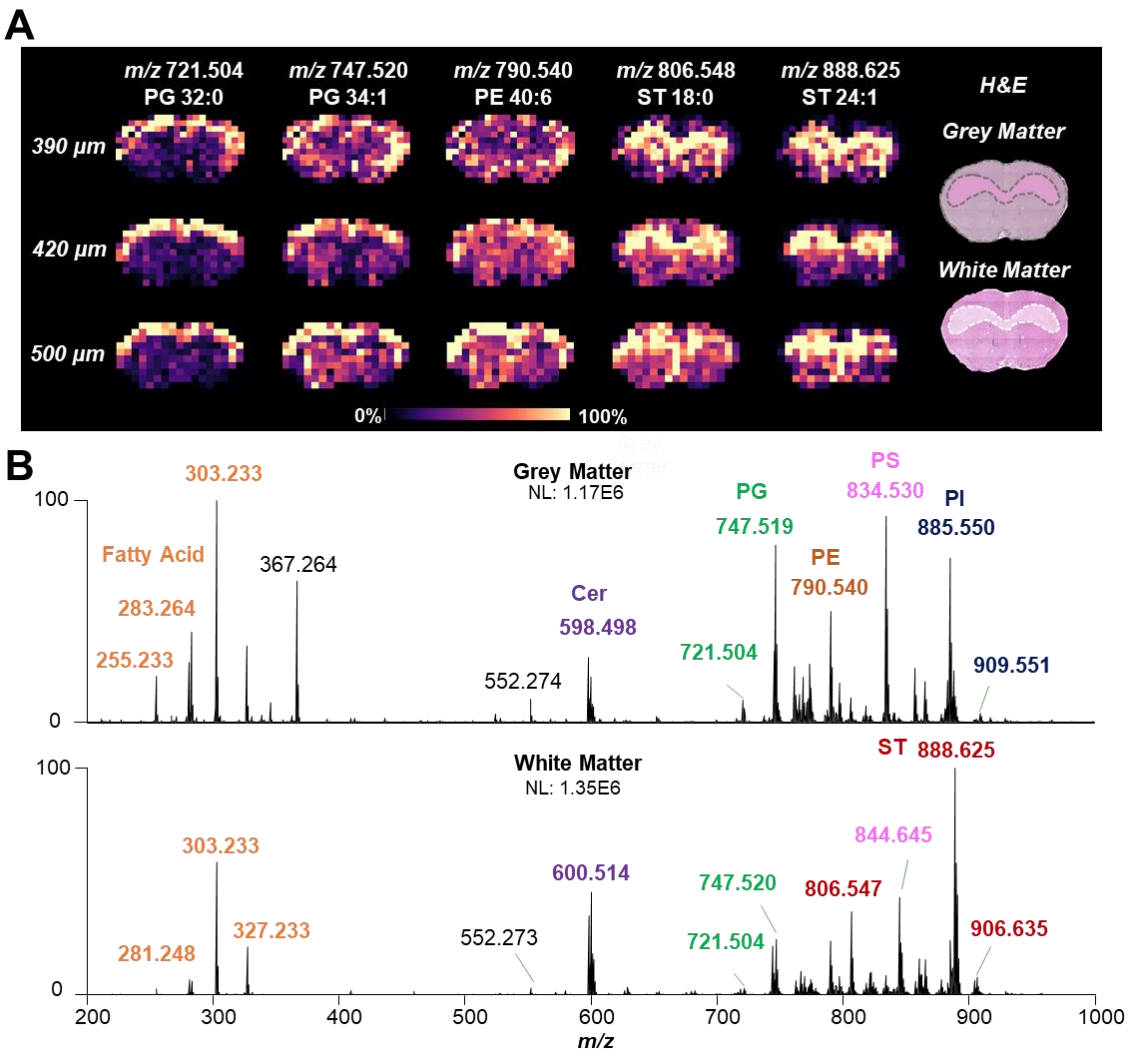

Figure 4.4: Ion images obtained using different droplet sizes from serial mouse brain tissue sections and optical images with grey and white matter regions outlined and shaded in grey and white, respectively (A). Representative mass spectra obtained from grey (top) and white matter regions (bottom) (B).

Lipid species are color-coded according to lipid class.

Analysis and imaging of cancerous tissue samples

We next used this platform to analyze normal and cancerous human ovarian tissue samples (n=5) using droplets of 491 ± 10 µm in diameter (20 nL), resulting in 600x560 µm pixel sizes. Heterogeneous distributions for a variety of different ions tentatively identified as deprotonated or chlorinated Cer, PE, PC, PG, PI, and diacylglycerol (DG) species (Table A3.5), among others, were observed, and their distribution correlated to histological differences within the tumor tissue samples, including stromal, tumor, and necrotic areas (Figure 4.5A). As reported in previous studies, an overall higher abundance of lipid species was detected from areas corresponding to high tumor cell concentrations (delineated in black), compared to the surrounding connective tissue (29,30). Figure 4.5B shows representative mass spectra obtained from high-grade serous carcinoma (SC), low-grade SC ovarian samples, and normal ovarian tissue. Rich metabolic profiles were obtained, with qualitative differences in species and abundances between the mass spectra obtained for each tissue type. For example, a higher abundance of PI species, such as *m/z* 885.553, was detected from high-grade SC tissue, while Cer, PE, and PC species were observed at a higher relative abundance from spectra obtained from low-grade SC tissue. A lower diversity of lipid species, such as PE and PC, were observed from normal ovarian tissue mass spectra. Yet, PE P-38:5 (*m/z* 748.531) was detected at higher relative abundances in normal ovarian tissue compared to cancer tissue. In addition, high relative abundance of lactosylceramide (LacCer) species, such as LacCer d38:1 (*m/z* 980.685) or LacCer d42:2 (*m/z* 1006.699) were observed in the mass spectral profiles obtained from necrotic tissue regions (outlined in red) (Figure A3.12), which corroborates previous reports (29,31).

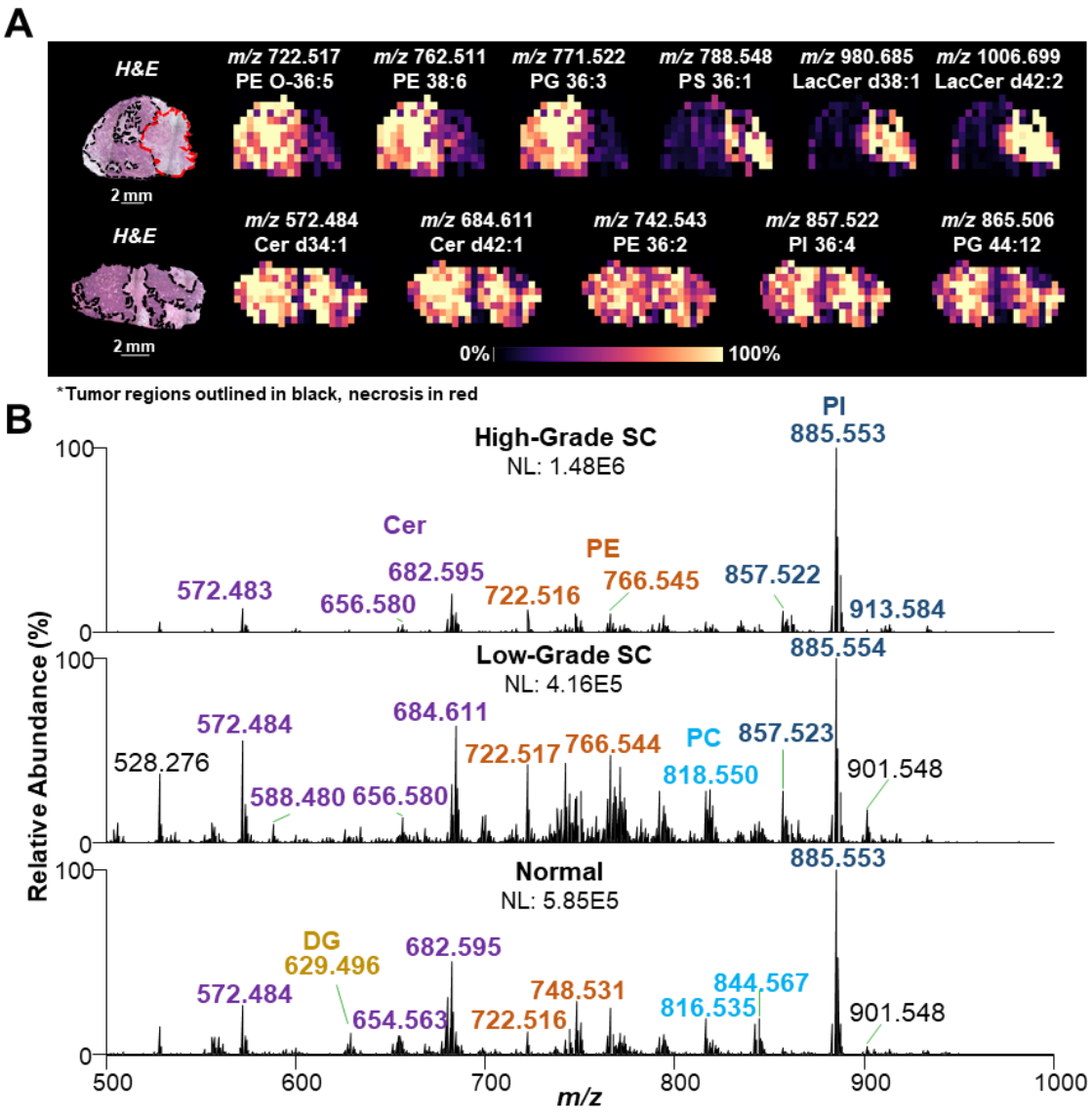

Figure 4.5: MS imaging of ovarian carcinoma samples (A). Representative mass spectra from high-grade serous carcinoma (top), low-grade serous carcinoma (middle), and normal ovarian tissue (bottom) (B).

Lipid species are color-coded according to lipid class.

We then applied the system to image a glioblastoma and a normal human brain tissue section (600x560 µm pixel size). Heterogeneous spatial distribution and distinct lipid profiles were observed in the ion images obtained from the glioblastoma tissue, corresponding to tumor and necrotic tissue regions as determined by pathological evaluation of the H&E stained tissue (Figure 4.6A, top). For example, ceramide species were detected at higher relative abundances from necrotic regions, while other lipids, such as PG 34:1 (*m/z* 747.520) or ST 36:1 (*m/z* 806.548) were detected at higher relative abundances within the tumor region. A depletion of a variety of lipid species, such as PI 36:2, PI 38:4, PS 40:6, or PE 40:6, among others, were observed in the glioblastoma tumor area when compared to normal brain tissue, similar to what has been reported (32,33). Ion images from normal brain tissue allowed visualization of white matter regions, characterized by the distribution of sulfatide species (e.g. ST 24:1, ST 24:1(OH), ST 24:0(OH), and ST 26:1) within the branching architectures of the tissue sample (Figure 4.6A, bottom). Other species, such as PE P-24:1 at *m/z* 700.529, displayed a homogeneous distribution throughout the entire tissue section, while PS 40:6 (*m/z* 834.529) was observed at higher relative abundance within the grey matter region, complementary to the distribution of sulfatides in the white matter. Representative mass spectra profiles obtained from regions identified as glioblastoma tissue, and grey and white matter from normal brain, are shown in Figure 4.6B, including tentative identification of several ions (Table A3.6). Overall, these results demonstrated that this discrete droplet sampling approach can be used to obtain molecular information characteristic of normal and cancerous tissues directly from tissue samples.

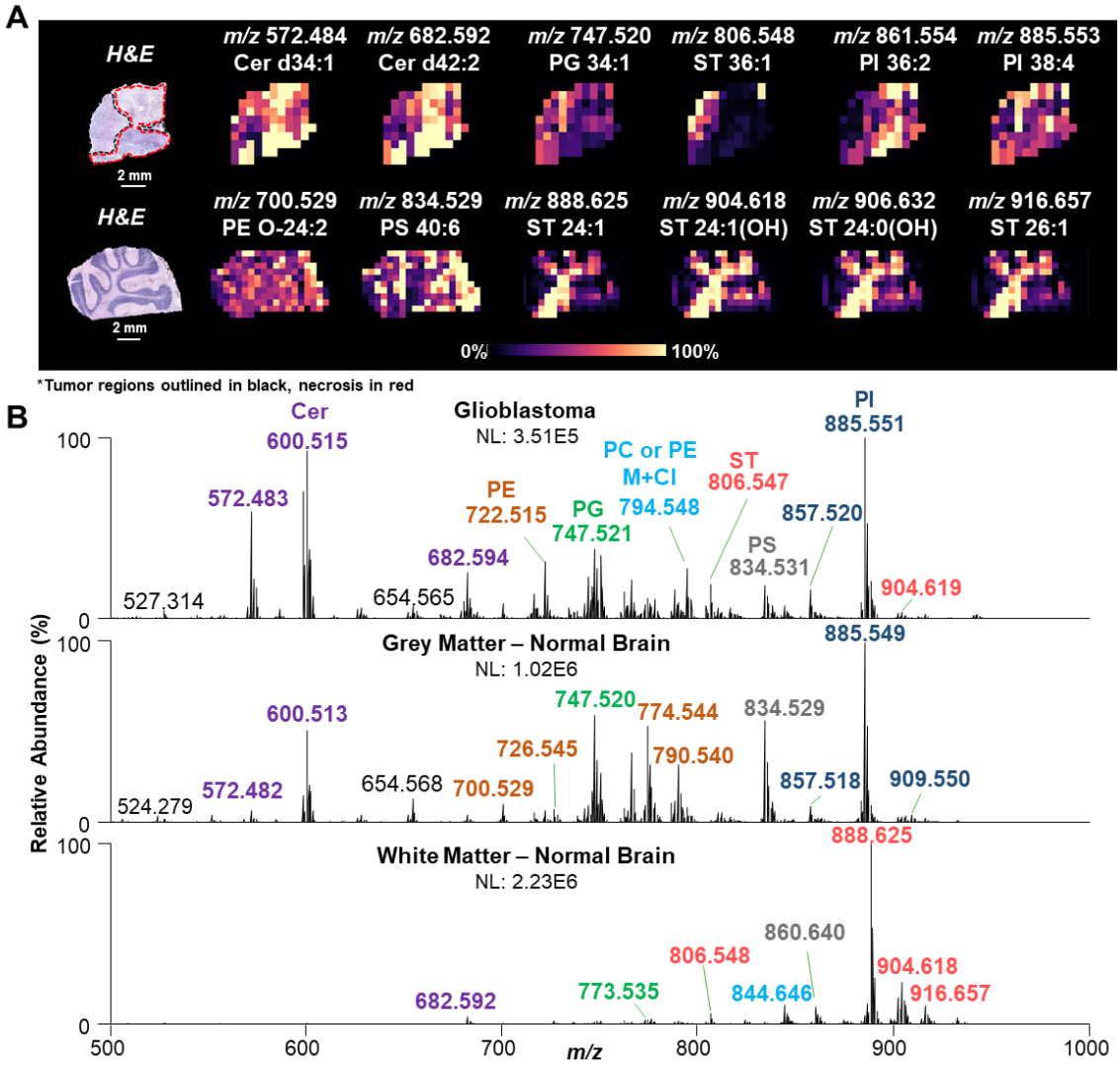

Figure 4.6: MS imaging of a glioblastoma tumor sample (top) and normal brain tissue (bottom) (A). Representative mass spectra from glioblastoma tissue (top), grey matter (middle) and white matter (bottom) normal brain tissue (B).

Lipid species are color-coded according to lipid class.

Analysis of human ovarian cell samples

In addition to tissue imaging, we tested the use of this method to analyze human ovarian cells deposited and dried onto a glass slide. Figure A3.13 shows representative mass spectra obtained from tumor ovarian cells (control) and two replicates of a genetically modified strain of human ovarian tumor cells, with the overexpression of the fatty acid binding protein (FABP4) gene. Rich molecular information, including various metabolites, fatty acid and lipid species were detected. Notably, a higher relative abundance of fatty acid species, such as m/z 281.249 (fatty acid – FA 18:1), m/z 303.324 (FA 20:4), and *m/z* 327.234 (FA 22:6) were detected in from the cell lines with FABP4 overexpression when compared to control tumor cells, which corroborates previous studies, and as discussed in Chapter 3 of this dissertation (34). A variety of lipid species, such as Cer, PG, and PI species were also detected in the spectra from the *m/z* 500 to 1000 range. These results showcase the capabilities of this approach to provide metabolic profiles representative of cell composition from cell samples dried on a glass slide.

Evaluation of method performance as a tool for imaging and analysis of biological samples

To evaluate method reproducibility, cosine analyses were performed on data acquired from mouse brain and human cancerous tissue samples. Cosine analysis compares mass spectra based on both the m/z values detected as well as their relative abundances, providing similarity values ranging from 0 (dissimilar or orthogonal vectors) to 1 (identical or parallel vectors). Average cosine values of 0.89 ± 0.09 (n=15) and 0.95 ± 0.05 (n=6) were obtained by comparing mass spectra acquired from grey matter pixels in three mouse brain tissue serial sections, and from pixels corresponding to a homogeneous ovarian tumor region from two serial sections, respectively (Table A3.7). To provide additional reproducibility metrics, the ratio between the ion abundances at *m/z* 834.530 and *m/z*

885.550, two abundant features in grey matter mass spectra, was evaluated from three serial sections, achieving consistent values with an RSD of 11.3% (n=15) (Table A3.8), which are comparable to what has been reported for DESI-MS (RSD = 8.0%, n=5)(35).

Carryover is a common performance concern caused by the presence of residual analyte from a previous run or analysis, thus affecting the accuracy and precision of measurements, in a variety of bioanalytical techniques, including MS (36,37). As our approach utilizes a silica capillary to transport solvated analytes to the MS inlet, potential adherence of residual analyte to the capillary inner wall could be a source of carryover. To prevent this, the silica capillary was washed after each line of droplets analyzed during an image. Using this approach, changes in the ion abundance between droplets in each vertical line were observed to correlate to tissue type and histology (i.e. brain white matter, grey matter, tumor, necrosis or connective tissue) (Figure A3.14), thus suggesting that washing between each line of droplets was sufficient to prevent significant carryover that could affect accurate localization of species in the resulting data and ion image. For example, the extracted ion chromatogram of *m/z* 904.618 was localized to the white matter branches of the brain tissue, independently of droplet number in the line dispensed, while the extracted ion chromatogram of *m/z* 700.529 stayed relatively consistent along the line analyzed. These changes in abundance in the tissue region analyzed agree with the histologic features of the tissue section, as previously discussed for their corresponding ion images in Figure 6a. These results suggest that carryover within a line of droplets does not play a significant role in the ion signal detected, and spatially accurate molecular information can be obtained using the same capillary for aspiration of consecutive droplets, although further studies are needed.

DISCUSSION

In this study, we described the design of a liquid extraction ambient ionization MS method for spatially controlled profiling and imaging of biological tissue samples. The system includes a piezoelectric picoliter solvent dispenser that enables controlled deposition of solvent droplets for accurate tuning of imaging spatial resolution. A similar aspiration mechanism has been previously described by the scanning mass spectrometry (SMS) probe, used to resolve chemical microenvironments within a large droplet (~100 μL)(38). In our system, a fused silica capillary was used to directly aspirate entire discrete droplets of small volume (2-50 nL) after analyte extraction from tissue surfaces. We optimized this method for the detection of metabolite and lipid information in the negative ion mode directly from biological samples, detecting a variety of small molecules, FAs, GPs, SPs, and sulfoglycolipids, such as STs. We demonstrated that this system can be used to image various tissue types, such as mouse brain, and normal and cancerous human ovarian and brain, yielding ion images and molecular information that are representative of histological differences present in the tissue samples (i.e. white vs grey matter, tumor vs normal areas) in a reproducible manner.

While other liquid extraction techniques such as LESA-MS, LMJ-SSP, and nano-DESI follow similar operational principles for direct profiling and imaging of biological tissue sections (9), the method we describe here is an alternative approach employing a microarray of solvent droplets and direct nanospray from a fused silica capillary (<5 seconds per spot) for direct tissue analysis. Different from LMJ-SSP and nano-DESI, which utilize a liquid microjunction through which a solvent flow is continuously delivered to a sample surface, the approach we described employs discrete solvent droplet deposited by a piezoelectric dispenser to perform liquid extraction from biological samples. The discrete droplets employed in this study are of considerably less volume (<100 nL) to those

used during LESA analyses (~1000-2000 nL) and are directly aspirated using a fused silica capillary instead of being robotically introduced onto a microfabricated chip for infusion (14). Despite the moderate resolution reported in this study (390 µm droplet size, 500x460 µm pixel size), which is lower than nano-DESI but comparable to what has been reported for LESA and LMJ-SSP, the ability to quantitatively tune spatial resolution in an automated way with a piezoelectric picoliter solvent dispenser is appealing for biological sample profiling and tissue imaging applications. Refinements in the design and engineering of the system will be pursued to improve spatial resolution and speed for MS imaging. Mounting the dispensing device to the 2D moving stage to sequentially dispense and analyze each droplet individually should prevent the need for spacing between droplets, allow aspiration of smaller DMF droplets, as well as exploring droplets of more volatile chemical composition. Further, this modification will also facilitate automation and improve sample throughput by circumventing manual transfer of the glass slides between the dispenser stage and the MS. Moving to dispenser stage in a spot by spot fashion instead of continuous rastering of the 2D stage will also highly increase sample throughput. Experiments using various solvent systems through the multi-channel dispensers as well as the incorporation of chemically reactive additives into the extraction solvents will be explored to expand chemical coverage for tissue analysis.

REFERENCES

1. McDonnell LA, Heeren RMA. Imaging mass spectrometry. Mass Spectrom Rev 2007;26:606-43
2. Buchberger AR, DeLaney K, Johnson J, Li LJ. Mass Spectrometry Imaging: A Review of Emerging Advancements and Future Insights. Anal Chem 2018;90:240-65
3. Seeley EH, Caprioli RM. MALDI imaging mass spectrometry of human tissue: method challenges and clinical perspectives. Trends Biotechnol 2011;29:136-43
4. Schwamborn K, Caprioli RM. MALDI imaging mass spectrometry--painting molecular pictures. Mol Oncol 2010;4:529-38
5. Fletcher JS, Vickerman JC, Winograd N. Label free biochemical 2D and 3D imaging using secondary ion mass spectrometry. Curr Opin Chem Biol 2011;15:733-40
6. Winograd N, Garrison BJ. Biological Cluster Mass Spectrometry. Annual Review of Physical Chemistry, Vol 61 2010;61:305-22
7. Kompauer M, Heiles S, Spengler B. Atmospheric pressure MALDI mass spectrometry imaging of tissues and cells at 1.4-mu m lateral resolution. Nat Methods 2017;14:90-6
8. Cooks RG, Ouyang Z, Takats Z, Wiseman JM. Ambient mass spectrometry. Science 2006;311:1566-70
9. Laskin J, Lanekoff I. Ambient Mass Spectrometry Imaging Using Direct Liquid Extraction Techniques. Anal Chem 2016;88:52-73
10. Ifa DR, Eberlin LS. Ambient Ionization Mass Spectrometry for Cancer Diagnosis and Surgical Margin Evaluation. Clin Chem 2016;62:111-23
11. Takats Z, Wiseman JM, Gologan B, Cooks RG. Mass spectrometry sampling under ambient conditions with desorption electrospray ionization. Science 2004;306:471-3
12. Wiseman JM, Ifa DR, Song QY, Cooks RG. Tissue imaging at atmospheric pressure using desorption electrospray ionization (DESI) mass spectrometry. Angew Chem Int Edit 2006;45:7188-92
13. Van Berkel GJ, Kertesz V. Application of a Liquid Extraction Based Sealing Surface Sampling Probe for Mass Spectrometric Analysis of Dried Blood Spots and Mouse Whole-Body Thin Tissue Sections. Anal Chem 2009;81:9146-52
14. Kertesz V, Van Berkel GJ. Fully automated liquid extraction-based surface sampling and ionization using a chip-based robotic nanoelectrospray platform. J Mass Spectrom 2010;45:252-60

15. Hall Z, Chu YJ, Griffin JL. Liquid Extraction Surface Analysis Mass Spectrometry Method for Identifying the Presence and Severity of Nonalcoholic Fatty Liver Disease. Anal Chem 2017;89:5161-70

16. Roach PJ, Laskin J, Laskin A. Nanospray desorption electrospray ionization: an ambient method for liquid-extraction surface sampling in mass spectrometry. Analyst 2010;135:2233-6

17. Lanekoff I, Heath BS, Liyu A, Thomas M, Carson JP, Laskin J. Automated Platform for High-Resolution Tissue Imaging Using Nanospray Desorption Electrospray Ionization Mass Spectrometry. Anal Chem 2012;84:8351-6

18. Rao W, Pan N, Yang ZB. High Resolution Tissue Imaging Using the Single-probe Mass Spectrometry under Ambient Conditions. J Am Soc Mass Spectr 2015;26:986-93

19. Laskin J, Heath BS, Roach PJ, Cazares L, Semmes OJ. Tissue imaging using nanospray desorption electrospray ionization mass spectrometry. Anal Chem 2012;84:141-8

20. Nguyen S, Sontag R, Carson J, Corley R, Ansong C, Laskin J. Towards High-Resolution Tissue Imaging Using Nanospray Desorption Electrospray Ionization Mass Spectrometry Coupled to Shear Force Microscopy. J Am Soc Mass Spectr 2018;29:316-22

21. Blatherwick EQ, Van Berkel GJ, Pickup K, Johansson MK, Beaudoin ME, Cole RO, et al. Utility of spatially-resolved atmospheric pressure surface sampling and ionization techniques as alternatives to mass spectrometric imaging (MSI) in drug metabolism. Xenobiotica 2011;41:720-34

22. Tillner J, Wu V, Jones EA, Pringle SD, Karancsi T, Dannhorn A, et al. Faster, More Reproducible DESI-MS for Biological Tissue Imaging. J Am Soc Mass Spectr 2017;28:2090-8

23. Berglund SP, Lee HC, Nunez PD, Bard AJ, Mullins CB. Screening of transition and post-transition metals to incorporate into copper oxide and copper bismuth oxide for photoelectrochemical hydrogen evolution. Phys Chem Chem Phys 2013;15:4554-65

24. Eberlin LS, Ferreira CR, Dill AL, Ifa DR, Cheng L, Cooks RG. Nondestructive, histologically compatible tissue imaging by desorption electrospray ionization mass spectrometry. Chembiochem 2011;12:2129-32

25. Konermann L, Ahadi E, Rodriguez AD, Vahidi S. Unraveling the Mechanism of Electrospray Ionization. Anal Chem 2013;85:2-9

26. Eberlin LS, Ifa DR, Wu C, Cooks RG. Three-Dimensional Vizualization of Mouse Brain by Lipid Analysis Using Ambient Ionization Mass Spectrometry. Angew Chem Int Edit 2010;49:873-6

27. Almeida R, Berzina Z, Arnspang EC, Baumgart J, Vogt J, Nitsch R, et al. Quantitative Spatial Analysis of the Mouse Brain Lipidome by Pressurized Liquid Extraction Surface Analysis. Anal Chem 2015;87:1749-56

28. Haler JRN, Sisley EK, Cintron-Diaz YL, Meitei SN, Cooper HJ, Fernandez-Lima F. Workflow for fast lipid tissue screening using LESA-FT-ICR-MS. Analytical Methods 2019;11:2385-95

29. Sans M, Gharpure K, Tibshirani R, Zhang J, Liang L, Liu J, et al. Metabolic Markers and Statistical Prediction of Serous Ovarian Cancer Aggressiveness by Ambient Ionization Mass Spectrometry Imaging. Cancer Res 2017;77:2903-13

30. Doria ML, McKenzie JS, Mroz A, Phelps DL, Speller A, Rosini F, et al. Epithelial ovarian carcinoma diagnosis by desorption electrospray ionization mass spectrometry imaging. Sci Rep-Uk 2016;6:39219

31. Alessandra Tata MW, Manuela Ventura, Nicholas Bernards, Milan Ganguly, Adam Gribble, Bindesh Shrestha, Emma Bluemke, Howard J. Ginsberg, Alex Vitkin, Jinzi Zheng & Arash Zarrine-Afsar. Rapid Detection of Necrosis in Breast Cancer with Desorption Electrospray Ionization Mass Spectrometry. Sci Rep-Uk 2016;6

32. Eberlin LS, Dill AL, Golby AJ, Ligon KL, Wiseman JM, Cooks RG, et al. Discrimination of Human Astrocytoma Subtypes by Lipid Analysis Using Desorption Electrospray Ionization Imaging Mass Spectrometry. Angewandte Chemie-International Edition 2010;49:5953-6

33. Pirro V, Llor RS, Jarmusch AK, Alfaro CM, Cohen-Gadol AA, Hattabd EM, et al. Analysis of human gliomas by swab touch spray-mass spectrometry: applications to intraoperative assessment of surgical margins and presence of oncometabolites. Analyst 2017;142:4058-66

34. Gharpure KM, Pradeep S, Sans M, Rupaimoole R, Ivan C, Wu SY, et al. FABP4 as a key determinant of metastatic potential of ovarian cancer. Nat Commun 2018;9

35. Dill AL, Eberlin LS, Costa AB, Ifa DR, Cooks RG. Data quality in tissue analysis using desorption electrospray ionization. Anal Bioanal Chem 2011;401:1949-61

36. Zeng W, Musson DG, Fisher AL, Wang AQ. A new approach for evaluating carryover and its influence on quantitation in high-performance liquid chromatography and tandem mass spectrometry assay. Rapid Commun Mass Spectrom 2006;20:635-40

37. Hughes NC, Wong EYK, Fan J, Bajaj N. Determination of carryover and contamination for mass spectrometry-based chromatographic assays. Aaps J 2007;9:E353-E60

38. Kottke PA, Degertekin FL, Fedorov AG. Scanning Mass Spectrometry Probe: A Scanning Probe Electrospray Ion Source for Imaging Mass Spectrometry of Submerged Interfaces and Transient Events in Solution. Anal Chem 2010;82:19-22

Chapter 5. Nondestructive Tissue Analysis for *Ex Vivo* and *In Vivo* Cancer Diagnosis Using a Handheld Mass Spectrometry System[5]

INTRODUCTION

Tissue assessment and diagnosis are critical in the clinical management of cancer patients. Tissue diagnosis is particularly important during surgical excision of solid cancers for surgical margin evaluation. Many women diagnosed with breast cancer, for example, undergo breast conserving surgery, which involves removing the lesion of interest with a rim of normal tissue and preserving the rest of the breast. One of the greatest challenges a breast cancer surgeon faces is determining the delicate boundary between cancerous and normal tissues to achieve negative margins for invasive and carcinoma in situ while optimizing aesthetic outcomes (1). Similarly, optimal surgical treatment of lung carcinomas includes complete local resection of the primary tumor (2) because adverse patient outcome is strongly associated with residual tumor at the bronchial resection margin (3). For high-grade serous ovarian cancer (HGSC) patients, postoperative residual disease after surgical debulking is also negatively associated with progression-free survival and response to adjuvant chemotherapy (4). Thus, accurate negative margin assessment and complete tumor excision are highly desirable across cancer surgeries because they offer the greatest potential for prolonged disease-free and overall survival (1, 5–7).

Intraoperative assessment of the extent of tumor involvement can be challenging through conventional histopathologic analysis of frozen sections. Frozen section preparation is time- and labor-intensive and requires skilled technicians and pathologists

[5] Adapted with permissions from Zhang J, Rector J, Lin JQ, Young JH, Sans M, Katta N, et al. Nondestructive tissue analysis for *ex vivo* and *in vivo* cancer diagnosis using a handheld mass spectrometry system. Sci Transl Med 2017;9:eaan3968. Copyright © 2017, American Association for the Advancement of Science. Authors contributed to design and development, data collection, statistical analysis and interpretation, and manuscript preparation. Sans M contributed to data collection and interpretation, and preparation of materials for the manuscript.

to produce and interpret the results. Moreover, freezing artifacts can negatively interfere with tissue structure and cell morphology, thus complicating pathological interpretation. Logistically, intraoperative frozen section analysis prolongs operative time, subjecting the patient to increased risks related to extended anesthesia. Therefore, margin specimens are frequently processed postoperatively as permanent specimens. However, when positive margins are found during the final pathologic evaluation, the patient is subjected to additional surgical procedures for re-excision of the involved margin, which increases health care costs and places the patient at risk for additional surgical complications, discomfort, and anxiety (1, 8).

Molecular analysis of cancer tissues offers the exciting opportunity to incorporate cancer-specific biomarkers into clinical decision-making for improved cancer detection and diagnosis. Several molecular imaging technologies have been developed and advanced to preclinical and clinical phases for *ex vivo* and *in vivo* tissue diagnosis. Immunohistochemistry protocols targeting protein biomarkers are routinely used in diagnostic pathology for postoperative evaluation of *ex vivo* tissue sections and typing of neoplasms (9). Gene sequencing technologies are powerful for postoperative identification of specific genetic mutations and chromosomal translocations in *ex vivo* tissue samples (10). Intraoperative real-time techniques including fluorescent probes that target tumor cells are currently being implemented for *in vivo* tumor and surgical margin visualization (11). Emerging optical technologies including Raman spectroscopy and stimulated Raman scattering microscopy have been recently applied for intraoperative diagnosis of brain cancers (12, 13). Mass spectrometry (MS) imaging approaches have been successfully applied for molecular imaging of cancer tissues (14–17).

Within the last decade, several ambient ionization MS techniques have been developed for rapid molecular diagnosis of cancer tissues and have shown exceptional

potential for clinical use (18). Desorption electrospray ionization MS imaging (DESI-MSI), for example, has been use for *ex vivo* cancer diagnosis and surgical margin evaluation of tissue sections and tissue smears (19, 20). Yet, technical incompatibilities including the use of a spray of organic solvents, high-pressure nebulizing gas, and high voltage have prevented the use of DESI-MSI for fresh tissue and *in vivo* analyses. A few approaches for direct MS analysis of cancer tissue specimens have been developed (18). Rapid evaporative ionization MS, or the iKnife, combines an electrocauterization device with MS for direct tissue analysis and classification and has been successfully used intraoperatively for *in vivo* cancer diagnosis (21, 22). Ultraviolet and infrared lasers have also been coupled with MS for characterization of cancer tissues (23, 24). Although these approaches offer the advantage of incorporating common surgical methods into an MS-based diagnostic workflow, these technologies rely on tissue damage to produce molecular ions or are operationally constrained to a specific surgical modality.

Here, we describe the development and application of an automated, biocompatible, disposable handheld device, the MasSpec Pen, for direct, real-time nondestructive sampling and molecular diagnosis of tissues. We tested the MasSpec Pen for *ex vivo* molecular evaluation of human normal and cancerous tissue samples from 253 patients. The mass spectra obtained presented rich molecular information including diagnostic metabolites, lipids, and proteins. Statistical analysis using the least absolute shrinkage and selector operator (Lasso) technique allowed prediction of cancer with high sensitivity and specificity (25). In a tumor bearing mouse model, we demonstrate that this technology is suited for *in vivo* use and diagnosis of breast cancer during surgery.

MATERIALS AND METHODS

Study design

The objective of this study was to evaluate the potential of an MS based probe to nondestructively analyze and diagnose cancer in human tissue samples. Here, we investigated the molecular profiles of human tissue samples obtained from 281 patients including normal and cancer breast, lung, thyroid, and ovary tissues. All patient samples were obtained from the CHTN (Cooperative Human Tissue Network), Asterand Bioscience, and the Baylor College of Medicine Tissue Bank under approved Institutional Review Board protocol. The mass spectra obtained using the MasSpec Pen in tissue samples were normalized, background subtracted, and analyzed using a statistical technique to build classification models. Expert, board-certified pathologists evaluated the H&E-stained tissue sections obtained from the tissue samples analyzed. The pathologists were blind to any information about the acquisition from MS analysis. Samples were excluded from statistical analysis if they were determined by the pathologist to have substantial heterogeneity in cell composition, which included 28 samples, resulting in a final sample set of 253 samples. The *in vivo* animal model experiments were conducted under approved Institutional Animal Care and Use Committee protocol.

Design and engineering of the MasSpec Pen

A three-dimensional (3D) printer (Model uPrint SE Plus) was used to print the key component, a polydimethylsiloxane (PDMS) (Dow Corning) probe tip. The pen tips were fabricated by casting an elastomer from a negative mold designed using SolidWorks computer-aided design software and then dissolving the mold away. PTFE tubing (ID, 1/32 inch; outer diameter, 1/16 inch; Cole-Parmer) was directly inserted into the probe tip for experiments.

Mass spectrometry data acquisition

All experiments were performed on a Q Exactive Hybrid Quadrupole- Orbitrap mass spectrometer (Thermo Fisher Scientific). Full scan was carried out at the range of m/z 120 to 1800, using a resolving power of 140,000, a capillary temperature of 350°C, and an S-lens radio frequency level of 100. Wild-type mouse brains were purchased from Bioreclamation IVT. Human tissue samples were obtained frozen and stored in a −80°C freezer until analysis, when they were thawed at room temperature. The tissues were placed on a glass slide and analyzed by the MasSpec Pen using the experimental steps described. After experiments, the tissue regions analyzed were annotated and frozen, and 16-mm tissue sections were prepared using a CryoStar NX50 cryostat. Additional tissue sections at different regions of the tissue piece were obtained for the MasSpec Pen analysis. Tissue sections were H&E-stained and evaluated by histopathology after analysis.

***In vivo* mouse experiments**

BT474 HER2+ cells were grown for 24 hours and injected subcutaneously into the right flank of the mouse (total injection of 100 ml) in Dr. Anna G. Sorace's laboratory at the University of Texas at Austin. Tumors were monitored weekly for growth until they reached 0.7 to 1.0 cm in diameter (average of 250 mm^3). *In vivo* experiments were performed during surgical resection of tumors using murine animal models while the mice were under anesthesia (2% isoflurane and 98%O_2). A surgical blade was used to open a flap of skin, leaving an estimated space of 1 to 2 cm around the tumors, and then, the skin flap was dissected from the surface of the tumor. The skin was flapped to expose the tumor and adjacent normal tissues, which were analyzed in several regions using the MasSpec Pen. Pieces of the tumor were then resected using a scalpel and analyzed *ex vivo*. Tumor

tissue pieces analyzed by the MasSpec Pen were annotated, flash-frozen, sectioned, and subjected to H&E staining for diagnosis.

Statistical analysis

Averages of three mass spectra obtained during each 10-s MasSpec Pen analysis were used to build molecular databases. The Xcalibur raw data were converted to Microsoft Excel spreadsheet format. The full mass range of the spectra was partitioned into bins by rounding *m/z* values to the nearest hundredth. All mass spectra were first normalized according to total ion count or to the absolute intensity of *m/z* 885.55 to account for slight fluctuations in signal intensities that may occur between experiments. Then, background peaks and peaks not appearing in at least 10% of the samples analyzed were excluded to reduce random noise. For each tissue sample type (breast, thyroid, lung, and ovary), the data were imported to R programming language. PCA was performed by centering the preprocessed data to mean zero and computing principal components using the prcomp function in R. The first three principal components were visualized with the rgl and pca3d packages for R. For tissue classification, the Lasso method was applied using the glmnet package in the CRAN R language library. Models generated using the Lasso are simpler to interpret than other regularization methods because it yields "sparse" models (models that involve only a subset of the features). A mathematical weight for each statistically informative feature is calculated by the Lasso depending on the importance that the mass spectral feature has in characterizing a certain class (cancer versus normal or a cancer subtype versus normal). Classification was performed using a leave one- out cross-validation approach to assess the predictive accuracy within the training set. Performance of trained classifiers was measured by sensitivity, specificity, accuracy, and AUC.

RESULTS

Optimization of the MasSpec Pen design and operation

We designed the MasSpec Pen (Figure 5.1A) as an automated and biocompatible handheld sampling probe that allows gentle and time- and volume-controlled extraction of molecules from a tissue sample using a discrete water droplet. Several prototypes of the system were engineered with the goal of minimizing tissue damage, maximizing tissue-analyte extraction, and maximizing solvent transfer to the mass spectrometer. The optimized system contains three primary components: (i) a syringe pump that is programmed to deliver a defined water volume (4 to 10 ml) to the sampling probe; (ii) small diameter [inner diameter (ID), 800 mm] polytetrafluoroethylene (PTFE) tubing conduits, which are integrated to a fast (8ms) two-way pinch valves for controlled solvent transport from the pump to the tissue and from the tissue to the mass spectrometer; and (iii) a handheld pen-sized probe for direct sampling of biological tissues.

The main component of the handheld pen-sized probe is a 3D printed PDMS tip (Figure 5.1B). The probe tip is designed with three ports: an incoming port that delivers a single water droplet to the probe tip (conduit 1), a central port for gas (N_2, CO_2, or air) delivery (conduit 2), and an outgoing port to transport molecular constituents in the water droplet from the tissue to the mass spectrometer (conduit 3). At the probe tip, all ports combine into a small reservoir where a single water droplet is retained and exposed to the tissue sample for a controlled amount of time (3 s), allowing efficient analyte extraction. After the 3-s extraction period, the MasSpec Pen is removed from the tissue. Concomitantly, conduit 3 is opened, allowing vacuum extraction of the droplet to the mass spectrometer, whereas positive pressure from a low-pressure gas delivery (<10 psi) is provided through conduit 2 (Figure 5.1C). The gas provided by the second tube does not

participate in the extraction process but is used instead to prevent the collapse of the system due to the vacuum used and to assist solvent transport from the tissue to the mass spectrometer. A subsequent flush step cleans the system; this is not used for extraction of biomolecules from tissues because there is no contact with the tissue during this period. Conduit 3 is directly connected to the transfer tube of a high–mass resolution Orbitrap mass spectrometer so that the negative pressure of the mass spectrometer vacuum system drives the movement of the droplet from the reservoir to the mass spectrometer for ionization and mass analysis. This setup simplifies the operational steps and precludes the use of ionization sources, although various connection and ionization methods could be coupled to our system.

The diameter of the reservoir at the probe tip determines the volume of solvent exposed to the tissue and the spatial resolution of the device. Using current tooling, we have designed MasSpec Pen tips with sampling sizes ranging from 1.5 to 5.0 mm, which is determined by the reservoir diameter. At a 2.77-mm reservoir diameter, a solvent volume of 10 ml is retained in the reservoir and contacts the tissue sample for a defined time period, whereas 4.4 ml is retained in a reservoir with a 1.5-mm diameter. Contact times of 1, 3, and 5 s between the droplet and the tissue sample were evaluated (Figure A4.1). The 3-s contact time was selected for all the experiments because it allowed ease of operation by the user and yielded mass spectra with sufficient total ion intensity. A tube length of 1.5 m was used for all the conduits to allow free handheld use of the device by an operator without geometrical or spatial constraints.

The tip design using three conduit tubes and high-speed actuated pinch valves allowed precise control of droplet motion and showed excellent performance and robustness. The entire process from sampling to mass spectral acquisition is completed in 10 s or less and is automated using an Arduino microcontroller so that each acquisition and

analysis is individually triggered through a one-step click using a foot pedal. System automation ensures that each solvent droplet is delivered separately to the inlet, yielding several mass spectra that are averaged for a final molecular profile of the sample. Controlled droplet delivery allowed the mass spectrometer to operate without any evident performance degradation. After each use, the MasSpec Pen was cleaned through a rapid and automated cleaning flush or by replacing the disposable tip. Contamination of the mass spectrometer was evaluated by installing commercially heated ESI source and acquiring mass spectra after the MasSpec Pen analysis. No lipid contamination was observed other than background peaks commonly observed in the mass spectra.

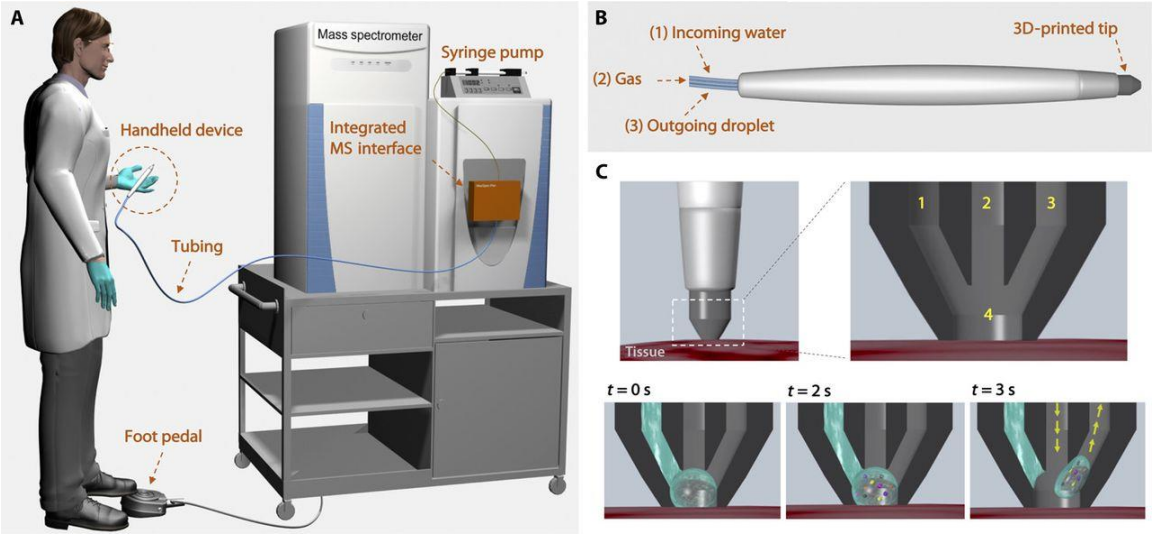

Figure 5.1: Schematic representation of the MasSpec Pen system and operational steps.

The pen-sized handheld device is directly integrated into a laboratory-built MS interface through PTFE tubing (A). The integrated MS interface houses the pinch valves, microcontroller, and tubing to connect the system to the mass spectrometer inlet. The system is triggered by the user through a foot pedal. The MasSpec Pen (handheld device) is designed with a PDMS tip and three PTFE conduits, which provide incoming water (1) and gas (2) to the tip and an outgoing conduit for the water droplet (3) (B). The tip contacts the tissue for analysis. Inset shows the three conduits (1 to 3) and solvent reservoir (4) within the tip. When the system is triggered (t = 0 s) by using the foot pedal, the syringe pump delivers a controlled volume of water to the reservoir. The discrete water droplet interacts with the tissue to extract the molecules (t = 2 s). After 3 s of extraction, the vacuum and the gas conduits are concomitantly opened (arrows) to transport the droplet from the MasSpec Pen to the mass spectrometer through the tubing system for molecular analysis (C).

Nondestructive molecular analysis of tissue samples

The MasSpec Pen was designed to operate directly on tissue specimens independently of tissue stiffness and morphology. We tested the performance of the MasSpec Pen to analyze soft tissue samples (0.1 to 5 g) from different organs including mouse brain and human breast, thyroid, lung, and ovary tissues. Tissue analyses were performed under ambient conditions through a simple one-step experiment, following the same operational steps described previously. The MasSpec Pen tip was gently brought into contact with the surface of the tissue sample for a period of 3 s during which extraction took place. The mass spectra obtained for a region of gray matter probed from a piece of fresh mouse brain tissue were reproducible (RSD= 4.6%; n = 10). MasSpec Pen analyses of human tissue samples provided similar rich molecular information, especially of tissues composed of epithelial and cancerous cells. Noncancerous tissue specimens that were mostly composed of soft connective tissue such as stroma provided less abundant mass spectra. Many of the normal breast tissue samples analyzed presented abundant fat content, which is immiscible with water and thus yielded lower total ion counts in the mass spectra when compared to breast cancer tissues or normal breast cancer glands.

Visual and microscopic inspection of the tissue samples after the MasSpec Pen analysis revealed no detectable damage to the tissue morphology in the region probed. Figure 5.2A shows optical images obtained from a lung tissue sample before, during, and after the MasSpec Pen analysis. No observable damage to the tissue was seen at the region analyzed, and rich mass spectra were obtained (Figure 5.2B). The automated and time-controlled operational steps of the MasSpec Pen prevent tissue damage because the tissue is only exposed to the small water droplet and not to the vacuum used to transport the droplet from the reservoir to the mass spectrometer. These results provide evidence that

the MasSpec Pen can obtain rich molecular information from tissue samples nondestructively.

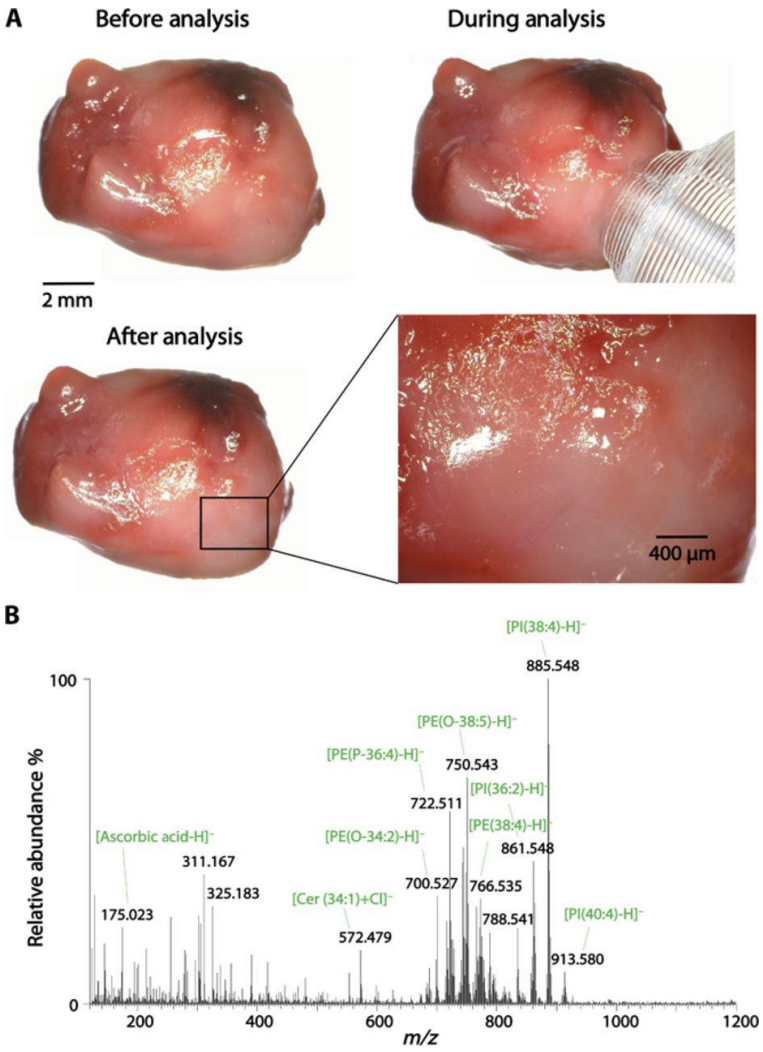

Figure 5.2: Nondestructive molecular analysis of human tissue samples using the MasSpec Pen.

Optical images show a lung adenocarcinoma tissue sample before, during, and after the MasSpec Pen analysis. A magnification of the tissue specimen (inset) shows no macroscopic damage to the tissue region analyzed by the MasSpec Pen. (A) Negative ion mode mass spectrum obtained for the tissue region analyzed including the identification of the most abundant molecular ions (B).

Molecular diagnosis and statistical prediction of cancer in human tissues

We next evaluated whether the molecular information obtained from human tissue samples using the MasSpec Pen was diagnostic and predictive of disease state. We analyzed a total of 253 human tissue specimens using the MasSpec Pen, including 95 lung samples (47 normal and 48 cancer samples including 17 adenocarcinoma, 17 squamous cell carcinoma, and 14 cancer samples of other histologic subtypes), 57 ovary samples (29 normal and 28 HGSC samples), 56 thyroid samples (27 normal, 11 FTA, and 18 PTC samples), and 45 breast samples (29 normal and 16 ductal carcinoma samples). Patient demographic information is provided in Table A4.1. After the MasSpec Pen analysis, the region analyzed was demarcated and registered through a series of optical images. Parallel pieces of the samples were frozen, sectioned at the demarcated region, hematoxylin and eosin (H&E)–stained, and evaluated by histopathology to derive a diagnosis. Only samples with a predominant cell composition and clear diagnosis were used to build molecular databases. The histologically validated mass spectra obtained for the cancerous samples presented molecular species identified as several lipids and metabolites previously described as potential disease markers using ambient ionization MS techniques. For the lung cancer tissue, characteristic molecular markers such as PI(36:1) (as *m/z* 863.565), PG(36:2) (*m/z* 773.542), PG(34:1) (*m/z* 747.514), and FA(18:1) (*m/z* 281.249) were observed (Figure 5.2B). For the normal lung, *m/z* 885.550, identified as PI(38:4), and *m/z* 744.552, identified as PE(36:1), were observed. The mass spectra obtained for breast cancer tissue presented diagnostic lipid markers previously described by DESI MSI (26, 27), including *m/z* 885.550, identified as PI(38:4), *m/z* 863.565, identified as PI(36:1), *m/z* 773.542, identified as PG(36:2), and several FA such as m/z 303.233, identified as FA(20:4), and *m/z* 281.249, identified as FA(18:1). PCA performed on the data obtained

from the 253 human tissue samples analyzed showed separation between cancer and normal tissues for each organ (Figure 5.3).

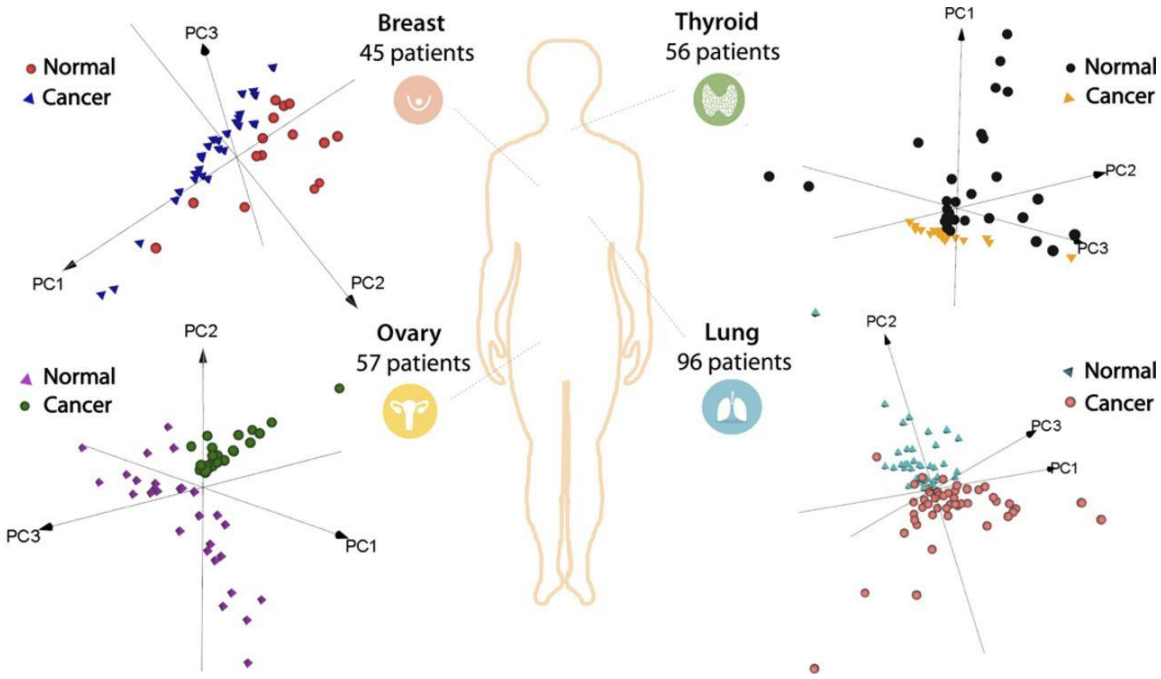

Figure 5.3: PCA of the data obtained from human tissue samples using the MasSpec Pen.

A total of 253 patient tissue samples were analyzed including breast (n = 45), thyroid (n = 56), ovary (n = 57), and lung (n = 96) cancer and normal tissue samples. 3D PCA (PC1, PC2, and PC3) score plots are shown for each tissue type. The first three PCs explain the 77, 69, 51, and 87% of the total variance of breast, thyroid, lung, and ovarian data sets, respectively.

To evaluate whether the MasSpec Pen molecular signatures are predictive of cancer and normal tissues, we applied the Lasso method to build classification models using the histologically validated mass spectral database. The performance of the model was evaluated through a leave-one-patient-out cross-validation approach and was measured by sensitivity and specificity for cancer, as well as accuracy and the area under the curve (AUC) (Table 5.1). For breast cancer (n = 45), 87.5% sensitivity, 100% specificity (AUC = 1.0), and an overall accuracy of 95.6% were achieved, which is comparable to the results reported using DESI-MSI (98.2% accuracy; n = 126) (27), the iKnife (95.5%accuracy; n = 10) (22), and matrix-assisted laser desorption/ionization imaging of lipids and proteins (94.1%accuracy; n = 68) (28). For HGSC (n = 57), 100% sensitivity, 89.7% specificity, and 94.7% accuracy were achieved (AUC = 0.98), which is also similar to classification results obtained by DESI-MSI (97.1% accuracy; n = 31, results described in Chapter 2) (29). For lung cancer (n = 96), 97.9% sensitivity, 95.7% specificity, and 96.8% accuracy were achieved (AUC = 0.97). When predicting on the basis of lung cancer histologic subtypes, 93.8 and 92.2% accuracy was achieved for squamous cell carcinoma and adenocarcinoma, respectively. Thyroid tumor samples investigated included benign FTA and malignant PTC samples. A classifier for each was built, yielding 94.7% accuracy for FTA and 97.8% accuracy for PTC. Overall, 96.4% sensitivity, 96.2% specificity, and 96.3% accuracy were achieved for all four types of cancer investigated. These results demonstrate that the molecular information obtained from human tissue samples by the MasSpec Pen can be used to identify cancer and indicate that the statistical classifiers built are robust and may be used in an automated approach for rapid clinical diagnosis of tissue samples.

Table 5.1: Human tissue sample details and results obtained using the MasSpec Pen.

Pathological diagnosis, number of patient samples, and the Lasso prediction sensitivity, specificity, accuracy, and AUC obtained using a leave-one-out cross-validation approach are shown. Lasso prediction results for lung are shown for normal versus all cancer tissues (first row), followed by normal versus lung adenocarcinoma (middle row) and normal versus squamous cell carcinoma (last row). Lasso prediction results for thyroid are shown for normal versus malignant papillary carcinoma and normal versus benign follicular adenoma.

Organ	**Pathologic evaluation**		**Number of patients**	**Lasso prediction**			
	Diagnosis	**Histologic type**		**Sensitivity**	**Specificity**	**Accuracy**	**AUC**
Breast	*Normal*		29	87.5%	100.0%	95.6%	1.00
	Cancer	*Ductal carcinoma*	16				
Lung	*Normal*		47	97.9%	95.7%	96.8%	0.97
	Cancer	*Adenocarcinoma*	17	88.2%	93.6%	92.2%	0.98
		Squamous cell	17	88.2%	95.7%	93.8%	0.93
		Others	14	-	-	-	-
Ovary	*Normal*		29	100.0%	89.7%	94.7%	0.98
	Cancer	*High-grade serous*	28				
Thyroid	*Normal*		27	-	-	-	-
	Tumor	*Papillary carcinoma*	18	94.4%	100.0%	97.8%	0.99
		Follicular adenoma	11	90.9%	96.3%	94.7%	0.93

Intrasample analysis of histologically distinct and cancer margin tissue regions

We evaluated the ability of the MasSpec Pen to identify histologically distinct regions in a single human tissue sample that contained regions of HGSC adjacent to normal ovarian stroma tissue. Five regions of the tissue sample were analyzed consecutively using a MasSpec Pen with a 1.5-mm probe tip diameter, as demarcated in the optical image shown in Figure 5.4A. A tissue section of the sample including the regions analyzed by the MasSpec Pen was subjected to H&E staining and evaluated by histopathology. Regions 1 and 2 were diagnosed by histopathology as normal stroma, whereas regions 4 and 5 were diagnosed as HGSC. Region 3 was in the margin between the cancer and normal stroma tissue regions, presenting ~50% tumor tissue and ~50% normal stroma tissue (Figure 5.4A, inset). Figure 5.4B shows the mass spectra obtained for regions 1, 3, and 5. The spectra obtained for region 5, HGSC, presented characteristic lipid markers detected in the HGSC tissues analyzed *ex vivo* to build our statistical classifier. The mass spectra obtained for region 1, diagnosed as normal ovarian stroma tissue, presented less abundant molecular ions as also observed for the other stroma tissues analyzed *ex vivo*. Region 3 presented molecular profiles characteristic of HGSC with lower total abundance due to the contribution of normal stroma tissue present within the region analyzed. The mass spectra obtained for the five regions were then evaluated by our ovarian cancer molecular classifier as an independent validation set. Our classifier correctly identified regions 1 and 2 as normal and regions 3 to 5 as cancer (Figure 5.4C). Similar results were obtained for a different tissue sample with histologically distinct regions (Figure A4.2). These results show that the molecular information obtained by the MasSpec Pen can be used to detect cancer in marginal regions with mixed composition of normal and cancer cells.

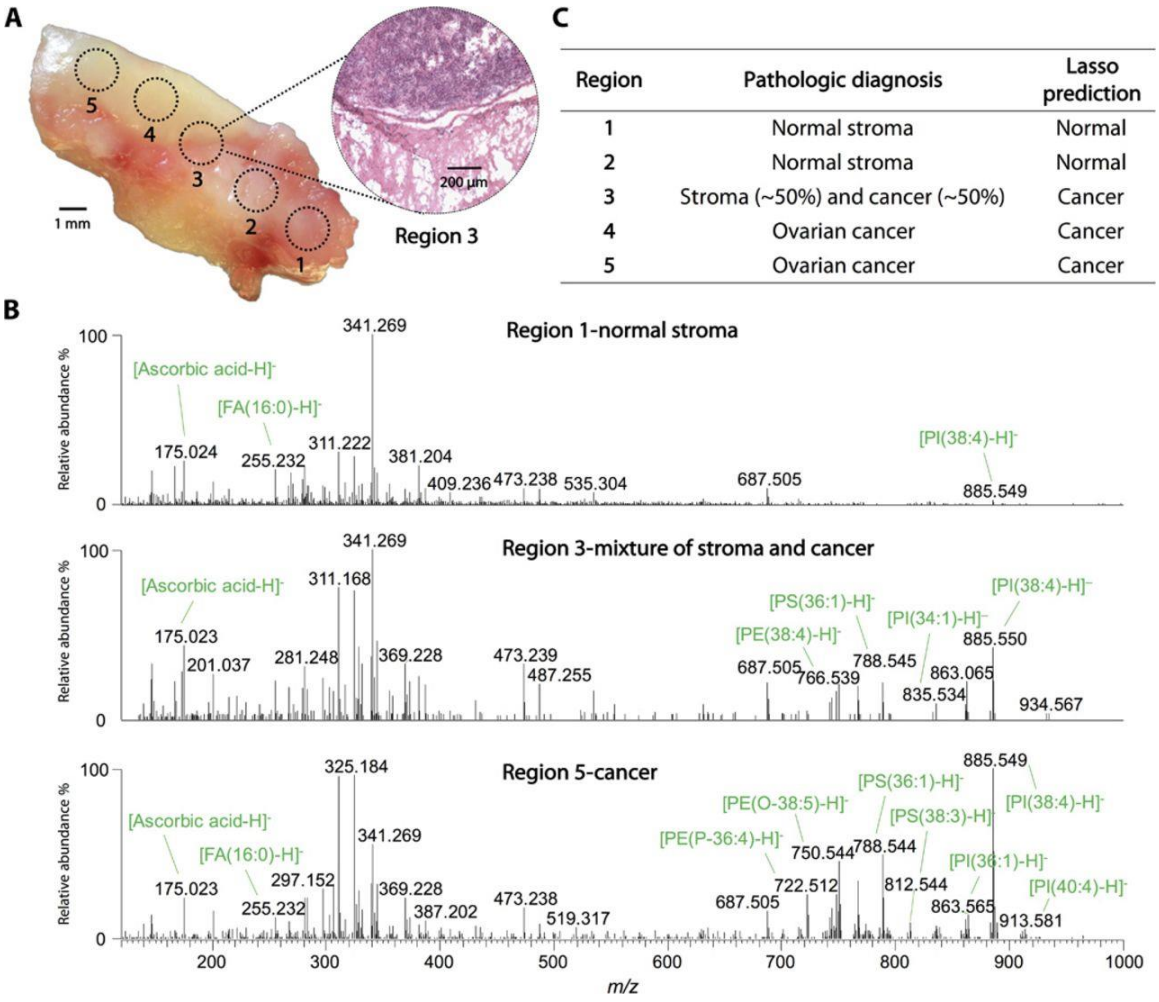

C

Region	Pathologic diagnosis	Lasso prediction
1	Normal stroma	Normal
2	Normal stroma	Normal
3	Stroma (~50%) and cancer (~50%)	Cancer
4	Ovarian cancer	Cancer
5	Ovarian cancer	Cancer

Figure 5.4: MasSpec Pen analysis of an HGSC tissue sample with mixed histologic composition.

Optical image shows the tissue sample that was analyzed at the demarcated regions (1 to 5) using a 1.5-mm-diameter MasSpec Pen. After the MasSpec Pen analysis, the tissue sample was frozen, sectioned, and H&E-stained. An optical image of the H&E-stained tissue section obtained at region 3 is shown (inset), presenting a mixed histologic composition including cancer and adjacent normal stroma tissue (A). The MasSpec Pen negative ion mode mass spectra are shown for regions 1 (normal stroma; average of n = 3 mass spectra), 3 (mixture of normal stroma and cancer; average of n = 3 mass spectra), and 5 (cancer; average of n=3 mass spectra) (B). Table listing the pathologic diagnosis of the five regions analyzed and the Lasso prediction results (C).

In vivo analysis of a murine model of human breast cancer during surgery

The MasSpec Pen was designed with biocompatible materials to ensure full compatibility as an *in vivo* molecular diagnostic tool. We tested the MasSpec Pen for *in vivo* tissue analysis using a murine model of human breast cancer. BT474 human epidermal growth factor receptor 2–positive (HER2+) breast cancer cells were implanted subcutaneously in nude athymic mice (n = 3). Under anesthesia, the skin overlying the tumors was dissected away, and several tissue regions were analyzed following the same automated experimental steps described previously, including multiple positions of the top of the tumor, the core of the tumor after partial tumor resection, and adjacent normal soft connective tissue. Figure 5.5A shows an optical image of the animal under anesthesia before initiation of surgery, before analysis (after surgical removal of the skin), during the MasSpec Pen analysis, and after the analysis. The mass spectra obtained for the tumor regions presented many molecular species observed in human breast tissue, with a distinctive profile from what was obtained for adjacent normal soft connective tissue regions (Figure 5.5B). Using optical microscopy, no observable macroscopic or microscopic damage to the tissue regions analyzed were detected due to MasSpec Pen analyses, as evident from the optical images obtained of the H&E-stained tissue sections (Figure A4.2). Further, no apparent effects to the health of the animals were observed due to the MasSpec Pen analysis during surgery. After *in vivo* analysis, freshly excised tumor specimens were also analyzed *ex vivo*, yielding mass spectra with common lipid species to those observed during *in vivo* analysis despite variations in relative abundances, which are likely due to the reanalysis process of the same tissue region (Figure A4.3). These results suggest that the MasSpec Pen is suitable for *in vivo* molecular evaluation and cancer diagnosis.

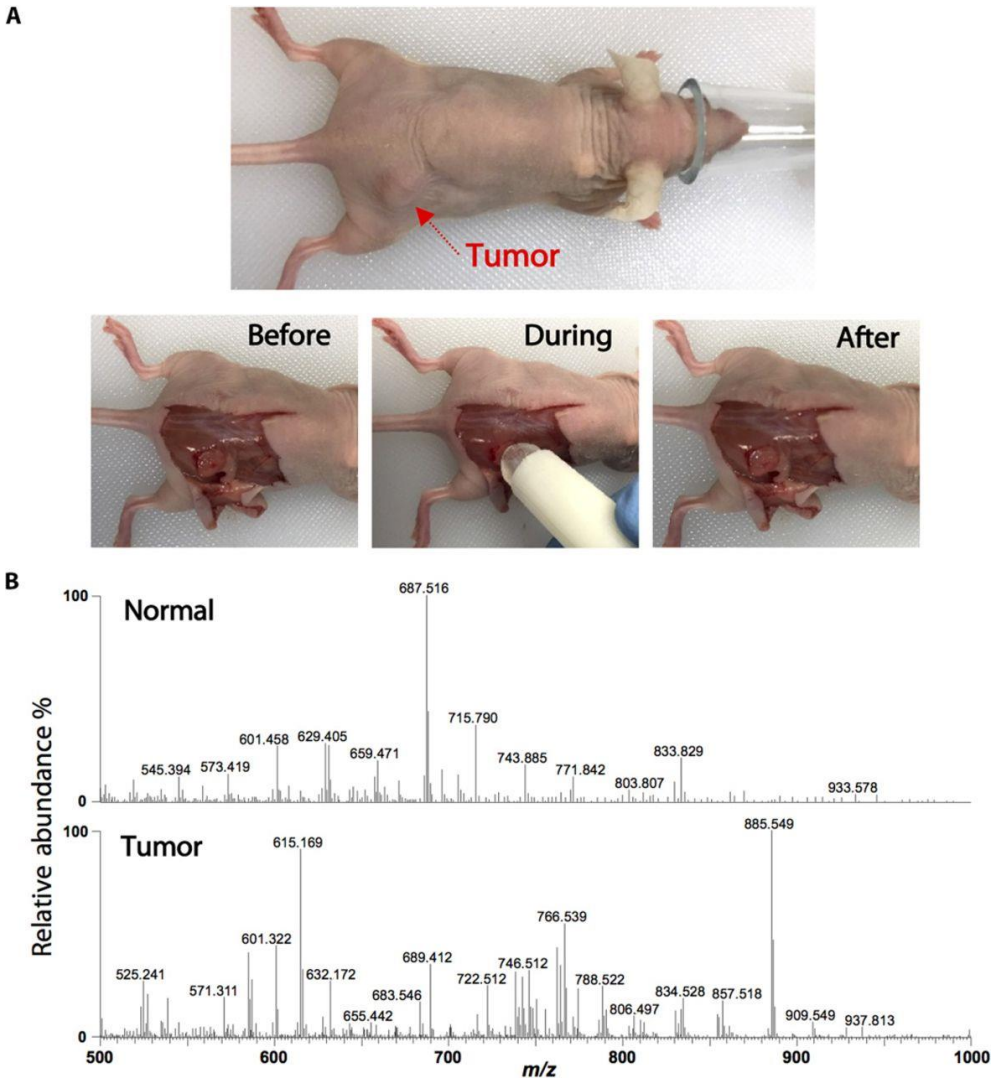

Figure 5.5: Intraoperative analysis of tumor and normal tissues in a murine model.

Experiments were performed *in vivo* in mice under anesthesia. Optical images show the animal under anesthesia and before, during, and after the MasSpec Pen analysis (A). Representative negative ion mode mass spectra show distinct molecular profiles from normal (average of n = 3 mass spectra) and tumor (average of n = 3 mass spectra) tissues (B).

DISCUSSION

We developed the MasSpec Pen as an automated and biocompatible handheld sampling probe that allows gentle and time- and volume-controlled extraction of molecules from a tissue sample using a discrete water droplet. Our results provide evidence that the MasSpec Pen is suited for rapid *ex vivo* and *in vivo* cancer diagnosis of tissue samples. The mass spectra obtained from the analysis 253 human tissue samples presented rich molecular information that is diagnostic of disease state. The chemical extraction process used is gentle so that the tissue is undamaged after molecular analysis. Statistical classifiers built from the mass spectra obtained provided high sensitivity and specificity for cancer detection (>96%), including prediction of histologic subtypes of lung cancer and benign and malignant thyroid tumors. Experiments performed in animal models demonstrate that this technology is suitable for *in vivo* molecular evaluation of cancer and normal tissues without causing observable tissue harm or evident stress to the animal. The MasSpec Pen provides rich mass spectra from biological samples characterized by a variety of singly and doubly charged ions of lipids and metabolites and multiply charged protein ions, similar to those obtained by DESI-MSI and ESI methods. A liquid-solid chemical extraction process is used to sample molecules from the tissue using a water droplet, without assistance from a gas or a strong electric field. Our results show that by depositing a discrete water droplet onto a tissue sample for a determined amount of time, efficient extraction of biomolecules is achieved while tissue integrity is preserved. The extraction process is similar to that reported for liquid extraction surface analysis (30), liquid microjunction surface sampling probe (31), and nanoDESI (32), although the latter two techniques use a continuous flow of solvent onto a sample surface, whereas the MasSpec Pen uses a single water droplet for extraction. In our current system, the water droplet containing analytes is transported as a liquid sample to the mass spectrometer and directly introduced to an extended transfer tube,

which is connected to the heated inlet. Vaporization and ionization occur in the inlet region of the mass spectrometer, similar to what has been observed in solvent-assisted inlet ionization (33). Additional means of ionization such as electric field or laser assistance were not applied, although various connection methods and ionization sources (ESI, atmospheric pressure chemical ionization, atmospheric pressure photoionization, and others) could be adapted for our system.

Biocompatibility has been recognized as a key functional requirement of next-generation medical devices (34). The MasSpec Pen was designed as a simple, disposable device made with biocompatible materials and chemicals for contact with living tissues. The probe tip material, the conduit tubes, and the chemical used were PDMS, PTFE, and water, respectively. PDMS and PTFE are widely recognized as biocompatible materials and have a long history of utilization in medical devices including catheters and long-term implants (35). Our experiments demonstrate that the low volume (10 µl or less) of high-purity water used caused no effect to the tissues analyzed *in vivo* and *ex vivo*. The MasSpec Pen has shown good compatibility for contact with living tissues, which should enable *in vivo* use.

We designed the MasSpec Pen as an automatic and user-friendly device that could be used during routine medical diagnosis. A drawback of many ambient ionization MS methods is the need for geometrical optimization and alignment between the source, the sample, and the mass spectrometer inlet to achieve good ion transmission. On the other hand, the MasSpec Pen operates in a geometry-free manner independently of sample stiffness and morphology and does not require optimization because all of the components required for solvent delivery, tissue sampling, and solvent retrieval are incorporated within the tip. The 1.5-m tube transport systems enable free motion and ease of use to the operator. The high-speed electronically and time-controlled pinch valves allowed precise control of

droplet motion and showed excellent performance, robustness, and reproducibility in the results obtained.

Our results suggest that the MasSpec Pen may provide the performance required for near real-time nondestructive molecular diagnosis of tissues *in vivo* and *ex vivo*. Intraoperative diagnosis and surgical margin evaluation continue to be research focuses of clinical ambient ionization MS, with efforts used to develop devices for *in vivo* diagnosis (18). For example, a sampling probe using a DESI-MSI source to produce a continuous high-pressure spray of microdroplets has been proposed for tissue analysis (36), but it has not been demonstrated for cancer diagnosis or *in vivo* use. Ultraviolet and infrared laser approaches have been reported for tissue analysis through ablation processes (23, 24). A resonant infrared laser ablation system was used to analyze a cancer tissue sample *ex vivo* and human finger skin *in vivo* (24). To date, the iKnife has been the most successful MS based technique demonstrated for *in vivo*, intraoperative diagnosis (21, 22). Yet, the electrocauterization process used by the iKnife is necessary for ion generation for MS analysis, resulting in thermal and mechanical damage of the analyzed tissue. Further, surgical modalities other than electrocauterization are used in oncologic surgeries, such as ultrasonic surgical aspiration, cold knife and mechanical stapled excisions, and laser surgery. Different from laser and electrocauterization approaches, an advantage of the proposed water-based MasSpec Pen technology is its nondestructive nature, which allows diagnosis of cancerous tissues without damage to normal tissues. Because the MasSpec Pen performs molecular diagnosis independently of any dissection tools, it has the potential to be used in many surgical modalities. Intraoperatively, we envision the MasSpec Pen to be used in conjunction with a surgical resection tool, depending on the oncologic surgery and the preference of the medical professional. Because surgeons routinely exchange handheld surgical instruments during surgery, with assistance from surgical technologists,

we expect the MasSpec Pen to be adapted into routine surgical workflows. Clinically, the MasSpec Pen could be suitable for pre- and postsurgical procedures that require diagnosis of *ex vivo* samples (fresh tissues, tissue sections, or biopsies) commonly examined by pathologists.

Our results show that the molecular information obtained using the MasSpec Pen is diagnostic of disease and can be used for rapid tissue classification, cancer diagnosis, and subtyping. We tested the MasSpec Pen using 253 patient tissue samples including the normal and tumorous breast, ovary, lung, and thyroid tissues. The mass spectra presented rich molecular profiles characterized by a variety of potential cancer biomarkers. The statistical classifiers built using machine learning algorithms and the histologically validated molecular information provided an overall sensitivity of 96.4%, specificity of 96.2%, and accuracy of 96.3% for cancer. Our classifiers allowed the identification of different histologic types of lung cancers and benign and malignant thyroid tumors when compared to normal tissue samples and correctly predicted ovarian cancer diagnosis in an independent test sample with mixed histologic features. Yet, as with any technology that relies on machine learning and statistical modeling of large data sets to provide predictive diagnosis, larger sample sets are needed to increase the training set size, improve the predictive accuracy of our classifiers including information on tumor cell concentration, and expand the histologic and molecular subtypes of neoplasms and normal tissues. Rigorous validation studies of the statistical results using large independent held-out test sets are necessary to determine possible overfitting of our statistical models and to more conclusively determine the overall performance of the method.

Here, we demonstrated that the MasSpec Pen is effective for *in vivo* diagnosis of cancer regions during murine oncological surgery. The entire procedure from triggering the system to data analysis is performed under 10 s, and further improvements are

envisioned. Compared with the time necessary for intraoperative pathologic frozen section analysis of excised species (~30 min) or postoperative final pathologic evaluation (several days), the time required for the MasSpec Pen analysis could expedite surgical procedures, diagnosis, and treatment. Our results demonstrate that the molecular information obtained using a 1.5-mm sampling size allows accurate identification of cancer in marginal tumor regions of mixed histologic composition, although further validation of these results with larger independent sample sets is needed. We are currently exploring other machining methods to increase sampling resolution; however, the 1.5-mm sampling size relates well with the degree of precision achieved during surgical resection.

We envision that the MasSpec Pen will become a valuable clinical technology for near real-time *in vivo* and *ex vivo* cancer diagnosis. Emerging technologies including fluorescence-guided surgery (11), Raman spectroscopy (12), optical coherence tomography (37), reflectance spectroscopy (38), and stimulated Raman scattering microscopy (13) have been proposed for cancer diagnosis and surgical guidance. Although powerful, many of these methods rely on injection of exogenous labels that target specific cell types for tumor visualization, require tissue excision and processing for analysis, suffer from moderate tissue specificity, or provide limited biochemical information. The approach we propose here leverages on the unparalleled sensitivity and specificity provided by MS for untargeted molecular evaluation and on its biocompatibility for disease diagnosis and clinical use. Yet, many challenges exist in translating and integrating new technologies into the workflow of a complex surgical and clinical environment (39). Integration of the MasSpecPen into laparoscopic and robotic surgical systems for minimally invasive procedures and improved communication and visualization tools will facilitate its inclusion in clinical workflows. Similarly, size- and cost-effective mass spectrometers with sufficient analytical performance for molecular evaluation are needed

for dedicated surgical use. Advances in building and validating databases for tissue identification, as well as automated computational methods for real time output of predictive results, are also necessary for broad use. Further work will require careful evaluation of the long-term benefits to patients to determine the value of new technologies in clinical practice. We expect that the excellent performance and simple design and operation of the MasSpec Pen, combined with its clinically desirable features, may enable its translation to the clinic for routine medical use, improving patient care and treatment.

REFERENCES

1. Buchholz TA, Somerfield MR, Griggs JJ, El-Eid S, Hammond ME, Lyman GH, et al. Margins for breast-conserving surgery with whole-breast irradiation in stage I and II invasive breast cancer: American Society of Clinical Oncology endorsement of the Society of Surgical Oncology/American Society for Radiation Oncology consensus guideline. J Clin Oncol 2014;32:1502-6
2. Maygarden SJ, Detterbeck FC, Funkhouser WK. Bronchial margins in lung cancer resection specimens: utility of frozen section and gross evaluation. Mod Pathol 2004;17:1080-6
3. Massard G, Doddoli C, Gasser B, Ducrocq X, Kessler R, Schumacher C, et al. Prognostic implications of a positive bronchial resection margin. Eur J Cardiothorac Surg 2000;17:557-65
4. Nick AM, Coleman RL, Ramirez PT, Sood AK. A framework for a personalized surgical approach to ovarian cancer. Nat Rev Clin Oncol 2015;12:239-U78
5. Han SS, Jang JY, Kim SW, Kim WH, Lee KU, Park YH. Analysis of long-term survivors after surgical resection for pancreatic cancer. Pancreas 2006;32:271-5
6. Zhang M, Li Z, Ma Y, Zhu G, Zhang H, Xue Y. Prognostic predictors of patients with carcinoma of the gastric cardia. Hepatogastroenterology 2012;59:930-3
7. Sanai N, Berger MS. Glioma extent of resection and its impact on patient outcome. Neurosurgery 2008;62:753-64; discussion 264-6
8. Macario A. What does one minute of operating room time cost? J Clin Anesth 2010;22:233-6
9. Mino-Kenudson M, Chirieac LR, Law K, Hornick JL, Lindeman N, Mark EJ, et al. A Novel, Highly Sensitive Antibody Allows for the Routine Detection of ALK-Rearranged Lung Adenocarcinomas by Standard Immunohistochemistry. Clin Cancer Res 2010;16:1561-71
10. Jones S. Personalized genomic analyses for cancer mutation discovery and interpretation. Science Translational Medicine 2015;7
11. Stummer W, Pichlmeier U, Meinel T, Wiestler OD, Zanella F, Hans-Jurgen R, et al. Fluorescence-guided surgery with 5-aminolevulinic acid for resection of malignant glioma: a randomised controlled multicentre phase III trial. Lancet Oncol 2006;7:392-401
12. Jermyn M, Mok K, Mercier J, Desroches J, Pichette J, Saint-Arnaud K, et al. Intraoperative brain cancer detection with Raman spectroscopy in humans. Science Translational Medicine 2015;7

13. Orringer DA, Pandian B, Niknafs YS, Hollon TC, Boyle J, Lewis S, et al. Rapid intraoperative histology of unprocessed surgical specimens via fibre-laser-based stimulated Raman scattering microscopy. Nat Biomed Eng 2017;1

14. Chughtai K, Heeren RMA. Mass Spectrometric Imaging for Biomedical Tissue Analysis. Chem Rev 2010;110:3237-77

15. Hsu CC, Dorrestein PC. Visualizing life with ambient mass spectrometry. Current Opinion in Biotechnology 2015;31:24-34

16. Wu CP, Dill AL, Eberlin LS, Cooks RG, Ifa DR. Mass spectrometry imaging under ambient conditions. Mass Spectrom Rev 2013;32:218-43

17. Norris JL, Caprioli RM. Analysis of Tissue Specimens by Matrix-Assisted Laser Desorption/Ionization Imaging Mass Spectrometry in Biological and Clinical Research. Chem Rev 2013;113:2309-42

18. Ifa DR, Eberlin LS. Ambient Ionization Mass Spectrometry for Cancer Diagnosis and Surgical Margin Evaluation. Clin Chem 2016;62:111-23

19. Eberlin LS, Norton I, Orringer D, Dunn IF, Liu XH, Ide JL, et al. Ambient mass spectrometry for the intraoperative molecular diagnosis of human brain tumors. P Natl Acad Sci USA 2013;110:1611-6

20. Jarmusch AK, Pirro V, Baird Z, Hattab EM, Cohen-Gadol AA, Cooks RG. Lipid and metabolite profiles of human brain tumors by desorption electrospray ionization-MS. P Natl Acad Sci USA 2016;113:1486-91

21. Schafer KC, Denes J, Albrecht K, Szaniszlo T, Balog J, Skoumal R, et al. In Vivo, In Situ Tissue Analysis Using Rapid Evaporative Ionization Mass Spectrometry. Angew Chem Int Edit 2009;48:8240-2

22. Balog J, Sasi-Szabo L, Kinross J, Lewis MR, Muirhead LJ, Veselkov K, et al. Intraoperative Tissue Identification Using Rapid Evaporative Ionization Mass Spectrometry. Science Translational Medicine 2013;5

23. Schafer KC, Szaniszlo T, Gunther S, Balog J, Denes J, Keseru M, et al. In Situ, Real-Time Identification of Biological Tissues by Ultraviolet and Infrared Laser Desorption Ionization Mass Spectrometry. Anal Chem 2011;83:1632-40

24. Fatou B, Saudemont P, Leblanc E, Vinatier D, Mesdag V, Wisztorski M, et al. In vivo Real-Time Mass Spectrometry for Guided Surgery Application. Sci Rep 2016;6:25919

25. Tibshirani R. Regression shrinkage and selection via the Lasso. J Roy Stat Soc B Met 1996;58:267-88

26. Calligaris D, Caragacianu D, Liu X, Norton I, Thompson CJ, Richardson AL, et al. Application of desorption electrospray ionization mass spectrometry imaging in breast cancer margin analysis. Proc Natl Acad Sci U S A 2014;111:15184-9

27. Guenther S, Muirhead LJ, Speller AV, Golf O, Strittmatter N, Ramakrishnan R, et al. Spatially resolved metabolic phenotyping of breast cancer by desorption electrospray ionization mass spectrometry. Cancer Res 2015;75:1828-37

28. Kang HS, Lee SC, Park YS, Jeon YE, Lee JH, Jung SY, et al. Protein and lipid MALDI profiles classify breast cancers according to the intrinsic subtype. Bmc Cancer 2011;11

29. Sans M, Gharpure K, Tibshirani R, Zhang J, Liang L, Liu J, et al. Metabolic Markers and Statistical Prediction of Serous Ovarian Cancer Aggressiveness by Ambient Ionization Mass Spectrometry Imaging. Cancer Res 2017;77:2903-13

30. Kertesz V, Van Berkel GJ. Fully automated liquid extraction-based surface sampling and ionization using a chip-based robotic nanoelectrospray platform. J Mass Spectrom 2010;45:252-60

31. Kertesz V, Ford MJ, Van Berkel GJ. Automation of a surface sampling probe/electrospray mass spectrometry system. Anal Chem 2005;77:7183-9

32. Laskin J, Heath BS, Roach PJ, Cazares L, Semmes OJ. Tissue imaging using nanospray desorption electrospray ionization mass spectrometry. Anal Chem 2012;84:141-8

33. Pagnotti VS, Chubatyi ND, McEwen CN. Solvent assisted inlet ionization: an ultrasensitive new liquid introduction ionization method for mass spectrometry. Anal Chem 2011;83:3981-5

34. Helmus MN, Gibbons DF, Cebon D. Biocompatibility: Meeting a Key Functional Requirement of Next- Generation Medical Devices. Toxicol Pathol 2008;36:70-80

35. Mokkaphan J, Banlunara W, Palaga T, Sombuntham P, Wanichwecharungruang S. Silicone Surface with Drug Nanodepots for Medical Devices. Acs Appl Mater Inter 2014;6:20188-96

36. Chen CH, Lin ZQ, Garimella S, Zheng LX, Shi RY, Cooks RG, et al. Development of a Mass Spectrometry Sampling Probe for Chemical Analysis in Surgical and Endoscopic Procedures. Anal Chem 2013;85:11843-50

37. Kut C, Chaichana KL, Xi JF, Raza SM, Ye XB, McVeigh ER, et al. Detection of human brain cancer infiltration ex vivo and in vivo using quantitative optical coherence tomography. Science Translational Medicine 2015;7

38. Rajaram N, Aramil TJ, Lee K, Reichenberg JS, Nguyen TH, Tunnell JW. Design and validation of a clinical instrument for spectral diagnosis of cutaneous malignancy. Appl Optics 2010;49:142-52

39. Zhang JL, Yu WD, Suliburk J, Eberlin LS. Will Ambient Ionization Mass Spectrometry Become an Integral Technology in the Operating Room of the Future? Clin Chem 2016;62:1172-4

Chapter 6. Performance of the MasSpec Pen for Rapid Diagnosis of Ovarian Cancer[6]

INTRODUCTION

Ovarian cancer is a highly lethal disease and the fifth leading cause of all cancer-related deaths in women (1, 2). Accurate diagnosis and stratification of ovarian cancer is important to develop personalized treatment approaches (3). High-grade serous carcinomas (HGSC) and low-grade serous carcinomas (LGSC) are common subtypes of ovarian cancers, with the latter accounting for just a small proportion of cases. HGSCs show aggressive features including rapid growth and invasive behavior, whereas LGSCs follow a more indolent course (4). Cytoreductive surgery in combination with chemotherapy is the primary course of treatment for HGSC and essential to maximize patient survival. However, the timing of cytoreductive surgery is of debate (5, 6). Patients likely to undergo complete resection commonly undergo surgery followed by chemotherapy, whereas patients likely to undergo incomplete resection are directed to neoadjuvant chemotherapy before surgery. In both scenarios, differentiation of tumor from normal tissue is critical to maximize cancer excision, although intraoperative identification through gross inspection can be difficult. For example, differentiation of tumor from scarring or fibrotic tissues resulting from neoadjuvant chemotherapy is challenging from metastatic sites, often requiring unnecessary resection of healthy tissue (7). Histopathologic analysis of tissue sections is commonly employed to diagnose surgical specimens, either intraoperatively

[6] Adapted from Sans M, Zhang J, Lin JQ, Feider CL, Giese N, Breen MT, et al. Performance of the MasSpec Pen for Rapid Diagnosis of Ovarian Cancer. Clin Chem 2019;65:674-83. Copyright © 2019, American Association for Clinical Chemistry. Sans M and Zhang J collected all the data presented in this manuscript. Sans M and Lin JQ performed statistical analysis. Sans M analyzed and interpreted the results, prepared all the materials, and wrote the manuscript. All authors contributed in revising the manuscript.

through frozen section analysis, or postoperatively through permanent tissue sections. Despite its relatively rapid turnaround (approximately 30 min), intraoperative frozen section evaluation results can be limited owing to freezing artifacts affecting tissue histology. Further, frozen section evaluation of multiple tissue specimens can be impractical, because numerous areas of concern are often identified during surgery. Postoperative tissue analysis is time consuming (approximately 1 week) and places the patient at additional health risks, discomfort, and anxiety (8). Thus, new technologies that allow rapid and accurate intraoperative tissue evaluation could improve diagnosis during cytoreductive surgery and the overall management of ovarian cancer patients (9, 10).

Mass spectrometry (MS) technologies have shown potential for clinical use and cancer diagnosis (11–23). Ambient ionization MS techniques are suitable for rapid and in situ analysis of biological tissues because of their operational simplicity at atmospheric pressure and minimal sample preparation requirements (24). Several ambient ionization techniques have been suggested and tested for intraoperative cancer diagnosis and surgical margin evaluation either through *ex vivo* tissue sections and tissue smears analyses (12–18), or *in vivo* (19–23). Desorption electrospray ionization-MS imaging, for example, has been applied for *ex vivo* analysis of metabolic profiles of borderline ovarian tumor, HGSC, and normal ovarian tissue sections, allowing cancer diagnosis and subtyping (25, 26). The rapid evaporative ionization MS technique was recently used for *in vivo* ovarian cancer diagnosis (27). Our team has previously described the development of a handheld device, named the MasSpec Pen, for *ex vivo* and *in vivo* nondestructive molecular analysis and diagnosis of tissues, discussed in Chapter 5 (21). In that study, we tested the MasSpec Pen for molecular evaluation and diagnosis of 253 human tissue samples (normal and cancer ovarian, lung, thyroid, and breast). For ovarian cancer (n = 29 normal and n = 28 HGSC),

a clinical sensitivity of 100%, specificity of 89.7%, and overall accuracy of 94.7% were achieved using leave-one-out cross-validation analysis.

Biocompatibility and the nondestructive nature of the MasSpec Pen analyses are clinically attractive and could facilitate translation into clinical use. Nevertheless, testing of the statistical classifiers using different sample cohorts is critical to evaluate model overfitting and validate its performance. Analysis of other histological subtypes, such as LGSC, is also desirable to evaluate potential for ovarian cancer diagnosis. Moreover, distinguishing ovarian cancer from surrounding healthy peritoneum tissue where ovarian cancer often spreads could improve surgical resection (28). Because fallopian tubes (FTs) have been proposed as the most likely site of HGSC origin, evaluation of FT tissue is also relevant (5,29). Finally, performance assessment using different mass spectrometers would demonstrate broad applicability of the technology. In particular, smaller, lower-cost, and lower-performance mass spectrometers, such as a linear ion trap (LIT), could ease technology translation into the clinical space (30–33). Yet, LIT exhibits lower mass resolving powers than orbitrap systems, which could potentially prevent accurate tissue diagnosis. To address these questions, here we evaluated the MasSpec Pen for ovarian cancer diagnosis across different sample sets, tissue types, and MS systems. Training, validation, and test sample sets were used to evaluate the predictive performance and molecular information obtained. LGSC, FT, and peritoneum samples were analyzed to explore the MasSpec Pen capabilities for cancer subtyping and differentiation from other healthy tissues in the abdominal cavity. Lastly, performance using a LIT mass analyzer was investigated to test method versatility across systems.

MATERIALS AND METHODS

Human tissue samples

In total, 160 deidentified ovarian frozen tissue samples were obtained from the Cooperative Human Tissue Network (CHTN; Table 5.1). Samples were requested by the research team and collected from different tissue banks within the CHTN network in 3 different batches, the first in the fall of 2015, the second in the fall of 2017, and the third in spring of 2018. Samples were selected following criteria based on tissue diagnosis (HGSC or LGSC) by gross anatomy and pathological evaluation, and specimen size (>200 mg). FT and peritoneum tissues (32 samples, 29 patients) were received as deidentified frozen specimens from the MD Anderson and CHTN Tissue Banks, or prospectively collected as fresh specimens during endometriosis surgery performed by MB (under approved IRB protocol#: 2017–08-0087) at the Seton Medical Center (Austin, TX; Table A5.1). Patients undergoing endometriosis surgery were consented. Information on disease severity (other than grade for ovarian cancer) and alternative diagnoses were not considered in our study. Samples were analyzed at room temperature in random order. The analyzed area of the tissue was demarcated and registered through optical images. The same demarcated tissue or a parallel piece was frozen and sectioned at 10–16 µm using a CryoStar NX50 cryostat (Thermo Fisher Scientific), stained by standard hematoxylin and eosin procedure, and evaluated by expert pathologists (not blinded from previous clinical information) to confirm diagnosis of the analyzed area. Of note, the final diagnoses were performed after MasSpec Pen analyses (Figure 6.1). Only samples with clear diagnosis (n = 164) were used for statistical analysis (see Figure A5.1).

Table 6.1: Patient demographic information.

Ovarian tissue samples were obtained from the CHTN Tissue Bank under approved IRB protocol. Samples were acquired as three independent sample sets (set 1 (n=57), set 2 (n=39), set 3 (n=64)).

Parameter	**Normal**	**High-grade SC**	**Low-Grade SC**
Sample Set 1			
Number of Patients (N)	29	28	-
Median Age, Years	50	62	-
Age Range, Years	(31,80)	(30,83)	-
Number of Patients by Race (White, Black, Asian, Hispanic, Unknown)	(22, 7, 0, 0, 0)	(25,2,0,0,1)	-
Sample Set 2			
Number of Patients (N)	14	11	14
Median Age, Years	57	61	57.5
Age Range, Years	(34,82)	(47,76)	(18,82)
Number of Patients by Race (White, Black, Asian, Hispanic, Unknown)	(10,3,1,0,0)	(6,1,0,0,4)	(14,0,0,0,0)
Sample Set 3			
Number of Patients (N)	35	29	-
Median Age, Years	53	65	-
Age Range, Years	(23,86)	(44,85)	-
Number of Patients by Race (White, Black, Asian, Hispanic, Unknown)	(22, 11, 0, 1, 1)	(24,2,1,0,2)	-

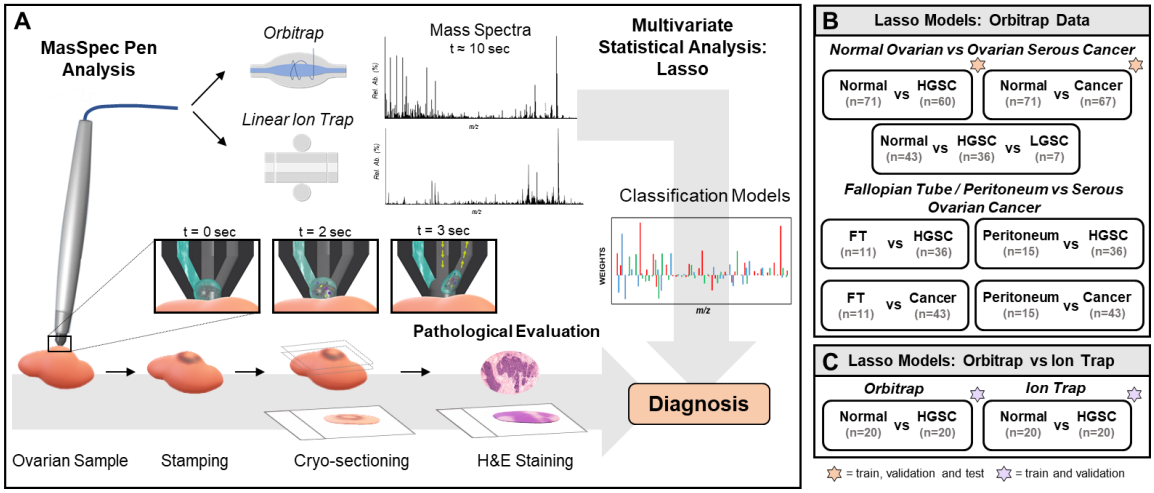

Figure 6.1: Tissue samples were analyzed with the MasSpec Pen using a discrete water droplet to extract molecular information after 3 seconds of contact time.

Mass spectra were obtained using an orbitrap and a linear ion trap mass analyzer. For pathological evaluation, tissue samples were stamped post-analysis, frozen, sectioned and hematoxylin and eosin (H&E) stained.

MasSpec Pen analysis

The MasSpec Pen with a 2.7-mm pen tip diameter was used for analysis, using the same procedures and system previously described in Chapter 5 of this dissertation (21). The MasSpec Pen uses a water droplet to extract molecules from tissues upon contact, which are then analyzed by an orbitrap mass spectrometer and statistical classifiers, resulting in a total analysis time of approximately 10 s. A new MasSpec Pen device was used for each of the tissue analyses described in this study to prevent any potential carryover between samples. Experiments were performed on a Q Exactive Orbitrap and an LTQ mass spectrometer (Thermo Fisher Scientific). Orbitrap analyses were performed from *m/z* 120–1800 at a resolving power of 140000 at *m/z* 200. Ion trap analysis analyses were performed from *m/z* 120 to 1000, at a capillary temperature of 350°C, and tube lens and capillary voltages of -110 V and -35 V, respectively. Note that while orbitrap

experiments were performed from *m/z* 120-1800, ion trap measurements were restricted to *m/z* 120-1000 due to the presence of background ions at higher mass ranges (*m/z* >1000). The *m/z* restriction was unavoidable, as the interfering ions are constantly observed in the mass spectra at *m/z* >1000 of the specific ion trap mass spectrometer that was available and used for this study. Tandem MS of selected ions was performed during MasSpec Pen analyses using high-energy collisional dissociation in the Q Exactive. Of note, the MasSpec Pen orbitrap analysis of sample set 1 (n = 57) and the resulting data were previously described (21), whereas all the remaining samples and analyses were new to this study.

Statistical analysis

Three mass spectra were averaged for each sample. The orbitrap and ion trap data were binned to *m/z* 0.01 and *m/z* 1, respectively, and normalized to the median absolute intensity. Note that other normalization methods, including normalizing by the total ion count and the ion count at *m/z* 885.551, were tested in this study, with median normalization providing the best performance. Background peaks and others not appearing in at least 10% of the samples analyzed were excluded. The Lasso method was applied to the preprocessed data using the glmnet package in the CRAN R language library (34). Five unique molecular models were built to differentiate between the tissue types from training sets of samples, by assigning mathematical weights to each statistically informative feature depending on its importance in characterizing a certain class. For HGSC and ovarian cancer prediction, data from sample sets 1 and 2 were randomly split between training and validation sets. Predictive accuracy within the training set was assessed by leave one-out CV. Those models were then used to predict on the validation set as well as on an independent test set (set 3) of samples. Classification performance was measured by sensitivity, specificity and accuracy. The "pROC" R package was used to select an optimal

threshold from the ROC curve (35). Cosine similarity analysis was performed in the CRAN R language using average mass spectra for each tissue type analyzed in each sample set.

RESULTS

MasSpec Pen analysis of ovarian tissue samples using an orbitrap mass analyzer

In our previous study described in Chapter 5, we analyzed a sample set including normal ovarian and HGSC tissue using the MasSpec Pen coupled to an orbitrap mass spectrometer (21). Here, 2 additional sample sets were obtained and analyzed using the same approach (Table 6.1). Figure 6.2 shows representative MasSpec Pen mass spectra from the 3 different tissue types from the second sample set. A variety of small metabolites, such as glutamate (*m/z* 146.045), ascorbate (*m/z* 175.025), and glutathione (*m/z* 306.077), as well as complex glyocerophospholipid (GP) species, such as glycerophosphoethanolamine (PE) P-18:0 20:4 (*m/z* 750.546), glycerophosphoserine (PS) 18:0 18:1 (*m/z* 788.546), and glycerophosphoinositol (PI) 18:0 20:4 (*m/z* 885.551), were detected. Identification and corresponding mass errors are provided in Table A5.2for species tentatively assigned using high mass accuracy and tandem MS/MS measurements. Representative MasSpec Pen MS/MS spectra of ovarian tissue samples are shown in Figure A5.2. The molecular profiles obtained from normal and HGSC from the second and the third sample sets presented similar trends to those previously observed from tissues analyzed in the first sample set (see Figure A5.3). In particular, mass spectra from normal ovarian tissue were characterized by high relative abundance of ascorbate and other small metabolites, whereas GP species appeared at higher relative abundances in the mass spectra from HGSC tissues (Figure 6.2). The mass spectra obtained from LGSC also presented a rich variety of GP species at higher relative abundances than in the mass spectra from normal tissues. Further, when comparing LGSC to HGSC, qualitative changes in the

relative abundances were observed between the mass spectra of the 2 cancer subtypes (Figure 6.2). For example, higher relative abundances of plasmalogen PE species, such as *m/z* 722.514 and *m/z* 750.546, were observed in the mass spectra from LGSC, whereas glutamate and glycerophosphatidic acid (PA) 18:0 18:1 (*m/z* 701.514) were at higher relative abundances in HGSC tissue. Cosine analysis was performed to evaluate the similarity in the mass spectra between the 3 sample sets for the same tissue class. Note that cosine analysis provided similarity values ranging from 0 (dissimilar) to 1 (identical). Similarity values of 0.76 ± 0.06 and 0.80 ± 0.06 were achieved from HGSC and normal data, respectively, showing data comparability between the 3 sample sets for the same tissue type.

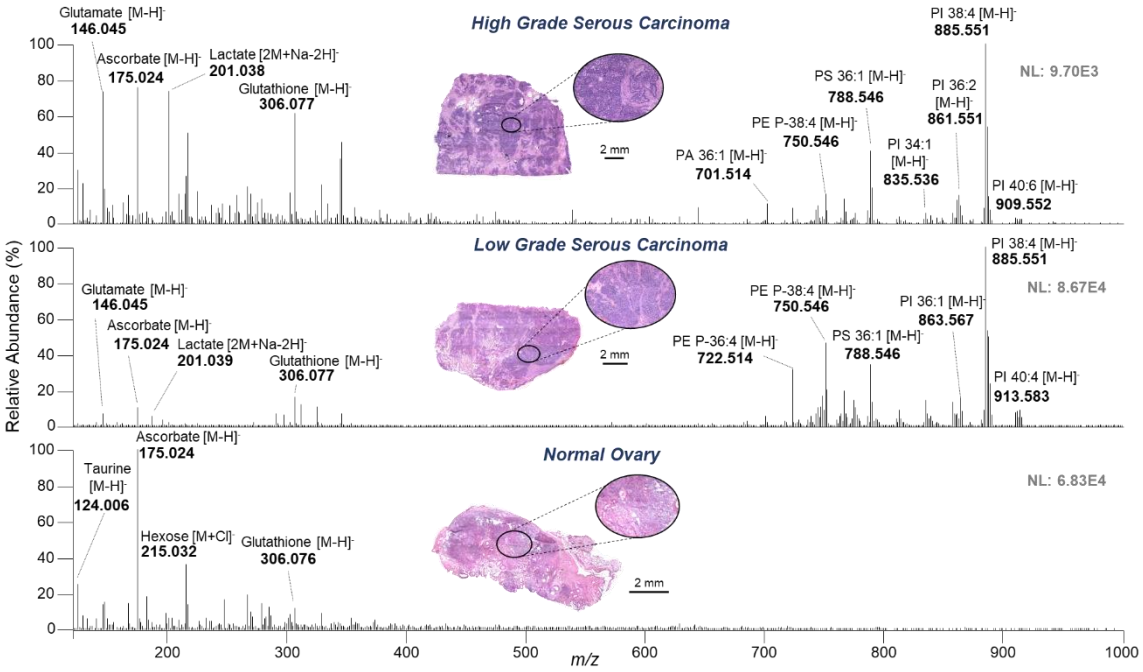

Figure 6.2: Representative MasSpec Pen mass spectra of high-grade serous carcinoma (top), low-grade serous carcinoma (middle, background subtracted) and normal ovarian tissue (bottom) obtained with an orbitrap mass analyzer.

Optical image of the stained parallel tissue section analyzed is provided. Tentative identifications are shown for selected ions. X:Y represents number of carbon atoms double bonds in the fatty acid chains.

Statistical prediction of ovarian cancer using training, validation, and test sample sets

Next, we evaluated if the molecular information obtained from MasSpec Pen analysis using the orbitrap mass spectrometer was predictive of normal, LGSC, and HGSC across different sample sets. In our previous study (21), a classifier for HGSC diagnosis was built from a sample set 1, a single sample batch, and evaluated using leave-one out cross-validation only. Here, the histologically validated mass spectra obtained from the second set of samples were combined with the first sample set data to improve and validate the statistical classifiers (n = 43 normal, n = 36 HGSC). First, the combined data set was

randomly split into a training set (n = 32 normal, n = 28 HGSC) to build the statistical model, and a validation set (n = 11 normal, n = 8 HGSC) to evaluate performance and test for possible overfitting. Using the training set, 100% clinical sensitivity, 96.8% clinical specificity, and 98.3% accuracy was achieved, which are an improvement over previously published results of 100% clinical sensitivity, 89.7% specificity, and 94.7% overall accuracy. In the validation set, 100% clinical sensitivity, specificity, and accuracy were obtained (Figure 6.3). Using our previous model (built on sample set 1 alone) to predict on sample set 2, we achieved 100% clinical sensitivity, 75% specificity, and 90.9% overall accuracy (Table A5.3), which was an overall lower performance than what we achieved by including samples from different batches in the training sample set. Note that tissue samples were grouped based on tissue type and, as such, the effect of sample source (or tissue bank) on method performance was not evaluated.

Next, a statistical classifier to discriminate between normal and serous cancer (SC) samples was also built by combining the HGSC and LGSC samples into a single class (n = 43 normal, n = 43 cancer). Similarly, the model exhibited high performance in both training (93.9% clinical sensitivity, 96.9% specificity, and 95.4% accuracy) and validation sample sets (100% clinical sensitivity, 90% specificity, and 95.0% accuracy). To further test the performance of the statistical models (HGSC vs normal and SC vs normal), prediction was performed on the third sample set (Figure 6.3). Results are reported for samples of clear diagnosis by pathology (n = 28 normal, n = 24 HGSC), corresponding to 91.7% clinical sensitivity, 92.9% specificity, and 92.3% overall accuracy, with 4 out of 52 samples misclassified.

A 3-class statistical model was also created to differentiate between normal ovarian, HGSC, and LGSC tissues. Because of the limited LGSC sample size (n = 7), the model was built using cross-validation on the entire data set. Despite the introduction of the new

LGSC subtype, all HGSC and normal ovarian samples were correctly classified (n = 79, 100% accuracy). For LGSC classification, an accuracy of 71.4% was achieved, with 2 out of the 7 samples misclassified as HGSC. Collectively, the 3-class model showed strong overall performance for cancer diagnosis, resulting in an overall accuracy of 97.7%. A summary of all results, including confusion matrices, classification performance, and number of metabolic species included in the models are provided in Tables A5.3 and A5.4

Among the species selected to generate the statistical models, ascorbate (*m/z* 175.024) and taurine (*m/z* 124.006) were selected as important for the discrimination of normal tissue, and lactate (*m*/z 201.038), glutathione (*m/z* 306.077), and the PI 18:0 20:4 (*m/z* 885.551) were characteristic of HGSC and the combined cancer class. For the 3-class model, PE P-18:0 20:4 at *m/z* 750.546 was given a positive weight for the characterization of LGSC, in agreement with the trends in relative abundances observed in the representative mass spectra shown in Figure 6.2. Gluconate (*m/z* 195.051) and glutamate (*m/z* 146.046) were also selected as important for discrimination of LGSC and HGSC samples.

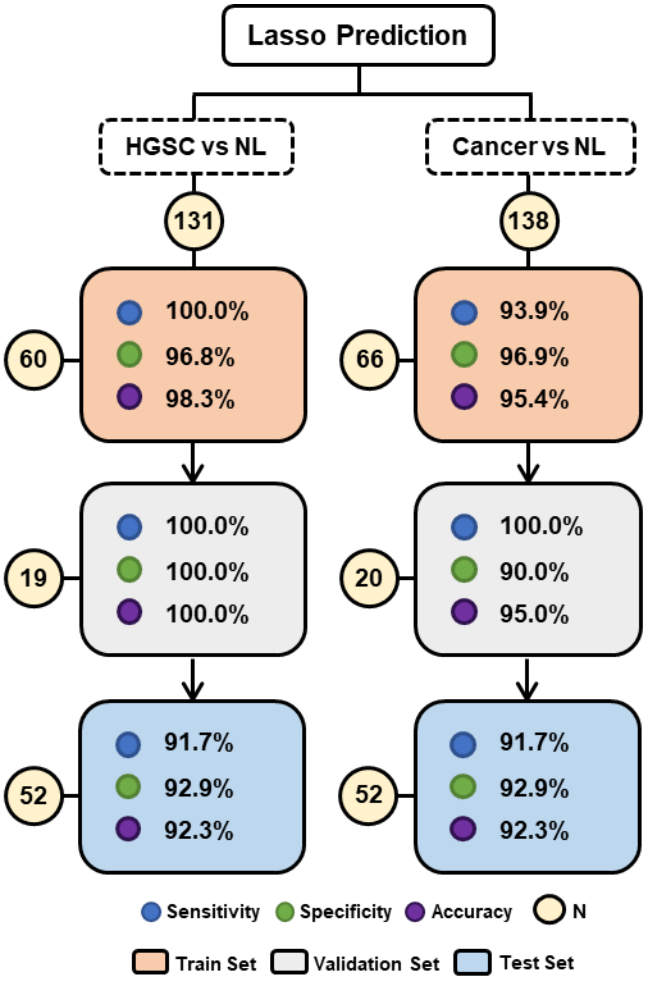

Figure 6.3: Lasso classification performance for ovarian cancer prediction based on MasSpec Pen data for the training, validation and test sets.

Results are shown in terms of sensitivity, specificity and overall accuracy. Confusion matrices with per patient prediction are shown in Table A5.3.

Distinguishing ovarian cancer from healthy FT and peritoneum tissue

FT (n = 15) and peritoneum (n = 17) tissue samples were also analyzed with the MasSpec Pen and compared to ovarian cancer tissues. Mass spectra obtained from peritoneum tissue were commonly characterized by fatty acid (FA) species, detected both

as monomers, such as FA 18:1 (*m/z* 281.247), and dimers, such as FA 18:0 –16:0 (*m/z* 537.487). Chlorinated triacylglyceride (TG) species were also detected at higher mass range, such as TG 52:3 (*m/z* 891.720), reflecting on the fat content characteristic of peritoneal and omental tissues. High abundance of complex lipids, such as PI, PE, and PS species, were observed from the lipid and metabolite profiles obtained from FT samples (Figure 6.4A). A list of tentatively identified species with mass errors is provided in Table A5.5.

Molecular models to discriminate peritoneum and FT tissue from ovarian cancer samples from batch 1 and 2 were built by leave-one-out cross-validation analysis (Figure 6.4B). A detailed summary of all classification results, including the number of metabolic species included in the models, is provided in Table A5.6. All peritoneum (n = 15) and FT (n = 11) samples were correctly classified when compared to HGSC and ovarian SC samples (100% clinical specificity). Clinical sensitivity values of 88.9% and 90.7% were achieved for HGSC (n = 36) and SC overall (n = 43) vs FT samples, respectively. When compared to peritoneum samples, lower clinical sensitivities were achieved for HG (80.0%) and SC (83.7%). Interestingly, many of the features selected by the models to characterize HGSC and ovarian SC tissue from FT and peritoneum tissue were similar to those used for discrimination against normal ovarian tissue, such as lactate, glutamate, or PI 38:4. Yet, ascorbate was given a positive weight for ovarian cancer classification. Hexose (*m/z* 215.031) was selected as predictive of both FT and peritoneum samples, whereas a species at *m/z* 267.073, tentatively identified as inosine, a purine nucleoside, was only associated to FT tissue.

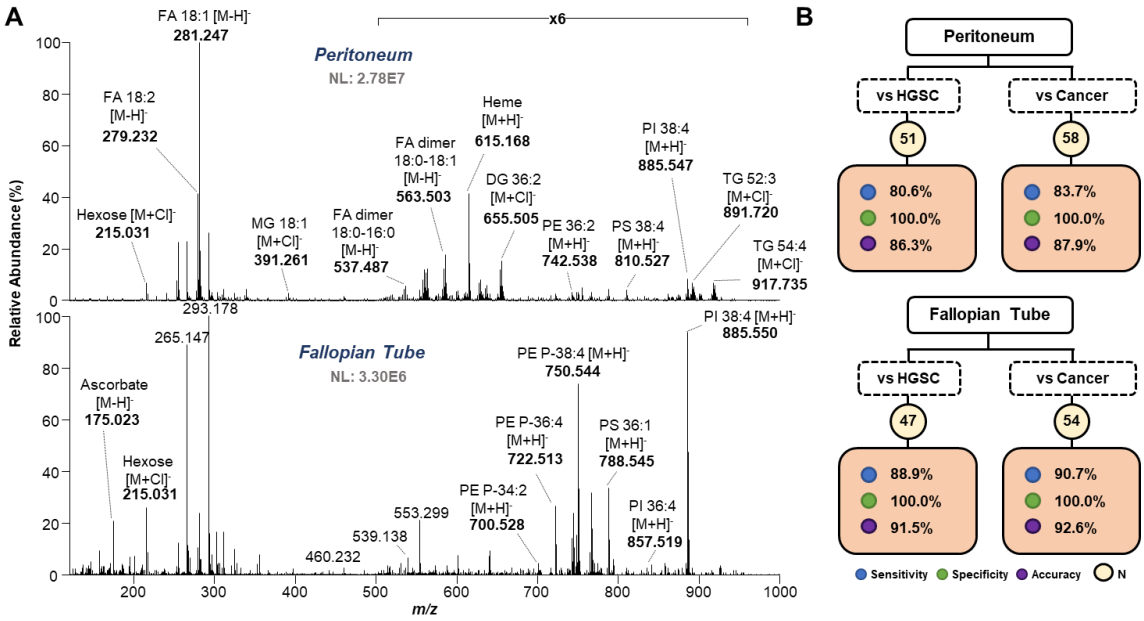

Figure 6.4: Differentiating ovarian cancer tissue from healthy peritoneum and fallopian tube tissue samples.

Representative mass spectra profile obtained from MasSpec Pen analysis of peritoneum (top) and fallopian tube (bottom) tissue. Tentative identifications are shown for selective ions (A). Lasso results for peritoneum (top) and fallopian tube (bottom) vs HGSC and cancer tissue differentiation (B).

Validation of the MasSpec Pen using and ion trap mass analyzer

The MasSpec Pen was coupled to a LIT and used to evaluate a subset of HGSC and normal ovarian samples (n = 20 normal, 20 HGSC). Note that the LIT provides lower performance for mass analysis with limited resolving power (1600 at *m/z* 885.7) and mass accuracy when compared to the resolving power (72000 at *m/z* 885.547) and mass accuracy (< 5 ppm) achieved with orbitrap mass analyzers. Figure 6.5A shows that the mass spectra obtained for the same HGSC sample analyzed by both systems are highly comparable, although a higher number of resolved lipid species were detected by orbitrap analysis, as anticipated. Distinctive metabolic profiles for HGSC and normal ovarian samples were obtained by MasSpec Pen and LIT analysis (Figure A5.4). Similar to the orbitrap data,

HGSC mass spectra were characterized by the high relative abundance of GP species, whereas normal samples displayed considerably lower lipid abundance and higher relative abundances of small metabolites.

Statistical classifiers were built to evaluate the predictive performance for HGSC diagnosis based on LIT data. The data was randomly split into a training (n = 30) and validation sets (n = 10), yielding excellent classification performance, with 100% clinical sensitivity, specificity, and accuracy in both sets (Figure 6.5B). For adequate comparison, a new model was built using orbitrap data from the same set of samples analyzed using the LIT (n = 40). High specificity was achieved in both the training (93.3%) and validation sets (100%) by the new orbitrap model, whereas lower clinical sensitivity was observed for the training (86.7%) and validation (80.0%) sets, respectively, with 3 HGSC samples misclassified as normal. Note that these 3 samples had been correctly classified by the model built using orbitrap data acquired from the larger training set (n = 60). A detailed comparison of the results obtained for the orbitrap and ion trap models is provided in Table A5.7.

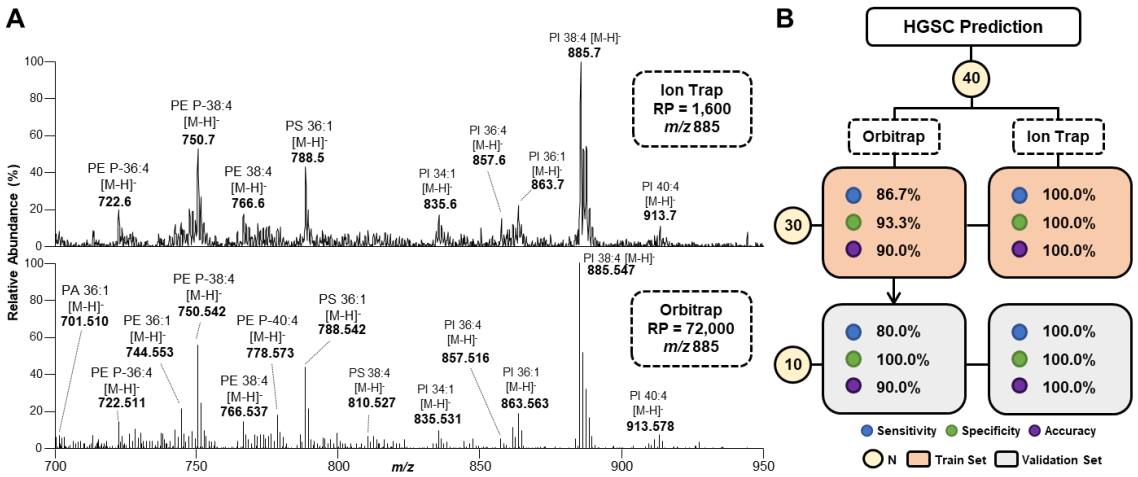

Figure 6.5: Representative mass spectra profile obtained from the same HGSC sample by ion trap (top, profile mode) and orbitrap (bottom, centroid mode) analysis. Tentative identifications are shown for selected ions (A). Lasso results for HGSC prediction comparing performance between the models built from orbitrap and ion trap data acquired from the same sample set (n=40) (B).

DISCUSSION

Validation of the diagnostic capabilities of the MasSpec Pen is paramount for potential clinical translation. Utilizing a cohort of 138 histologically validated ovarian cancer and normal tissue samples, we demonstrate here the predictive power of the statistical models built from MasSpec Pen analyses. Machine learning and classification algorithms are not parametrically constrained and thus are more susceptible to overfitting than other more traditional methods (36). Overfitting occurs when a model uses spurious correlations within a single data set rather than relationships within the population. Here, statistical validation and evaluation of model overfitting were performed using training (to fit the model), validation (to provide an unbiased evaluation while tuning parameters such as data normalization methods), and test (to provide an unbiased evaluation of a final model) sets of samples. Improved performance was achieved for HGSC diagnosis using a

new training set that combines samples from different batches, compared to what we have previously reported using a single sample batch (21). These results show that including samples from different batches in the training set helps improve the predictive power of the classifiers. High prediction accuracies were also observed in both the validation and test sets, indicating that the model was not overfitting to the training set. Similar results were obtained for the normal vs SC classifier, demonstrating that the MasSpec Pen and machine learning provide robust predictive models for ovarian cancer diagnosis.

Discrimination between LGSC and HGSC tissue was also explored. Owing to the lower clinical occurrence of LGSC, sample availability was limited. Nevertheless, trends in lipid and metabolite composition between the 2 cancer types were and reflected by the moderate classification accuracy achieved. Collection of additional LGSC tissues is ongoing to continue MasSpec Pen validation for ovarian cancer subtyping. Four molecular models were also built to discriminate HGSC and SC from healthy FT and peritoneum samples, yielding 100% clinical specificity and sensitivity from 80.6% to 90.7% for cancer diagnosis. Assessment of the mass spectra from the cancer samples misclassified as FT revealed unusually high abundance of *m/z* 215.031, weighted toward FT classification, and an overall low lipid abundance in samples misclassified as peritoneum. Interestingly, 3 out of the 7 cancer tissues misclassified as peritoneum were obtained from ovarian cancer metastasis to the omentum. Segregation of primary or metastatic samples will be evaluated to investigate differences in molecular information that may be correlated to misclassification, as well as refinement of the statistical models. Nonetheless, the overall accuracies (>86%) achieved demonstrate the MasSpec Pen potential to differentiate SC from surrounding normal ovarian and abdominal healthy tissues.

The features chosen by the lasso models as predictive for ovarian cancer diagnosis and subtyping were identified as biologically relevant species. For example, ascorbic acid,

which has an important role in normal ovarian functions (37), was selected as important for normal ovarian tissue characterization, whereas GP lipids, such as PI 18:0 20:4, were at high relative abundance in cancer tissue and selected as predictive markers. Gluconate and glutamate were selected as important for the discrimination of LGSC and HGSC samples. Similar trends and species have also been reported using desorption electrospray ionization MS (26). Moreover, increased abundance of glutamate has been reported previously in invasive ovarian carcinomas compared to borderline tumors by gas chromatography and MS analyses (38). Another interesting feature selected was inosine at *m/z* 267.073, which was associated with FT tissue. Inosine is rapidly metabolized from adenosine, a nucleoside known to modulate neurotransmission and contractile responses in the FTs (39) and has been previously detected in oviduct cells (40).

Smaller and lower-cost equipment could facilitate translation of MS technologies to the clinic (30). LIT mass spectrometers are attractive for clinical use due to their scalability, tolerance for higher operating pressure, and lower cost (31). However, LIT analyzers provide limited mass resolution, which could potentially compromise performance. To demonstrate that the MasSpec Pen can be compatible with a mass spectrometer platform other than an orbitrap, and to further investigate how classification performance is affected by collecting data with lower performance mass analyzers, we coupled the MasSpec Pen to a LIT system. Using a smaller sample set than what collectively explored for orbitrap analysis, we achieved 100% accuracy for HGSC classification in training and validation. The higher performance achieved compared to the orbitrap data could be related to the absence of batch effects in the LIT data and will be further investigated. Overall, similarities between the detected metabolic profiles and statistical models observed between orbitrap and LIT data support the validity and robustness of the predictive molecular species and further support that the MasSpec Pen

provides consistent molecular analysis across MS systems. More testing of the LIT and other mass spectrometers is needed across multiple sample sets and cancer subtypes.

In conclusion, our study demonstrates high performance and versatility of the MasSpec Pen technology and statistical models across different sample sets and MS platforms, as well as feasibility for cancer subtyping. The MasSpec Pen leverages on its nondestructive nature for direct and gentle analysis of tissues and the sensitivity, specificity, and speed provided by MS for untargeted and accurate molecular diagnosis. Further, its simple design, ease of operation, and biocompatibility are attractive for clinical use. Thus, we envision the MasSpec Pen to be employed in the operating room (OR) for *in vivo* and/or *ex vivo* use in conjunction with standard surgical tools. Yet, this study represents a first step toward validating the performance of the MasSpec Pen for ovarian cancer diagnosis. Several challenges still need to be addressed and further validation pursued to demonstrate the usefulness of the MasSpec Pen in its envisioned application in the OR. Although our experiments performed on *ex vivo* tissues obtained from tissue banks yield diagnostic molecular results, *in vivo* and freshly excised tissues in the OR may present slightly different molecular profiles. Moreover, extensive analyses of benign ovarian disease and tissues with varied histologic composition are needed to further demonstrate its value in more complex surgical pathology cases. As such, *in vivo* OR experiments utilizing the MasSpec Pen for ovarian cancer diagnosis are currently planned to further evaluate its diagnostic capabilities. Performance evaluation across different institutions, instrumentation, and users are also envisioned to further validate our results and evaluate its usefulness in patient care.

REFERENCES

1. Torre LA, Trabert B, DeSantis CE, Miller KD, Samimi G, Runowicz CD, et al. Ovarian cancer statistics, 2018. CA Cancer J Clin 2018;68:284 –96.
2. Siegel RL, Miller KD, Jemal A. Cancer statistics, 2018. CA Cancer J Clin 2018;68:7–30.
3. Leong HS, Galletta L, Etemadmoghadam D, George J, Kobel M, Ramus SJ, et al. Efficient molecular subtype classification of high-grade serous ovarian cancer. J Pathol 2015;236:272–7.
4. Vang R, Shih IM, Kurman RJ. Ovarian low-grade and high-grade serous carcinoma pathogenesis, clinicopathologic and molecular biologic features, and diagnostic problems. Adv Anat Pathol 2009;16:267– 82.
5. Coleman RL, Monk BJ, Sood AK, Herzog TJ. Latest research and treatment of advanced-stage epithelial ovarian cancer. Nat Rev Clin Oncol 2013;10:211–24.
6. Williams TI, Toups KL, Saggese DA, Kalli KR, Cliby WA, Muddiman DC. Epithelial ovarian cancer: disease etiology, treatment, detection, and investigational gene, metabolite, and protein biomarkers. J Proteome Res 2007;6:2936 – 62.
7. Nick AM, Coleman RL, Ramirez PT, Sood AK. A framework for a personalized surgical approach to ovarian cancer. Nat Rev Clin Oncol 2015;12:239 – 45.
8. Macario A. What does one minute of operating room time cost? J Clin Anesth 2010;22:233– 6.
9. Jones S, Anagnostou V, Lytle K, Parpart-Li S, Nesselbush M, Riley DR, et al. Personalized genomic analyses for cancer mutation discovery and interpretation. Sci Transl Med 2015;7:283ra53.
10. Mino-Kenudson M, Chirieac LR, Law K, Hornick JL, Lindeman N, Mark EJ, et al. A novel, highly sensitive antibody allows for the routine detection of ALK-rearranged lung adenocarcinomas by standard immunohistochemistry. Clin Cancer Res 2010;16:1561–71.
11. Ifa DR, Eberlin LS. Ambient ionization mass spectrometry for cancer diagnosis and surgical margin evaluation. Clin Chem 2016;62:111–23.
12. Jarmusch AK, Pirro V, Baird Z, Hattab EM, Cohen-Gadol AA, Cooks RG. Lipid and metabolite profiles of human brain tumors by desorption electrospray ionization-MS. Proc Natl Acad Sci U S A 2016;113:1486 –91.
13. Eberlin LS, Tibshirani RJ, Zhang J, Longacre TA, Berry GJ, Bingham DB, et al. Molecular assessment of surgical-resection margins of gastric cancer by massspectrometric imaging. Proc Natl Acad Sci U S A 2014;111:2436-41.

14. Calligaris D, Caragacianu D, Liu X, Norton I, Thompson CJ, Richardson AL, et al. Application of desorption electrospray ionization mass spectrometry imaging in breast cancer margin analysis. Proc Natl Acad Sci U S A 2014;111:15184 –9.

15. Eberlin LS, Norton I, Dill AL, Golby AJ, Ligon KL, Santagata S, et al. Classifying human brain tumors by lipid imaging with mass spectrometry. Cancer Res 2012;72: 645–54.

16. Guenther S, Muirhead LJ, Speller AV, Golf O, Strittmatter N, Ramakrishnan R, et al. Spatially resolved metabolic phenotyping of breast cancer by desorption electrospray ionization mass spectrometry. Cancer Res 2015;75:1828 –37.

17. Zhang J, Yu W, Ryu SW, Lin J, Buentello G, Tibshirani R, et al. Cardiolipins are biomarkers of mitochondria-rich thyroid oncocytic tumors. Cancer Res 2016;76:6588 – 97.

18. Dill AL, Eberlin LS, Costa AB, Zheng C, Ifa DR, Cheng LA, et al. Multivariate statistical identification of human bladder carcinomas using ambient ionization imaging mass spectrometry. Chemistry 2011;17:2897–902.

19. Schafer KC, Denes J, Albrecht K, Szaniszlo T, Balog J, Skoumal R, et al. In vivo, in situ tissue analysis using rapid evaporative ionization mass spectrometry. Angew Chem Int Ed Engl 2009;48:8240 –2.

20. Fatou B, Saudemont P, Leblanc E, Vinatier D, Mesdag V, Wisztorski M, et al. In vivo real-time mass spectrometry for guided surgery application. Sci Rep 2016;6:25919.

21. Zhang JL, Rector J, Lin JQ, Young JH, Sans M, Katta N, et al. Nondestructive tissue analysis for ex vivo and in vivo cancer diagnosis using a handheld mass spectrometry system. Sci Transl Med 2017;9:eaan3968.

22. Schafer KC, Szaniszlo T, Gunther S, Balog J, Denes J, Keseru M, et al. In situ, real-time identification of biological tissues by ultraviolet and infrared laser desorption ionization mass spectrometry. Anal Chem 2011; 83:1632– 40.

23. Saudemont P, Quanico J, Robin YM, Baud A, Balog J, Fatou B, et al. Real-time molecular diagnosis of tumors using water-assisted laser desorption/ionization mass spectrometry technology. Cancer Cell 2018;34:840 – 51.e4.

24. Laskin J, Lanekoff I. Ambient mass spectrometry imaging using direct liquid extraction techniques. Anal Chem 2016;88:52–73.

25. Doria ML, McKenzie JS, Mroz A, Phelps DL, Speller A, Rosini F, et al. Epithelial ovarian carcinoma diagnosis by desorption electrospray ionization mass spectrometry imaging. Sci Rep 2016;6:39219.

26. Sans M, Gharpure K, Tibshirani R, Zhang J, Liang L, Liu J, et al. Metabolic markers and statistical prediction of serous ovarian cancer aggressiveness by ambient ionization mass spectrometry imaging. Cancer Res 2017; 77:2903–13.

27. Phelps DL, Balog J, Gildea LF, Bodai Z, Savage A, El-Bahrawy MA, et al. The surgical intelligent knife distinguishes normal, borderline and malignant gynaecological tissues using rapid evaporative ionisation mass spectrometry (REIMS). Br J Cancer 2018;118:1349 –58.

28. Lengyel E. Ovarian cancer development and metastasis. Am J Pathol 2010;177:1053– 64.

29. Kurman RJ, Shih Ie M. Molecular pathogenesis and extraovarian origin of epithelial ovarian cancer–shifting the paradigm. Hum Pathol 2011;42:918 –31.

30. Zhang JL, Yu WD, Suliburk J, Eberlin LS. Will ambient ionization mass spectrometry become an integral technology in the operating room of the future? Clin Chem 2016;62:1172– 4.

31. Peng Y, Austin DE. New approaches to miniaturizing ion trap mass analyzers. Trends Analyt Chem 2011;30: 1560 –7.

32. Douglas DJ, Frank AJ, Mao DM. Linear ion traps in mass spectrometry. Mass Spectrom Rev 2005:24:1-29.

33. Marshall AG, Hendrickson CL. High-resolution mass spectrometers. Annu Rev Anal Chem 2008;1:579 –99.

34. Tibshirani R. Regression shrinkage and selection via the lasso. J Roy Stat Soc B Met 1996;58:267– 88.

35. Robin X, Turck N, Hainard A, Tiberti N, Lisacek F, Sanchez JC, Muller M. pROC: an open-source package for R and S+ to analyze and compare ROC curves. BMC Bioinformatics 2011;12:77.

36. James G, Witten D, Hastie T, Tibshirani R. An introduction to statistical learning: with applications in R. New York: Springer; 2013. 426 pp.

37. Devine PJ, Perreault SD, Luderer U. Roles of reactive oxygen species and antioxidants in ovarian toxicity. Biol Reprod 2012;86:27.

38. Denkert C, Budczies J, Kind T, Weichert W, Tablack P, Sehouli J, et al. Mass spectrometry-based metabolic profiling reveals different metabolite patterns in invasive ovarian carcinomas and ovarian borderline tumors. Cancer Res 2006;66:10795– 804.

39. Wiklund NP, Samuelson UE, Brundin J. Adenosine modulation of adrenergic neurotransmission in the human fallopian tube. Eur J Pharmacol 1986;123:11– 8.

40. Cometti B, Dubey RK, Imthurn B, Jackson EK, Rosselli M. Oviduct cells express the cyclic amp adenosine pathway. Biol Reprod 2003;69:868 –75.

Chapter 7: Conclusions and Perspectives

Investigating metabolic trends in ovarian cancer tissue can provide powerful insights into the mechanisms driving disease development and progression and the opportunity to introduce molecular information into routine clinical diagnoses. The unparalleled analytical specificity and sensitivity of MS, together with the clinically fitting features of ambient ionization, such as minimal sample requirements and experimental simplicity, offer highly suitable capabilities to achieve these objectives. The studies described in this dissertation demonstrate the versatility of ambient ionization MS methods to analyze cancer tissue *ex vivo* as thin tissue sections or fresh-frozen specimens and showcase feasibility for *in vivo* analyses from viable tissue. The continued technical development of these technologies to address current challenges in ambient ionization MS as well as improve robustness and ease-of-use can further advance performance to pursue additional clinically relevant areas in ovarian cancer research. Additional factors, including successful validation in pilot and trial studies to evaluate clinical impact and meet regulatory standards, will need to be considered to achieve implementation of these technologies for clinical use.

DESI-MS imaging has been widely applied to distinguish between healthy and diseased tissue, as well as to differentiate between various cancer subtypes, determining potential metabolic markers associated with each particular tissue type. Future studies should focus in critical oncological areas that can truly benefit from the high diagnostic accuracy and efficiency provided by DESI-MS and multivariate statistical analyses, such as those cases not solvable with current tools available to pathologists, or those that represent a great burden to process and diagnose. Moreover, going beyond cancer diagnosis and predicting patient prognosis, including surgical outcome, treatment response, or progression-free survival rates might offer a higher impact to the care and management of

ovarian cancer patients. Investigating molecular features associated with clinical response could also have large implications in understanding resistance and sensitivity to current treatment strategies, such as chemo and immunotherapies, currently a critical problem in ovarian cancer treatment. Importantly, correlating DESI-MS lipid data to protein and genetic molecular changes could provide additional mechanistic information into the development of tumorigenic pathways in ovarian cancer. To facilitate routine use by non-experts in clinical laboratories and pathology rooms, advances in DESI-MS technology to ameliorate ease of method optimization and robustness, as well as reduce user-dependability, will also be crucial.

Alternative methods for ambient ionization MS tissue section analysis, such as the one described in Chapter 4, can address current analytical limitations in spatially controlled metabolic profiling and molecular coverage by exploiting the capabilities to easily tune droplet volume and composition, including the introduction of chemical additives for enhanced molecular detection and on-tissue derivatization. These approaches could be of high relevance for improved protein and peptide detection from tissue samples by ambient ionization MS technology. Future testing and refining of this method for characterization of biological tissue samples will determine its overall potential impact in ovarian cancer research. Importantly, this method also provides a suitable platform for an in-depth investigation of the mechanisms driving molecular extraction and ionization in liquid extraction ambient MS technologies. Even though various ambient ionization MS methods employ liquid extraction mechanisms to interrogate tissue samples, such as DESI-MS and the MasSpec Pen, little is known about the parameters and conditions driving the sampling and detection of molecular ions in these experiments. Conducting an investigation to separately study extraction and ionization events using the method described in Chapter 4

of this dissertation will ultimately provide important insights to advance and optimize these technologies for detection of molecular species from tissue samples.

The development of ambient ionization MS methods capable of providing distinctive molecular profiles of various cancer types *in vivo*, such as ovarian cancer, opens a new set of applications previously considered unattainable with MS technology. It is truly striking that a technique such as the MasSpec Pen is capable of extracting sufficient molecules from a tissue sample using only a droplet of water in under 10 seconds, and that this information can be used to generate robust statistical models with machine learning algorithms to predict cancer diagnosis. Importantly, the ease-of-use of this technology, including the handheld device and automated platform, enables surgeons and other clinicians to easily introduce the MasSpec Pen into their clinical workflow. This technology could help improve the accuracy and efficiency of ovarian cancer cytoreductive surgeries, minimizing residual disease and improving patient outcome. After demonstrating adequate capabilities for *ex vivo* use, as described in Chapters 5 and 6, testing of this technology during human surgeries is currently underway and planned to continue through multiple pilot clinical studies, and will be imperative to validate performance and pursue implementation for clinical use. The opportunity to evaluate viable tissue with vascular and dynamic biological activity, commonly also accompanied by blood and other bodily fluids at the surface analyzed, is an invaluable experience to gather powerful observations to direct future refinements and developments towards improved clinical use. The optimization of MS instrumentation to allow for routine analysis of surgical specimens, such as adapting the MasSpec Pen to miniaturized mass spectrometers and developing robust ion optics interfaces, will also facilitate testing and translating the MasSpec Pen and other technologies to various clinical practices.

Importantly, most of the findings and data interpretations discussed in this dissertation were generated based on evaluations and results provided by advanced statistical and computational methods, such as those developed by our collaborator Prof. Tibshirani. Thus, careful interpretation of the outputs provided by these analyses is extremely important, understanding the underlying assumptions and thus the limitations, if any, of the resulting conclusions. Moreover, rigorous testing and validation of the results should be performed to ensure unbiased observations, and with the ultimate goal of reaching a conclusion representative of the whole population. Preprocessing of MS data prior to data analysis can be challenging yet is paramount to ensure reliable and accurate results. The development, optimization, and standardization of data handling methods for MS will enable widespread use by researchers and clinical professionals and facilitate comparisons between results obtained by different institutions and laboratories. Improvements in open-source data analysis and visualization tools that provide informative interpretations from the highly complex and large MS imaging datasets are also needed to assist in data evaluation. The further advancement of methods for data preprocessing, modeling, and prediction will only continue to improve the capabilities of MS for tissue characterization and diagnosis.

All-inclusive, the studies described in this dissertation suggest that ambient ionization MS technology can provide powerful information to address various applications in ovarian cancer research and diagnosis. Continued technical development of these technologies will facilitate widespread use in bioanalytical laboratories and reveal new applications in cancer research. To achieve implementation as a routine diagnostic tool for rapid and direct assessment of tissue samples, additional considerations need to be addressed. Apart from testing feasibility with clinical samples in the same environments envisioned for *ex vivo* and *in vivo* use, careful validation with current standard of care will

be crucial to evaluate the need and ultimate impact of these approaches. Thus, collaboration and partnership with clinicians and hospitals to provide the required infrastructure and logistics to conduct rigorous validation studies will be of highest importance. Adapting the operation and capabilities of these methods to facilitate use by pathologists and surgeons, mimicking other technologies routinely employed in the frozen section or operating room, and developing a user-friendly platform that can provide straight-forward information in a timely and robust matter will also need to be pursued. Ultimately, the incorporation of MS technology as a routine tool used for cancer diagnosis and surgical guidance will rely on regulatory approval by federal and international organizations as medical devices and/*or in vitro* diagnostics. With MS-based clinical diagnostics being a relatively new field, guidance from regulatory experts will be highly valuable to continue the development and testing of these technologies and to define future studies required to achieve clearance. It goes without saying that the implementation of MS technology, foreign to most surgical and oncological practices, for routine cancer diagnosis will be no easy task, but the potential benefits that these methods can provide to cancer patients, clinicians, and to the health care system significantly outweigh the challenges ahead.

Appendices

APPENDIX A1. METABOLIC MARKERS AND STATISTICAL PREDICTION OF SEROUS OVARIAN CANCER AGGRESSIVENESS BY AMBIENT IONIZATION MASS SPECTROMETRY IMAGING

Table A1.1: Patient demographic table.

Tissue samples were obtained from the Cooperative Human Tissue Network (CHTN) and from the MD Anderson Cancer Center Tissue Bank.

	Patient Group		
Parameter	**Normal**	**Borderline**	**High-grade**
Number of Patients (N)	15	15	48
Median Age, Years	53	48	64
Age Range, Years	(39,77)	(23,78)	(43,84)
Number of Patients by Race (White, Black, Asian, Unknown)	(10,4,0,1)	(11,2,0,2)	(38,6,1,3)
Tissue Bank	CHTN	CHTN	CHTN (N=24)
			MD Anderson (N=24)

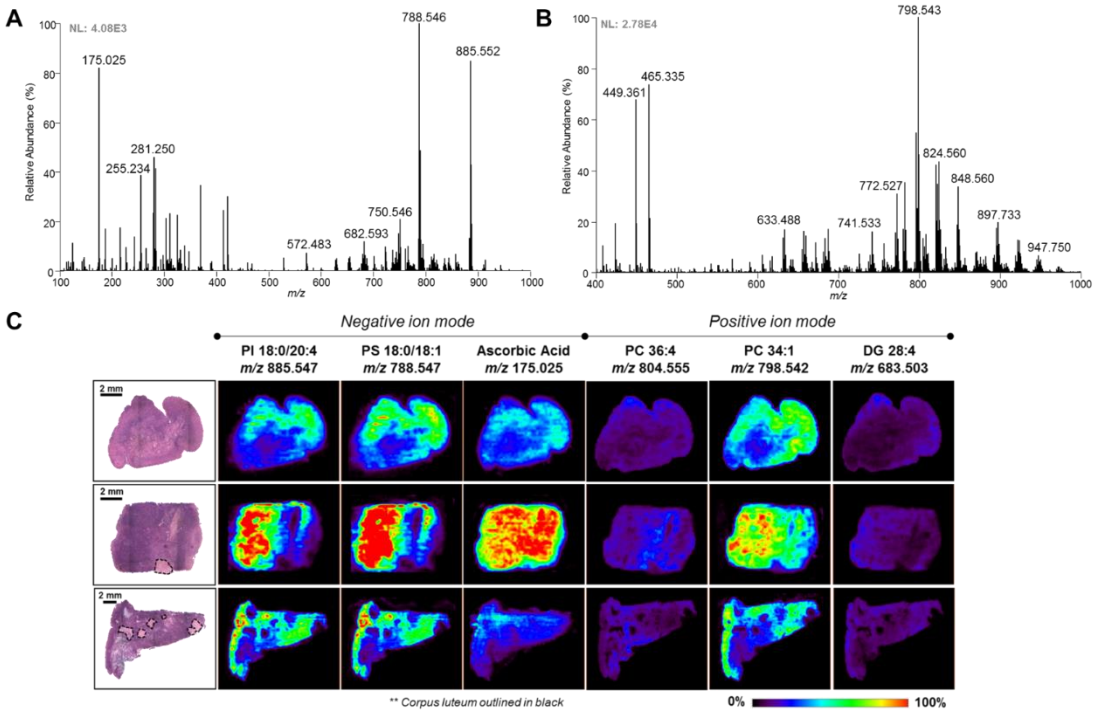

Figure A1.1: Representative DESI mass spectrum for normal ovarian tissue sections.

Negative ion mode (A). Positive ion mode (B). DESI-MS representative ion images. Adjacent tissue sections were used for negative and positive ion mode analysis (C). Corpus luteum areas are outlined in black. Areas of red intensity within the ion images represent highest (100%) and black lowest (0%) relative abundances. PI: glycerophosphoinositol PG: glycerophosphoglycerol CL: PC: glycerophosphocholine DG: Diacylglyceride. Lipid species are described by number of fatty acid chain carbons and double bonds.

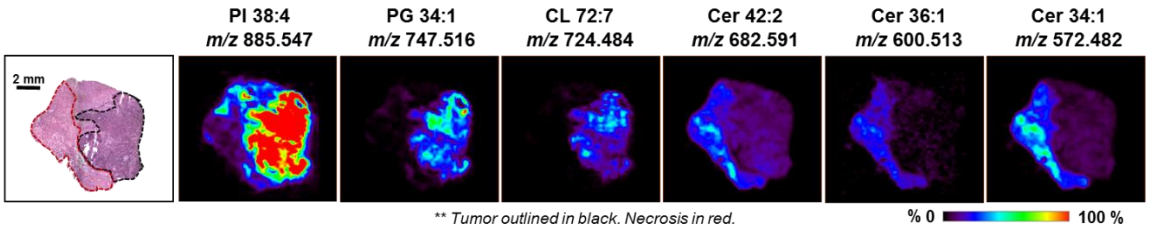

Figure A1.2: Representative negative ion images characteristic for HG tumorous and necrotic regions for sample HGSC_1.

PI 38:4, PG 34:1 and CL 72:7 were found overexpressed in the cancer regions, while necrosis was characterized by higher relative abundances for Cer d42:2, Cer d36:1 (mass error = 1.8 ppm) and Cer d34:1. Tumor regions are outlined in black, necrosis in red. Areas of red intensity within the ion images represent highest (100%) and black lowest (0%) relative abundances. PI: glycerophosphoinositol PG: glycerophosphoglycerol CL: cardiolipin Cer: ceramide. Lipid species are described by number of fatty acid chain carbons and double bonds.

Table A1.2: Lasso results based on pixel and patient analysis for normal vs high-grade SOC classification, for negative and positive ion polarities.

Negative (Normal N=15, High-grade N=48). Positive (Normal N=10, High-grade N=46). Results show agreements for CV (cross-validation) and validation sets. Rows represent classification based on pathological evaluation, columns represent classification based on LASSO prediction. Agreements per pixels are calculated based on percentage of correctly classified pixels over total pixels classified. Per patient analysis by the Lasso is based on classification results for the majority of pixels from the patient. AUC (area under the curve).

Analysis	Data Set	Pathology	Normal	High-Grade	Agreement (%)	Overall Agreement (%)	AUC
Negative Ion Mode							
Per Pixel	**CV**	**Normal**	5554	44	99.2	97.1	0.98
		High-Grade	532	13952	96.3		
	Validation	**Normal**	5377	151	97.3	96.5	0.97
		High-Grade	497	12646	96.2		
Per Patient	**CV**	**Normal**	8	0	100	100.0	-
		High-Grade	0	23	100		
	Validation	**Normal**	7	0	100	96.5	-
		High-Grade	1	24	96.9		
Positive Ion Mode							
Per Pixel	**CV**	**Normal**	3946	272	93.6	96.7	0.96
		High-Grade	376	14798	97.5		
	Validation	**Normal**	3684	200	94.9	95.5	0.95
		High-Grade	760	16584	95.6		
Per Patient	**CV**	**Normal**	5	0	100	100.0	-
		High-Grade	0	23	100		
	Validation	**Normal**	5	0	100	89.3	-
		High-Grade	3	20	87		

Table A1.3: Identified species selected by the Lasso as significant contributors to high-grade versus normal discrimination with attributed weights.

Weights attributed with respect to high-grade classification: positive weights represent an increase in relative abundances in high-grade tissue samples in comparison to normal tissue samples, while negative weights represent lower relative abundances in high-grade tissue samples in comparison to normal tissue samples. Tentative molecular formulas and chemical identification were attributed by high mass accuracy/high mass resolution and tandem MS analyses. Molecular formulas correspond to ionized molecule. Double negative and double positives correspond to greater contributions to the model. Negative ion mode: Lasso weights: '++' '- -' $\geq \left| 0.001 \right|$; '+' '-' $< \left| 0.001 \right|$. Positive ion mode: Lasso weights: '++' '- -' $\geq \left| 0.0001 \right|$; '+' '-' $< \left| 0.0001 \right|$.

NEGATIVE ION MODE				
Attribution	**Weights by LASSO**	**Detected m/z**	**Molecular Formula**	**Mass error (ppm)**
Succinate	++	117.020	C4H5O4	-1.7
Malate	++	133.014	C4H5O5	-1.5
N-acetylaspartic acid	++	174.041	C6H8NO5	0.1
Ascorbic acid	-	175.025	C6H7O6	0.1
Didehydro-D-gluconic acid	-	226.996	C6H8O7Cl	0.9
FA 16:0	+	255.233	C16H31O2	0.8
FA 18:2	-	279.233	C18H31O2	-1.1
FA 20:4	+	303.233	C20H31O2	-1.0
FA 20:3	+	305.248	C20H33O2	-1.0
FA 22:4	+	331.264	C22H35O2	-1.2
PE (18:1/1:0)	- -	528.273	C26H43NO8P	-0.8
Cer d34:1	+	572.481	C34H67NO3Cl	1.2
DG 28:4	- -	679.508	C41H72O5Cl	-0.3
Cer d42:3	-	680.575	C42H79NO3Cl	-0.6
Cer d42:2	- -	682.590	C42H81NO3Cl	1.5
Cer d42:1	++	684.607	C42H83NO3Cl	-0.1
CL 72:8	+	723.479	C81H140O17P2	-0.4
CL 72:7	+	724.484	C81H142O17P2	3.6
PG 16:0/18:1	++	747.520	C40H76O10P	-1.9
PS 16:0/18:1	- -	760.515	C40H75NO10P	-2.0
PG 18:1/18:1	++	773.533	C42H78O10P	0.9
PS 18:0/18:1	-	788.547	C42H79NO10P	-2.4
PI 18:0/18:2	+	861.552	C45H82O13P	-2.1
PI 18:0/18:1	++	863.567	C45H84O13P	-1.5
PI 18:0/20:4	+	885.552	C47H82O13P	-2.1
POSITIVE ION MODE				
Attribution	**Weights by LASSO**	**Detected m/z**	**Molecular Formula**	**Mass error (ppm)**
Choline group	+	104.107	C5H14NO	2.9
Aminopentanoic acid	++	156.042	C5H11NO2K	-1.3

Hexacosanedioic acid	-	465.335	C26H50O4K	-1.3
PC 21:4	++	610.291	C29H50NO8PK	-0.7
DG 34:2	- -	631.471	C37H68O5K	-1.1
DG 34:1	- -	633.486	C37H70O5K	-1.4
CE 18:2	- -	671.575	C45H76O2Na	-2.2
DG 28:4	- -	683.503	C41H72O5K	-2.0
CE 20:3	++	697.589	C47H78O2Na	0.1
CE 20:4	++	711.548	C47H76O2K	-0.4
SM 34:1	- -	725.558	C39H79N2O6PNa	-1.4
PC 32:1	++	770.511	C40H78NO8PK	-1.6
PC 32:0	++	772.527	C40H80NO8PK	-1.9
PC 34:1	- -	798.542	C42H82NO8PK	-1.5
PC 36:4	-	804.555	C44H80NO8PNa	-4.4
PC 36:3	++	822.542	C44H82NO8PK	-0.9
PC 38:5	+	846.539	C46H82NO8PK	2.8
22:1-Glc-Cholesterol	++	891.708	C57H95O7	-1.3
Ubiquinone	++	901.648	C59H90O4K	-1.1
TG 54:4	++	921.729	C57H102O6K	2.1
TG 58:4	++	971.746	C61H104O6K	0.7

Table A1.4: Lasso results based on pixel and patient analysis for borderline vs high-grade SOC classification, for negative and positive ion polarities.

Negative (Borderline N=15, High-grade N=48). Positive (Borderline N=15, High-grade N=46). Results show agreements for CV (cross-validation) and validation sets. Rows represent classification based on pathological evaluation; columns represent classification based on LASSO prediction. Agreements per pixels are calculated based on percentage of correctly classified pixels over total pixels classified. Per patient analysis by the Lasso is based on classification results for the majority of pixels from the patient. AUC (area under the curve).

Analysis	Data Set	Pathology	Borderline	High-Grade	Agreement (%)	Overall Agreement (%)	AUC
Negative Ion Mode							
Per Pixel	**CV**	Borderline	2573	144	94.7	93.2	0.97
		High-Grade	1098	14375	92.9		
	Validation	Borderline	973	295	76.8	91.8	0.93
		High-Grade	806	11348	93.4		
Per Patient	**CV**	Borderline	9	1	90.0	93.8	-
		High-Grade	1	21	95.5		
	Validation	Borderline	4	1	80.0	93.9	-
		High-Grade	1	25	96.0		
Positive Ion Mode							
Per Pixel	**CV**	Borderline	1484	494	75.0	90.4	0.92
		High-Grade	1508	17366	92.0		
	Validation	Borderline	1421	69	95.4	97.5	0.99
		High-Grade	305	13339	97.8		
Per Patient	**CV**	Borderline	7	2	77.8	93.1	-
		High-Grade	0	20	100		
	Validation	Borderline	6	0	100	96.9	-
		High-Grade	1	25	96.0		

Table A1.5: Identified species selected by the Lasso as significant contributors to high-grade versus borderline discrimination with attributed weights.

Weights attributed with respect to high-grade classification: positive weights represent an increase in relative abundances in high-grade tissue samples in comparison to borderline, while negative weights represent lower relative abundances in high-grade tissue samples in comparison to borderline. Tentative molecular formulas and chemical identification were attributed by high mass accuracy/high mass resolution and tandem MS analyses. Molecular formulas correspond to ionized molecule. Double negative and double positives correspond to greater contributions to the model. Negative ion mode: Lasso weights: '++' '- -' $\geq |0.001|$; '+' '-' $< |0.001|$. Positive ion mode: Lasso weights: '++' '- -' $\geq |0.0001|$; '+' '-' $< |0.0001|$.

NEGATIVE ION MODE				
Attribution	**Weights by Lasso**	**Molecular Formula**	**Detected m/z**	**Mass error (ppm)**
Succinate	++	C4H5O4	117.020	-1.7
Glutamic acid	- -	C5H8NO4	146.046	-0.7
N-acetyl-aspartic acid	++	C6H8NO5	174.041	0.1
Ascorbic acid	+	C6H7O6	175.025	0.1
Gluconic acid	++	C6H11O7	195.051	0.5
Hexose	- -	C6H12O6Cl	215.033	0.9
FA 16:0	++	C16H31O2	255.233	0.8
FA 18:1	-	C18H33O2	281.248	-0.7
FA 20:4	-	C20H31O2	303.233	-1.0
FA 20:3	++	C20H33O2	305.248	-1.0
FA 20:2	- -	C20H35O2	307.264	-0.7
FA 20:1	-	C20H37O2	309.280	-0.3
FA 22:4	++	C22H35O2	331.264	-1.2
MG 16:0	+	C19H38O4Cl	365.246	-1.6
PE 18:1/1:0	+	C24H45NO8P	506.288	-1.8
Cer d34:1	-	C34H67ClNO3	572.481	1.2
DG 34:1	++	C37H70O5Cl	629.491	0.8
Cer d40:1	+	C40H79NO3Cl	656.575	0.3
Cer d41:1	++	C41H81NO3Cl	670.589	2.4
CL 72:7	-	C81H142O17P2	724.484	3.6
GlcCer d34:1	- -	C40H77NO8Cl	734.535	-0.7
PE 18:1/18:1	++	C41H78NO8P	742.538	1.9
PE 38:4	+	C43H77NO8P	766.538	1.3
PS 18:1/18:1 or 18:0/18:2	-	C42H77NO10P	786.528	-1.5
PS 18:0/18:1	-	C42H79NO10P	788.547	-2.4
PG 20:4/18:1	++	C44H76O10P	795.515	-3.0
PS 38:4	+	C44H77NO10P	810.528	-1.5
PS 18:0/20:3	- -	C44H79NO10P	812.544	-1.2
PS 40:6	- -	C46H77O10NP	834.527	-2.4
PS 22:4/18:0	++	C46H81NO10P	838.560	0.5

PI 18:0/18:2	+	C45H82O13P	861.552	-2.1
PI 18:0/18:1	++	C45H85O13P	863.567	-1.5
PI 18:0/20:4	-	C47H83O13P	885.552	-2.1
PI 18:0/20:3	+	C47H84O13P	887.563	-3.4
POSITIVE ION MODE				
Attribution	**Weights by LASSO**	**Molecular Formula**	**Detected m/z**	**Mass error (ppm)**
choline group	++	C5H14NO	104.107	2.9
DG 36:3	++	C41H72O5K	657.487	-2.4
CE 18:2	- -	C45H76O2Na	671.575	-2.2
PC 34:1	- -	C42H82NO13PNa	782.569	-2.0
PC 34:2	++	C42H80NO8PK	796.526	-1.1
PC 36:4	++	C44H80NO8PK	820.526	-1.3
TG 54:4	+	C57H102O6K	921.729	2.1

Table A1.6: Lasso results based on pixel and patient analysis for normal, high-grade and borderline classification, for negative and positive ion polarities.

Results show agreements for CV (cross-validation) and validation sets. Rows represent classification based on pathological reports, columns represent classification based on molecular model. Agreements are calculated based on percentage of correctly classified pixels over total pixels classified. Patients are assigned as normal, borderline or high-grade based on highest amount of pixels classified by the Lasso.

Data Set	Pathology	Normal	Borderline	High-Grade	Agreement (%)	Pathology	Agreement (%)
Negative Ion Mode – Per Pixel							
CV	**Normal**	6751	36	343	94.7	**Normal**	94.7
	Borderline	254	1690	288	75.7	**Tumor**	96.2
	High-Grade	242	347	10274	94.6		
Val	**Normal**	3185	0	811	79.7	**Normal**	79.7
	Borderline	0	1111	642	63.4	**Tumor**	100
	High-Grade	7	1112	15645	93.3		
Negative Ion Mode – Per Patient							
CV	**Normal**	8	0	1	88.9	**Normal**	88.9
	Borderline	0	7	2	77.8	**Tumor**	100
	High-Grade	0	0	21	100		
Val	**Normal**	5	0	1	83.3	**Normal**	83.3
	Borderline	0	5	1	83.3	**Tumor**	100
	High-Grade	0	2	25	92.6		
Positive Ion Mode – Per Pixel							
CV	**Normal**	4229	544	214	84.8	**Normal**	84.8
	Borderline	308	1224	446	61.9	**Tumor**	97.2
	High-Grade	285	521	18068	95.7		
Val	**Normal**	3074	23	18	98.7	**Normal**	98.7
	Borderline	26	1155	309	77.5	**Tumor**	98.4
	High-Grade	215	14	13415	98.3		
Positive Ion Mode – Per Patient							
CV	**Normal**	5	1	0	83.3	**Normal**	83.3
	Borderline	2	6	1	66.7	**Tumor**	93.1
	High-Grade	0	0	20	100		
Val	**Normal**	4	0	0	100	**Normal**	100
	Borderline	0	5	1	83.3	**Tumor**	96.9
	High-Grade	1	0	25	96.1		

Table A1.7: Chemical identity and molecular formula tentatively attributed by high mass accuracy/high mass resolution and tandem MS analyses for identified species selected by the Lasso as significant contributors to high-grade, borderline and normal classification.

Weights to the model are provided in Table A2.1.

NEGATIVE ION MODE				*POSITIVE ION MODE*			
Attribution	**Detected m/z**	**Molecular Formula**	**Mass error (ppm)**	**Attribution**	**Detected m/z**	**Molecular Formula**	**Mass error (ppm)**
Succinate	117.020	$C_4H_5O_4$	-1.7	**Choline group**	104.1067	$C_5H_{14}NO$	2.9
Taurine	124.008	$C_2H_6NO_3S$	-0.8	**DG 36:3**	657.4871	$C_{39}H_{70}O_5K$	-2.4
Malate	133.014	$C_4H_5O_5$	-1.5	**CE 18:2**	671.5753	$C_{45}H_{76}O_2Na$	-2.2
Glutamic acid	146.046	$C_5H_8NO_4$	-0.7	**CE 18:1**	673.5906	$C_{45}H_{78}O_2Na$	-1.8
N-acetylaspartic acid	174.041	$C_6H_8NO_5$	0.1	**CE 20:4**	711.5480	$C_{47}H_{76}O_2K$	-0.4
Ascorbic acid	175.025	$C_6H_7O_6$	0.1	**SM 34:1**	725.5578	$C_{39}H_{79}N_2O_6PNa$	-1.4
Gluconic acid	195.051	$C_6H_{11}O_7$	0.5	**PC 32:1**	770.5109	$C_{40}H_{78}NO_8PK$	-1.6
Glucose	215.033	$C_6H_{12}O_6Cl$	0.9	**PC 32:0**	772.5268	$C_{40}H_{80}NO_8PK$	-1.9
Didehydro-gluconic acid	226.996	$C_6H_8O_7Cl$	0.9	**PC 34:1**	782.5686	$C_{42}H_{82}NO_8PNa$	-2.0
FA 16:0	255.233	$C_{16}H_{31}O_2$	0.8	**PC 34:2**	796.5262	$C_{42}H_{80}NO_8PK$	-1.1
FA 18:2	279.233	$C_{18}H_{31}O_2$	-1.1	**PC 34:1**	798.5422	$C_{42}H_{82}NO_8PK$	-1.5
FA 18:1	281.248	$C_{18}H_{33}O_2$	-0.7	**PC 36:4**	820.5264	$C_{44}H_{80}NO_8PK$	-1.3
FA 18:0	283.264	$C_{18}H_{35}O_2$	-1.1	**PC 36:3**	822.5417	$C_{44}H_{82}NO_8PK$	-0.9
FA 20:4	303.233	$C_{20}H_{31}O_2$	-1.0	**PC 36:2**	824.5581	$C_{44}H_{84}NO_8PK$	-1.8
FA 20:3	305.248	$C_{20}H_{33}O_2$	-1.0	**PC 38:4**	848.5585	$C_{46}H_{84}NO_8PK$	-2.2
FA 20:1	309.280	$C_{20}H_{37}O_2$	-1.3	**22:1-Glc-Cholesterol**	891.7043	$C_{55}H_{96}O_7Na$	0.6
FA 22:4	331.264	$C_{22}H_{35}O_2$	-1.2	**TG 52:3**	895.7157	$C_{55}H_{100}O_6K$	-0.7
MG 16:0	365.246	$C_{19}H_{38}O_4Cl$	-1.6	**Ubiquinone**	901.6481	$C_{59}H_{90}O_4K$	-1.1
Cer d34:2	570.466	$C_{34}H_{65}NO_3Cl$	-0.7	**TG 54:4**	921.7289	$C_{57}H_{102}O_6K$	2.1
Cer d34:1	572.481	$C_{34}H_{67}NO_3Cl$	-1.2	**TG 56:6**	945.7295	$C_{59}H_{102}O_6K$	1.4
Cer d42:3	680.575	$C_{42}H_{79}NO_3Cl$	-0.6	**TG 56:4**	949.7595	$C_{59}H_{106}O_6K$	2.7
Cer d42:2	682.590	$C_{42}H_{81}NO_3Cl$	-1.5				
Cer d42:1	684.607	$C_{42}H_{83}NO_3Cl$	0.1				
GlcCer d34:1	734.535	$C_{40}H_{77}NO_8Cl$	0.7				
PE 36:2	742.538	$C_{41}H_{77}NO_8P$	-1.9				
PG 16:0/18:1	747.520	$C_{40}H_{76}O_{10}P$	1.9				
PS 16:0/18:1	760.515	$C_{40}H_{75}NO_{10}P$	2.0				
PG 18:1/18:1	773.533	$C_{42}H_{78}O_{10}P$	-0.9				
PG 18:0/18:1	775.548	$C_{42}H_{80}O_{10}P$	-1.7				
PS 18:1/18:1 or 18:0/18:2	786.528	$C_{42}H_{77}NO_{10}P$	-1.5				
PS 18:0/18:1	788.547	$C_{42}H_{79}NO_{10}P$	2.4				
PG 20:4/18:1	795.515	$C_{44}H_{76}O_{10}P$	-3.0				
PS 18:0/20:3	812.544	$C_{44}H_{79}NO_{10}P$	-1.2				
PS 18:0/22:4	838.560	$C_{46}H_{81}NO_{10}P$	0.5				
PI 18:0/18:2	861.552	$C_{45}H_{82}O_{13}P$	2.1				
PI 18:0/18:1	863.567	$C_{45}H_{84}O_{13}P$	1.5				
PI 18:0/20:4	885.552	$C_{47}H_{82}O_{13}P$	2.1				
PI 18:0/20:3	887.563	$C_{47}H_{84}O_{13}P$	-3.4				

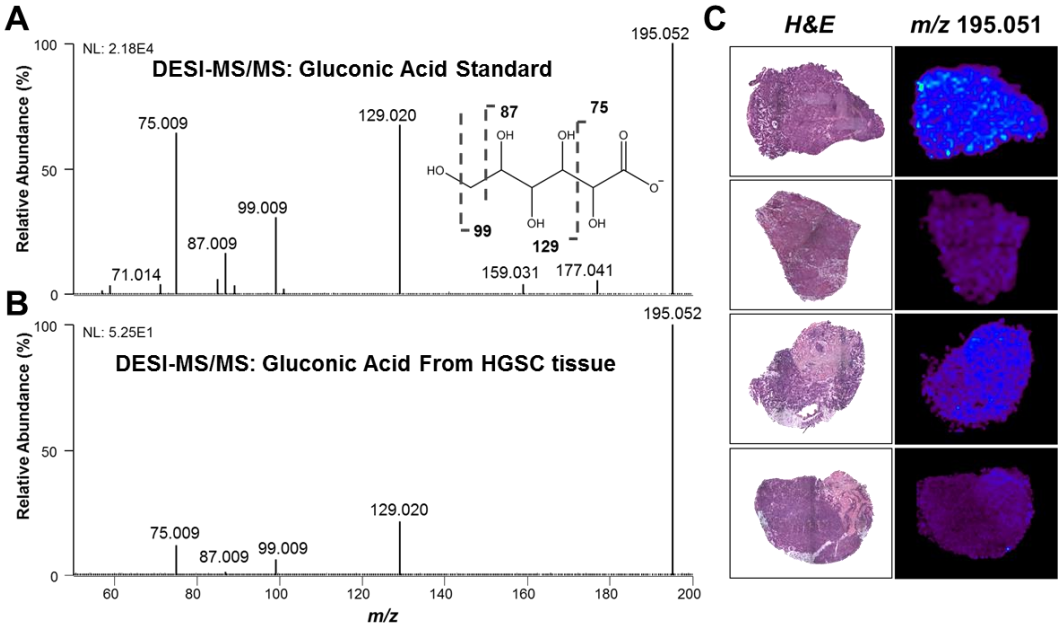

Figure A1.3: Fragmentation patterns obtained by higher collisional induced dissociation (HCD) MS/MS analysis of gluconic acid standard (A) and *m/z* 195.051 from HGSC tissue sample (B). DESI-MS images for *m/z* 195.051 for four HGSC tissue samples (C).

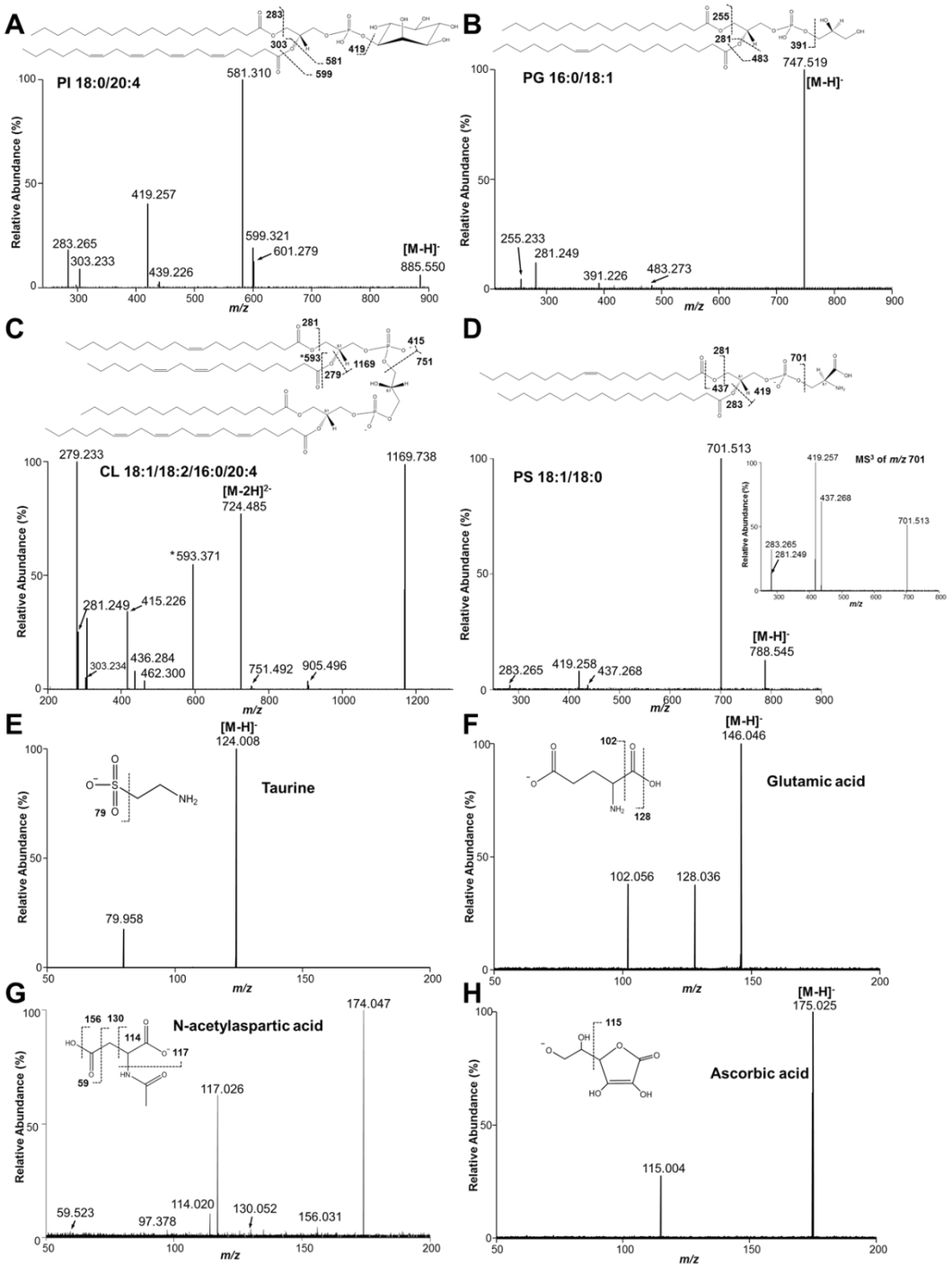

Figure A1.4: Tandem MS spectra in the negative ion mode for representative complex GPs and metabolites with significant contributions to the classification model.

Proposed molecular structure and fragmentation sites are shown for each species. A) $[M-H]^-$ Glycerophosphoinositol PI 18:0/20:4 B) $[M-H]^-$ Glycerophosphoglycerol PG 18:0/18:1 C) $[M-2H]^{2-}$ Cardiolipin CL 18:1/18:2/16:0/20:4. * represents doubly charged fragment species. D) $[M-H]^-$Glycerophosphoserine PS 18:1/18:0 E) $[M-H]^-$ Amino acid taurine F) $[M-H]^-$ Glutamic acid G) $[M-H]^-$ Ascorbic acid.

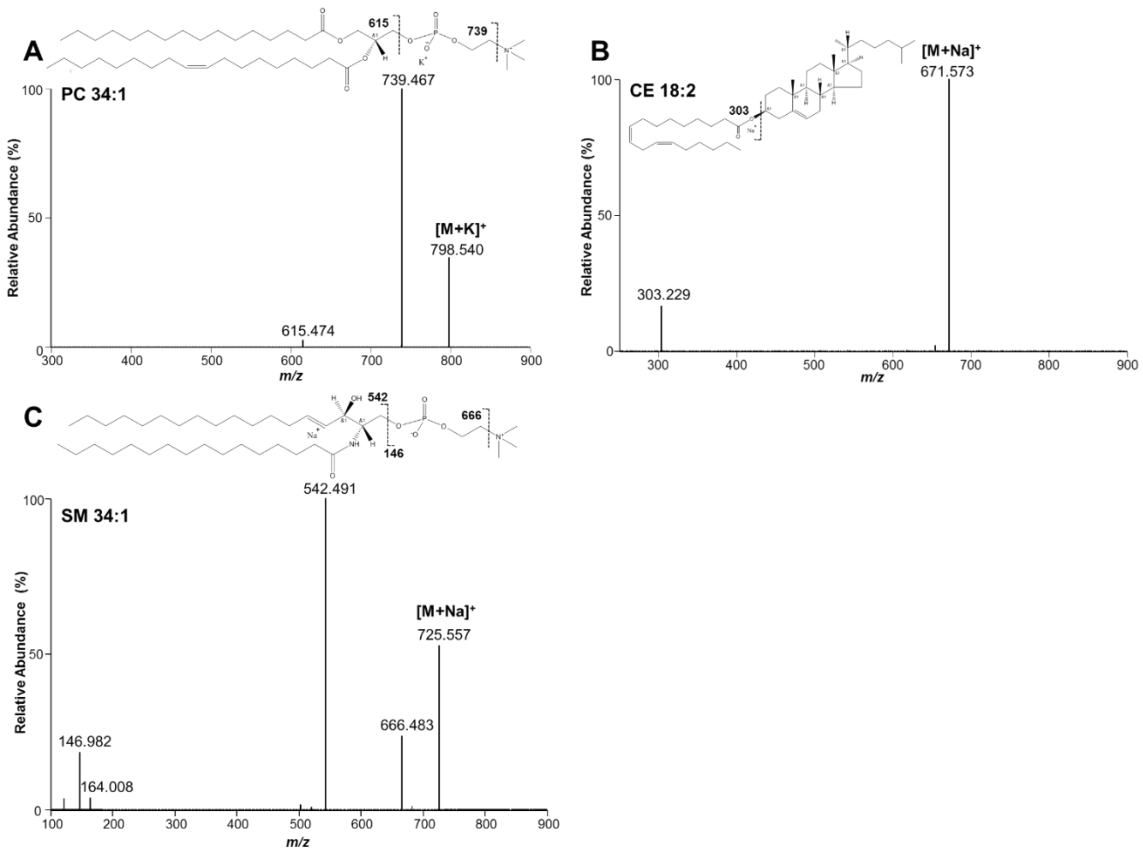

Figure A1.5: Tandem MS spectra in the positive ion mode for representative species contributing to the classification model.

Proposed molecular structure and fragmentation sites are shown for each species. A) $[M+K]^+$ Glycerophosphocholine PC 34:1 B) $[M+Na]^+$ Cholesteryl Ester CE 18:2 C) Sphingomyelin SM 34:1.

Table A1.8: Lasso per pixel results for tumor and stroma classification for five HGSC patients based on negative ion mode DESI-MS data.

Lasso models were built individually for each patient. Rows represent classification based on pathological reports, columns represent classification based on Lasso prediction. Agreements are calculated based on percentage of correctly classified pixels over total pixels classified.

		Lasso Prediction			
Patient #	**Pathology**	**Tumor**	**Stroma**	**Agreement (%)**	**Overall Agreement (%)**
1	**Tumor**	678	4	99.4	99.5
	Stroma	2	455	99.6	
2	**Tumor**	509	2	99.6	99.6
	Stroma	4	961	99.6	
3	**Tumor**	269	3	98.9	97.9
	Stroma	10	338	97.1	
4	**Tumor**	345	1	99.7	99.4
	Stroma	6	869	99.3	
5	**Tumor**	565	1	99.8	99.8
	Stroma	2	882	99.8	

APPENDIX A2. INVESTIGATING THE EFFECTS OF FABP4 EXPRESSION IN OVARIAN CANCER METABOLISM

Table A2.1: Lipid and metabolites identified by SAM as differentially expressed in human patient samples belonging to low- and high-FABP4-expression groups based on DESI-MS imaging data analysis performed in the negative ion mode.

Positive SAM scores represent higher relative abundance in samples with low-FABP4-expression, negative SAM scores represent higher relative abundance in samples with high-FABP4-expression. Tentative molecular formulas and chemical identification were attributed by high mass accuracy/high mass resolution and tandem MS analyses and are provided in supplemental Table 2.

LOW FABP4 EXPRESSION		**HIGH FABP4 EXPRESSION**	
Attribution	**SAM Score**	**Attribution**	**SAM Score**
Metabolites		*Metabolites*	
Fumarate	18.1	N-acetylaspartic acid	-17.2
Acetyl-glycine	11.1	Ascorbic acid	-5.9
Succinate	31.0	Gluconic acid	-41.9
2-Hydroxy-3-methylbutyric acid	19.1	Phosphatidic acid	-6.8
Taurine	27.3	*Fatty Acids*	
Pyroglutamate	8.3	FA 14:1	-23.7
Aspartate	18.9	FA 17:0	-0.5
3-Hydroxypicolinic acid	40.8	FA hydroxy 16:0	-13.8
Glutamine	20.8	FA 18:3	-4.1
Glutamic acid	26.9	FA 18:2	-11.1
2-Hydroxyglutarate	21.0	FA 18:1	-5.4
Xanthine	37.7	FA 18:0	-3.6
Glycerophosphoglycerol	18.4	FA 20:5	-12.2
Glutathione	42.8	FA 20:4	-27.4
Fatty Acids		FA 18:2	-17.2
FA 8:0	29.7	FA 18:1	-21.3
FA 9:0	29.8	FA hydroxy 20:4	-18.9
FA 15:0	4.9	FA 18:0	-22.2
FA 16:1	3.5	FA hydroxy 20:3	-8.6
FA 20:3	15.1	FA 22:6	-21.3
FA 20:2	11.2	FA 22:5	-22.6
FA 20:1	20.2	FA 22:4	-37.6
FA 20:0	8.8	FA 22:3	-6.2
FA 22:0	10.8	FA 20:4	-32.2
FA 23:1	11.2	FA hydroxy 22:6	-6.0
FA 23:0	7.6	FA 24:5	-16.6
FA 24:1	21.3	FA 24:4	-17.5
FA 24:0	21.7	FA 24:3	-0.9
FA 26:3	11.4	FA 22:4	-33.4
FA 26:2	17.7	FA hydroxy 24:0	-2.8
FA 26:1	11.7	*Glycerolipids*	

FA 26:0	29.9
Glycerolipids	
DG 24:0/0:0	10.5
Glycerophosphoethanolamines	
PE 18:1/1:0	11.0
PE 20:3/1:0	21.3
PE O-34:3 or PE P-34:2	23.0
PE O-34:2 or PE P-34:1	21.5
PE 34:2	25.3
PE 34:1	21.4
PE O-36:3 or P-36:2	15.8
PE 35:1	9.6
PE 36:3	27.4
PE 36:2	18.3
PE 38:3	27.7
Glycerophosphoglycerols	
PG 18:0/18:1	19.9
PG 18:0/18:0	13.6
PG 38:4	6.5
PG 38:3	14.0
PG 38:2	12.2
PG 42:7	9.5
Ceramides	
Cer d18:16:0	13.1
Cer m18:1/22:0	7.3
Cer m18:1/24:1	20.0
Cer m42:1	16.9
Cer d18:1/23:0	5.7
Cer d40:0(2OH)	16.9
Cer d42:1	10.0
Cer d42:0	21.9
Cer d18:1/25:0	11.7
Cer d18:1/26:1	11.4
Cer d18:1/26:0	6.8
PE - Cer 36:3	11.3
GlcCer d34:1	5.9
PE-Cer d37:1	14.7
Monoacylglycerophosphates	
PA 32:0	17.3
PA 24:2	17.9
PA 24:1	22.3
PA 36:4	11.9
PA 36:3	12.8
Cardiolipins	
CL 68:5	5.2
CL 70:7	25.3
CL 70:6	20.9
CL 70:5	11.3
CL 72:8	20.7
CL 72:7	26.9
CL 72:6	26.0
MG 18:0	-7.5
MG 22:6	-6.8
DG 32:1/0:0	-8.2
DG 32:0/0:0	-3.5
DG 34:3/0:0	-2.3
DG 34:2/0:0	-6.7
DG 34:1/0:0	-14.2
DG 36:4/0:0	-13.3
DG 36:3/0:0	-4.8
DG 36:2/0:0	-15.7
DG 38:6/0:0	-18.9
DG 38:5/0:0	-16.0
DG 38:4/0:0	-15.4
DG 40:7/0:0	-2.8
DG 40:6/0:0	-15.6
DG 40:5/0:0	-15.1
Glycerophosphoethanolamines	
LysoPE P-16:0	-3.5
LysoPE O-18:1	-30.4
LysoPE 18:1	-4.2
LysoPE 18:0	-5.8
LysoPE 20:4	-18.6
PE 20:4/1:0	-36.2
PE 34:0	-0.7
PE P-18:0/18:4	-10.5
PE O-38:5 or PE P-38:4	-35.7
PE 38:5	-24.4
PE 38:4	-6.4
PE 38:2	-4.1
PE 38:1	-19.2
PE 39:6	-17.6
PE 39:5	-17.6
PE O-40:5 or PE P-40:4	-20.1
PE 40:5	-10.2
PE 37:1	-4.9
PE 40:4	-20.8
PE 39:4	-4.4
PE 39:2	-12.7
PE 39:1	-16.6
PE 41:6	-14.7
PE 41:5	-26.4
PE 41:4	-25.0
PE 43:6	-7.3
PE 43:2	-8.2
Glycerophosphoglycerols	
LysoPG 16:0	-7.1
LysoPG 18:2	-20.2
LysoPG 18:1	-18.4
LysoPG 22:6	-11.5
PG 34:3	-0.7
PG 34:2	-1.2

CL 74:10	13.3
CL 74:9	22.1
CL 74:8	22.5
CL 74:7	18.9
CL 76:10	19.9
CL 76:9	15.0
CL 76:8	14.3
CL 76:7	13.4
CL 36:4	2.8
Glycerophosphoinositols	
LysoPI (16:0/0:0)	4.4
PI (32:1)	22.3
PI (32:0)	25.4
PI (34:2)	28.1
PI (34:1)	25.5
PI (O-23:0)	7.8
PI (25:1)	21.5
PI (36:4)	2.9
PI (36:3)	31.7
PI (36:2)	45.5
PI (36:1)	25.7
PI (37:3)	17.9
PI (38:6)	20.6
PI (38:3)	18.7
PI (40:6)	9.9
PI (39:4)	20.0
Glycerophosphoserines	
PS P-34:1	4.3
PS 16:0/18:1	18.6
PS P-36:2 or PS O-36:3	14.4
PS O-36:2 or PS P-36:1	4.3
PS 36:3	28.2
PS 36:2	34.3
PS 18:0/18:1	17.5
PS O-38:4 or P-38:3	4.3
PS 38:3	31.9
PS 38:2	30.3
PS 38:1	23.5
PS 40:6	13.3
PS 40:2	17.7
PS 40:1	21.3
PS 42:3	15.4
PS 42:2	17.8
PS 42:1	20.3

PG 16:0/18:1	-4.3
PG 36:4	-18.5
PG 18:2/18:1	-4.8
PG 18:1/18:1	-2.3
PG 38:6	-7.6
PG 38:5	-2.8
PG 40:8	-6.2
PG 40:7	-2.8
PG 40:6	-0.7
PG 40:5	-0.7
PG 22:6/22:6	-8.0
Ceramides	
Cer d32:1	-8.9
Cer d16:1/17:0	-16.2
Cer d34:2	-8.5
Cer d34:1	-1.1
Cer d36:2	-4.7
Cer d36:1	-17.6
Cer d38:1	-8.2
Cer d41:2	-1.3
Cer d42:0	-0.5
Cer d42:1	-1.2
PE-Cer d36:1	-4.1
Monoacylglycerophosphates	
PA 36:1	-18.2
PA O-38:2 or PA P-38:1	-11.9
Cardiolipins	
CL 72:4	-7.5
Glycerophosphoinositols	
LysoPI 15:0	-16.3
LysoPI O-16:0	-5.8
LysoPI 18:0	-20.1
Lyso PI 20:4	-15.7
PI O-33:2 or PI P-33:1	-13.0
PI P-18:0/17:2	-15.2
PI O-35:2 or PI P-35:1	-1.0
PI 37:4	-3.6
PI 38:6	-15.6
PI 38:5	-15.2
PI 38:4	-27.6
PI 40:4	-18.1
PI 40:3	-8.5
Glycerophosphoserines	
PS O-36:4 or PS P-36:3	-6.7
PS 38:4	-0.5
PS O-39:0	-0.5
PS O-40:4 or PS P-40:3	-12.3
PS 39:2	-4.9

Table A2.2: Lipid and metabolite molecular attributions for *m/z* values selected by SAM as differentially expressed in human patient samples belonging to low- and high-FABP4-expression groups based on DESI-MS imaging data analysis performed in the negative ion mode. Tentative molecular formulas and chemical identification were attributed by high mass accuracy/high mass resolution and tandem MS analyses.

Attribution	**Molecular Formula**	**Detected *m/z***	**Mass error (ppm)**
Metabolites			
Fumarate	$C_{47}H_{84}O_{13}P$	115.004	-1.7
Acetyl-glycine	$C_4H_6NO_3$	116.035	1.7
Succinate	$C_4H_5O_4$	117.020	-1.7
2-Hydroxy-3-methylbutyric acid	$C_5H_9O_3$	117.056	-1.7
Taurine	$C_2H_6NO_3S$	124.008	-0.8
Pyroglutamate	$C_5H_6NO_3$	128.036	-1.6
Aspartate	$C_4H_6NO_4$	132.031	-2.3
3-Hydroxypicolinic acid	$C_6H_4NO_3$	138.020	-0.7
Glutamine	$C_5H_9N_2O_3$	145.062	-1.4
Glutamic acid	$C_5H_8NO_4$	146.046	0.7
2-Hydroxyglutarate	$C_5H_7O_5$	147.030	-2.0
Xanthine	$C_5H_3N_4O_2$	151.026	-1.3
N-acetylaspartic acid	$C_6H_8NO_5$	174.041	0.1
Ascorbic acid	$C_6H_7O_6$	175.025	2.3
Gluconic acid	$C_6H_{11}O_7$	195.051	0.5
Phosphatidic acid	$C_6H_8O_7Cl$	226.996	0.9
Glycerophosphoglycerol	$C_6H_{14}O_8P$	245.043	-0.8
Glutathione	$C_{10}H_{82}N_3O_6S$	306.076	2.6
Fatty Acids			
FA 8:0	$C_8H_{15}O_2$	143.108	0.7
FA 9:0	$C_9H_{17}O_2$	157.124	-0.6
FA 14:1	$C_{14}H_{25}O_2$	225.186	-0.9
FA 15:0	$C_{15}H_{29}O_2$	241.218	4.1
FA 16:1	$C_{16}H_{29}O_2$	253.217	-0.8
FA 17:0	$C_{17}H_{33}O_2$	269.248	0.7
FA hydroxy 16:0	$C_{16}H_{31}O_3$	271.228	0.4
Ceramides			
Cer d32:1	$C_{32}H_{63}NO_3Cl$	544.452	0.9
Cer d16:1/17:0	$C_{33}H_{65}NO_3Cl$	558.466	0.7
Cer d34:2	$C_{34}H_{65}NO_3Cl$	570.466	1.8
Cer d34:1	$C_{34}H_{67}NO_3Cl$	572.481	0.5
Cer d18:16:0	$C_{34}H_{69}NO_3Cl$	574.496	1.6
Cer d36:2	$C_{36}H_{69}NO_3Cl$	598.496	-1.7
Cer d36:1	$C_{36}H_{71}NO_3Cl$	600.512	-2.4
Cer m18:1/22:0	$C_{40}H_{79}NO_2Cl$	640.580	1.4
Cer d38:1	$C_{40}H_{79}NO_3Cl$	656.575	-0.1
Cer m18:1/24:1	$C_{42}H_{81}NO_2Cl$	666.597	2.1
Cer d41:2	$C_{41}H_{79}NO_3Cl$	668.577	-0.4
Cer m42:1	$C_{42}H_{83}NO_2Cl$	668.611	1.3
Cer d18:1/23:0	$C_{41}H_{81}NO_2Cl$	670.590	2.4
Cer d40:0(2OH)	$C_{40}H_{81}NO_4Cl$	674.587	-2.1
Cer d42:0	$C_{42}H_{81}NO_3Cl$	682.590	1.3
Cer d42:1	$C_{42}H_{83}NO_3Cl$	684.607	1.0
Cer d42:1	$C_{42}H_{83}NO_3Cl$	684.607	0.1
Cer d42:0	$C_{42}H_{85}NO_3Cl$	686.622	0.3
PE-Cer d36:1	$C_{38}H_{76}N_2O_6P$	687.545	-0.4
Cer d18:1/25:0	$C_{43}H_{85}NO_3Cl$	698.622	0.3
Cer d18:1/26:1	$C_{44}H_{85}NO_3Cl$	710.626	4.9
Cer d18:1/26:0	$C_{44}H_{87}NO_3Cl$	712.637	1.5
PE - Cer 36:3	$C_{38}H_{73}N_2O_6PCl$	719.488	2.6
GlcCer d34:1	$C_{40}H_{77}NO_8Cl$	734.532	2.7
PE-Cer d37:1	$C_{39}H_{79}N_2O_6PCl$	737.536	1.5
Cardiolipins			

FA 18:3	$C_{18}H_{29}O_2$	277.217	0.7	CL 68:5	$C_{77}H_{138}O_{17}P_2$	698.472	0.9
FA 18:2	$C_{18}H_{31}O_2$	279.233	1.1	CL 70:7	$C_{79}H_{138}O_{17}P_2$	710.470	1.8
FA 18:1	$C_{18}H_{32}O_2$	281.248	0.7	CL 70:6	$C_{79}H_{140}O_{17}P_2$	711.477	3.0
FA 18:0	$C_{18}H_{35}O_2$	283.264	1.1	CL 70:5	$C_{79}H_{142}O_{17}P_2$	712.484	4.2
FA 20:5	$C_{20}H_{29}O_2$	301.217	0.7	CL 72:8	$C_{81}H_{140}O_{17}P_2$	723.479	0.4
FA 20:4	$C_{20}H_{31}O_2$	303.233	1.0	CL 72:7	$C_{81}H_{142}O_{17}P_2$	724.484	3.6
FA 20:3	$C_{20}H_{33}O_2$	305.248	-1.0	CL 72:6	$C_{81}H_{144}O_{17}P_2$	725.494	0.6
FA 20:2	$C_{20}H_{35}O_2$	307.264	-1.6	CL 72:4	$C_{81}H_{148}O_{17}P_2$	727.507	-1.9
FA 20:1	$C_{20}H_{37}O_2$	309.280	2.3	CL 74:10	$C_{83}H_{140}O_{17}P_2$	735.478	1.2
FA 20:0	$C_{20}H_{39}O_2$	311.295	-1.3	CL 74:9	$C_{83}H_{142}O_{17}P_2$	736.485	2.0
FA 18:2	$C_{18}H_{32}O_2Cl$	315.209	1.3	CL 74:8	$C_{83}H_{144}O_{17}P_2$	737.492	3.3
FA 18:1	$C_{18}H_{34}O_2Cl$	317.225	1.3	CL 74:7	$C_{83}H_{146}O_{17}P_2$	738.501	1.1
FA hydroxy 20:4	$C_{20}H_{31}O_3$	319.228	-1.6	CL 76:10	$C_{85}H_{144}O_{17}P_2$	749.492	2.8
FA 18:0	$C_{18}H_{36}O_2Cl$	319.241	0.6	CL 76:9	$C_{85}H_{146}O_{17}P_2$	750.504	2.9
FA hydroxy 20:3	$C_{20}H_{33}O_3$	321.243	2.5	CL 76:8	$C_{85}H_{148}O_{17}P_2$	751.509	2.0
FA 22:6	$C_{22}H_{31}O_2$	327.233	1.2	CL 76:7	$C_{85}H_{150}O_{17}P_2$	752.516	2.5
FA 22:5	$C_{22}H_{33}O_2$	329.248	1.2	CL 36:4	$C_{45}H_{82}O_{15}P_2Cl$	959.482	2.4
FA 22:4	$C_{22}H_{35}O_2$	331.264	1.2	*Glycerophosphoinositols*			
FA 22:3	$C_{22}H_{37}O_2$	333.279	1.5	LysoPI (16:0/0:0)	$C_{25}H_{48}O_{12}P$	571.290	1.8
FA 20:4	$C_{20}H_{32}O_2Cl$	339.209	0.9	PI (32:1)	$C_{41}H_{76}O_{13}P$	807.502	1.6
FA 22:0	$C_{22}H_{43}O_2$	339.326	1.5	PI (32:0)	$C_{41}H_{78}O_{13}P$	809.514	5.6
FA hydroxy 22:6	$C_{22}H_{31}O_3$	343.230	-5.0	PI (34:2)	$C_{43}H_{78}O_{13}P$	833.517	2.4
FA 23:1	$C_{23}H_{43}O_2$	351.326	2.3	PI (34:1)	$C_{43}H_{80}O_{13}P$	835.532	2.5
FA 23:0	$C_{23}H_{45}O_2$	353.342	1.4	PI (O-23:0)	$C_{42}H_{83}O_{12}PCl$	845.532	0.2
FA 24:5	$C_{24}H_{37}O_2$	357.280	1.1	PI (25:1)	$C_{44}H_{82}O_{13}P$	849.552	-2.4
FA 24:4	$C_{24}H_{39}O_2$	359.295	0.8	PI (36:4)	$C_{45}H_{78}O_{13}P$	857.517	1.6
FA 24:3	$C_{24}H_{41}O_2$	361.311	1.7	PI (36:3)	$C_{45}H_{80}O_{13}P$	859.535	-0.6
FA 24:1	$C_{24}H_{45}O_2$	365.342	1.4	PI (36:2)	$C_{45}H_{82}O_{13}P$	861.549	1.5
FA 22:4	$C_{22}H_{36}O_2Cl$	367.242	-1.9	PI (36:1)	$C_{45}H_{84}O_{13}P$	863.565	2.8
FA 24:0	$C_{24}H_{47}O_2$	367.358	1.1	PI (37:3)	$C_{46}H_{82}O_{13}P$	873.551	-0.8
FA hydroxy 24:0	$C_{24}H_{47}O_3$	383.353	1.3	PI (38:6)	$C_{47}H_{78}O_{13}P$	881.520	1.1
FA 26:3	$C_{26}H_{45}O_2$	389.342	0.8	PI (38:3)	$C_{47}H_{84}O_{13}P$	887.565	-0.2
FA 26:2	$C_{26}H_{47}O_2$	391.358	1.0	PI (40:6)	$C_{49}H_{82}O_{13}P$	909.547	-3.0
FA 26:1	$C_{26}H_{49}O_5$	393.373	1.0	PI (39:4)	$C_{48}H_{85}O_{13}PCl$	935.544	2.0
FA 26:0	$C_{26}H_{51}O_2$	395.389	1.5	*Glycerophosphoinositols*			
Glycerolipids				LysoPI 15:0	$C_{24}H_{46}O_{12}P$	557.273	0.5
MG 18:0	$C_{21}H_{40}O_4Cl$	391.262	1.5	LysoPI O-16:0	$C_{25}H_{50}O_{11}P$	557.309	0.9
MG 22:6	$C_{25}H_{38}O_4Cl$	437.246	1.1	LysoPI 18:0	$C_{27}H_{52}O_{12}P$	599.320	0.5
DG 24:0/0:0	$C_{27}H_{51}O_5$	455.376	4.0	Lyso PI 20:4	$C_{29}H_{48}O_{12}P$	619.290	-2.4
DG 32:1/0:0	$C_{35}H_{66}O_5Cl$	601.459	1.7	PI O-33:2 or PI P-33:1	$C_{42}H_{79}O_{12}PCl$	841.501	-1.0
DG 32:0/0:0	$C_{35}H_{68}O_5Cl$	603.476	0.5	PI P-18:0/17:2	$C_{44}H_{81}O_{12}PCl$	867.516	0.2
DG 34:3/0:0	$C_{37}H_{66}O_5Cl$	625.459	1.6	PI O-35:2 or PI P-35:1	$C_{44}H_{83}O_{12}PCl$	869.531	0.5
DG 34:2/0:0	$C_{37}H_{68}O_5Cl$	627.475	1.1	PI 37:4	$C_{46}H_{80}O_{13}P$	871.534	3.3

DG 34:1/0:0	$C_{37}H_{70}O_5Cl$	629.491	0.6
DG 36:4/0:0	$C_{39}H_{68}O_5Cl$	651.475	1.2
DG 36:3/0:0	$C_{39}H_{70}O_5Cl$	653.492	0.2
DG 36:2/0:0	$C_{39}H_{72}O_5Cl$	655.507	0.3
DG 38:6/0:0	$C_{41}H_{68}O_5Cl$	675.475	1.3
DG 38:5/0:0	$C_{41}H_{70}O_5Cl$	677.493	-2.2
DG 38:4/0:0	$C_{41}H_{72}O_5Cl$	679.509	-2.2
DG 40:7/0:0	$C_{43}H_{70}O_5Cl$	701.489	3.6
DG 40:6/0:0	$C_{43}H_{72}O_5Cl$	703.506	1.6
DG 40:5/0:0	$C_{43}H_{74}O_5Cl$	705.523	1.1
Glycerophosphoethanolamines			
LysoPE P-16:0	$C_{21}H_{43}NO_6P$	436.284	-2.3
LysoPE O-18:1	$C_{23}H_{47}NO_6P$	464.316	-2.8
LysoPE 18:1	$C_{23}H_{45}NO_7P$	478.295	-2.5
LysoPE 18:0	$C_{23}H_{47}NO_7P$	480.311	-2.7
LysoPE 20:4	$C_{23}H_{43}NO_7P$	500.280	-2.6
PE 18:1/1:0	$C_{24}H_{45}NO_8P$	506.288	1.2
PE 20:4/1:0	$C_{26}H_{43}NO_8P$	528.273	-0.8
PE 20:3/1:0	$C_{26}H_{45}NO_8P$	530.291	-4.5
PE O-34:3 or PE P-34:2	$C_{39}H_{73}NO_7P$	698.515	3.3
PE O-34:2 or PE P-34:1	$C_{39}H_{75}NO_7P$	700.527	2.1
PE 34:2	$C_{39}H_{73}NO_8P$	714.505	3.8
PE 34:1	$C_{39}H_{75}NO_8P$	716.522	2.1
PE 34:0	$C_{23}H_{47}NO_6P$	718.538	1.9
PE P-18:0/18:4	$C_{41}H_{73}NO_7Cl$	722.512	1.9
PE O-36:3 or P-36:2	$C_{41}H_{77}NO_7P$	726.545	0.8
PE 35:1	$C_{40}H_{77}NO_8P$	730.537	3.3
PE 36:3	$C_{41}H_{75}NO_8P$	740.520	3.8
PE 36:2	$C_{41}H_{77}NO_8P$	742.538	1.9
PE O-38:5 or PE P-38:4	$C_{43}H_{77}NO_7P$	750.543	-1.2
PE 38:5	$C_{43}H_{75}NO_8P$	764.522	-3.2
PE 38:4	$C_{43}H_{77}NO_8P$	766.538	6.2
PE 38:3	$C_{43}H_{79}NO_8P$	768.557	-3.3
PE 38:2	$C_{43}H_{81}NO_8P$	770.566	1.2
PE 38:1	$C_{43}H_{83}NO_8P$	772.585	1.9
PE 39:6	$C_{44}H_{75}NO_8P$	776.522	1.8
PE 39:5	$C_{44}H_{77}NO_8P$	778.538	-1.0
PE O-40:5 or PE P-40:4	$C_{45}H_{81}NO_7P$	778.576	0.5
PE 40:5	$C_{45}H_{79}NO_8P$	792.555	-1.6
PE 37:1	$C_{42}H_{82}NO_8PCl$	794.549	-0.8
PI 38:6	$C_{47}H_{78}O_{13}P$	881.516	3.1
PI 38:5	$C_{47}H_{80}O_{13}P$	883.533	1.1
PI 38:4	$C_{47}H_{82}O_{13}P$	885.548	1.8
PI 40:4	$C_{49}H_{86}O_{13}P$	913.579	2.1
PI 40:3	$C_{49}H_{88}O_{13}P$	915.595	1.7
Glycerophosphoserines			
PS P-34:1	$C_{40}H_{75}NO_9P$	744.518	1.1
PS 16:0/18:1	$C_{40}H_{75}NO_{10}P$	760.515	2.0
PS O-36:4 or PS P-36:3	$C_{42}H_{75}NO_9P$	768.521	-3.4
PS P-36:2 or PS O-36:3	$C_{42}H_{77}NO_9P$	770.532	2.2
PS O-36:2 or PS P-36:1	$C_{42}H_{79}NO_9P$	772.549	1.0
PS 36:3	$C_{42}H_{75}NO_{10}P$	784.513	0.1
PS 36:2	$C_{42}H_{77}NO_{10}P$	786.528	1.5
PS 18:0/18:1	$C_{42}H_{79}NO_{10}P$	788.546	-2.4
PS O-38:4 or P-38:3	$C_{44}H_{79}NO_9P$	796.547	3.9
PS 38:4	$C_{44}H_{77}NO_{10}P$	810.528	1.5
PS 38:3	$C_{44}H_{79}NO_{10}P$	812.544	1.2
PS 38:2	$C_{44}H_{81}NO_{10}P$	814.558	3.3
PS 38:1	$C_{44}H_{83}NO_{10}P$	816.574	1.8
PS O-39:0	$C_{45}H_{89}NO_9P$	818.625	4.3
PS O-40:4 or PS P-40:3	$C_{46}H_{83}NO_9P$	824.581	0.1
PS 39:2	$C_{45}H_{83}NO_{10}P$	828.572	4.3
PS 40:6	$C_{46}H_{77}NO_{10}P$	834.527	2.4
PS 40:2	$C_{46}H_{85}NO_{10}P$	842.591	1.3
PS 40:1	$C_{46}H_{87}NO_{10}P$	844.606	2.0
PS 42:3	$C_{48}H_{87}NO_{10}P$	868.603	-5.1
PS 42:2	$C_{48}H_{89}NO_{10}P$	870.622	-1.1
PS 42:1	$C_{48}H_{91}NO_{10}P$	872.637	-1.9
Glycerophosphoglycerols			
LysoPG 16:0	$C_{22}H_{44}O_9P$	483.273	-2.1
LysoPG 18:2	$C_{24}H_{44}O_9P$	507.274	-3.1
LysoPG 18:1	$C_{24}H_{46}O_9P$	509.288	-2.9
LysoPG 22:6	$C_{28}H_{44}O_9P$	555.274	-0.7
PG 34:3	$C_{40}H_{72}O_{10}P$	743.489	-2.8
PG 34:2	$C_{40}H_{74}O_{10}P$	745.502	1.5
PG 16:0/18:1	$C_{40}H_{76}O_{10}P$	747.520	1.6
PG 36:4	$C_{42}H_{74}O_{10}P$	769.501	2.3
PG 18:2/18:1	$C_{42}H_{76}O_{10}P$	771.520	-2.5
PG 18:1/18:1	$C_{42}H_{78}O_{10}P$	773.533	0.9
PG 18:0/18:1	$C_{42}H_{80}O_{10}P$	775.548	1.7

PE 40:4	$C_{45}H_{81}NO_8P$	794.571	0.7
PE 39:4	$C_{44}H_{80}NO_8PCl$	816.531	0.7
PE 39:2	$C_{44}H_{84}NO_8PCl$	820.562	2.9
PE 39:1	$C_{44}H_{86}NO_8PCl$	822.576	-4.0
PE 41:6	$C_{46}H_{80}NO_8PCl$	840.535	-2.7
PE 41:5	$C_{46}H_{82}NO_8PCl$	842.550	1.1
PE 41:4	$C_{46}H_{84}NO_8PCl$	844.562	-1.4
PE 43:6	$C_{48}H_{84}NO_8PCl$	868.564	-3.4
PE 43:2	$C_{48}H_{92}NO_8PCl$	876.629	0.8
Monoacylglycerophosphates			
PA 32:0	$C_{35}H_{68}O_8P$	647.468	3.2
PA 24:2	$C_{37}H_{68}O_8P$	671.464	2.2
PA 24:1	$C_{37}H_{70}O_8P$	673.481	1.6
PA 36:4	$C_{39}H_{68}O_8P$	695.465	1.6
PA 36:3	$C_{39}H_{70}O_8P$	697.480	1.9
PA 36:1	$C_{39}H_{74}O_8P$	701.512	1.0
PA O-38:2 or PA P-38:1	$C_{41}H_{79}O_7PCl$	749.528	1.3
PG 18:0/18:0	$C_{42}H_{82}O_{10}P$	777.565	0.3
PG 38:6	$C_{44}H_{74}O_{10}P$	793.501	1.9
PG 38:5	$C_{44}H_{76}O_{10}P$	795.515	4.7
PG 38:4	$C_{44}H_{78}O_{10}P$	797.531	3.1
PG 38:3	$C_{44}H_{80}O_{10}P$	799.547	3.5
PG 38:2	$C_{44}H_{82}O_{10}P$	801.563	2.1
PG 40:8	$C_{46}H_{74}O_{10}P$	817.501	1.7
PG 40:7	$C_{46}H_{76}O_{10}P$	819.516	2.7
PG 40:6	$C_{46}H_{78}O_{10}P$	821.531	3.5
PG 40:5	$C_{46}H_{80}O_{10}P$	823.548	1.8
PG 42:7	$C_{48}H_{80}O_{10}P$	847.546	3.8
PG 22:6/22:6	$C_{50}H_{74}O_{10}P$	865.500	3.4

APPENDIX A3: SPATIALLY CONTROLLED MOLECULAR ANALYSIS OF BIOLOGICAL SAMPLES USING NANODROPLET ARRAYS AND DIRECT DROPLET ASPIRATION

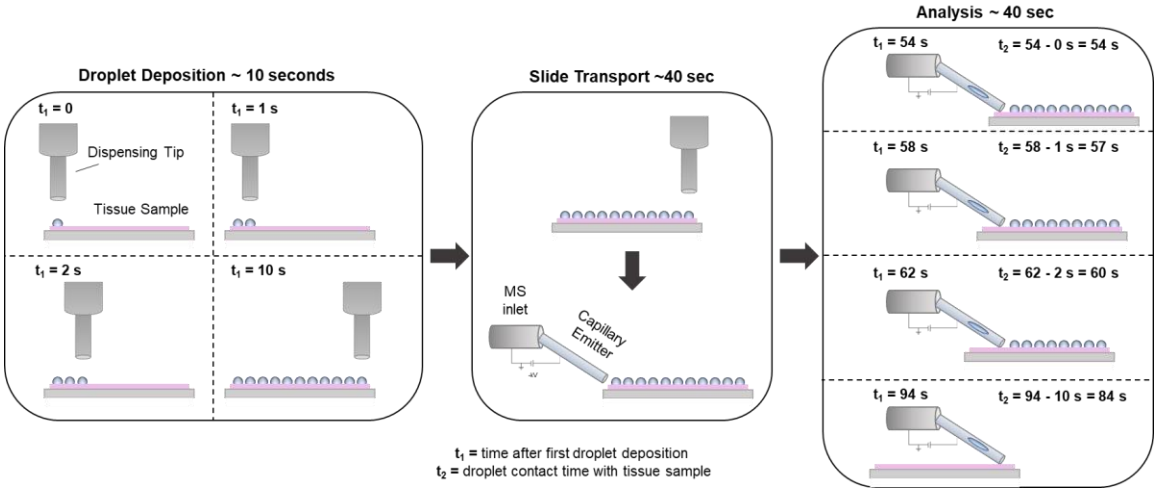

Figure A3.1: Imaging workflow with uncoupled droplet deposition and analysis, illustrated for a single line of 11 droplets.

Droplets were deposited onto tissue samples at a rate of a droplet per second. The sample slide was transported after deposition of the droplet line and mounted on a 2D moving stage in approximately under 40 seconds. Time between droplet analysis was measured to be 4.1 ± 1.1 s (n=10). Note that maximum difference in t_2 is 30 s between the first and last droplet. t_2 (droplet contact time with tissue sample), t_1 (time after first droplet deposition).

Vial	Drops added	Δ mass	Volume per drop (nL)
1	5000	0.0024	0.50
2	5000	0.0023	0.48
3	5000	0.0024	0.50
4	6000	0.0027	0.47
5	6000	0.0027	0.47
6	6000	0.0028	0.49

$$0.0024\ g\ \times \frac{1.00\ mL}{0.9605\ g} = 0.0024986\ mL$$

$$\frac{0.0024986\ mL}{5000\ drops} = 4.9974\ x\ 10^{-7} mL\ per\ drop \sim 0.50\ nL\ per\ drop$$

Figure A3.2: Volume determination for single DMF droplets using change in mass.

Using the picoliter dispenser, drops were dispensed into plastic Eppendorf tubes and sealed prior to obtaining mass of the dispensed droplets. Density of DMF was experimentally determined gravimetrically, and was used to determine the volume dispensed, and the volume per drop for each trial. Dispensed drops were determined to contain 0.49 ± 0.01 nL DMF per drop (avg ± st dev).

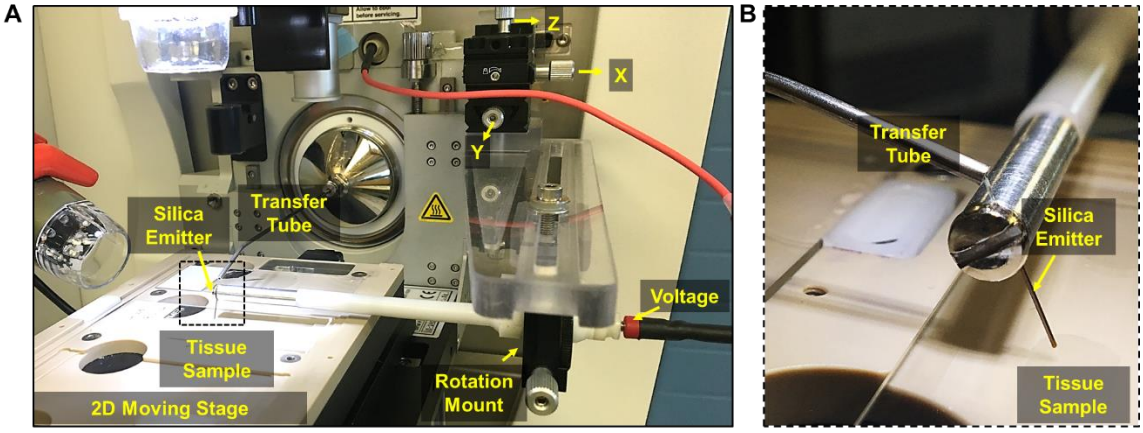

Figure A3.3: Optical image of the discrete droplet sampling setup coupled to a Q Exactive Orbitrap system.

A cable connecting the MS voltage source and the emitter arm was used to provide a voltage bias to the silica emitter. A metal rod going from the voltage pin to the emitter grasper ensured conductivity through the arm holder. The rest of the arm material was made from PTFE to reduce weight and protect the user from the high voltage source (A). Zoom-in view of the silica emitter grasped by the arm holder and aligned with the transfer tube connected to the MS inlet (B).

Table A3.1: Properties of different solvent systems used for lipid analysis by MS.

Properties	**DMF**	**Water**	**Ethanol**	**ACN**	**Methanol**
Vapor Pressure (Torr)	3	18	44	89	97
Surface Tension (mN/m)	37	73	22	19	23
Dielectric Constant	38	80	25	37	33

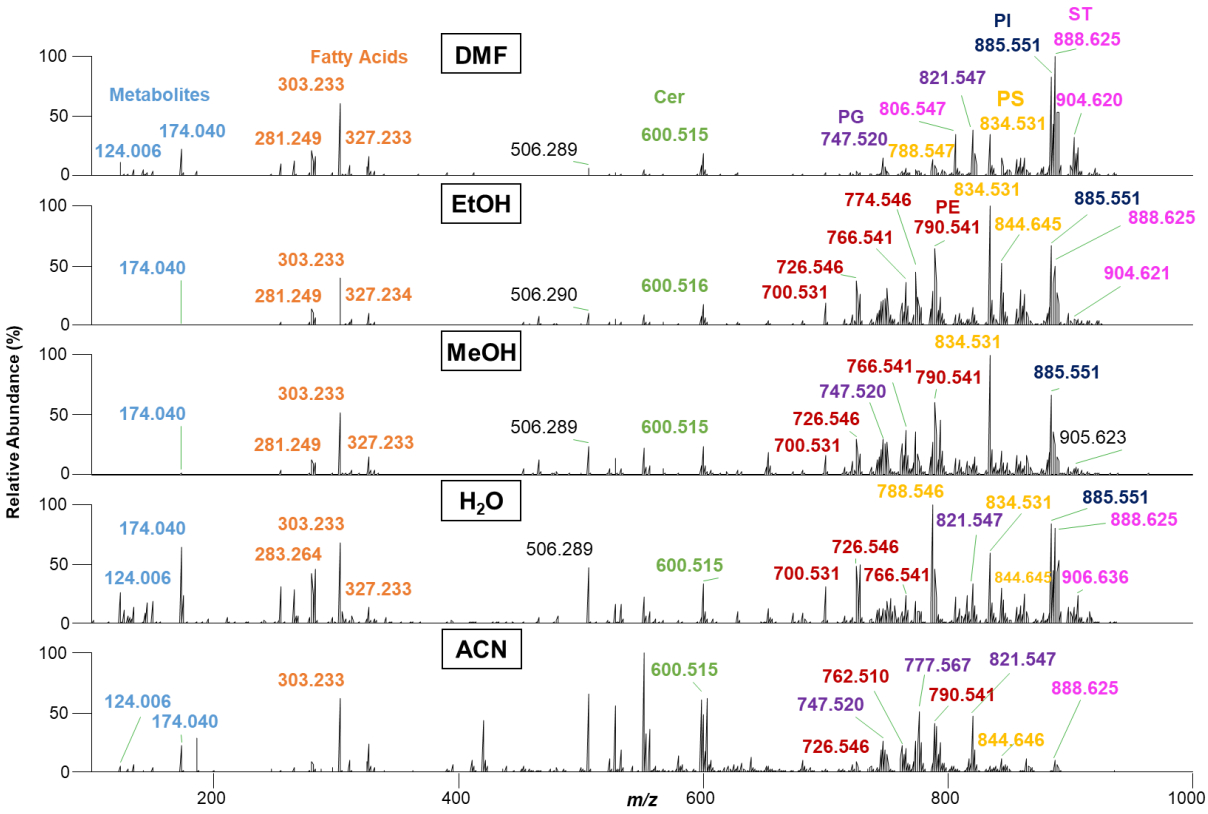

Figure A3.4: Discrete droplet sampling spectra obtained from analyzing droplets of different solvent composition deposited on mouse brain homogenate tissue sections.

Species are color-coded according to class: metabolites, fatty acids, ceramides (Cer), glycerophosphoglycerol (PG), glycerophosphoserine (PS), sulfatide (ST), glycerophosphoethanolamine (PE), glycerophosphoinositol (PI).

Table A3.2: Diameters and corresponding volumes and number of drops for droplets dispensed as arrays onto mouse brain tissue samples.

Standard deviations and RSDs are shown as metrics for size reproducibility of replicate droplets. Measurements were obtained using a calibrated Dino Lite Microscope camera.

Volume (nL)	**Number of drops**	**Diameter (µm)**	**N**	**SD (µm)**	**RSD (%)**	**Average RSD (%)**
50.0	100	647.0	6	6.0	0.9	1.5
45.0	90	629.0	5	3.8	0.6	**St. Dev RSD (%)**
40.0	80	610.3	10	6.7	1.1	0.7
35.0	70	593.2	10	6.0	1.0	
32.5	65	566.1	10	6.4	1.1	
30.0	60	554.5	10	7.7	1.4	
27.5	55	546.5	10	4.9	0.9	
25.0	50	519.6	10	6.9	1.3	
22.5	45	499.1	10	15.9	3.2	
20.0	40	491.4	10	10.2	2.1	
17.5	35	474.3	10	6.3	1.3	
15.0	30	457.3	10	8.2	1.8	
12.5	25	437.1	10	8.9	2.0	
10.0	20	399.6	10	3.4	0.9	
7.5	15	370.6	10	5.7	1.5	
5.0	10	322.6	10	5.9	1.8	
2.5	5	250.7	10	7.6	3.0	

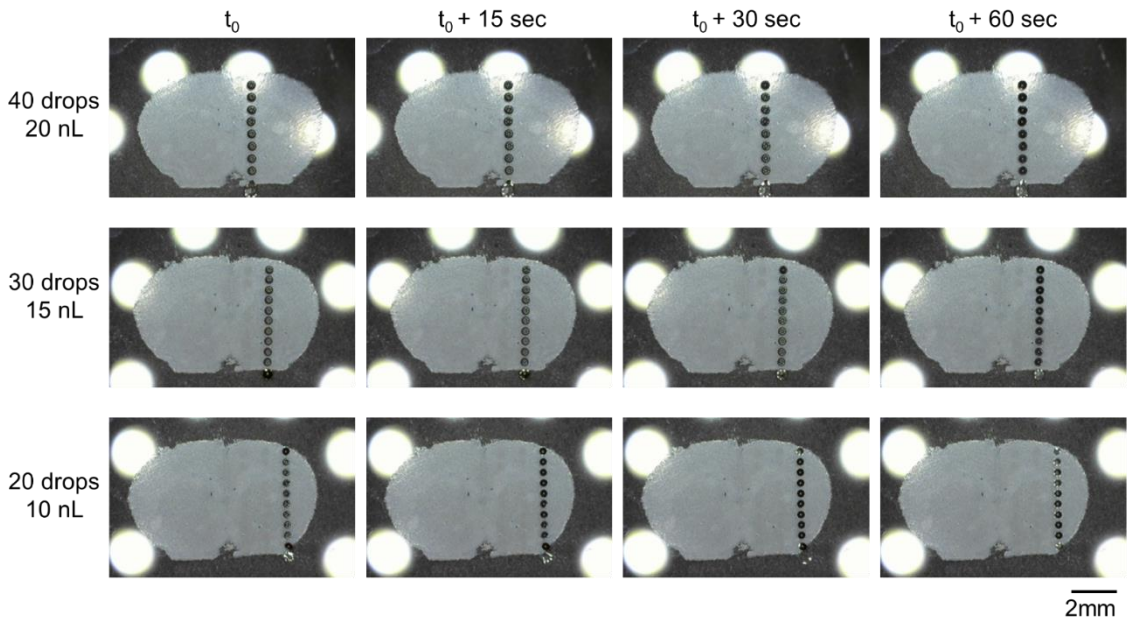

Figure A3.5: Lines of droplets of 20, 15, and 10 nL volumes deposited onto mouse brain tissue sections.

Optical images were taken following dispensing of the droplets and transferring the slide to the microscope stage (t_0), and at multiple time points thereafter.

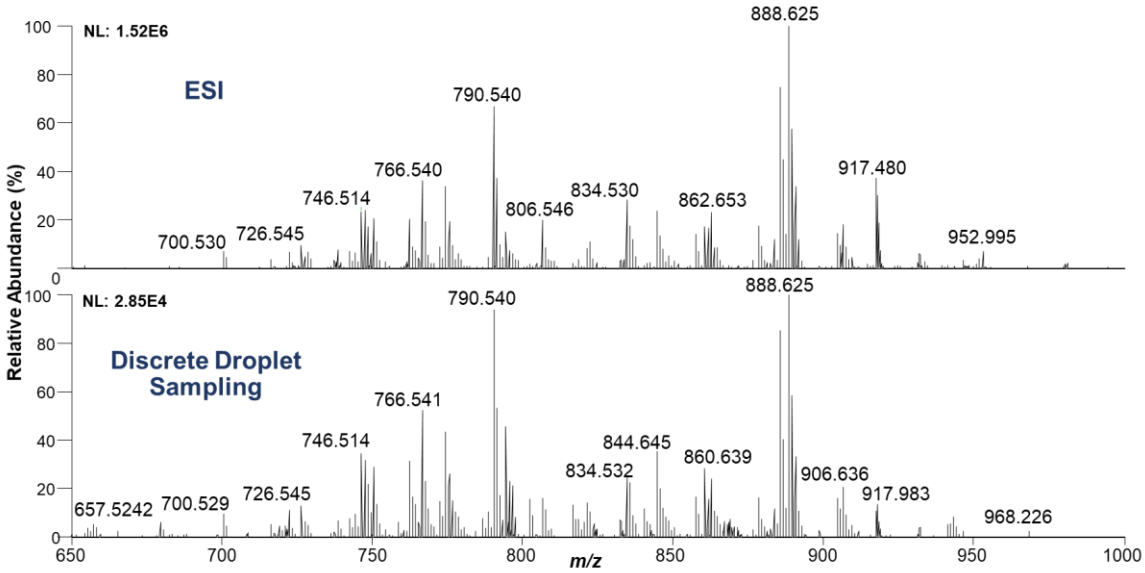

Figure A3.6: Comparison of mass spectra obtained from brain lipid extract analysis by ESI (top) and discrete droplet sampling (bottom).

Lipids were extracted directly from brain tissue sections with DMF and diluted in a 1:1 mixture of ACN:DMF. A 5 µL/min flow rate of was used for ESI experiments. Lipid droplets of 0.2 µL volume were analyzed. Note that the solution used for direct droplet sampling was 4 times more concentrated.

Table A3.3: Measured diameters for droplets used in MS imaging of mouse brain tissue samples shown in Figure 4.3.

Measurements were obtained using a calibrated Dino Lite Microscope camera. Note that these values are slightly different than those reported Table S2 due to slight changes in working dispenser parameters and pneumatic pressures.

	Diameter (µm)	**N**	**St. Dev**	**RSD (%)**
20 drops	386.6	10	11.9	3.1
30 drops	424.1	7	10.8	2.6
40 drops	496.3	8	11.6	2.3

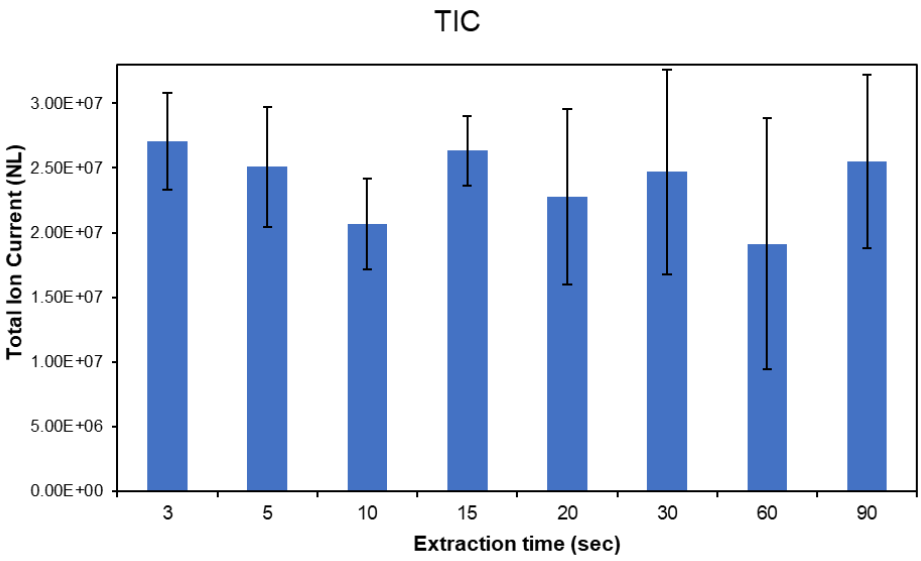

Figure A3.7: Total ion count versus droplet-to-surface contact time (extraction time).

Replicate lines of 50 nL droplets (n= 7-13 droplets per extraction time) were deposited onto mouse brain homogenate tissue samples and analyzed by discrete droplet sampling. No overall trend in total ion count was observed as a function of extraction time within the times evaluated. An ANOVA test was also performed (p-value = 0.079) revealing a non-significant change between all groups.

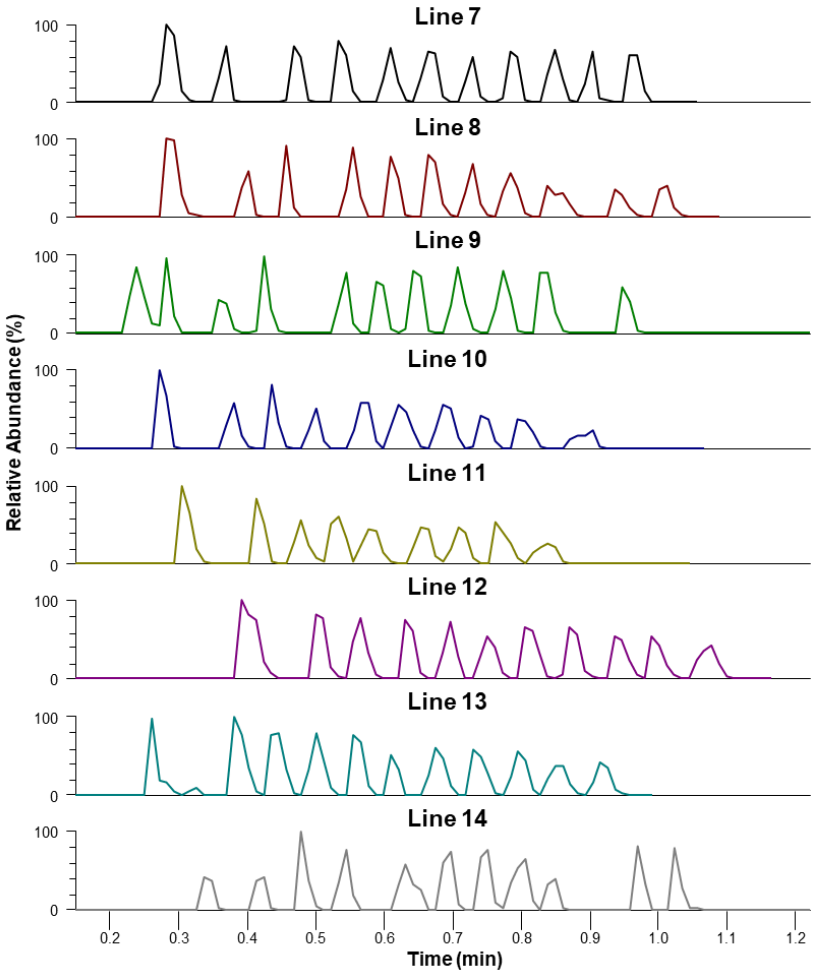

Figure A3.8: Total ion current chromatograms for eight consecutive droplet lines used for MS imaging of a mouse brain tissue sample at a spatial resolution of 424 ± 11 µm.

Each spike in ion current corresponds to the analysis of an individual droplet of ~15 nL volume. Note that the number of spikes/droplets changes between the lines due to changes in the tissue section dimension in the y-axis.

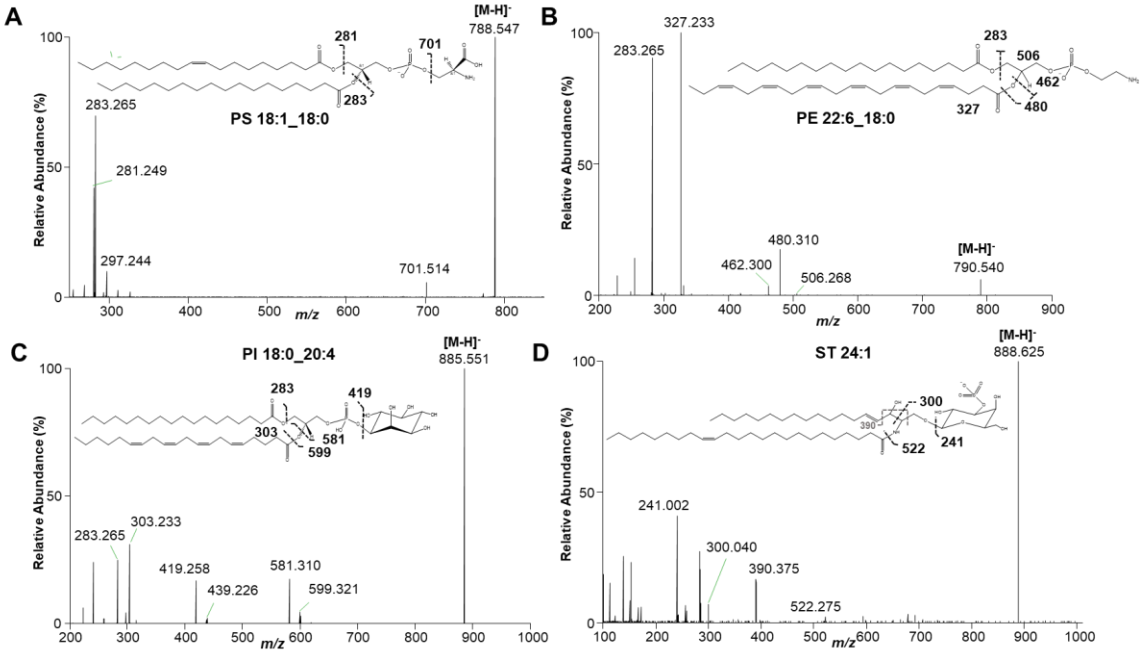

Figure A3.9: Representative MS/MS spectra of lipid species detected from mouse brain tissue samples.

Tandem MS measurements were performed using HCD and the orbitrap for analysis. Note that fatty acid chain stereochemistry, as well as double bond positions, are not determined by this approach.

Table A3.4: Most abundant *m/z* values detected from MS analysis of mouse brain tissue sections.

Attributions were assigned based on high mass accuracy and tandem MS measurements. Lipid species are defined by number of carbons and double bonds in the fatty acid chains.

Detected *m/z*	**Ion**	**Attribution**	**Molecular Formula**	**Mass Error (ppm)**
255.233	M-H	FA 16:1	$C_{16}H_{33}O_2$	0.4
281.249	M-H	FA 18:1	$C_{18}H_{33}O_2$	-0.4
283.264	M-H	FA 18:0	$C_{18}H_{35}O_2$	0.4
303.233	M-H	FA 20:4	$C_{20}H_{31}O_2$	-0.1
327.233	M-H	FA 22:6	$C_{22}H_{31}O_2$	-0.6
598.498	M+Cl	Cer d36:2	$C_{36}H_{69}NO_3Cl$	-1.7
600.513	M+Cl	Cer d36:1	$C_{36}H_{71}NO_3Cl$	-0.8
721.504	M-H	PG 32:0	$C_{38}H_{74}O_{10}P$	-1.9
747.519	M-H	PG 34:1	$C_{40}H_{76}O_{10}P$	-1.1
762.509	M-H	PE 38:6	$C_{43}H_{73}NO_8P$	-1.2
766.541	M-H	PE 38:4	$C_{43}H_{77}NO_8P$	-1.8
774.544	M-H	PE P-18:0/22:6	$C_{45}H_{77}NO_7P$	-0.1
788.546	M-H	PS 34:1	$C_{42}H_{79}NO_{10}P$	-1.3
790.540	M-H	PE 40:6	$C_{45}H_{77}NO_8P$	-0.9
806.546	M-H	ST 18:0	$C_{42}H_{80}NO_{11}S$	-0.4
822.545	M-H	ST 18:0 (OH)	$C_{42}H_{80}NO_{12}S$	-5.1
834.530	M-H	PS 40:6	$C_{46}H_{77}NO_{10}P$	-1.2
844.645	M+Cl	Gal/GluCer d24:1	$C_{48}H_{91}NO_8Cl$	-1.7
857.519	M-H	PI 36:4	$C_{45}H_{78}O_{13}P$	-0.8
865.503	M-H	PG 44:12	$C_{50}H_{74}O_{10}P$	-0.8
885.550	M-H	PI 38:4	$C_{47}H_{82}O_{13}P$	-0.1
888.625	M-H	ST 24:1	$C_{48}H_{90}NO_{11}S$	-0.6

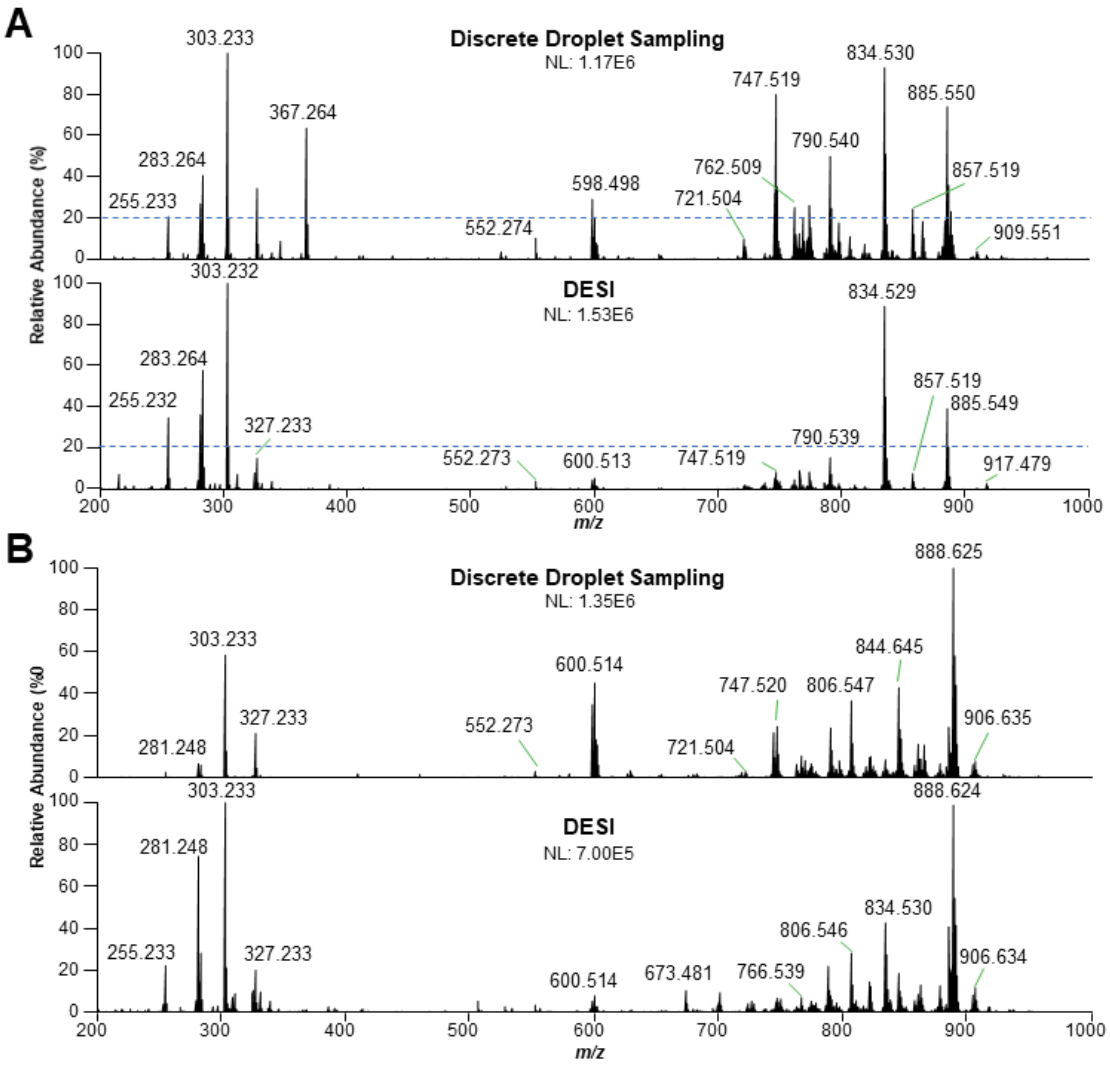

Figure A3.10: Representative mouse brain tissue mass spectra acquired using discrete droplet sampling and DESI from grey matter (A) and white matter (B).

A dashed blue line is included in the grey matter spectra to show the difference in the number of species detected above 20% relative abundance between the two methods.

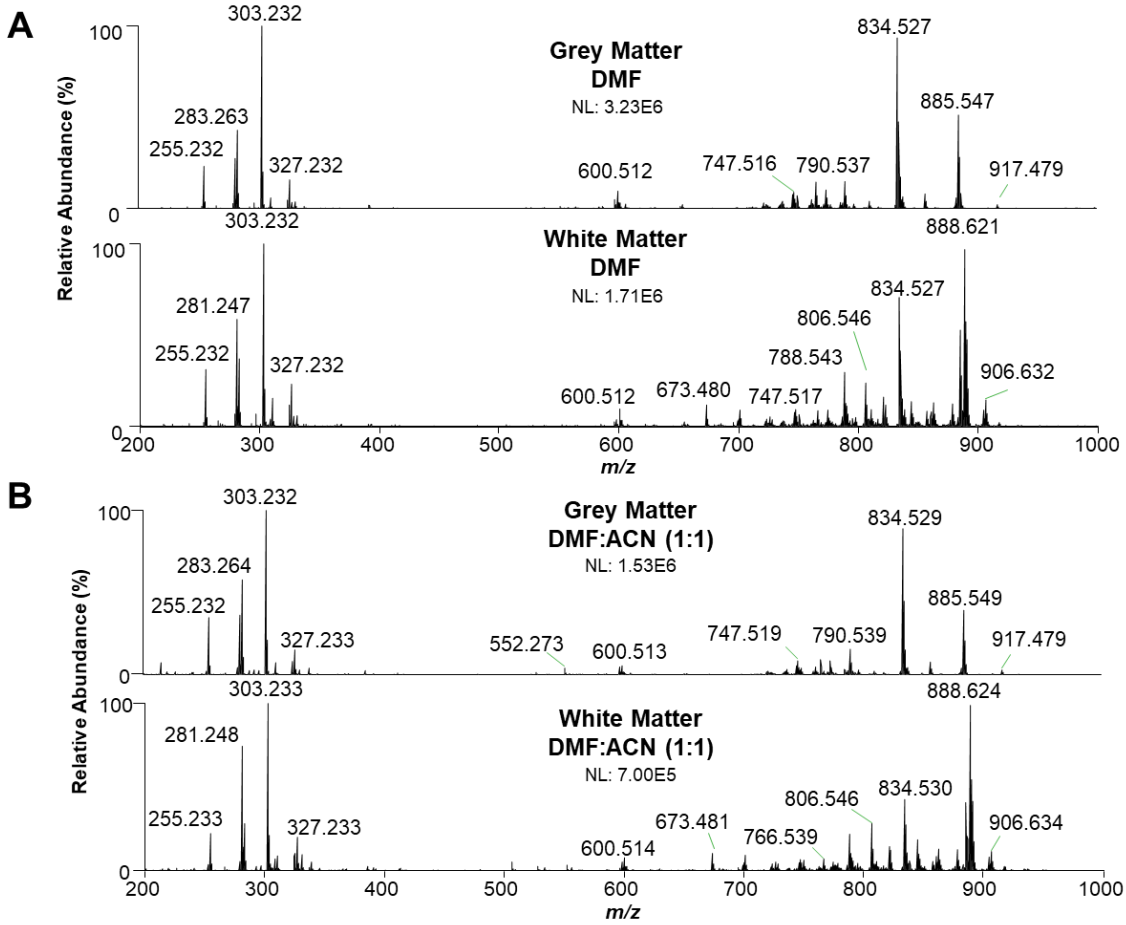

Figure A3.11: Representative mouse brain tissue DESI-MS spectra acquired using DMF (A) and a 1:1 ACN:DMF mixture (B) as the solvent system.

Table A3.5: Most abundant *m/z* values detected from analysis of ovarian cancerous and normal tissue samples.

Attributions were assigned based on high mass accuracy and tandem MS measurements. Lipid species are defined by number of carbons and double bonds in the fatty acid chains. *Species mostly found in ovarian cancer necrotic spectra.

Detected *m/z*	Ion	Attribution	Molecular Formula	Mass Error (ppm)
124.006	M-H	Taurine	$C_2H_6NO_3S$	9.7
175.024	M-H	Ascorbic Acid	$C_6H_7O_6$	3.4
281.249	M-H	FA 18:1	$C_{18}H_{33}O_2$	-1.8
572.483	M+Cl	Cer d34:1	$C_{34}H_{67}NO_3Cl$	-3.3
588.478	M+Cl	Cer d34:1 (2OH)	$C_{34}H_{67}NO_4Cl$	-3.2
600.515	M-Cl	Cer d36:1	$C_{36}H_{71}NO_3Cl$	-4.3
629.496	M+Cl	DG 34:1	$C_{37}H_{70}O_5Cl$	-6.5
656.580	M+Cl	Cer d40:2	$C_{40}H_{79}NO_3Cl$	-6.7
682.595	M+Cl	Cer d42:2	$C_{42}H_{81}NO_3Cl$	-5.7
684.608	M+Cl	Cer d42:1	$C_{42}H_{83}NO_3Cl$	-1.5
722.516	M-H	PE P-36:4	$C_{41}H_{73}NO_7P$	-3.7
**734.537*	M+Cl	Glu/GalCer d 34:1	$C_{40}H_{77}NO_8Cl$	-3.1
742.543	M-H	PE 36:2	$C_{41}H_{77}NO_8P$	-5.3
744.558	M-H	PE 36:1	$C_{41}H_{79}NO_8P$	-3.9
747.521	M-H	PG 34:1	$C_{40}H_{76}O_{10}P$	-4.1
748.531	M-H	PE P-38:5	$C_{43}H_{75}NO_7P$	-3.6
750.546	M-H	PE P-38:4	$C_{43}H_{77}NO_7P$	-2.7
766.543	M-H	PE 38:4	$C_{43}H_{77}NO_8P$	-4.4
771.519	M-H	PG 36:3	$C_{42}H_{76}O_{10}P$	-1.2
773.535	M-H	PG 36:2	$C_{42}H_{78}O_{10}P$	-2.1
788.549	M-H	PS 34:1	$C_{42}H_{79}NO_{10}P$	-6.0
792.533	M+Cl	PC 34:2	$C_{42}H_{80}NO_8PCl$	-1.3
794.548	M+Cl	PC 34:1	$C_{42}H_{82}NO_8PCl$	-1.1
816.535	M+Cl	PC 36:4	$C_{44}H_{80}NO_8PCl$	-3.8
818.550	M+Cl	PC 36:3	$C_{44}H_{82}NO_8PCl$	-3.4
835.537	M-H	PI 34:1	$C_{43}H_{80}O_{13}P$	-3.8
842.551	M+Cl	PC 38:4	$C_{46}H_{82}NO_8PCl$	-4.0
844.567	M+Cl	PC 38:3	$C_{46}H_{84}NO_8PCl$	-5.1
857.522	M-H	PI 36:4	$C_{45}H_{78}O_{13}P$	-3.8
861.553	M-H	PI 36:2	$C_{45}H_{82}O_{13}P$	-3.2
865.506	M-H	PG 44:12	$C_{50}H_{74}O_{10}P$	-4.3
885.553	M-H	PI 38:4	$C_{47}H_{82}O_{13}P$	-3.3
**896.591*	M+Cl	PC 42:6	$C_{50}H_{88}NO_8PCl$	3.7
913.584	M-H	PI 40:4	$C_{49}H_{86}O_{13}P$	-3.0
**980.685*	M+Cl	LacCer(d40:1)	$C_{52}H_{99}NO_{13}Cl$	-3.6
**1004.685*	M+Cl	LacCer(d18:1/24:0)	$C_{54}H_{99}ClNO_{13}$	-4.1
*1006.700	M+Cl	LacCer(d42:2)	$C_{54}H_{101}ClNO_{13}$	-3.5

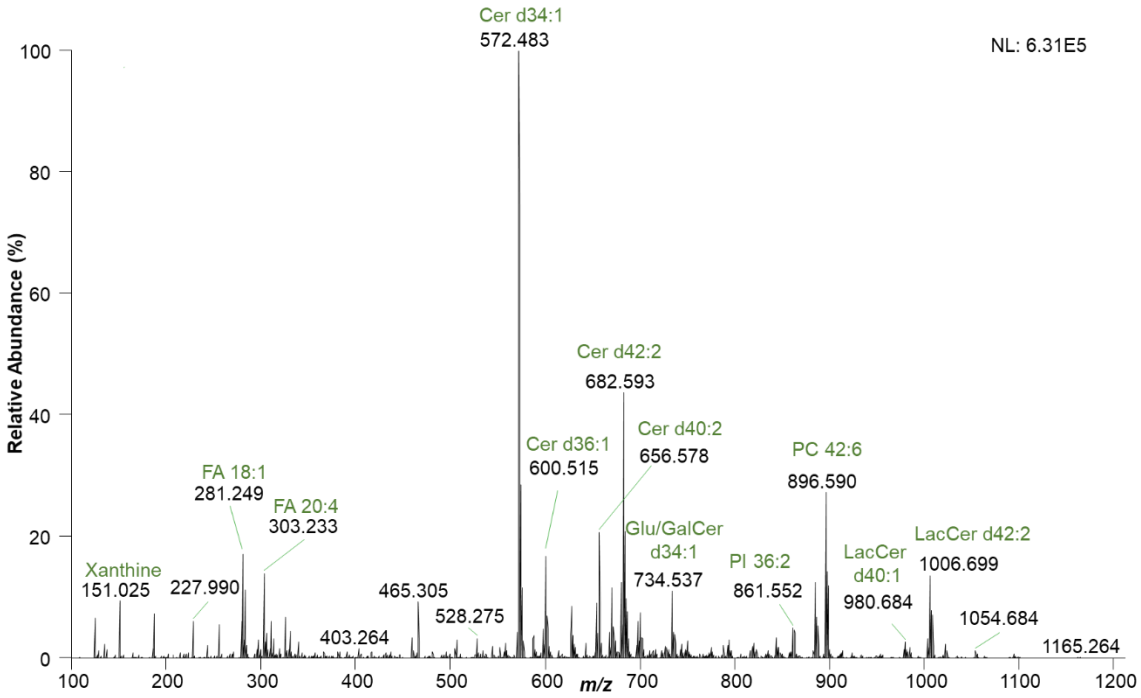

Figure A3.12: Representative MS profile obtained from a necrotic region of a cancerous ovarian tissue section.

Table A3.6: Most abundant *m/z* values detected from MS analysis of human cancerous and normal brain tissue samples.

Attributions were assigned based on high mass accuracy and tandem MS measurements. Lipid species are defined by number of carbons and double bonds in the fatty acid chains.

Detected *m/z*	Ion	Attribution	Molecular Formula	Mass Error (ppm)
124.006	M-H	Taurine	$C_2H_6NO_3S$	12.1
126.904	M	Iodine	I	11.0
151.025	M-H	Xanthine	$C_5H_3N_4O_2$	7.9
174.040	M-H	NAA	$C_6H_8NO_5$	6.3
175.024	M-H	Ascorbic Acid	$C_6H_7O_6$	6.9
215.032	M+Cl	Hexose	$C_6H_{12}O_6Cl$	3.7
255.233	M-H	FA 16:1	$C_{16}H_{33}O_2$	1.6
281.249	M-H	FA 18:1	$C_{18}H_{33}O_2$	-0.4
283.264	M-H	FA 18:0	$C_{18}H_{35}O_2$	1.4
303.233	M-H	FA 20:4	$C_{20}H_{31}O_2$	2.0
327.233	M-H	FA 22:6	$C_{22}H_{31}O_2$	0.9
331.265	M-H	FA 22:4	$C_{22}H_{35}O_2$	-0.9
572.483	M+Cl	Cer d34:1	$C_{34}H_{67}NO_3Cl$	-3.3
598.499	M+Cl	Cer d36:2	$C_{36}H_{69}NO_3Cl$	-2.7
600.515	M-Cl	Cer d36:1	$C_{36}H_{71}NO_3Cl$	-3.2
682.594	M+Cl	Cer d42:2	$C_{42}H_{81}NO_3Cl$	-3.8
700.529	M-H	PE P-24:1	$C_{39}H_{75}NO_7P$	-0.4
722.515	M-H	PE P-36:4	$C_{41}H_{73}NO_7P$	-2.5
726.545	M-H	PE P-36:2	$C_{41}H_{77}NO_7P$	-1.2
742.541	M-H	PE 36:2	$C_{41}H_{77}NO_8P$	-2.8
744.557	M-H	PE 36:1	$C_{41}H_{79}NO_8P$	-2.4
747.521	M-H	PG 34:1	$C_{40}H_{76}O_{10}P$	-3.3
748.530	M-H	PE P-38:5	$C_{43}H_{75}NO_7P$	-1.5
750.545	M-H	PE P-38:4	$C_{43}H_{77}NO_7P$	-0.8
766.543	M-H	PE 38:4	$C_{43}H_{77}NO_8P$	-4.4
774.544	M-H	PE P-40:6	$C_{45}H_{77}NO_7P$	0.4
788.549	M-H	PS 34:1	$C_{42}H_{79}NO_{10}P$	-6.0
790.540	M-H	PE 40:6	$C_{45}H_{77}NO_8P$	-0.9
794.548	M+Cl	PC 34:1	$C_{42}H_{82}NO_8PCl$	-1.1
806.548	M-H	ST 18:0	$C_{42}H_{80}NO_{11}S$	-2.1
810.530	M-H	PS 38:4	$C_{44}H_{77}NO_{10}P$	-0.9
816.532	M+Cl	PC 36:4	$C_{44}H_{80}NO_8PCl$	-0.4
834.531	M-H	PS 40:6	$C_{46}H_{77}NO_{10}P$	-2.8
838.563	M-H	PS 40:4	$C_{46}H_{81}NO_{10}P$	-2.5
844.646	M-H	PS P-41:0	$C_{47}H_{91}NO_9P$	-2.4
857.520	M-H	PI 36:4	$C_{45}H_{78}O_{13}P$	-1.9
860.639	M-H	PS 41:0	$C_{47}H_{91}NO_{10}P$	-0.8
885.551	M-H	PI 38:4	$C_{47}H_{82}O_{13}P$	-1.4
888.625	M-H	ST 24:1	$C_{48}H_{90}NO_{11}S$	-1.2
904.618	M-H	ST 24:1 (OH)	$C_{48}H_{90}NO_{12}S$	1.4
906.632	M-H	ST 24:0 (OH)	$C_{48}H_{92}NO_{12}S$	2.4
909.550	M-H	PI 40:6	$C_{49}H_{82}O_{13}P$	0.1
916.657	M-H	ST 26:1	$C_{50}H_{94}NO_{11}S$	-1.9
932.652	M-H	ST 26:1 (OH)	$C_{50}H_{94}NO_{12}S$	-1.5

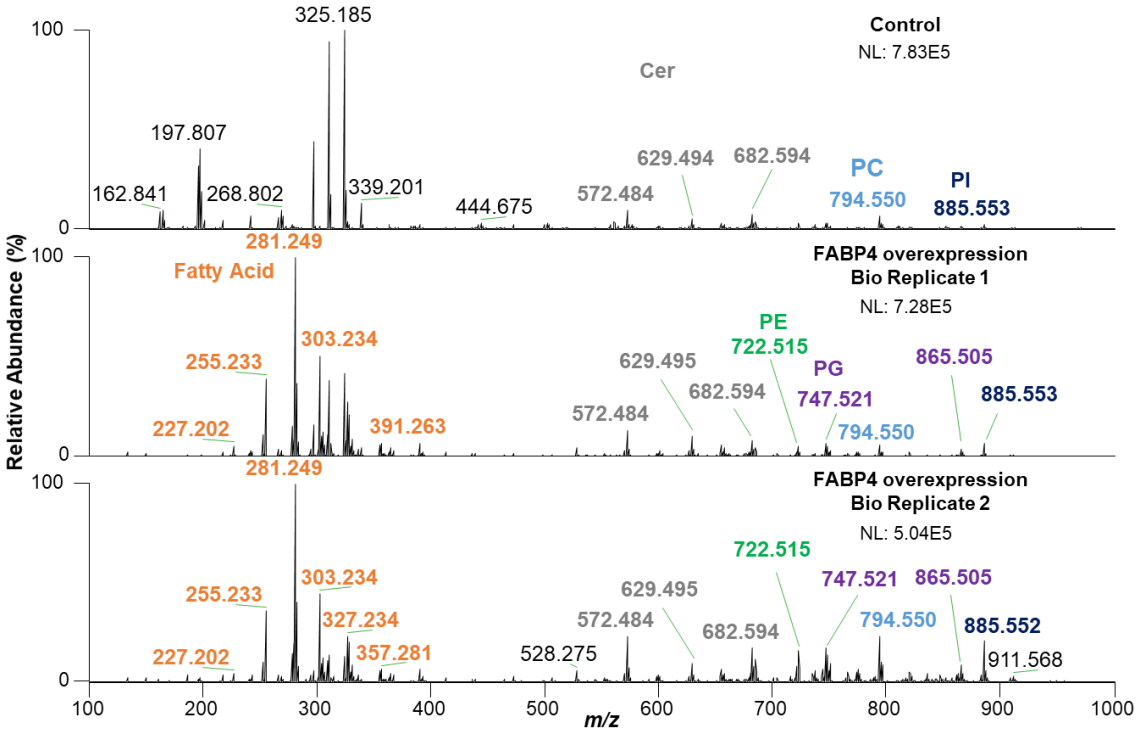

Figure A3.13: Representative MS profiles detected from human ovarian cell pellets deposited and dried on a glass slide. Droplets of 0.2 µL volume were manually deposited onto the sample surface.

Table A3.7: Method reproducibility.

Cosine analyses comparing mass spectra from the same pixels in three mouse brain tissue serial sections (top), and from pixels in a homogenous ovarian tumor region from two serial sections (bottom). Note that cosine analysis provides similarity values ranging from 0 (dissimilar or orthogonal vectors) to 1 (identical or parallel vectors).

Cosine Analysis						
Mouse Brain	***Pixel 1***	***Pixel 2***	***Pixel 3***	***Pixel 4***	***Pixel 5***	***All Pixels Combined***
Line 1 vs Line 2	0.970	0.898	0.955	0.914	0.920	-
Line 1 vs Line 3	0.692	0.904	0.885	0.987	0.918	-
Line 2 vs Line 3	0.721	0.983	0.892	0.944	0.800	-
Average	0.794	0.928	0.911	0.948	0.880	0.892
SD	0.153	0.047	0.039	0.037	0.069	0.089
Ovarian Tumor	***Pixel 1 vs Pixel 1***	***Pixel 2 vs Pixel 2***	***Pixel 1 vs Pixel 2***	***Pixel 2 vs Pixel 1***	-	-
Line 1 vs Line 2	0.902	0.829	0.897	0.881	-	-
Line 1 vs Line 2	-	-	0.957	0.908	-	-
Average	0.957					
SD	0.053					

Table A3.8: Ratio between ion abundances at *m/z* 834.530 and 885.550 evaluated from three serial sections grey matter mouse brain spectra.

Pixel	**Line**	**885/834 Ratio**
1	1	0.688
	2	0.673
	3	0.822
2	1	0.688
	2	0.904
	3	0.784
3	1	0.686
	2	0.786
	3	0.931
4	1	0.707
	2	0.769
	3	0.700
5	1	0.703
	2	0.659
	3	0.696
AVG		0.746
SD		0.084
RSD (%)		11.31

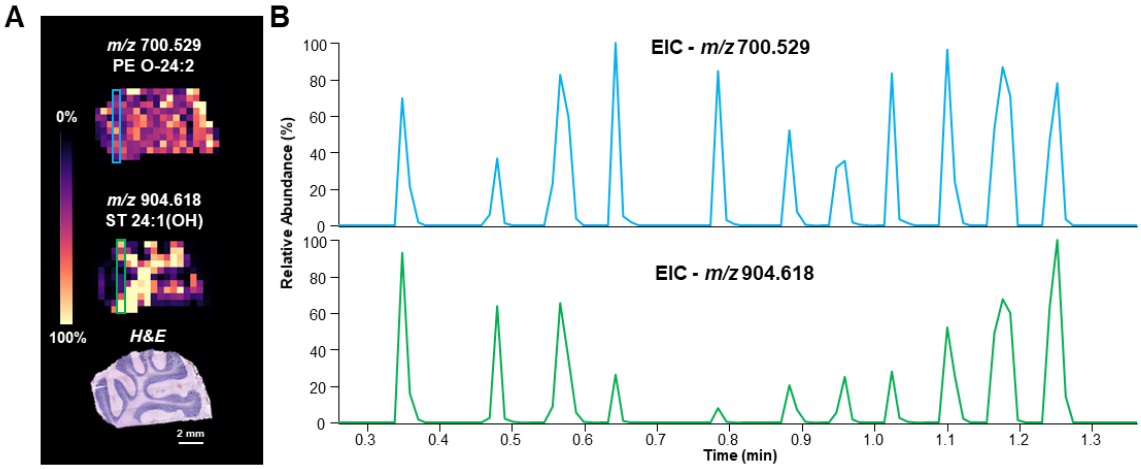

Figure A3.14: Demonstrating imaging performance.

Ion images and corresponding hematoxylin & eosin (H&E) stain of a normal human brain tissue sample (A). Extracted ion chromatographs for ion *m/z* 700.529 (top) and *m/z* 904.618 (bottom) for the highlighted lines in panel A (B).

APPENDIX A4: NONDESTRUCTIVE TISSUE ANALYSIS FOR *EX VIVO* AND *IN VIVO* CANCER DIAGNOSIS USING A HANDHELD MASS SPECTROMETRY SYSTEM

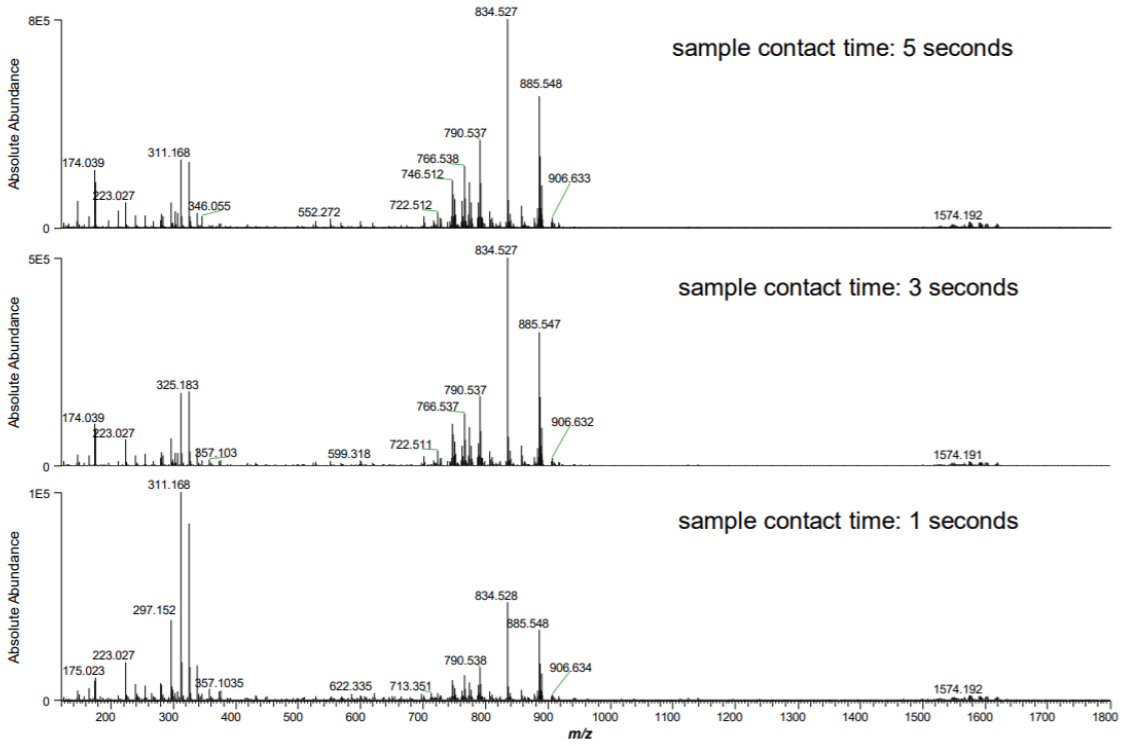

Figure A4.1: Effect of MasSpec Pen contact time on the mass spectra obtained.

Representative negative ion mode mass spectra obtained from mouse brain tissue sections with different extraction times, 5 s, 3 s, and 1 s (average of n=3 mass spectra each).

Table A4.1: Patient demographics of the 253 human tissue samples used in this study.

Patient Diagnosis		Median Age, Years	Age Range, Years	Number of Patients by Gender (Male, Female)	Number of Patients by Race (White, Black, Asian, Unknown)
Breast	Normal	47	24-76	(0,29)	(21,7,1,0)
	Cancer	58	41-75	(2,14)	(10,2,4,0)
Lung	Normal	57	12-82	(33,14)	(35,12,0,0)
	Cancer	66	22-84	(25,23)	(35,7,0,6)
Ovary	Normal	50	31-80	(0,29)	(22,7,0,0)
	Cancer	62	30-83	(0,28)	(25,2,0,1)
Thyroid	Normal	40	18-80	(10,17)	(18,7,0,2)
	Cancer	49	16-81	(12,17)	(21,4,0,4)

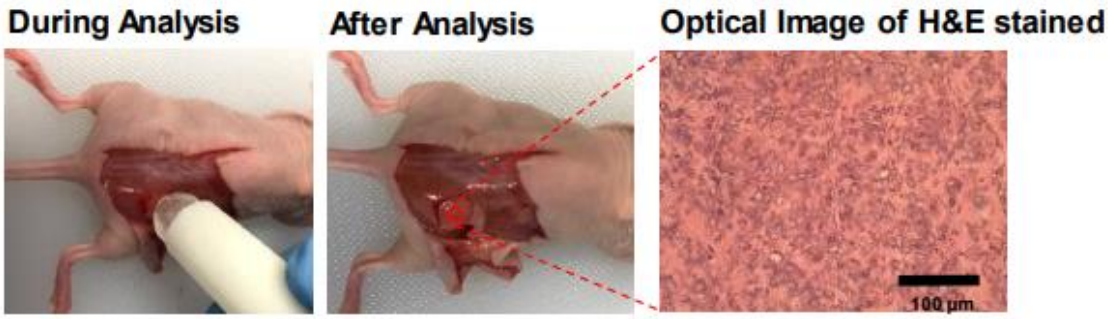

Figure A4.2: Intraoperative analysis of tumor and normal tissues in a murine model.

Optical and histological images of tissue during and after intraoperative MassSpec pen analysis in a mouse model. The H&E stained tissue section (inset) was obtained from the same region resected after MassSpec Pen analysis.

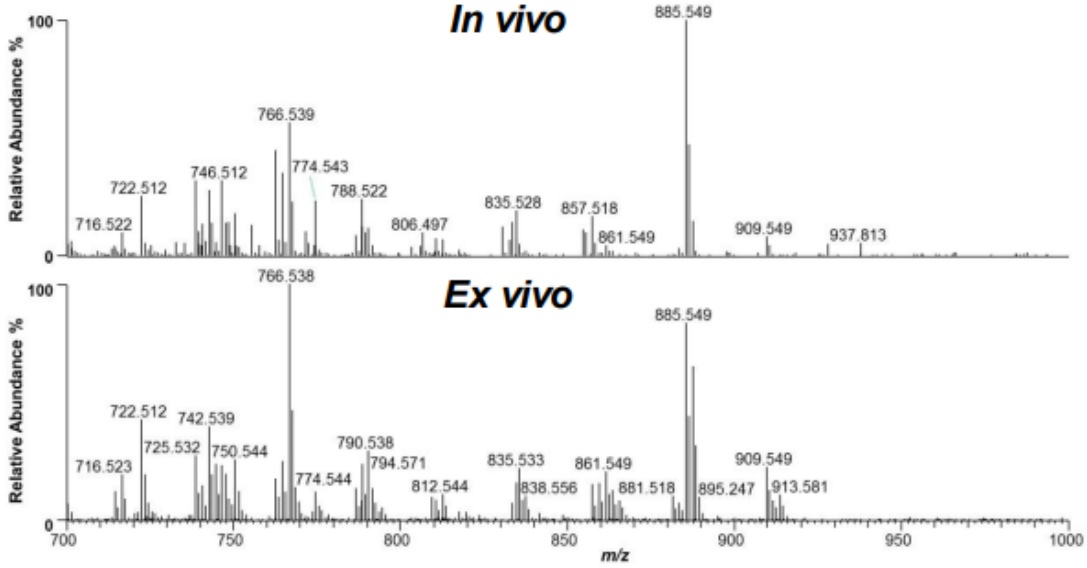

Figure A4.3: MasSpec Pen analysis of the same tissue sample *in vivo* and *ex vivo*.

Representative MasSpec Pen negative ion mode mass spectra obtained *in vivo* and *ex vivo* of the same tumor sample from a mouse model are shown (average of n=3 mass spectra each).

APPENDIX A5: PERFORMANCE OF THE MASSPEC PEN FOR RAPID DIAGNOSIS OF OVARIAN CANCER

Table A5.1: Patient demographic information for fallopian tube and peritoneum samples analyzed with the MasSpec Pen.

FT (n=7) and peritoneum (n=4) frozen tissue samples were received from the MD Anderson and CHTN Tissue Banks, respectively. Additional FT (n=8 samples from 6 patients) and peritoneum samples (n=12 samples from 11 patients) were prospectively collected by the Seton Medical Center (Austin, TX) as fresh surgical specimens from endometriosis resection surgery.

Parameter	**Fallopian Tube**	**Peritoneum**
Number of Patients (N)	13	16
Tissue Origin (MD Anderson Tissue Bank, CHTN, Tissue Bank, Seton Medical Center)	(7,0,6)	(0,4,12)
Median Age, Years	61	36
Age Range, Years	(31,86)	(29, 74)
Number of Patients by Race *(White, Black, Asian, Hispanic, Unknown)*	(9,0,0,0,6)	(3, 0,0,0,13)

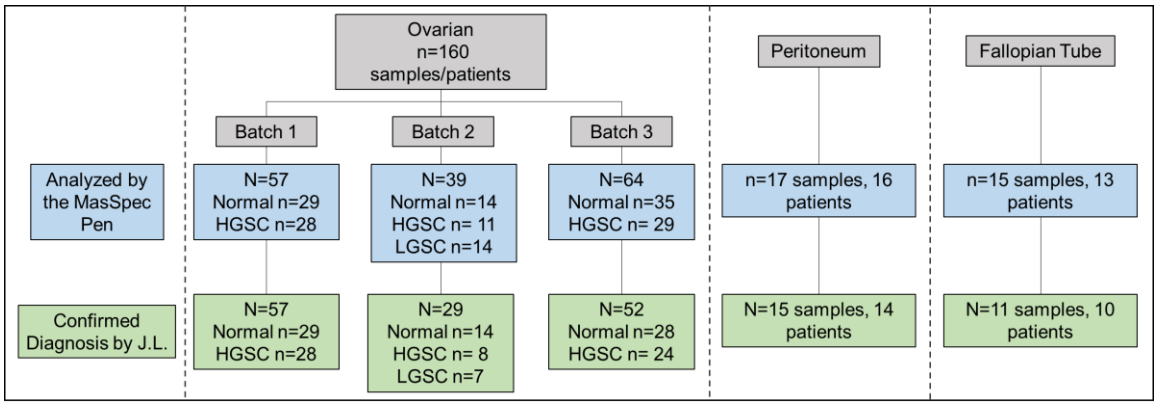

Figure A5.1: Flow of samples and participants from the presented study.

Table A5.2: Ion identities and molecular formula attributed by high mass accuracy/high mass resolution and tandem MS measurements for species detected from MasSpec Pen analysis of HGSC, LGSC and normal ovarian tissue.

Deviations from exact mass are provided as mass error in ppm. Stereochemistry or double bond position is not known for the identified species.

Detected *m/z*	**Ion**	**Tentative Attribution**	**Proposed Molecular Formula**	**Mass Error (ppm)**
124.007	$[M-H]^-$	Taurine	$C_2H_6NO_3S$	5.6
146.046	$[M-H]^-$	Glutamate	$C_5H_8NO_4$	2.7
175.025	$[M-H]^-$	Ascorbate	$C_6H_7O_6$	0.2
201.038	$[2M-2H+Na]^-$	Lactate	$C_6H_{10}O_6Na$	0.5
215.033	$[M+Cl]^-$	Hexose	$C_6H_{12}O_6Cl$	-2.8
306.077	$[M-H]^-$	Glutathione	$C_{10}H_{16}N_3O_6S$	-2.3
701.514	$[M-H]^-$	PA 18:0_18:1	$C_{39}H_{74}O_8P$	-1.7
722.514	$[M-H]^-$	PE P-16:0_20:4	$C_{41}H_{73}NO_7P$	-1.7
750.546	$[M-H]^-$	PE P-18:0_20:4	$C_{43}H_{77}NO_7P$	-1.7
788.546	$[M-H]^-$	PS 18:0_18:1	$C_{42}H_{79}NO_{10}P$	-1.8
835.536	$[M-H]^-$	PI 18:1_16:0 or 18:0_16:1	$C_{43}H_{80}O_{13}P$	-1.6
861.551	$[M-H]^-$	PI 18:1_18:1 or 18:0_18:2	$C_{45}H_{82}O_{13}P$	-1.6
863.567	$[M-H]^-$	PI 18:1_18:0	$C_{45}H_{84}O_{13}P$	-2.2
885.551	$[M-H]^-$	PI 18:0_20:4	$C_{47}H_{82}O_{13}P$	-1.6
909.552	$[M-H]^-$	PI 18:0_22:6	$C_{49}H_{82}O_{13}P$	-2.3
913.582	$[M-H]^-$	PI 18:0_22:4	$C_{49}H_{86}O_{13}P$	-0.7

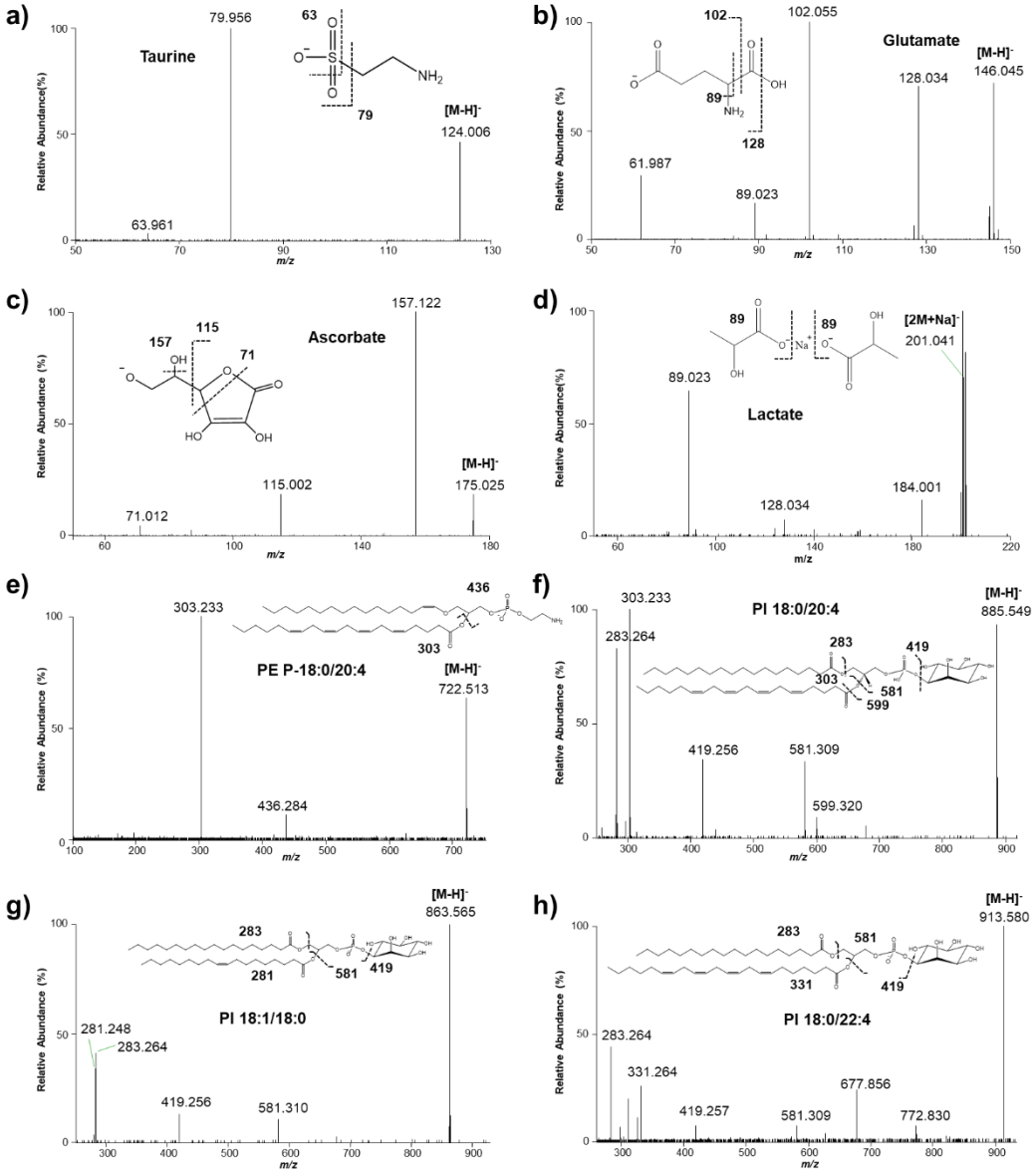

Figure A5.2: Tandem mass spectra obtained by higher-energy collision induced dissociation and MasSpec Pen analysis of ovarian tissue samples in the negative ion mode.

Representative complex glycerophospholipids and metabolites were evaluated. Proposed molecular structure and fragmentation sites are shown for each species. $[M-H]^-$ Taurine (A), $[M-H]^-$ Glutamate (B), $[M-H]^-$ Ascorbate (C), $[2M-2H+Na]^-$Lactate (D), $[M-H]^-$ PE P-18:0/20:4 (E), $[M-H]^-$ PI 18:0/20:4 (F), $[M-H]^-$ PI 18:1/18:0 (G), $[M-H]^-$ PI 18:0/22:4 (H).

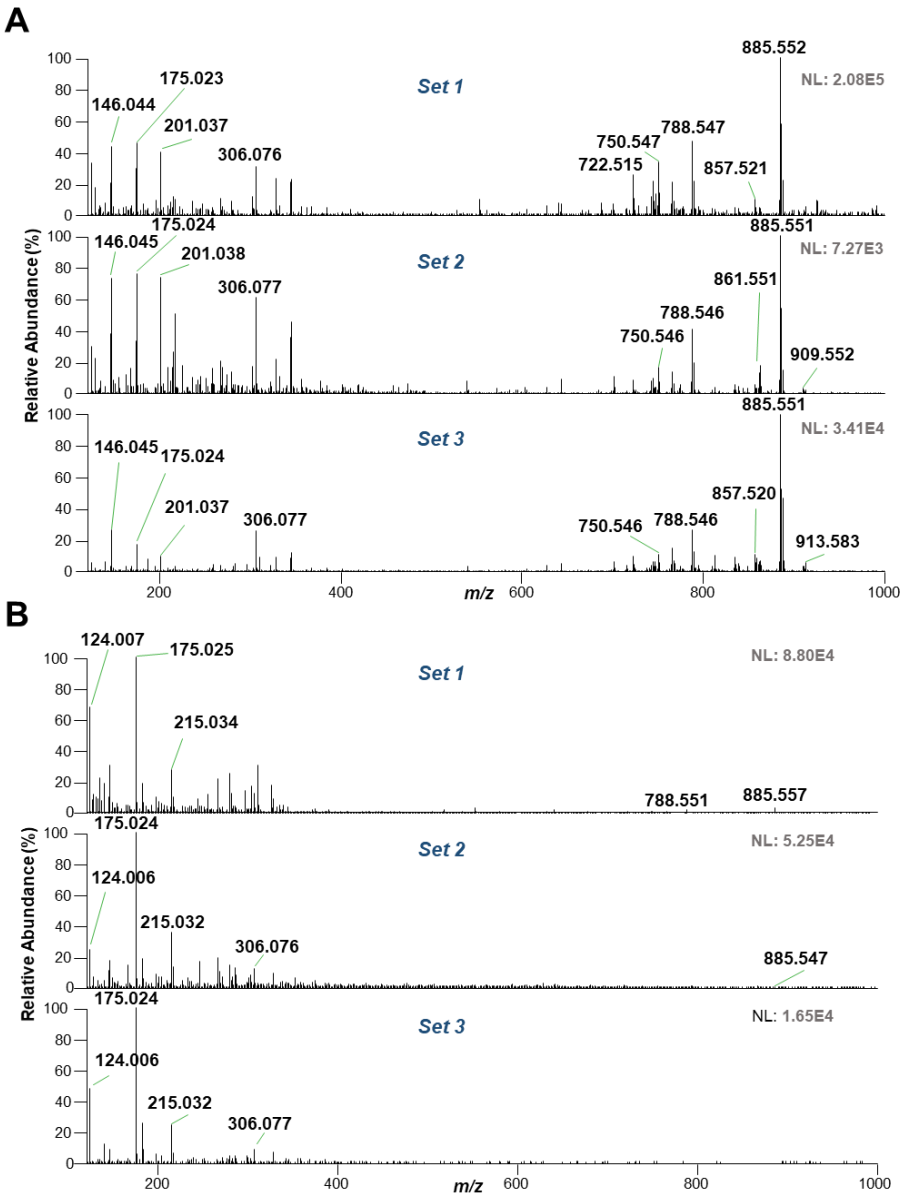

Figure A5.3: Representative MasSpec Pen mass spectra obtained from the three analyzed sample sets of high-grade serous carcinoma (A), and normal ovarian tissue (B).

Table A5.3: Lasso results for normal versus HGSC (top), normal versus cancer (middle), and normal versus HGSC versus LGSC (bottom) classification.

Rows represent classification based on pathological evaluation, columns represent classification based on Lasso prediction. Results show agreements with pathology for train and test sets, when applicable. Performance is reported as sensitivity (true positive rate), specificity (true negative rate) and overall accuracy (% of correctly classified patients for all tissue types).

Model	Sample Set	Pathology	Lasso Prediction					
Normal vs HGSC			**Normal**	**HGSC**	**-**	**Sensitivity (%)**	**Specificity (%)**	**Overall Accuracy (%)**
	Train	**Normal**	31	1	-	100.0	96.8	98.3
		HGSC	0	28	-			
	Validation	**Normal**	11	0	-	100.0	100.0	100.0
		HGSC	0	8	-			
	Test	**Normal**	26	2	-	91.7	92.9	92.3
		HGSC	2	22	-			
Normal vs Cancer			**Normal**	**Cancer**		**Sensitivity (%)**	**Specificity (%)**	**Overall Accuracy (%)**
	Train	**Normal**	32	1		93.9	96.9	95.4
		Cancer	2	31				
	Validation	**Normal**	9	1		100.0	90.0	95.0
		Cancer	0	10				
	Test	**Normal**	26	2		91.7	92.9	92.3
		Cancer	2	22				
Normal vs HGSC vs LGSC			**Normal**	**HGSC**	**LGSC**	**Class Accuracy (%)**		**Overall Accuracy (%)**
	Train	**Normal**	43	0	0	100.0		97.7
		HGSC	0	36	0	100.0		
		LGSC	0	2	5	71.4		

Table A5.4: Ion identities and molecular formula attributed by high mass accuracy/high mass resolution and tandem MS measurements for species detected from MasSpec Pen analysis of fallopian tube and peritoneum tissue samples.

Deviations from exact mass are provided as mass error in ppm. Stereochemistry or double bond position is not known for the identified species.

Detected *m/z*	**Ion**	**Attribution**	**Molecular Formula**	**Mass Error**
175.023	M-H	Ascorbate	$C_6H_7O_6$	9.2
215.031	M+Cl	Glucose	$C_6H_{12}O_6Cl$	7.0
267.073	M-H	Inosine	$C_{10}H_{11}N_4O_5$	3.0
279.232	M-H	FA 18:2	$C_{18}H_{31}O_2$	3.9
281.247	M-H	FA 18:1	$C_{18}H_{33}O_2$	4.3
391.261	M+Cl	MG 18:1	$C_{21}H_{40}O_4Cl$	3.6
537.487	M-H	FA dimer 18:0 - 16:0	$C_{34}H_{65}O_4$	3.5
563.503	M-H	FA dimer 18:1 - 18:0	$C_{36}H_{67}O_4$	3.5
585.485	M+Na-2H	FA dimer 18:1 - 18:0	$C_{36}H_{66}O_4Na$	3.1
615.168	M-H	Heme	$C_{34}H_{31}FeN_4O_4$	3.4
655.505	M+Cl	DG 36:2	$C_{39}H_{72}O_5Cl$	3.2
700.528	M-H	PE P-34:1	$C_{39}H_{75}NO_7P$	1.0
701.514	M-H	PA 36:1	$C_{39}H_{74}O_8P$	-1.7
722.514	M-H	PE P-36:4	$C_{41}H_{73}NO_7P$	-1.7
742.538	M-H	PE 36:2	$C_{41}H_{77}NO_8P$	2.3
750.546	M-H	PE O-38:5	$C_{43}H_{77}NO_7P$	-1.7
788.546	M-H	PS 36:1	$C_{42}H_{79}NO_{10}P$	-1.8
810.527	M-H	PS 38:4	$C_{44}H_{77}NO_{10}P$	2.5
835.536	M-H	PI 34:1	$C_{43}H_{80}O_{13}P$	-1.6
857.519	M-H	PI 36:4	$C_{45}H_{78}O_{13}P$	-0.8
861.551	M-H	PI 36:2	$C_{45}H_{82}O_{13}P$	-1.6
863.567	M-H	PI 36:1	$C_{45}H_{84}O_{13}P$	-2.2
885.551	M-H	PI 38:4	$C_{47}H_{82}O_{13}P$	-1.6
891.720	M+Cl	TG 52:3	$C_{55}H_{100}O_6Cl$	2.1
909.552	M-H	PI 40:6	$C_{49}H_{82}O_{13}P$	-2.3
913.582	M-H	PI 40:4	$C_{49}H_{86}O_{13}P$	-0.7
917.735	M+Cl	TG 54:4	$C_{57}H_{102}O_6Cl$	2.3

Table A5.5: Ion identities and molecular formula attributed by high mass accuracy/high mass resolution and tandem MS measurements for species detected from MasSpec Pen analysis of fallopian tube and peritoneum tissue samples.

Deviations from exact mass are provided as mass error in ppm. Stereochemistry or double bond position is not known for the identified species.

Detected *m/z*	**Ion**	**Attribution**	**Molecular Formula**	**Mass Error**
175.023	M-H	Ascorbate	$C_6H_7O_6$	9.2
215.031	M+Cl	Glucose	$C_6H_{12}O_6Cl$	7.0
267.073	M-H	Inosine	$C_{10}H_{11}N_4O_5$	3.0
279.232	M-H	FA 18:2	$C_{18}H_{31}O_2$	3.9
281.247	M-H	FA 18:1	$C_{18}H_{33}O_2$	4.3
391.261	M+Cl	MG 18:1	$C_{21}H_{40}O_4Cl$	3.6
537.487	M-H	FA dimer 18:0 - 16:0	$C_{34}H_{65}O_4$	3.5
563.503	M-H	FA dimer 18:1 - 18:0	$C_{36}H_{67}O_4$	3.5
585.485	M+Na-2H	FA dimer 18:1 - 18:0	$C_{36}H_{66}O_4Na$	3.1
615.168	M-H	Heme	$C_{34}H_{31}FeN_4O_4$	3.4
655.505	M+Cl	DG 36:2	$C_{39}H_{72}O_5Cl$	3.2
700.528	M-H	PE P-34:1	$C_{39}H_{75}NO_7P$	1.0
701.514	M-H	PA 36:1	$C_{39}H_{74}O_8P$	-1.7
722.514	M-H	PE P-36:4	$C_{41}H_{73}NO_7P$	-1.7
742.538	M-H	PE 36:2	$C_{41}H_{77}NO_8P$	2.3
750.546	M-H	PE O-38:5	$C_{43}H_{77}NO_7P$	-1.7
788.546	M-H	PS 36:1	$C_{42}H_{79}NO_{10}P$	-1.8
810.527	M-H	PS 38:4	$C_{44}H_{77}NO_{10}P$	2.5
835.536	M-H	PI 34:1	$C_{43}H_{80}O_{13}P$	-1.6
857.519	M-H	PI 36:4	$C_{45}H_{78}O_{13}P$	-0.8
861.551	M-H	PI 36:2	$C_{45}H_{82}O_{13}P$	-1.6
863.567	M-H	PI 36:1	$C_{45}H_{84}O_{13}P$	-2.2
885.551	M-H	PI 38:4	$C_{47}H_{82}O_{13}P$	-1.6
891.720	M+Cl	TG 52:3	$C_{55}H_{100}O_6Cl$	2.1
909.552	M-H	PI 40:6	$C_{49}H_{82}O_{13}P$	-2.3
913.582	M-H	PI 40:4	$C_{49}H_{86}O_{13}P$	-0.7
917.735	M+Cl	TG 54:4	$C_{57}H_{102}O_6Cl$	2.3

Table A5.6: Lasso results for discrimination of HGSC and cancer samples from FT and peritoneum.

Rows represent classification based on pathological evaluation, columns represent classification based on Lasso prediction. Results show agreements with pathology for train and test sets, when applicable. Performance is reported as sensitivity (true positive rate), specificity (true negative rate) and overall accuracy (% of correctly classified patients for all tissue types).

Pathology	**Lasso Prediction**				
	HGSC	**FT**	**Sensitivity (%)**	**Specificity (%)**	**Overall Accuracy (%)**
HGSC	32	4	88.9	100.0	91.5
FT	0	11			
	Cancer	**FT**			
Cancer	39	4	90.7	100.0	92.6
FT	0	11			
	HGSC	**Peritoneum**			
HGSC	29	7	80.6	100.0	86.3
Peritoneum	0	15			
	Cancer	**Peritoneum**			
Cancer	36	7	83.7	100.0	87.9
Peritoneum	0	15			

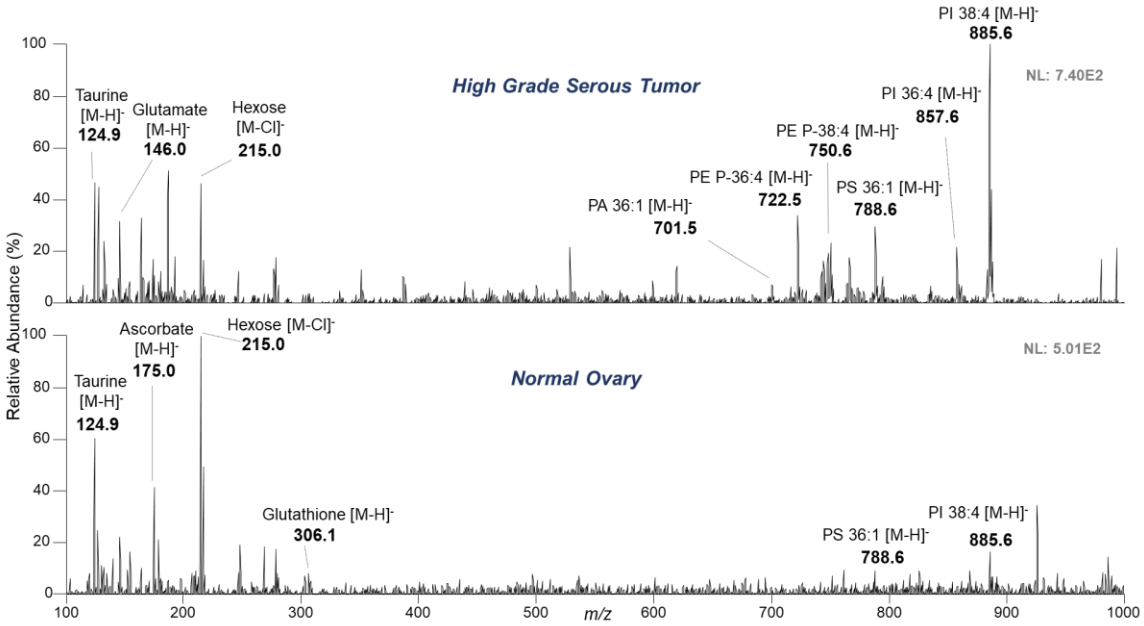

Figure A5.4: Representative metabolic profiles obtained by averaging three mass spectra obtained from MasSpec Pen analysis of high-grade serous carcinoma (top), and normal ovarian tissue (bottom) with an ion trap analyzer.

Lipid species are described by lipid class, number of fatty-acid chain carbons and double bonds.

Table A5.7: Comparison of Lasso prediction results for normal vs HGSC using the MasSpec Pen coupled to an orbitrap (top) or ion trap (bottom) mass analyzer.

Rows represent classification based on pathological evaluation, columns represent classification based on Lasso prediction. Results show agreements with pathology for train and test sets. Performance is reported as sensitivity (true positive rate), specificity (true negative rate) and overall accuracy (% of correctly classified patients for all tissue types).

Analyzer	**Sample Set**	**Pathology**	**Lasso Prediction**				
Orbitrap			**Normal**	**HGSC**	**Sensitivity (%)**	**Specificity (%)**	**Overall Accuracy (%)**
	Train	**Normal**	14	1	86.7	93.3	90.0
		HGSC	2	13			
	Validation	**Normal**	5	0	80.0	100.0	90.0
		HGSC	1	4			
Ion Trap			**Normal**	**HGSC**	**Sensitivity (%)**	**Specificity (%)**	**Overall Accuracy (%)**
	Train	**Normal**	15	0	100.0	100.0	100.0
		HGSC	0	15			
	Validation	**Normal**	5	0	100.0	100.0	100.0
		HGSC	0	5			

Bibliography

CHAPTER 1

1. Fenn JB, Mann M, Meng CK, Wong SF, Whitehouse CM. Electrospray Ionization for Mass-Spectrometry of Large Biomolecules. Science 1989;246:64-71
2. Siuzdak G. The emergence of mass spectrometry in biochemical research. Proc Natl Acad Sci U S A 1994;91:11290-7
3. Karas M, Bachmann D, Bahr U, Hillenkamp F. Matrix-Assisted Ultraviolet-Laser Desorption of Nonvolatile Compounds. International Journal of Mass Spectrometry and Ion Processes 1987;78:53-68
4. Norris JL, Caprioli RM. Analysis of Tissue Specimens by Matrix-Assisted Laser Desorption/Ionization Imaging Mass Spectrometry in Biological and Clinical Research. Chem Rev 2013;113:2309-42
5. Schwamborn K, Caprioli RM. INNOVATION Molecular imaging by mass spectrometry - looking beyond classical histology. Nat Rev Cancer 2010;10:639-46
6. Seeley EH, Caprioli RM. MALDI imaging mass spectrometry of human tissue: method challenges and clinical perspectives. Trends Biotechnol 2011;29:136-43
7. Alexandrov T. MALDI imaging mass spectrometry: statistical data analysis and current computational challenges. Bmc Bioinformatics 2012;13
8. Takats Z, Wiseman JM, Gologan B, Cooks RG. Mass spectrometry sampling under ambient conditions with desorption electrospray ionization. Science 2004;306:471-3
9. Cooks RG, Ouyang Z, Takats Z, Wiseman JM. Ambient mass spectrometry. Science 2006;311:1566-70
10. Ifa DR, Eberlin LS. Ambient Ionization Mass Spectrometry for Cancer Diagnosis and Surgical Margin Evaluation. Clin Chem 2016;62:111-23
11. Wu CP, Dill AL, Eberlin LS, Cooks RG, Ifa DR. Mass spectrometry imaging under ambient conditions. Mass Spectrom Rev 2013;32:218-43
12. Hanel L, Kwiatkowski M, Heikaus L, Schluter H. Mass spectrometry-based intraoperative tumor diagnostics. Futur Sci Oa 2019;5
13. Costa AB, Cooks RG. Simulated splashes: Elucidating the mechanism of desorption electrospray ionization mass spectrometry. Chem Phys Lett 2008;464:1-8
14. Eberlin LS, Ferreira CR, Dill AL, Ifa DR, Cheng L, Cooks RG. Nondestructive, histologically compatible tissue imaging by desorption electrospray ionization mass spectrometry. Chembiochem 2011;12:2129-32

15. Porcari AM, Zhang JL, Garza KY, Rodrigues-Peres RM, Lin JQ, Young JH, et al. Multicenter Study Using Desorption-Electrospray-Ionization-Mass-Spectrometry Imaging for Breast-Cancer Diagnosis. Anal Chem 2018;90:11324-32

16. Eberlin LS, Tibshirani RJ, Zhang J, Longacre TA, Berry GJ, Bingham DB, et al. Molecular assessment of surgical-resection margins of gastric cancer by mass-spectrometric imaging. Proc Natl Acad Sci U S A 2014;111:2436-41

17. Guenther S, Muirhead LJ, Speller AV, Golf O, Strittmatter N, Ramakrishnan R, et al. Spatially resolved metabolic phenotyping of breast cancer by desorption electrospray ionization mass spectrometry. Cancer Res 2015;75:1828-37

18. Calligaris D, Feldman DR, Norton I, Brastianos PK, Dunn IF, Santagata S, et al. Molecular typing of meningiomas by desorption electrospray ionization mass spectrometry imaging for surgical decision-making. Int J Mass Spectrom 2015;377:690-8

19. Eberlin LS, Dill AL, Costa AB, Ifa DR, Cheng L, Masterson T, et al. Cholesterol Sulfate Imaging in Human Prostate Cancer Tissue by Desorption Electrospray Ionization Mass Spectrometry. Anal Chem 2010;82:3430-4

20. Eberlin LS, Norton I, Orringer D, Dunn IF, Liu XH, Ide JL, et al. Ambient mass spectrometry for the intraoperative molecular diagnosis of human brain tumors. P Natl Acad Sci USA 2013;110:1611-6

21. Jarmusch AK, Pirro V, Baird Z, Hattab EM, Cohen-Gadol AA, Cooks RG. Lipid and metabolite profiles of human brain tumors by desorption electrospray ionization-MS. P Natl Acad Sci USA 2016;113:1486-91

22. Santagata S, Eberlin LS, Norton I, Calligaris D, Feldman DR, Ide JL, et al. Intraoperative mass spectrometry mapping of an onco-metabolite to guide brain tumor surgery. P Natl Acad Sci USA 2014;111:11121-6

23. Laskin J, Lanekoff I. Ambient Mass Spectrometry Imaging Using Direct Liquid Extraction Techniques. Anal Chem 2016;88:52-73

24. Van Berkel GJ, Kertesz V. Application of a Liquid Extraction Based Sealing Surface Sampling Probe for Mass Spectrometric Analysis of Dried Blood Spots and Mouse Whole-Body Thin Tissue Sections. Anal Chem 2009;81:9146-52

25. Kertesz V, Van Berkel GJ. Fully automated liquid extraction-based surface sampling and ionization using a chip-based robotic nanoelectrospray platform. J Mass Spectrom 2010;45:252-60

26. Roach PJ, Laskin J, Laskin A. Nanospray desorption electrospray ionization: an ambient method for liquid-extraction surface sampling in mass spectrometry. Analyst 2010;135:2233-6

27. Kertesz V, Calligaris D, Feldman DR, Changelian A, Laws ER, Santagata S, et al. Profiling of adrenocorticotropic hormone and arginine vasopressin in human

pituitary gland and tumor thin tissue sections using droplet-based liquid-microjunction surface-sampling-HPLC-ESI-MS-MS. Anal Bioanal Chem 2015;407:5989-98

28. Laskin J, Heath BS, Roach PJ, Cazares L, Semmes OJ. Tissue imaging using nanospray desorption electrospray ionization mass spectrometry. Anal Chem 2012;84:141-8

29. Nguyen S, Sontag R, Carson J, Corley R, Ansong C, Laskin J. Towards High-Resolution Tissue Imaging Using Nanospray Desorption Electrospray Ionization Mass Spectrometry Coupled to Shear Force Microscopy. J Am Soc Mass Spectr 2018;29:316-22

30. Blatherwick EQ, Van Berkel GJ, Pickup K, Johansson MK, Beaudoin ME, Cole RO, et al. Utility of spatially-resolved atmospheric pressure surface sampling and ionization techniques as alternatives to mass spectrometric imaging (MSI) in drug metabolism. Xenobiotica 2011;41:720-34

31. Tillner J, Wu V, Jones EA, Pringle SD, Karancsi T, Dannhorn A, et al. Faster, More Reproducible DESI-MS for Biological Tissue Imaging. J Am Soc Mass Spectr 2017;28:2090-8

32. Garza KY, Feider CL, Klein DR, Rosenberg JA, Brodbelt JS, Eberlin LS. Desorption Electrospray Ionization Mass Spectrometry Imaging of Proteins Directly from Biological Tissue Sections. Anal Chem 2018;90:7785-9

33. Towers MW, Karancsi T, Jones EA, Pringle SD, Claude E. Optimised Desorption Electrospray Ionisation Mass Spectrometry Imaging (DESI-MSI) for the Analysis of Proteins/Peptides Directly from Tissue Sections on a Travelling Wave Ion Mobility Q-ToF. J Am Soc Mass Spectrom 2018

34. Schaefer K-C, Denes J, Albrecht K, Szaniszlo T, Balog J, Skoumal R, et al. In Vivo, In Situ Tissue Analysis Using Rapid Evaporative Ionization Mass Spectrometry. Angew Chem Int Edit 2009;48:8240-2

35. Balog J, Sasi-Szabo L, Kinross J, Lewis MR, Muirhead LJ, Veselkov K, et al. Intraoperative Tissue Identification Using Rapid Evaporative Ionization Mass Spectrometry. Science Translational Medicine 2013;5

36. St John ER, Rossi M, Pruski P, Darzi A, Takats Z. Intraoperative tissue identification by mass spectrometric technologies. Trac-Trend Anal Chem 2016;85:2-9

37. St John ER, Balog J, McKenzie JS, Rossi M, Covington A, Muirhead L, et al. Rapid evaporative ionisation mass spectrometry of electrosurgical vapours for the identification of breast pathology: towards an intelligent knife for breast cancer surgery. Breast Cancer Res 2017;19

38. Phelps DL, Balog J, Gildea LF, Bodai Z, Savage A, El-Bahrawy MA, et al. The surgical intelligent knife distinguishes normal, borderline and malignant gynaecological tissues using rapid evaporative ionisation mass spectrometry (REIMS). Br J Cancer 2018;118:1349-58

39. Jemal A, Siegel R, Ward E, Hao YP, Xu JQ, Thun MJ. Cancer Statistics, 2009. Ca-Cancer J Clin 2009;59:225-49

40. Torre LA, Trabert B, DeSantis CE, Miller KD, Samimi G, Runowicz CD, et al. Ovarian Cancer Statistics, 2018. Ca-Cancer J Clin 2018;68:284-96

41. Lheureux S, Gourley C, Vergote I, Oza AM. Epithelial ovarian cancer. Lancet 2019;393:1240-53

42. Society AC. Cancer Facts & Figures 2020. Atlanta: American Cancer Society 2020

43. Bowtell DDL. The genesis and evolution of high-grade serous ovarian cancer. Nat Rev Cancer 2010;10:803-8

44. Hart WR. Borderline epithelial tumors of the ovary. Modern Pathol 2005;18:S33-S50

45. Matulonis UA, Sood AK, Fallowfield L, Howitt BE, Sehouli J, Karlan BY. Ovarian cancer. Nat Rev Dis Primers 2016;2

46. Bowtell DD, Bohm S, Ahmed AA, Aspuria PJ, Bast RC, Beral V, et al. Rethinking ovarian cancer II: reducing mortality from high-grade serous ovarian cancer. Nat Rev Cancer 2015;15:668-79

47. Kurman RJ, Shih Ie M. Molecular pathogenesis and extraovarian origin of epithelial ovarian cancer--shifting the paradigm. Hum Pathol 2011;42:918-31

48. Karnezis AN, Cho KR, Gilks CB, Pearce CL, Huntsman DG. The disparate origins of ovarian cancers: pathogenesis and prevention strategies. Nat Rev Cancer 2017;17:65-74

49. Tucker SL, Gharpure K, Herbrich SM, Unruh AK, Nick AM, Crane EK, et al. Molecular biomarkers of residual disease after surgical debulking of high-grade serous ovarian cancer. Clin Cancer Res 2014;20:3280-8

50. Md Arshad NZ, Ng BK, Md Paiman NA, Abdullah Mahdy Z, Mohd Noor R. Intra-Operative Frozen Sections for Ovarian Tumors - A Tertiary Center Experience. Asian Pac J Cancer Prev 2018;19:213-8

51. Nick AM, Coleman RL, Ramirez PT, Sood AK. A framework for a personalized surgical approach to ovarian cancer. Nat Rev Clin Oncol 2015;12:239-U78

52. Macario A. What does one minute of operating room time cost? J Clin Anesth 2010;22:233-6

53. Tibshirani R. Regression shrinkage and selection via the Lasso. J Roy Stat Soc B Met 1996;58:267-88

54. Gharpure K, Pradeep S, Sans M, Rupaimoole R, Ivan C, Wu SY, et al. FABP4 as a molecular determinant of residual disease in ovarian cancer. Nat Commun 2017;In Revision

55. Tusher VG, Tibshirani R, Chu G. Significance analysis of microarrays applied to the ionizing radiation response. P Natl Acad Sci USA 2001;98:5116-21

CHAPTER 2

1. Mino-Kenudson M, Chirieac LR, Law K, Hornick JL, Lindeman N, Mark EJ, et al. A novel, highly sensitive antibody allows for the routine detection of alk-rearranged lung adenocarcinomas by standard immunohistochemistry. Clin Cancer Res 2010;16:1561–71.
2. Jones S, Anagnostou V, Lytle K, Parpart-Li S, Nesselbush M, Riley DR, et al. Personalized genomic analyses for cancer mutation discovery and interpretation. Sci Transl Med 2015;7.
3. McDonnell LA, Heeren RMA. Imaging mass spectrometry. Mass Spectrom Rev 2007;26:606 – 43.
4. Walch A, Rauser S, Deininger S-O, Hoefler H. Maldi imaging mass spectrometry for direct tissue analysis: A new frontier for molecular histology. Histochem Cell Biol 2008;130:421–34.
5. Seeley EH, Caprioli RM. Molecular imaging of proteins in tissues by mass spectrometry. Proc Natl Acad Sci USA 2008;105:18126 –31.
6. Braun RM, Blenkinsopp P, Mullock SJ, Corlett C, Willey KF, Vickerman JC, Winograd N. Performance characteristics of a chemical imaging time-of-flight mass spectrometer. Rapid Comm Mass Spectrom 1998;12: 1246 –52.
7. Sarsby J, Griffiths RL, Race AM, Bunch J, Randall EC, Creese AJ, Cooper HJ. Liquid extraction surface analysis mass spectrometry coupled with field asymmetric waveform ion mobility spectrometry for analysis of intact proteins from biological substrates. Anal Chem 2015;87: 6794 – 800.
8. Yang J, Caprioli RM. Matrix precoated targets for direct lipid analysis and imaging of tissue. Anal Chem 2013; 85:2907–12.
9. Carado A, Kozole J, Passarelli M, Winograd N, Loboda A, Bunch J, et al. Biological tissue imaging with a hybrid cluster sims quadrupole time-of-flight mass spectrometer. Appl Surf Sci 2008;255:1572–5.
10. Kiss A, Smith DF, Jungmann JH, Heeren RMA. Cluster secondary ion mass spectrometry microscope mode mass spectrometry imaging. Rap Commun Mass Spectrom 2013;27:2745–50.
11. Klitzing HA, Weber PK, Kraft ML. Secondary ion mass spectrometry imaging of biological membranes at high spatial resolution. Meth Mol Biol 2013;950:483–501.
12. Nemes P, Vertes A. Laser ablation electrospray ionization for atmospheric pressure, in vivo, and imaging mass spectrometry. Anal Chem 2007;79:8098 –106.
13. Santos VG, Regiani T, Dias FFG, Romao W, Jara JLP, Klitzke CF, et al. Venturi easy ambient sonic-spray ionization. Anal Chem 2011;83:1375– 80.

14. Alberici RM, Simas RC, Sanvido GB, Romao W, Lalli PM, Benassi M, et al. Ambient mass spectrometry: Bringing ms into the ”real world“. Anal Bioanal Chem 2010;398: 265–94.

15. Wu C, Dill AL, Eberlin LS, Cooks RG, Ifa DR. Mass spectrometry imaging under ambient conditions. Mass Spectrom Rev 2013;32:218 – 43.

16. Hsu C-C, Dorrestein PC. Visualizing life with ambient mass spectrometry. Curr Opin Biotechnol 2015;31: 24 –34.

17. Harris GA, Galhena AS, Fernandez FM. Ambient sampling/ ionization mass spectrometry: Applications and current trends. Anal Chem 2011;83:4508 –38.

18. Ellis SR, Bruinen AL, Heeren RMA. A critical evaluation of the current state-of-the-art in quantitative imaging mass spectrometry. Anal Bioanal Chem 2014;406: 1275– 89.

19. Takats Z, Wiseman JM, Gologan B, Cooks RG. Mass spectrometry sampling under ambient conditions with desorption electrospray ionization. Science 2004;306: 471–3.

20. Badu-Tawiah AK, Eberlin LS, Ouyang Z, Cooks RG.Chem aspects of the extractive methods of ambient ionization mass spectrometry. Ann Rev Phys Chem 2013;64:481–505.

21. Ifa DR, Wiseman JM, Song Q, Cooks RG. Development of capabilities for imaging mass spectrometry under ambient conditions with desorption electrospray ionization (desi). Int J Mass Spectrom 2007;259:8 –15.

22. Eberlin LS, Norton I, Orringer D, Dunn IF, Liu X, Ide JL, et al. Ambient mass spectrometry for the intraoperative molecular diagnosis of human brain tumors. Proc Natl Acad Sci USA 2013;110:1611– 6.

23. Campbell DI, Ferreira CR, Eberlin LS, Cooks RG. Improved spatial resolution in the imaging of biological tissue using desorption electrospray ionization. Anal Bioanal Chem 2012;404:389 –98.

24. Kertesz V, Van Berkel GJ. Improved imaging resolution in desorption electrospray ionization mass spectrometry. Rapid Commun Mass Spectrom 2008;22:2639 – 44.

25. Hiraoka K, Nishidate K, Mori K, Asakawa D, Suzuki S. Development of probe electrospray using a solid needle. Rapid Commun Mass Spectrom 2007;21:3139 – 44.

26. Mandal MK, Yoshimura K, Saha S, Ninomiya S, Rahman MO, Yu Z, et al. Solid probe assisted nanoelectrospray ionization mass spectrometry for biological tissue diagnostics. Analyst 2012;137:4658 – 61.

27. Kerian KS, Jarmusch AK, Cooks RG. Touch spray mass spectrometry for in situ analysis of complex samples. Analyst 2014;139:2714 –20.

28. Schaefer K-C, Denes J, Albrecht K, Szaniszlo T, Balog J, Skoumal R, et al. In vivo, in situ tissue analysis using rapid evaporative ionization mass spectrometry. Angew Chem Int Ed 2009;48:8240 –2.

29. Balog J, Szaniszlo T, Schaefer K-C, Denes J, Lopata A, Godorhazy L, et al. Identification of biological tissues by rapid evaporative ionization mass spectrometry. Anal Chem 2010;82:7343–50.

30. Wiseman JM, Puolitaival SM, Takats Z, Cooks RG, Caprioli RM. Mass spectrometric profiling of intact biological tissue by using desorption electrospray ionization. Angew Chem Int Ed 2005;44:7094 –7.

31. Wiseman JM, Ifa DR, Song QY, Cooks RG. Tissue imaging at atmospheric pressure using desorption electrospray ionization (desi) mass spectrometry. Angew Chem Int Ed 2006;45:7188 –92.

32. Dill AL, Ifa DR, Manicke NE, Zheng O, Cooks RG. Mass spectrometric imaging of lipids using desorption electrospray ionization. J Chromatogr B Analyt Technol Biomed Life Sci 2009;877:2883–9.

33. Eberlin LS, Ferreira CR, Dill AL, Ifa DR, Cheng L, Cooks RG. Non-destructive, histologically compatible tissue imaging by desorption electrospray ionization mass spectrometry.Chembiochem 2011;12:2129 –32.

34. Tata A, Zheng J, Ginsberg HJ, Jaffray DA, Ifa DR, Zarrine- Afsar A. Contrast agent mass spectrometry imaging reveals tumour heterogeneity. Anal Chem 2015;87: 7683–9.

35. Eberlin LS, Ferreira CR, Dill AL, Ifa DR, Cooks RG. Desorption electrospray ionization mass spectrometry for lipid characterization and biological tissue imaging. Biochim Biophys Acta Mol Cell Biol Lipids 2011;1811: 946 – 60.

36. Bishop JM. Molecular themes in oncogenesis. Cell 1991;64:235– 48.

37. Corda D, Zizza P, Varone A, Filippi BM, Mariggio S. The glycerophosphoinositols: Cellular metabolism and biological functions. Cell Mol Life Sci 2009;66:3449 – 67.

38. Soga T. Cancer metabolism: Key players in metabolic reprogramming. Cancer Sci 2013;104:275– 81.

39. Utsugi T, Schroit AJ, Connor J, Bucana CD, Fidler IJ. Elevated expression of phosphatidylserine in the outermembrane leaflet of human tumor-cells and recognition by activated human blood monocytes. Cancer Res 1991;51:3062– 6.

40. Dobrzynska I, Szachowicz-Petelska B, Sulkowski S, Figaszewski Z. Changes in electric charge and phospholipids composition in human colorectal cancer cells. Mol Cell Biochem 2005;276:113–9.

41. Masterson TA, Dill AL, Eberlin LS, Mattarozzi M, Cheng L, Beck SDW, et al. Distinctive glycerophospholipid profiles of human seminoma and adjacent normal tissues by desorption electrospray ionization imaging mass spectrometry. J Am Soc Mass Spectrom 2011;22: 1326 –33.

42. Dill AL, Eberlin LS, Costa AB, Zheng C, Ifa DR, Cheng L, et al. Multivariate statistical identification of human bladder carcinomas using ambient ionization imaging mass spectrometry. Chem-Eur J 2011;17:2897–902.

43. Dill AL, Eberlin LS, Zheng C, Costa AB, Ifa DR, Cheng LA, et al. Multivariate statistical differentiation of renal cell carcinomas based on lipidomic analysis by ambient ionization imaging mass spectrometry. Anal Bioanal Chem 2010;398:2969 –78.

44. Eberlin LS, Tibshirani RJ, Zhang J, Longacre TA, Berry GJ, Bingham DB, et al. Molecular assessment of surgical-resection margins of gastric cancer by massspectrometric imaging. Proc Natl Acad Sci USA 2014; 111:2436 – 41.

45. Eberlin LS, Dill AL, Golby AJ, Ligon KL, Wiseman JM, Cooks RG, Agar NYR. Discrimination of human astrocytoma subtypes by lipid analysis using desorption electrospray ionization imaging mass spectrometry. Angew Chem Int Edit 2010;49:5953– 6.

46. Eberlin LS, Norton I, Dill AL, Golby AJ, Ligon KL, Santagata S, et al. Classifying human brain tumors by lipid imaging with mass spectrometry. Cancer Res 2012;72: 645–54.

47. Santagata S, Eberlin LS, Norton I, Calligaris D, Feldman DR, Ide JL, et al. Intraoperative mass spectrometry mapping of an onco-metabolite to guide brain tumor surgery. Proc Natl Acad Sci USA 2014;111:11121– 6.

48. Eberlin LS, Gabay M, Fan AC, Gouw AM, Tibshirani RJ, Felsher DW, Zare RN. Alteration of the lipid profile in lymphomas induced by myc overexpression. Proc Natl Acad Sci USA 2014;111:10450 –5.

49. Morrish F, Isern N, Sadilek M, Jeffrey M, Hockenbery DM. C-myc activates multiple metabolic networks to generate substrates for cell-cycle entry. Oncogene 2009;28:2485–91.

50. Wolfer A, Wittner BS, Irimia D, Flavin RJ, Lupien M, Gunawardane RN, et al. Myc regulation of a ”poorprognosis“ metastatic cancer cell state. Proc Natl Acad Sci USA 2010;107:3698 –703.

51. Gerbig S, Golf O, Balog J, Denes J, Baranyai Z, Zarand A, et al. Analysis of colorectal adenocarcinoma tissue by desorption electrospray ionization mass spectrometric imaging. Anal Bioanal Chem 2012;403:2315–25.

52. Sjolander A, Yamamoto K, Huber BE, Lapetina EG. Association of p21ras with phosphatidylinositol 3-kinase. Proc Natl Acad Sci USA 1991;88:7908 –12.

53. Mandal MK, Saha S, Yoshimura K, Shida Y, Takeda S, Nonami H, Hiraoka K. Biomolecular analysis and cancer diagnostics by negative mode probe electrospray ionization. Analyst 2013;138:1682– 8.

54. Calligaris D, Feldman DR, Norton I, Brastianos PK, Dunn IF, Santagata S, Agar NYR. Molecular typing of meningiomas by desorption electrospray ionization mass spectrometry imaging for surgical decisionmaking. Int J Mass Spectrom 2015;377:690 – 8.

55. Calligaris D, Caragacianu D, Liu X, Norton I, Thompson CJ, Richardson AL, et al. Application of desorption electrospray ionization mass spectrometry imaging in breast cancer margin analysis. Proc Natl Acad Sci USA 2014;111:15184 –9.

56. Guenther S, Muirhead LJ, Speller AVM, Golf O, Strittmatter N, Ramakrishnan R, et al. Spatially resolved metabolic phenotyping of breast cancer by desorption electrospray ionization mass spectrometry. Cancer Res 2015;75:1828 –37.

57. Pavlides S, Whitaker-Menezes D, Castello-Cros R, Flomenberg N, Witkiewicz AK, Frank PG, et al. The reverse warburg effect aerobic glycolysis in cancer associated fibroblasts and the tumor stroma. Cell Cycle 2009; 8:3984 – 4001.

58. Balog J, Sasi-Szabo L, Kinross J, Lewis MR, Muirhead LJ, Veselkov K, et al. Intraoperative tissue identification using rapid evaporative ionization mass spectrometry. Sci Transl Med 2013;5.

59. Golf O, Strittmatter N, Karancsi T, Pringle SD, Speller AVM, Mroz A, et al. Rapid evaporative ionization mass spectrometry imaging platform for direct mapping from bulk tissue and bacterial growth media. Anal Chem 2015;87:2527–34.

60. Schaefer K-C, Szaniszlo T, Guenther S, Balog J, Denes J, Keseru M, et al. In situ, real-time identification of biological tissues by ultraviolet and infrared laser desorption ionization mass spectrometry. Anal Chem 2011; 83:1632– 40.

61. Agar NYR, Golby AJ, Ligon KL, Norton I, Mohan V, Wiseman JM, et al. Development of stereotactic mass spectrometry for brain tumor surgery. Neurosurg 2011;68: 280 –90.

62. Schaefer K-C, Balog J, Szaniszlo T, Szalay D, Mezey G, Denes J, et al. Real time analysis of brain tissue by direct combination of ultrasonic surgical aspiration and sonic spray mass spectrometry. Anal Chem 2011;83: 7729 –35

63. Kerian KS, Jarmusch AK, Pirro V, Koch MO, Masterson TA, Cheng L, Cooks RG. Differentiation of prostate cancer from normal tissue in radical prostatectomy specimens by desorption electrospray ionization and touch spray ionization mass spectrometry. Analyst 2015;140: 1090 – 8.

64. Chen C-H, Lin Z, Garimella S, Zheng L, Shi R, Cooks RG, Ouyang Z. Development of a mass spectrometry sampling probe for chemical analysis in surgical and endoscopic procedures. Anal Chem 2013;85:11843–50.

65. Bojko B, Pawliszyn J. In vivo and ex vivo spme: A low invasive sampling and sample preparation tool in clinical bioanalysis. Bioanalysis 2014;6:1227–39.

66. Fatou B, Wisztorski M, Focsa C, Ziskind M, Salzet M, Fournier I. Development of a novel instrument for exvivo and in-vivo real-time analysis. Oral session presented at: 63rd ASMS Conference on Mass Spectrometry and Allied Topics; 2015 May 31–Jun 4; St. Louis, MO.

67. Abdelmoula WM, Skraskova K, Balluff B, Carreira RJ, Tolner EA, Lelieveldt BPF, et al. Automatic generic registration of mass spectrometry imaging data to histology using nonlinear stochastic embedding. Anal Chem 2014;86:9204 –11.

68. Bemis KD, Harry A, Eberlin LS, Ferreira C, van de Ven SM, Mallick P, et al. Cardinal: An r package for statistical analysis of mass spectrometry-based imaging experiments. Bioinformatics 2015;31:2418 –20.

69. Krasny L, Hoffmann F, Ernst G, Trede D, Alexandrov T, Havlicek V, et al. Spatial segmentation of maldi ft-icr msi data: A powerful tool to explore the head and neck tumor in situ lipidome. J AmSoc Mass Spectrom 2015; 26:36 – 43.

70. Chen H, Gamez G, Zenobi R. What can we learn from ambient ionization techniques? J Am Soc Mass Spectrom 2009;20:1947– 63.

71. Eberlin LS, Dill AL, Costa AB, Ifa DR, Cheng L, Masterson T, et al. Cholesterol sulfate imaging in human prostate cancer tissue by desorption electrospray ionization mass spectrometry. Anal Chem 2010;82:3430 – 4.

72. Mandal MK, Yoshimura K, Chen LC, Yu Z, Nakazawa T, Katoh R, et al. Application of probe electrospray ionization mass spectrometry (pesi-ms) to clinical diagnosis: Solvent effect on lipid analysis. J Am Soc Mass Spectrom 2012;23:2043–7.

73. Calligaris D, Norton I, Feldman DR, Ide JL, Dunn IF, Eberlin LS, et al. Mass spectrometry imaging as a tool for surgical decision-making. J Mass Spectrom 2013; 48:1178 – 87.

74. Abbassi-Ghadi N, Veselkov K, Kumar S, Huang J, Jones E, Strittmatter N, et al. Discrimination of lymph node metastases using desorption electrospray ionisationmass spectrometry imaging. ChemCommun2014;50: 3661– 4.

CHAPTER 3

1. du Bois A, Reuss A, Pujade-Lauraine E, Harter P, Ray-Coquard I, Pfisterer J. Role of surgical outcome as prognostic factor in advanced epithelial ovarian cancer: a combined exploratory analysis of 3 prospectively randomized phase 3 multicenter trials: by the Arbeitsgemeinschaft Gynaekologische Onkologie Studiengruppe Ovarialkarzinom (AGO-OVAR) and the Groupe d'Investigateurs Nationaux Pour les Etudes des Cancers de l'Ovaire (GINECO). Cancer-Am Cancer Soc 2009;115:1234-44
2. Hoskins WJ, Bundy BN, Thigpen JT, Omura GA. The influence of cytoreductive surgery on recurrence-free interval and survival in small-volume stage III epithelial ovarian cancer: a Gynecologic Oncology Group study. Gynecol Oncol 1992;47:159-66
3. Nick AM, Coleman RL, Ramirez PT, Sood AK. A framework for a personalized surgical approach to ovarian cancer. Nat Rev Clin Oncol 2015;12:239-U78
4. Tucker SL, Gharpure K, Herbrich SM, Unruh AK, Nick AM, Crane EK, et al. Molecular biomarkers of residual disease after surgical debulking of high-grade serous ovarian cancer. Clin Cancer Res 2014;20:3280-8
5. Hamilton CA, Miller A, Miller C, Krivak TC, Farley JH, Chernofsky MR, et al. The impact of disease distribution on survival in patients with stage III epithelial ovarian cancer cytoreduced to microscopic residual: a Gynecologic Oncology Group study. Gynecol Oncol 2011;122:521-6
6. Aragones G, Saavedra P, Heras M, Cabre A, Girona J, Masana L. Fatty acid-binding protein 4 impairs the insulin-dependent nitric oxide pathway in vascular endothelial cells. Cardiovasc Diabetol 2012;11:72
7. Djousse L, Gaziano JM. Plasma levels of FABP4, but not FABP3, are associated with increased risk of diabetes. Lipids 2012;47:757-62
8. Holm S, Ueland T, Dahl TB, Michelsen AE, Skjelland M, Russell D, et al. Fatty Acid binding protein 4 is associated with carotid atherosclerosis and outcome in patients with acute ischemic stroke. Plos One 2011;6:e28785
9. Makowski L, Brittingham KC, Reynolds JM, Suttles J, Hotamisligil GS. The fatty acid-binding protein, aP2, coordinates macrophage cholesterol trafficking and inflammatory activity. Macrophage expression of aP2 impacts peroxisome proliferator-activated receptor gamma and IkappaB kinase activities. J Biol Chem 2005;280:12888-95
10. Elmasri H, Ghelfi E, Yu CW, Traphagen S, Cernadas M, Cao H, et al. Endothelial cell-fatty acid binding protein 4 promotes angiogenesis: role of stem cell factor/c-kit pathway. Angiogenesis 2012;15:457-68

11. Harjes U, Bridges E, McIntyre A, Fielding BA, Harris AL. Fatty acid-binding protein 4, a point of convergence for angiogenic and metabolic signaling pathways in endothelial cells. J Biol Chem 2014;289:23168-76

12. Harjes U, Bridges E, Gharpure KM, Roxanis I, Sheldon H, Miranda F, et al. Antiangiogenic and tumour inhibitory effects of downregulating tumour endothelial FABP4. Oncogene 2017;36:912-21

13. Herroon MK, Rajagurubandara E, Hardaway AL, Powell K, Turchick A, Feldmann D, et al. Bone marrow adipocytes promote tumor growth in bone via FABP4-dependent mechanisms. Oncotarget 2013;4:2108-23

14. Nieman KM, Kenny HA, Penicka CV, Ladanyi A, Buell-Gutbrod R, Zillhardt MR, et al. Adipocytes promote ovarian cancer metastasis and provide energy for rapid tumor growth. Nat Med 2011;17:1498-503

15. Sans M, Gharpure K, Tibshirani R, Zhang J, Liang L, Liu J, et al. Metabolic Markers and Statistical Prediction of Serous Ovarian Cancer Aggressiveness by Ambient Ionization Mass Spectrometry Imaging. Cancer Res 2017;77:2903-13

16. Eberlin LS, Tibshirani RJ, Zhang J, Longacre TA, Berry GJ, Bingham DB, et al. Molecular assessment of surgical-resection margins of gastric cancer by mass-spectrometric imaging. Proc Natl Acad Sci U S A 2014;111:2436-41

17. Tibshirani R. Regression shrinkage and selection via the Lasso. J Roy Stat Soc B Met 1996;58:267-88

18. Ke C, Li A, Hou Y, Sun M, Yang K, Cheng J, et al. Metabolic phenotyping for monitoring ovarian cancer patients. Sci Rep 2016;6:23334

19. Tania M, Khan MA, Song Y. Association of lipid metabolism with ovarian cancer. Curr Oncol 2010;17:6-11

20. Johanning GL, Lin TY. Unsaturated fatty acid effects on human breast cancer cell adhesion. Nutr Cancer 1995;24:57-66

21. Kim H, Rodriguez-Navas C, Kollipara RK, Kapur P, Pedrosa I, Brugarolas J, et al. Unsaturated Fatty Acids Stimulate Tumor Growth through Stabilization of beta-Catenin. Cell Rep 2015;13:495-503

22. Vinciguerra M, Carrozzino F, Peyrou M, Carlone S, Montesano R, Benelli R, et al. Unsaturated fatty acids promote hepatoma proliferation and progression through downregulation of the tumor suppressor PTEN. J Hepatol 2009;50:1132-41

23. Park JH, Vithayathil S, Kumar S, Sung PL, Dobrolecki LE, Putluri V, et al. Fatty Acid Oxidation-Driven Src Links Mitochondrial Energy Reprogramming and Oncogenic Properties in Triple-Negative Breast Cancer. Cell Rep 2016;14:2154-65

24. Monet M, Gkika D, Lehen'kyi V, Pourtier A, Vanden Abeele F, Bidaux G, et al. Lysophospholipids stimulate prostate cancer cell migration via TRPV2 channel activation. Biochim Biophys Acta 2009;1793:528-39

25. Sutphen R, Xu Y, Wilbanks GD, Fiorica J, Grendys EC, LaPolla JP, et al. Lysophospholipids are potential biomarkers of ovarian cancer. Cancer Epidem Biomar 2004;13:1185-+

CHAPTER 4

1. McDonnell LA, Heeren RMA. Imaging mass spectrometry. Mass Spectrom Rev 2007;26:606-43
2. Buchberger AR, DeLaney K, Johnson J, Li LJ. Mass Spectrometry Imaging: A Review of Emerging Advancements and Future Insights. Anal Chem 2018;90:240-65
3. Seeley EH, Caprioli RM. MALDI imaging mass spectrometry of human tissue: method challenges and clinical perspectives. Trends Biotechnol 2011;29:136-43
4. Schwamborn K, Caprioli RM. MALDI imaging mass spectrometry--painting molecular pictures. Mol Oncol 2010;4:529-38
5. Fletcher JS, Vickerman JC, Winograd N. Label free biochemical 2D and 3D imaging using secondary ion mass spectrometry. Curr Opin Chem Biol 2011;15:733-40
6. Winograd N, Garrison BJ. Biological Cluster Mass Spectrometry. Annual Review of Physical Chemistry, Vol 61 2010;61:305-22
7. Kompauer M, Heiles S, Spengler B. Atmospheric pressure MALDI mass spectrometry imaging of tissues and cells at 1.4-mu m lateral resolution. Nat Methods 2017;14:90-6
8. Cooks RG, Ouyang Z, Takats Z, Wiseman JM. Ambient mass spectrometry. Science 2006;311:1566-70
9. Laskin J, Lanekoff I. Ambient Mass Spectrometry Imaging Using Direct Liquid Extraction Techniques. Anal Chem 2016;88:52-73
10. Ifa DR, Eberlin LS. Ambient Ionization Mass Spectrometry for Cancer Diagnosis and Surgical Margin Evaluation. Clin Chem 2016;62:111-23
11. Takats Z, Wiseman JM, Gologan B, Cooks RG. Mass spectrometry sampling under ambient conditions with desorption electrospray ionization. Science 2004;306:471-3
12. Wiseman JM, Ifa DR, Song QY, Cooks RG. Tissue imaging at atmospheric pressure using desorption electrospray ionization (DESI) mass spectrometry. Angew Chem Int Edit 2006;45:7188-92
13. Van Berkel GJ, Kertesz V. Application of a Liquid Extraction Based Sealing Surface Sampling Probe for Mass Spectrometric Analysis of Dried Blood Spots and Mouse Whole-Body Thin Tissue Sections. Anal Chem 2009;81:9146-52
14. Kertesz V, Van Berkel GJ. Fully automated liquid extraction-based surface sampling and ionization using a chip-based robotic nanoelectrospray platform. J Mass Spectrom 2010;45:252-60

15. Hall Z, Chu YJ, Griffin JL. Liquid Extraction Surface Analysis Mass Spectrometry Method for Identifying the Presence and Severity of Nonalcoholic Fatty Liver Disease. Anal Chem 2017;89:5161-70

16. Roach PJ, Laskin J, Laskin A. Nanospray desorption electrospray ionization: an ambient method for liquid-extraction surface sampling in mass spectrometry. Analyst 2010;135:2233-6

17. Lanekoff I, Heath BS, Liyu A, Thomas M, Carson JP, Laskin J. Automated Platform for High-Resolution Tissue Imaging Using Nanospray Desorption Electrospray Ionization Mass Spectrometry. Anal Chem 2012;84:8351-6

18. Rao W, Pan N, Yang ZB. High Resolution Tissue Imaging Using the Single-probe Mass Spectrometry under Ambient Conditions. J Am Soc Mass Spectr 2015;26:986-93

19. Laskin J, Heath BS, Roach PJ, Cazares L, Semmes OJ. Tissue imaging using nanospray desorption electrospray ionization mass spectrometry. Anal Chem 2012;84:141-8

20. Nguyen S, Sontag R, Carson J, Corley R, Ansong C, Laskin J. Towards High-Resolution Tissue Imaging Using Nanospray Desorption Electrospray Ionization Mass Spectrometry Coupled to Shear Force Microscopy. J Am Soc Mass Spectr 2018;29:316-22

21. Blatherwick EQ, Van Berkel GJ, Pickup K, Johansson MK, Beaudoin ME, Cole RO, et al. Utility of spatially-resolved atmospheric pressure surface sampling and ionization techniques as alternatives to mass spectrometric imaging (MSI) in drug metabolism. Xenobiotica 2011;41:720-34

22. Tillner J, Wu V, Jones EA, Pringle SD, Karancsi T, Dannhorn A, et al. Faster, More Reproducible DESI-MS for Biological Tissue Imaging. J Am Soc Mass Spectr 2017;28:2090-8

23. Berglund SP, Lee HC, Nunez PD, Bard AJ, Mullins CB. Screening of transition and post-transition metals to incorporate into copper oxide and copper bismuth oxide for photoelectrochemical hydrogen evolution. Phys Chem Chem Phys 2013;15:4554-65

24. Eberlin LS, Ferreira CR, Dill AL, Ifa DR, Cheng L, Cooks RG. Nondestructive, histologically compatible tissue imaging by desorption electrospray ionization mass spectrometry. Chembiochem 2011;12:2129-32

25. Konermann L, Ahadi E, Rodriguez AD, Vahidi S. Unraveling the Mechanism of Electrospray Ionization. Anal Chem 2013;85:2-9

26. Eberlin LS, Ifa DR, Wu C, Cooks RG. Three-Dimensional Vizualization of Mouse Brain by Lipid Analysis Using Ambient Ionization Mass Spectrometry. Angew Chem Int Edit 2010;49:873-6

27. Almeida R, Berzina Z, Arnspang EC, Baumgart J, Vogt J, Nitsch R, et al. Quantitative Spatial Analysis of the Mouse Brain Lipidome by Pressurized Liquid Extraction Surface Analysis. Anal Chem 2015;87:1749-56

28. Haler JRN, Sisley EK, Cintron-Diaz YL, Meitei SN, Cooper HJ, Fernandez-Lima F. Workflow for fast lipid tissue screening using LESA-FT-ICR-MS. Analytical Methods 2019;11:2385-95

29. Sans M, Gharpure K, Tibshirani R, Zhang J, Liang L, Liu J, et al. Metabolic Markers and Statistical Prediction of Serous Ovarian Cancer Aggressiveness by Ambient Ionization Mass Spectrometry Imaging. Cancer Res 2017;77:2903-13

30. Doria ML, McKenzie JS, Mroz A, Phelps DL, Speller A, Rosini F, et al. Epithelial ovarian carcinoma diagnosis by desorption electrospray ionization mass spectrometry imaging. Sci Rep-Uk 2016;6:39219

31. Alessandra Tata MW, Manuela Ventura, Nicholas Bernards, Milan Ganguly, Adam Gribble, Bindesh Shrestha, Emma Bluemke, Howard J. Ginsberg, Alex Vitkin, Jinzi Zheng & Arash Zarrine-Afsar. Rapid Detection of Necrosis in Breast Cancer with Desorption Electrospray Ionization Mass Spectrometry. Sci Rep-Uk 2016;6

32. Eberlin LS, Dill AL, Golby AJ, Ligon KL, Wiseman JM, Cooks RG, et al. Discrimination of Human Astrocytoma Subtypes by Lipid Analysis Using Desorption Electrospray Ionization Imaging Mass Spectrometry. Angewandte Chemie-International Edition 2010;49:5953-6

33. Pirro V, Llor RS, Jarmusch AK, Alfaro CM, Cohen-Gadol AA, Hattabd EM, et al. Analysis of human gliomas by swab touch spray-mass spectrometry: applications to intraoperative assessment of surgical margins and presence of oncometabolites. Analyst 2017;142:4058-66

34. Gharpure KM, Pradeep S, Sans M, Rupaimoole R, Ivan C, Wu SY, et al. FABP4 as a key determinant of metastatic potential of ovarian cancer. Nat Commun 2018;9

35. Dill AL, Eberlin LS, Costa AB, Ifa DR, Cooks RG. Data quality in tissue analysis using desorption electrospray ionization. Anal Bioanal Chem 2011;401:1949-61

36. Zeng W, Musson DG, Fisher AL, Wang AQ. A new approach for evaluating carryover and its influence on quantitation in high-performance liquid chromatography and tandem mass spectrometry assay. Rapid Commun Mass Spectrom 2006;20:635-40

37. Hughes NC, Wong EYK, Fan J, Bajaj N. Determination of carryover and contamination for mass spectrometry-based chromatographic assays. Aaps J 2007;9:E353-E60

38. Kottke PA, Degertekin FL, Fedorov AG. Scanning Mass Spectrometry Probe: A Scanning Probe Electrospray Ion Source for Imaging Mass Spectrometry of Submerged Interfaces and Transient Events in Solution. Anal Chem 2010;82:19-22

CHAPTER 5

1. Buchholz TA, Somerfield MR, Griggs JJ, El-Eid S, Hammond ME, Lyman GH, et al. Margins for breast-conserving surgery with whole-breast irradiation in stage I and II invasive breast cancer: American Society of Clinical Oncology endorsement of the Society of Surgical Oncology/American Society for Radiation Oncology consensus guideline. J Clin Oncol 2014;32:1502-6
2. Maygarden SJ, Detterbeck FC, Funkhouser WK. Bronchial margins in lung cancer resection specimens: utility of frozen section and gross evaluation. Mod Pathol 2004;17:1080-6
3. Massard G, Doddoli C, Gasser B, Ducrocq X, Kessler R, Schumacher C, et al. Prognostic implications of a positive bronchial resection margin. Eur J Cardiothorac Surg 2000;17:557-65
4. Nick AM, Coleman RL, Ramirez PT, Sood AK. A framework for a personalized surgical approach to ovarian cancer. Nat Rev Clin Oncol 2015;12:239-U78
5. Han SS, Jang JY, Kim SW, Kim WH, Lee KU, Park YH. Analysis of long-term survivors after surgical resection for pancreatic cancer. Pancreas 2006;32:271-5
6. Zhang M, Li Z, Ma Y, Zhu G, Zhang H, Xue Y. Prognostic predictors of patients with carcinoma of the gastric cardia. Hepatogastroenterology 2012;59:930-3
7. Sanai N, Berger MS. Glioma extent of resection and its impact on patient outcome. Neurosurgery 2008;62:753-64; discussion 264-6
8. Macario A. What does one minute of operating room time cost? J Clin Anesth 2010;22:233-6
9. Mino-Kenudson M, Chirieac LR, Law K, Hornick JL, Lindeman N, Mark EJ, et al. A Novel, Highly Sensitive Antibody Allows for the Routine Detection of ALK-Rearranged Lung Adenocarcinomas by Standard Immunohistochemistry. Clin Cancer Res 2010;16:1561-71
10. Jones S. Personalized genomic analyses for cancer mutation discovery and interpretation. Science Translational Medicine 2015;7
11. Stummer W, Pichlmeier U, Meinel T, Wiestler OD, Zanella F, Hans-Jurgen R, et al. Fluorescence-guided surgery with 5-aminolevulinic acid for resection of malignant glioma: a randomised controlled multicentre phase III trial. Lancet Oncol 2006;7:392-401
12. Jermyn M, Mok K, Mercier J, Desroches J, Pichette J, Saint-Arnaud K, et al. Intraoperative brain cancer detection with Raman spectroscopy in humans. Science Translational Medicine 2015;7

13. Orringer DA, Pandian B, Niknafs YS, Hollon TC, Boyle J, Lewis S, et al. Rapid intraoperative histology of unprocessed surgical specimens via fibre-laser-based stimulated Raman scattering microscopy. Nat Biomed Eng 2017;1

14. Chughtai K, Heeren RMA. Mass Spectrometric Imaging for Biomedical Tissue Analysis. Chem Rev 2010;110:3237-77

15. Hsu CC, Dorrestein PC. Visualizing life with ambient mass spectrometry. Current Opinion in Biotechnology 2015;31:24-34

16. Wu CP, Dill AL, Eberlin LS, Cooks RG, Ifa DR. Mass spectrometry imaging under ambient conditions. Mass Spectrom Rev 2013;32:218-43

17. Norris JL, Caprioli RM. Analysis of Tissue Specimens by Matrix-Assisted Laser Desorption/Ionization Imaging Mass Spectrometry in Biological and Clinical Research. Chem Rev 2013;113:2309-42

18. Ifa DR, Eberlin LS. Ambient Ionization Mass Spectrometry for Cancer Diagnosis and Surgical Margin Evaluation. Clin Chem 2016;62:111-23

19. Eberlin LS, Norton I, Orringer D, Dunn IF, Liu XH, Ide JL, et al. Ambient mass spectrometry for the intraoperative molecular diagnosis of human brain tumors. P Natl Acad Sci USA 2013;110:1611-6

20. Jarmusch AK, Pirro V, Baird Z, Hattab EM, Cohen-Gadol AA, Cooks RG. Lipid and metabolite profiles of human brain tumors by desorption electrospray ionization-MS. P Natl Acad Sci USA 2016;113:1486-91

21. Schafer KC, Denes J, Albrecht K, Szaniszlo T, Balog J, Skoumal R, et al. In Vivo, In Situ Tissue Analysis Using Rapid Evaporative Ionization Mass Spectrometry. Angew Chem Int Edit 2009;48:8240-2

22. Balog J, Sasi-Szabo L, Kinross J, Lewis MR, Muirhead LJ, Veselkov K, et al. Intraoperative Tissue Identification Using Rapid Evaporative Ionization Mass Spectrometry. Science Translational Medicine 2013;5

23. Schafer KC, Szaniszlo T, Gunther S, Balog J, Denes J, Keseru M, et al. In Situ, Real-Time Identification of Biological Tissues by Ultraviolet and Infrared Laser Desorption Ionization Mass Spectrometry. Anal Chem 2011;83:1632-40

24. Fatou B, Saudemont P, Leblanc E, Vinatier D, Mesdag V, Wisztorski M, et al. In vivo Real-Time Mass Spectrometry for Guided Surgery Application. Sci Rep 2016;6:25919

25. Tibshirani R. Regression shrinkage and selection via the Lasso. J Roy Stat Soc B Met 1996;58:267-88

26. Calligaris D, Caragacianu D, Liu X, Norton I, Thompson CJ, Richardson AL, et al. Application of desorption electrospray ionization mass spectrometry imaging in breast cancer margin analysis. Proc Natl Acad Sci U S A 2014;111:15184-9

27. Guenther S, Muirhead LJ, Speller AV, Golf O, Strittmatter N, Ramakrishnan R, et al. Spatially resolved metabolic phenotyping of breast cancer by desorption electrospray ionization mass spectrometry. Cancer Res 2015;75:1828-37

28. Kang HS, Lee SC, Park YS, Jeon YE, Lee JH, Jung SY, et al. Protein and lipid MALDI profiles classify breast cancers according to the intrinsic subtype. Bmc Cancer 2011;11

29. Sans M, Gharpure K, Tibshirani R, Zhang J, Liang L, Liu J, et al. Metabolic Markers and Statistical Prediction of Serous Ovarian Cancer Aggressiveness by Ambient Ionization Mass Spectrometry Imaging. Cancer Res 2017;77:2903-13

30. Kertesz V, Van Berkel GJ. Fully automated liquid extraction-based surface sampling and ionization using a chip-based robotic nanoelectrospray platform. J Mass Spectrom 2010;45:252-60

31. Kertesz V, Ford MJ, Van Berkel GJ. Automation of a surface sampling probe/electrospray mass spectrometry system. Anal Chem 2005;77:7183-9

32. Laskin J, Heath BS, Roach PJ, Cazares L, Semmes OJ. Tissue imaging using nanospray desorption electrospray ionization mass spectrometry. Anal Chem 2012;84:141-8

33. Pagnotti VS, Chubatyi ND, McEwen CN. Solvent assisted inlet ionization: an ultrasensitive new liquid introduction ionization method for mass spectrometry. Anal Chem 2011;83:3981-5

34. Helmus MN, Gibbons DF, Cebon D. Biocompatibility: Meeting a Key Functional Requirement of Next- Generation Medical Devices. Toxicol Pathol 2008;36:70-80

35. Mokkaphan J, Banlunara W, Palaga T, Sombuntham P, Wanichwecharungruang S. Silicone Surface with Drug Nanodepots for Medical Devices. Acs Appl Mater Inter 2014;6:20188-96

36. Chen CH, Lin ZQ, Garimella S, Zheng LX, Shi RY, Cooks RG, et al. Development of a Mass Spectrometry Sampling Probe for Chemical Analysis in Surgical and Endoscopic Procedures. Anal Chem 2013;85:11843-50

37. Kut C, Chaichana KL, Xi JF, Raza SM, Ye XB, McVeigh ER, et al. Detection of human brain cancer infiltration ex vivo and in vivo using quantitative optical coherence tomography. Science Translational Medicine 2015;7

38. Rajaram N, Aramil TJ, Lee K, Reichenberg JS, Nguyen TH, Tunnell JW. Design and validation of a clinical instrument for spectral diagnosis of cutaneous malignancy. Appl Optics 2010;49:142-52

39. Zhang JL, Yu WD, Suliburk J, Eberlin LS. Will Ambient Ionization Mass Spectrometry Become an Integral Technology in the Operating Room of the Future? Clin Chem 2016;62:1172-4

CHAPTER 6

1. Torre LA, Trabert B, DeSantis CE, Miller KD, Samimi G, Runowicz CD, et al. Ovarian cancer statistics, 2018. CA Cancer J Clin 2018;68:284 –96.
2. Siegel RL, Miller KD, Jemal A. Cancer statistics, 2018. CA Cancer J Clin 2018;68:7–30.
3. Leong HS, Galletta L, Etemadmoghadam D, George J, Kobel M, Ramus SJ, et al. Efficient molecular subtype classification of high-grade serous ovarian cancer. J Pathol 2015;236:272–7.
4. Vang R, Shih IM, Kurman RJ. Ovarian low-grade and high-grade serous carcinoma pathogenesis, clinicopathologic and molecular biologic features, and diagnostic problems. Adv Anat Pathol 2009;16:267– 82.
5. Coleman RL, Monk BJ, Sood AK, Herzog TJ. Latest research and treatment of advanced-stage epithelial ovarian cancer. Nat Rev Clin Oncol 2013;10:211–24.
6. Williams TI, Toups KL, Saggese DA, Kalli KR, Cliby WA, Muddiman DC. Epithelial ovarian cancer: disease etiology, treatment, detection, and investigational gene, metabolite, and protein biomarkers. J Proteome Res 2007;6:2936 – 62.
7. Nick AM, Coleman RL, Ramirez PT, Sood AK. A framework for a personalized surgical approach to ovarian cancer. Nat Rev Clin Oncol 2015;12:239 – 45.
8. Macario A. What does one minute of operating room time cost? J Clin Anesth 2010;22:233– 6.
9. Jones S, Anagnostou V, Lytle K, Parpart-Li S, Nesselbush M, Riley DR, et al. Personalized genomic analyses for cancer mutation discovery and interpretation. Sci Transl Med 2015;7:283ra53.
10. Mino-Kenudson M, Chirieac LR, Law K, Hornick JL, Lindeman N, Mark EJ, et al. A novel, highly sensitive antibody allows for the routine detection of ALK-rearranged lung adenocarcinomas by standard immunohistochemistry. Clin Cancer Res 2010;16:1561–71.
11. Ifa DR, Eberlin LS. Ambient ionization mass spectrometry for cancer diagnosis and surgical margin evaluation. Clin Chem 2016;62:111–23.
12. Jarmusch AK, Pirro V, Baird Z, Hattab EM, Cohen-Gadol AA, Cooks RG. Lipid and metabolite profiles of human brain tumors by desorption electrospray ionization-MS. Proc Natl Acad Sci U S A 2016;113:1486 –91.
13. Eberlin LS, Tibshirani RJ, Zhang J, Longacre TA, Berry GJ, Bingham DB, et al. Molecular assessment of surgical-resection margins of gastric cancer by massspectrometric imaging. Proc Natl Acad Sci U S A 2014;111:2436-41.

14. Calligaris D, Caragacianu D, Liu X, Norton I, Thompson CJ, Richardson AL, et al. Application of desorption electrospray ionization mass spectrometry imaging in breast cancer margin analysis. Proc Natl Acad Sci U S A 2014;111:15184 –9.

15. Eberlin LS, Norton I, Dill AL, Golby AJ, Ligon KL, Santagata S, et al. Classifying human brain tumors by lipid imaging with mass spectrometry. Cancer Res 2012;72: 645–54.

16. Guenther S, Muirhead LJ, Speller AV, Golf O, Strittmatter N, Ramakrishnan R, et al. Spatially resolved metabolic phenotyping of breast cancer by desorption electrospray ionization mass spectrometry. Cancer Res 2015;75:1828 –37.

17. Zhang J, Yu W, Ryu SW, Lin J, Buentello G, Tibshirani R, et al. Cardiolipins are biomarkers of mitochondria-rich thyroid oncocytic tumors. Cancer Res 2016;76:6588 – 97.

18. Dill AL, Eberlin LS, Costa AB, Zheng C, Ifa DR, Cheng LA, et al. Multivariate statistical identification of human bladder carcinomas using ambient ionization imaging mass spectrometry. Chemistry 2011;17:2897–902.

19. Schafer KC, Denes J, Albrecht K, Szaniszlo T, Balog J, Skoumal R, et al. In vivo, in situ tissue analysis using rapid evaporative ionization mass spectrometry. Angew Chem Int Ed Engl 2009;48:8240 –2.

20. Fatou B, Saudemont P, Leblanc E, Vinatier D, Mesdag V, Wisztorski M, et al. In vivo real-time mass spectrometry for guided surgery application. Sci Rep 2016;6:25919.

21. Zhang JL, Rector J, Lin JQ, Young JH, Sans M, Katta N, et al. Nondestructive tissue analysis for ex vivo and in vivo cancer diagnosis using a handheld mass spectrometry system. Sci Transl Med 2017;9:eaan3968.

22. Schafer KC, Szaniszlo T, Gunther S, Balog J, Denes J, Keseru M, et al. In situ, real-time identification of biological tissues by ultraviolet and infrared laser desorption ionization mass spectrometry. Anal Chem 2011; 83:1632– 40.

23. Saudemont P, Quanico J, Robin YM, Baud A, Balog J, Fatou B, et al. Real-time molecular diagnosis of tumors using water-assisted laser desorption/ionization mass spectrometry technology. Cancer Cell 2018;34:840 – 51.e4.

24. Laskin J, Lanekoff I. Ambient mass spectrometry imaging using direct liquid extraction techniques. Anal Chem 2016;88:52–73.

25. Doria ML, McKenzie JS, Mroz A, Phelps DL, Speller A, Rosini F, et al. Epithelial ovarian carcinoma diagnosis by desorption electrospray ionization mass spectrometry imaging. Sci Rep 2016;6:39219.

26. Sans M, Gharpure K, Tibshirani R, Zhang J, Liang L, Liu J, et al. Metabolic markers and statistical prediction of serous ovarian cancer aggressiveness by ambient ionization mass spectrometry imaging. Cancer Res 2017; 77:2903–13.

27. Phelps DL, Balog J, Gildea LF, Bodai Z, Savage A, El-Bahrawy MA, et al. The surgical intelligent knife distinguishes normal, borderline and malignant gynaecological tissues using rapid evaporative ionisation mass spectrometry (REIMS). Br J Cancer 2018;118:1349 –58.

28. Lengyel E. Ovarian cancer development and metastasis. Am J Pathol 2010;177:1053– 64.

29. Kurman RJ, Shih Ie M. Molecular pathogenesis and extraovarian origin of epithelial ovarian cancer–shifting the paradigm. Hum Pathol 2011;42:918 –31.

30. Zhang JL, Yu WD, Suliburk J, Eberlin LS. Will ambient ionization mass spectrometry become an integral technology in the operating room of the future? Clin Chem 2016;62:1172– 4.

31. Peng Y, Austin DE. New approaches to miniaturizing ion trap mass analyzers. Trends Analyt Chem 2011;30: 1560 –7.

32. Douglas DJ, Frank AJ, Mao DM. Linear ion traps in mass spectrometry. Mass Spectrom Rev 2005:24:1-29.

33. Marshall AG, Hendrickson CL. High-resolution mass spectrometers. Annu Rev Anal Chem 2008;1:579 –99.

34. Tibshirani R. Regression shrinkage and selection via the lasso. J Roy Stat Soc B Met 1996;58:267– 88.

35. Robin X, Turck N, Hainard A, Tiberti N, Lisacek F, Sanchez JC, Muller M. pROC: an open-source package for R and S+ to analyze and compare ROC curves. BMC Bioinformatics 2011;12:77.

36. James G, Witten D, Hastie T, Tibshirani R. An introduction to statistical learning: with applications in R. New York: Springer; 2013. 426 pp.

37. Devine PJ, Perreault SD, Luderer U. Roles of reactive oxygen species and antioxidants in ovarian toxicity. Biol Reprod 2012;86:27.

38. Denkert C, Budczies J, Kind T, Weichert W, Tablack P, Sehouli J, et al. Mass spectrometry-based metabolic profiling reveals different metabolite patterns in invasive ovarian carcinomas and ovarian borderline tumors. Cancer Res 2006;66:10795– 804.

39. Wiklund NP, Samuelson UE, Brundin J. Adenosine modulation of adrenergic neurotransmission in the human fallopian tube. Eur J Pharmacol 1986;123:11– 8.

40. Cometti B, Dubey RK, Imthurn B, Jackson EK, Rosselli M. Oviduct cells express the cyclic amp adenosine pathway. Biol Reprod 2003;69:868 –75.

Vita

Marta Sans Escofet was born in Castellar del Valles, Barcelona, Spain. After finishing High School, Marta moved to the US where she received an athletic scholarship as a tennis student-athlete and pursued a bachelor's degree in Chemistry at the University of New Orleans. In August 2015, she entered the Graduate School at the University of Texas at Austin to begin her doctoral studies in Analytical Chemistry under the advising of Prof. Livia S. Eberlin.

Permanent email address: martasansescofet@gmail.com

This dissertation was typed by the author.